AD-A125 760 INTERPRETATION OF HYDROGRAPHIC FEATURES USING LANDSAT IMAGES(U) NAVAL OCEAN RESEARCH AND DEVELOPMENT ACTIVITY NSTL STATION MS R A ARNONE ET AL. JUN 81 NORDA-39 1/3

UNCLASSIFIED F/G 8/10 NL

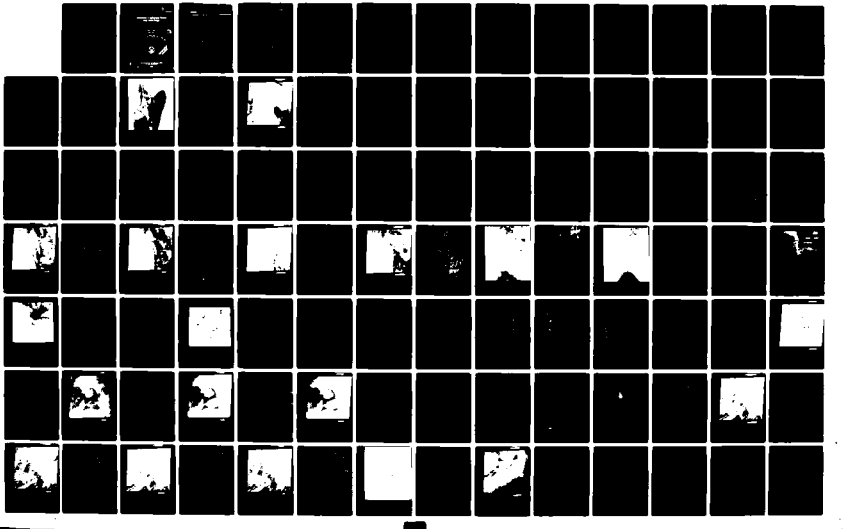

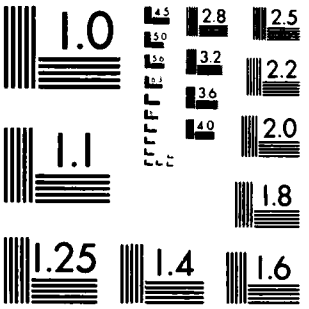

AD A125760

[redacted]

Robert A. Arnone
B. Edward Arthur, Jr.

Oceanography Division
Naval Oceans and Technology Laboratory

June 1981

Distribution Unlimited

[redacted]

[redacted]

[redacted] interpretation of [redacted] provides a basis for exploitation of [redacted] hydrographic features and coastal processes.

With funding from the Defense Mapping Agency, Hydrographic/Topographic Center, the Naval Ocean Research and Development Activity has prepared this document to assist in using Landsat data in the preparation and updating of hydrographic charts.

It is intended that this document be the forerunner of a series of interpretation keys directed at exploiting the multi-disciplines of remote sensing technology for hydrographic charting.

D. J. Phelps

D.T. Phelps, Captain, USN
Commanding Officer
NORDA

EXECUTIVE SUMMARY

Landsat imagery provides a means for updating hydrographic charts. This manual is designed to instruct analysts in interpreting hydrographic features and coastal processes using Landsat imagery. Explanations are given of both the physical processes and remote sensing technology as related to interpretation of hydrographic features. Through comparisons of hydrographic charts, aerial photography and the various spectral channels of Landsat imagery, the manual clearly illustrates examples of interpreting hydrographic features and processes. Various case histories, illustrating different coastal regimes and hydrographic features, are presented with descriptions of the techniques used for interpretation. Methodologies for exploitation of Landsat imagery for updating nautical charts (inclusive of hazard detection, chart revision, zones of safe passages and survey planning) are described.

ACKNOWLEDGEMENTS

Appreciation is extended to DMA's Multi-Sensor Hydrographic Exploitation Project/Program for providing funds for completion of this work. The generous suggestions of J. Hammack (DMA) are appreciated. The U. S. Geological Survey EROS Data Center at Sioux Falls, S. D., provided prompt and excellent quality Landsat imagery and aerial photography. Thanks is also extended to NORDA's Technical Information Branch for their graphics and reproduction efforts. Finally, a strong appreciation is extended to the other members of the Remote Sensing Branch for their comments/suggestions and typing efforts.

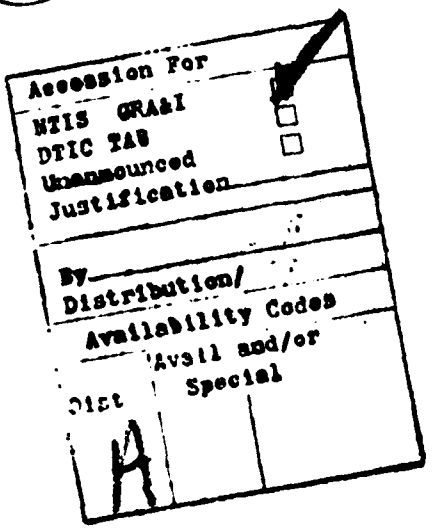

CONTENTS

ILLUSTRATIONS

I. INTRODUCTION

I. Introduction

Landsat satellite imagery is currently used to interpret subsurface oceanographic features and processes. Interpretation of Landsat imagery can provide detection of obstructions to navigation such as shoals, reefs, ships, and changes in bathymetry. Landsat provides a rapid world coverage of the shallow water areas and provides a means of updating navigation charts in areas where dynamically changing coastlines and subbottom features occur. Landsat can be used to determine the relative location and shape of hydrographic obstructions to navigation and provide a rapid technique to be used for updating charts and survey planning.

The objective of this report is to provide the analyst a useful interpretation key of hydrographic obstructions and oceanographic processes as viewed from aerial photography and Landsat imagery. The key is directed at acquainting the analyst with a basic understanding of some oceanographic principles/processes and how they can be used for hydrographic interpretation of Landsat imagery. A series of illustrated case histories explain the techniques of interpretation.

The hydrographic analysis of imagery is basically divided into two categories: I. The direct detection of an obstruction such as a reef, shoal or shallow water area. II. The interpretation of an obstruction through a secondary indicator, such as breaking waves which indicate shallow water. The hydrographic analysis of an image requires an understanding and familiarization with oceanographic processes and remote sensing technology to prevent misinterpretation of hydrographic features.

The selected case histories will familiarize the analyst with numerous examples of each of these analysis procedures and oceanographic processes in addition to potentially misinterpreted physical phenomenon.

II. INTERPRETATION ELEMENTS IN HYDROGRAPHIC INTERPRETATION

II. Interpretation Elements in Hydrrographic Interpretation

Besides a familiarization with Landsat imagery and a general understanding of both oceanographic processes and remote sensing technology, the analyst essentially uses nine basic elements in image interpretation. These include: shape, size, tone, color, shadow, pattern, texture, site, association and resolution (Reeves, 1975; Holtz, 1973). The analyst should understand how these elements apply to each hydrographic interpretation. Figure 1, which is a color aerial photograph of North Cat Cay in the Bahama Islands taken at 6000 ft, and Figure 2, which is a Landsat image (channel 4) taken in the Bimini Islands in the Bahamas, illustrate these interpretative elements. (North Cat Cay is located within the Landsat image in the island chain (C).)

A. Shape

The shape or form of some hydrographic features is so distinctive that their identities may be discerned solely by this criterion. Figure 1 illustrates examples of interpretation through shape for such features as channels (A), houses (B), boats and docks (C), submerged spits (D), and islands (E).

B. Size

The size of an object refers to its actual surface or volume dimensions. An interpreter can use size along with shape to make an initial identification of a feature. Knowing the scale of the standard Landsat photographic product (1:1,000,000), the actual ground size of an object on the photograph can be determined.

Size can be directly used to identify an object. Shape is a useful factor in interpretation, but without knowledge of size, features may be misinterpreted.

Without knowledge of the scale of a photograph, the known size of objects may be used to determine the approximate scale. A few examples of such features, illustrated in Figure 1, include tennis courts (L), houses (B), and boats (C).

C. Tone and Color

Because different surface materials and water types reflect light differently, variations in the tone, color, or density occur. Use of this interpretation element is extremely powerful and requires a strong understanding of earth reflectance properties and remote sensing technology. Some examples illustrated in Figure 1 include a relative estimate of water depth in the homogeneous lighter areas; lighter tones represent shallower water, darker tones represent deeper water (as shown in areas F and F', respectively). Also illustrated in this figure are isolated patches of turtle grass (thalassia) (J) which are located within a large sand field and have a slightly darker, unique tone than the brighter sand. Figure 2 illustrates similar tone characteristics in regard to estimating water depth. The Bimini reef appears much lighter than the neighboring deeper waters. The far left side of Figure 2 (East Florida Coast) illustrates the lighter shallow near coastal water grading to the darker offshore waters (D). Use of tone for water depth should not be confused with differences in bottom types/reflection properties or differences with water mass turbidity boundaries, as described later. An example on Figure 2 is the dark tone due to deep water (K) and the dark tone due to bottom vegetation (L).

D. Shadow

Presence of shadow can be either an aid or a hindrance to the interpreter. It can provide information on the size and shape of features based on the shadow they cast. Conversely, shadow may limit the amount of detail in the image by substantially reducing the amount of reflected light. Boats, buildings, and trees are examples of shadow illustrated in Figure 1 at annotation O.

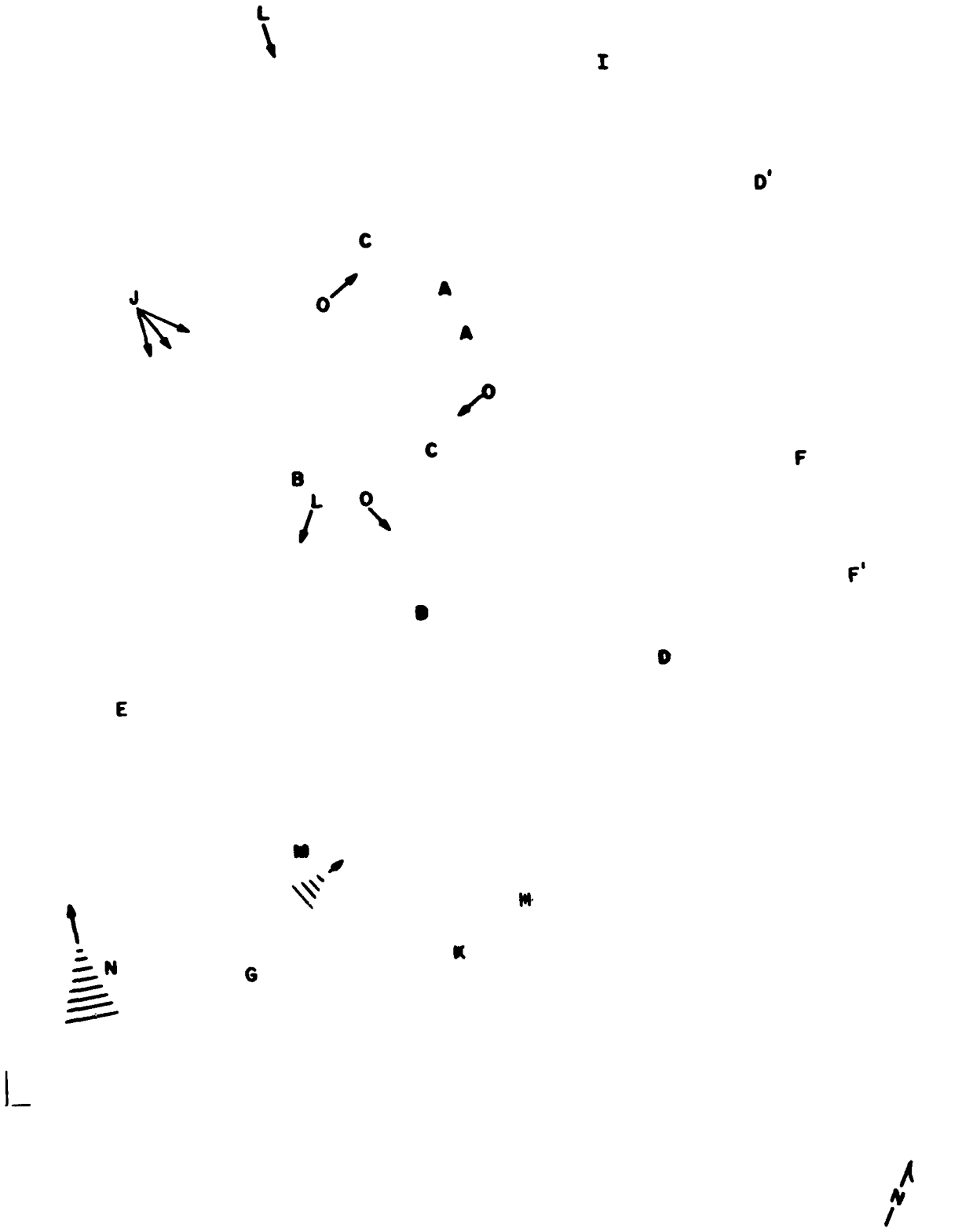

(AERIAL PHOTOGRAPH) NORTH CAT CAY, BAHAMAS
10 JUL 79

Figure 1. Interpretation elements color aerial photograph (1:12,000), Cat Cay, Bahamas, July 10, 1979

(LANDSAT) BAHAMAS 25 FEB 77

Figure 2. Interpretation elements, Landsat Bimini Reef, Bahamas (25 Feb 77)

E. Pattern

The pattern or repetition of features is characteristic of many manmade features and some naturally occurring hydrographic features. Figure 1 has several examples on use of pattern as an interpretation guide. Dredged channels (A) appear very similar and have a definite pattern in this image, as they will have in other images. The formation and resulting sand bars and spit pattern (D) are typically repetitious in beach processes. The oval-shaped bright area in the lower left of Figure 1 (G) is sunglint and is a pattern with which an analyst should become familiar in order to recognize it on aerial photographs and Landsat images. In the Landsat image (Figure 2), patterns of strings of clouds (F) are typically observed. Smoke from an industry (M) should not be confused with the strings of clouds. The analyst can note the direction of the smoke and the cloud strings and assume wind direction. This image also illustrates the general patterns of islands, reefs, and deep waters with which a hydrographic interpreter should be familiar.

F. Texture

The visible impressions of roughness or smoothness created by some features are valuable clues in interpretation. Figure 1 illustrates some examples of texture. Within the sunglint area (G), the sea surface reflectance shows a texture typical of the mixing of several surface wave groups traveling in different directions. Close examination of this texture shows at least two sets of waves (M, N) as well as a change in directionality resulting from wave refraction (K), which is explained in Appendix A. The texture of the sea bottom in the low-energy back lagoon area (I), illustrated in Figure 1, has a somewhat regular matted appearance characteristic of patchy vegetation areas (dark tone) in a matrix of lighter sand areas. Figure 2 illustrates examples of texture by striated features of variations in bottom reflectance (G) that result from changing bottom types. Dendritic bottom channels in the sand bottom, migrating away from the Bimini Island chain (H), also illustrate a unique texture.

G. Site

The location of features with respect to the local terrain and other features is often useful in interpretation. Use of this interpretative technique for hydrographic applications requires a basic understanding in oceanographic and coastal processes in addition to coastal geomorphology. Figure 1 illustrates several examples of the use of site in interpretation. The large gap between the islands near the bottom center of the image (K) should aid the interpreter in defining the generated tidal current directions in this area. A fan of bottom or suspended sediment and/or patterns of bottom vegetation will often indicate the major current direction (H). Also note the placement of the large dredged channels (A) and that their site location connects harbors with deeper water.

Note also that between the major channels (A) numerous bright tone striations occur in the sea bottom. Because of their proximity to the harbor, it is possible that boats are stirring the bottom and redistributing the vegetation, resulting in boat trails.

H. Association

Some hydrographic features are commonly associated with other hydrographic features or processes, and one tends to indicate or confirm the other. For example, in Figure 1 the surface wave pattern tends to refract around the channel entrance (K). Refraction tends to be a good interpretive aid in determining bottom shape in shallow areas (see Appendix A). The submerged sand spit formations at D and D' are indications of long-term current processes. In this case, tidal flow patterns are gradually building the spits. The lack of sand features in the western portion

of Figure 1, as compared to the eastern, illustrates an erosional or high-energy environment in the west and the resulting deposition and accretion of the island on the east in the lagoon. Similarly in Figure 2, the striated banding patterns of bottom features (G), which are represented by migration of sand and bottom vegetating patterns, characterize the dominant current directions occurring within the bank. These complex patterns are shown as migrating toward and inundating the relic reef system (I). Reefs are characterized by patchy tonal differences, since they exhibit a highly variable water depth and bottom reflectance, as compared with the more contiguous brighter tonal properties of the migrating sand fields, illustrated south of the reef (I). From use of association, the direction from which the reef is extending is toward the northwest. Therefore, hydrographic surveys will most likely be required on the northwestern portion of the island for chart updates.

I. Resolution

Resolution places a practical limit on interpretation. Some objects are too small, or are otherwise lacking (i.e. insufficient contrast), to form a distinguishable feature on the image. The ability of an imaging system (including lens, filter, detector, emulsion, and processing) to record fine detail in a distinguishable manner is referred to as the resolution, or resolving power, of the system. The analyst should understand the resolution limitations of the product/system he is interpreting and if possible use enhancement techniques (processing, contrast stretching, filtering) to increase the apparent resolution. Several examples of improving the detail in images will be illustrated in later case histories.

The use of the Landsat multispectral scanning system for interpretation of hydrographic features/obstructions can provide more interpretive techniques than the nine previously described elements. The interpreter will need to understand how earth surface reflectance and hydrographic features interact and are imaged in each of the four spectral channels on Landsat. The temporal variation of hydrographic features also provides a powerful tool for the interpreter. Examples of these types of interpretive techniques will also be illustrated in case histories.

III. LANDSAT - SYSTEM

III. Landsat - System

The Landsat system to date is composed of three individual satellites, Landsats 1, 2 and 3. Details and descriptions of these satellites are contained in Figure 3.

A. Basic Principles of the Electromagnetic Spectrum

Prior to illustrating the numerous techniques and case histories in Landsat interpretation, it is important to understand exactly what Landsat is sensing and the operation of how the sensing is done. In this way the analyst will have a better insight for interpretation of hydrographic imagery.

Landsat has two sensor systems on board, Return Beam Vidicon (RBV) and the Multispectral Scanning System (MSS), which sense the earth's surface in different regions of the electromagnetic spectrum. The RBV system senses the earth's surface in three spectral regions, Camera 1 (0.475-0.575 μm), Camera 2 (0.580-0.680 μm), and Camera 3 (0.690-0.830 μm). The MSS systems on Landsat, illustrated in the case histories, sense the earth's surface in four regions of the electromagnetic spectrum:

Channel 4	0.5-0.6 μm	(green)
Channel 5	0.6-0.7 μm	(red)
Channel 6	0.7-0.8 μm	reflective IR
Channel 7	0.8-1.1 μm	reflective IR

The position of where these regions are located in the electromagnetic spectrum is illustrated in Figure 4. The electromagnetic spectrum separates waves or particles of energy (radiation) based on wavelength and/or frequency. Radiation energy of visible light occupies a small region of the electromagnetic spectrum in which two of Landsat's MSS channels (4 and 5) are located. Visible light ranges from 0.4 μm (blue light) to 0.7 μm (red light). Channel 4 corresponds to the region of the spectrum of approximately green light, and Channel 5 corresponds to approximately the visible red portion of the spectrum.

Landsat's MSS, in viewing the earth's surface, measures the reflected radiation of the sun's rays in these specific regions. Reflected radiation is measured in units from 0 to 127, with 127 being maximum reflection in Channels 4, 5, and 6, and in Channel 7 values range from 0 to 63. Channels 6 and 7 are in the near-infrared range and measure the reflectance of the sun's rays off the surface of the earth in this spectral region, which is outside the range of light sensitivity of the human eye (Williams and Carter, 1976).

The importance of the spectral sensing of earth surface features is that materials reflect radiation differently in each of the MSS's four channels. An understanding of the spectral reflection of surface features gives the analyst a powerful tool for interpretation. For example, water, for the most part, totally absorbs the sun's rays (see Section III. B) and only poorly reflects infrared (IR) radiation. Thus, clear water will appear black or measure near-zero radiation on Channels 6 and 7 (0-20 in Channel 6 and 0-10 in Channel 7), whereas land features will reflect IR radiation and will not appear black. However, in the visible channels (4 and 5), water and the ocean bottom will both reflect the sun's rays, dependent on the water color, depth and/or bottom reflectance characteristics (approximate values of 0-60 in Channel 5 and 30-127 in Channel 4). It is therefore evident that the IR channels provide an interpretive technique of distinguishing water and land. Interpretive techniques using surface reflectance characteristics will be illustrated in the following case histories.

B. Basic Water Optical Properties

The reflectance of the earth's surface in each of the MSS's channels depends on: (1) the amount of incoming (incident) radiation at each of the channels and (2) the type of material being illuminated. Incoming radiation at the earth's surface from the sun's rays has

January 1981

LANDSAT SATELLITE DESCRIPTIONS

SATELLITE	LAUNCH DATE	SENSOR	SPECTRAL RESPONSE (Micrometers)	AVAILABLE DATA FILM	AVAILABLE DATA CCT's	RESOLUTION (Meters)	COMMENTS
Landsat 1 (formerly ERTS)	Jul 72	MSS	Band 4 0.5-0.6 5 0.6-0.7 6 0.7-0.8 7 0.8-1.1	XX (Electron Beam Recorder (EBR) generated	XX	56 x 79	MSS ceased operation in Jan 1978
		RBV	Camera 1 .475-.575 2 .580-.680 3 .690-.830	XX EBR generated		30	RBV ceased operation in Aug 1972
Landsat 2	Jan 75 (9 day delay from Landsat 1)	MSS	Band 4 0.5-0.6 5 0.6-0.7 6 0.7-0.8 7 0.8-1.1	XX EBR generated until Feb 79 Laser Beam Recorder (LBR) after Feb 79		56x79	MSS shutdown Jan 80 restarted Jun 80
		RBV	Camera 1 .475-.575 2 .580-.680 3 .690-.830	XX EBR generated until Feb 79 LBR after Feb 79		30	
Landsat 3	Mar 78 (9 day delay from Landsat 2)	MSS	Band 4 0.5 - 0.6 5 0.6-0.7 6 0.7-0.8 7 0.8-1.1 8 10.4-12.6	XX	XX	56x79	MSS ceased operation Dec 80 Band 8 ceased operation Dec 80
		RBV	Camera 1 & 2 .505-.750	XX LBR generated after Sep 80	XX After Sep 80	30	
Landsat D	Planned 1982 or 1983	MSS	Band 4 0.5-0.6 5 0.6-0.7 6 0.7-0.8 7 0.8-1.1 8 10.4-12.6			56x79	Landsat D & D' will have 16 day cycle
Landsat D'	To follow Landsat D	MSS	Band 4 0.5-0.6 5 0.6-0.7 6 0.7-0.8 7 0.8-1.1 8 10.4-12.6			56x79	
		TM	Band 1 .45-.52 2 .52-.60 3 .63-.69 4 .76-.90 5 1.55-1.75 6 10.4-12.5 7 2.08-2.35			30	

Figure 3. Landsat satellite descriptions

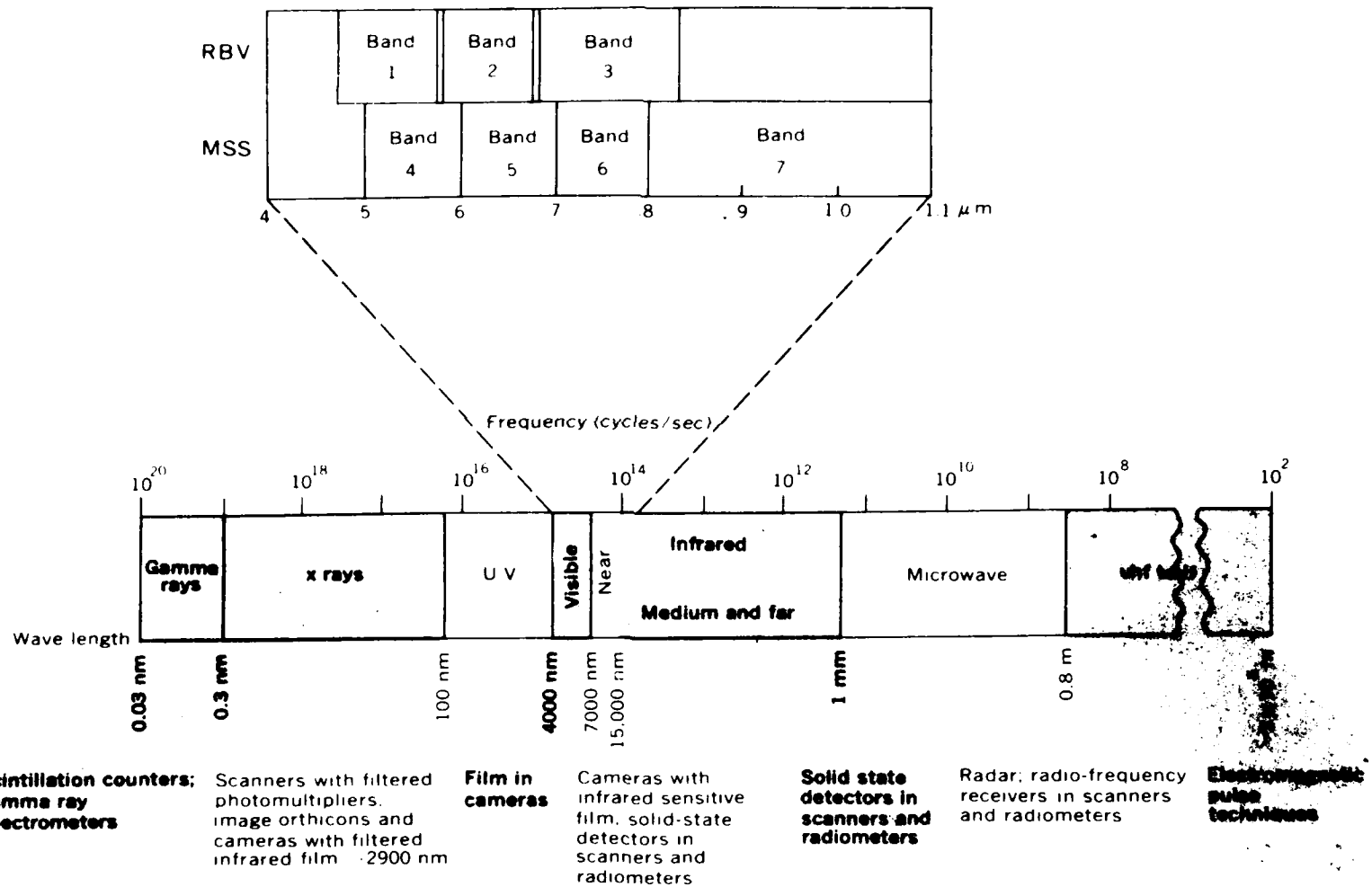

Figure 4. The electromagnetic spectrum and Landsat sensor relationships. (Modified from Parker and Wolff, 1965, Remote Sensing: International Science and Technology, July.)

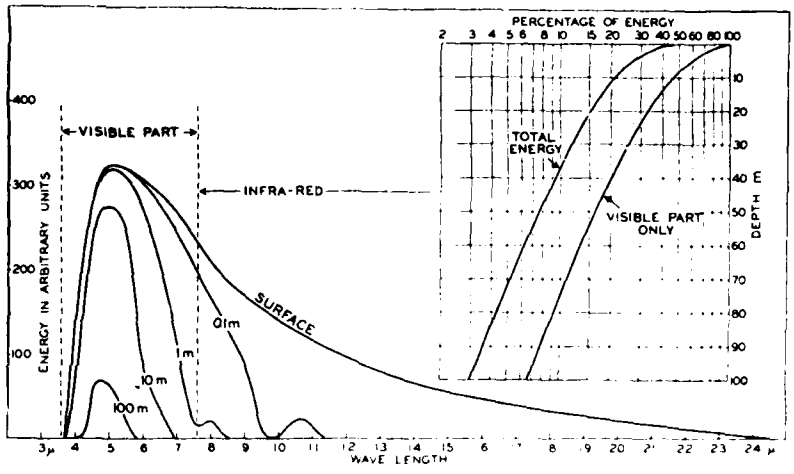

Figure 5. Schematic representation of the energy spectrum of the radiation from the sun and the sky which penetrates the sea surface, and of the energy spectra in pure water at depths of 0.1, 1, 10, and 100m, Inset: Percentages of total energy and of energy in the visible part of the spectrum reaching different depths. (Sverdrup, et al., 1942)

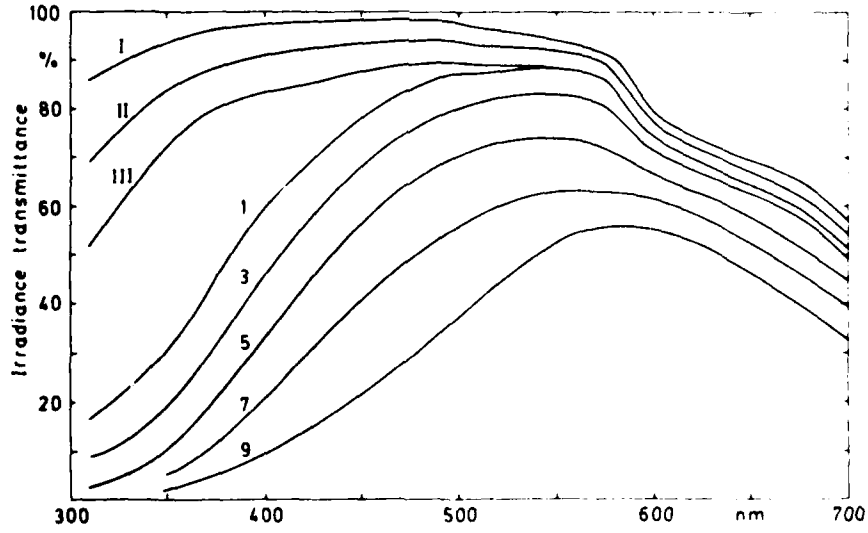

Figure 6. Transmittance per meter of downward radiant energy in the surface layer for optical water types. Oceanic types I, II, III, and coastal types 1, 3, 5, 7, 9 (Jerlov, 1976)

a spectral distribution illustrated in Figure 5. Note that the sun's maximum incoming radiation occurs in the visible part of the spectrum and that the MSS channels cover this major region of the electromagnetic spectrum. For hydrographic considerations, the spectral radiation that penetrates the sea surface is also represented in Figure 5. Note the reduction in intensity of incoming radiation as the depth of water increases. Also note that the energy in the visible part of the spectrum penetrated to an appreciable depth while the ultraviolet (UV) and IR radiation only slightly penetrate the water surface. Within the visible portion of the spectrum, Figure 5 illustrates that the radiation energy at 0.48 μm (blue-green light) penetrates water the deepest. Radiation energy at 0.6-0.75 μm (red) is shown to penetrate in only shallow, 1-10 meter waters.

Penetration dependence on water depth and wavelength is important in Landsat applications, since it is directly proportional to the intensity of radiation which Landsat sensors are measuring. Therefore, Channel 4 (0.5-0.6 μm) will measure reflectant energy in water at deeper depths than Channel 5 (0.6-0.7 μm). Since IR radiant energy does not penetrate deeper than ≈0.5 meter in Channel 6 and 0.1 meter in Channel 7, only a small amount of radiation measured in these channels arises from within the water. (Another source of radiation measured by the Landsat sensors arises from the reflection of the sea surface. Reflected radiation will be further discussed later and is a major source of IR radiation measured in water in Channels 6 and 7.)

What has been illustrated has been for only one water type, and it is evident that there are numerous water types ranging from muddy, very turbid, coastal waters to clear oceanic waters. Landsat does distinguish differences in water types or color changes, as will be shown later. This distinction results from variation in spectral reflectance of different waters.

Figure 6 illustrates the spectral transparency of radiant energy for different types of ocean and coastal waters. The classification of characteristic optical water types comes from Jerlov (1976). Note that as the water becomes more turbid, the percent transmittance decreases as does the depth to which radiant energy penetrates. This depth of penetration explains why one can see deeper in clear water than in turbid water. Also note that, as the water becomes more turbid, a spectral shift from the shorter wavelengths (0.4-0.45 m; blue) to longer wavelengths (0.5-0.55 m; brown) occurs. The spectral transmittance of deep water is indirectly proportional to the water's spectral reflectance, which is measured by Landsat. Thus, clear deepwater appears dark, and deep turbid water appears brighter in Landsat's MSS. (Brighter water tones in Landsat imagery result from increased backscattering and reflection of radiation from suspended particles in turbid water.) Tonal variations in water color is markedly evident in Landsat's visible channels, though distinctions are also observed in the IR Channels. In very shallow waters where radiant energy reflects off the bottom, the reflectance measured by Landsat is dependent on the bottom reflectance and the spectral transmittance of the water. Clear waters over a bright, highly reflective sand bottom will appear bright in Channel 4, whereas clear water over a poorly reflective (vegetation) bottom will appear dark. The clarity of the water, as noted in Figure 6, defines the depth to which the bottom can be sensed with the Landsat's visible channels. Problems occur with interpretation of Landsat at deciphering bright tonal areas as deep turbid water versus shallow clear water with high bottom reflectance and, similarly, deciphering a tonal area as deep clear water versus shallow clear water with a dark vegetation bottom. Though this problem may appear unsolvable, use of pattern and association interpretation elements can be used successfully. Examples of interpretation techniques

that can help resolve some of these discrepancies will be illustrated in the case histories.

C. Multispectral Scanner (MSS) Subsystem

1. Operation

The MSS gathers data by imaging the surface of the earth in four spectral channels simultaneously through the same optical system. The MSS scans cross track swaths of 185 km (100 nautical miles) width, imaging six scan lines across in each of the four spectral bands simultaneously. The object plane is scanned by means of an oscillating flat mirror between the scene and the double-reflector, telescope-type optical chain. The 11.56° cross track field of view is scanned as the mirror oscillates approximately ±2.89° about its nominal position, as shown in Figure 7. The instantaneous field of view of each detector subtends an earth-area square of 79 m on a side from the orbital altitude. Field stops are formed for each line imaged during a scan, and for each spectral channel, by the square input end of an optical fiber. Six of these fibers in each of four channels are arranged in a 4 by 6 matrix in the focused area of the telescope (U.S. Geological Survey, 1976).

Light impinging on each glass fiber is conducted to an individual detector through an optical filter, unique to the spectral channel served. An image of a line across the swath is swept across the fiber each time the mirror scans, causing a video signal to be produced at the scanner electronics output for each of 24 channels. These signals are then sampled, digitized and formatted into a serial digital data stream by a multiplexer.

The along-track scan is produced by the orbital motion of the spacecraft. The subsatellite point will have moved 474 m relative to the earth's surface during the 73.42 ms active scan and retrace cycle. Complete 79 m coverage of the earth's surface is achieved by the six detectors simultaneously sweeping the scan. The line scanned by the first detector in one cycle of the active mirror scan lies adjacent to the line scanned by the sixth detector of the previous mirror scan. Figure 8 shows the composite scan pattern (U.S. Geological Survey, 1976).

2. Orbit

Systematic, repetitive earth coverage under nearly constant observation conditions is provided for maximum utility of the RBV and MSS images collected by Landsat. Each spacecraft operates in a circular, sunsynchronous, near-polar orbit at an altitude of approximately 920 km (570 miles). They circle the earth every 103 minutes, completing 14 orbits per day and viewing the entire earth every 18 days. The launch of Landsat 1 in July 1972 was followed by the launch of Landsat 2 in January 1975, which was timed so that its orbit follows the orbital track of Landsat 1 with a delay of nine days. Together, the two observatories passed over and provided coverage of ground points every nine days. The orbit is selected and timed so that each satellite ground trace repeats its earth coverage at the same local time (0915-0945) every day. Repetitive image centers are maintained to within 37 km (20 nm). A typical one-day ground coverage trace for one observatory is shown in Figure 9 for the daylight portion of each orbital revolution (U.S. Geological Survey, 1976).

3. Gain Setting

On board Landsat, the analog sensor samples of radiance, which are eventually digitized, can be linearly or nonlinearly amplified by ground issued spacecraft commands. Signal compression is generally employed to improve the signal-to-noise ratio in Channels 4, 5 and 6. By compressing high radiance level signals, the quantization noise more nearly matches photomultiplier noise. Channel 7 signals, derived from silicon photodiodes, are never compressed

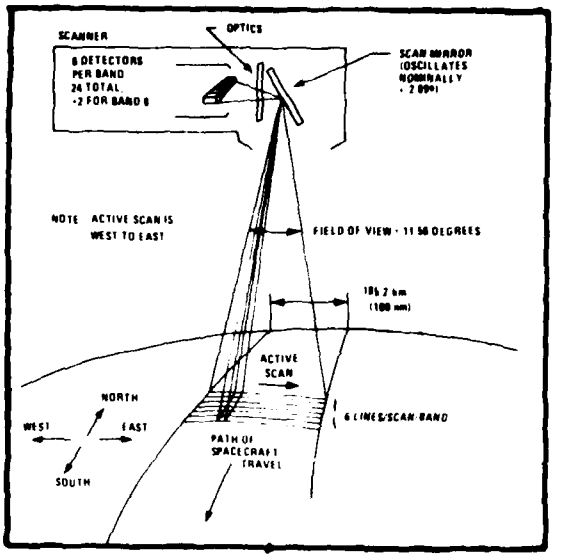

Figure 7. MSS scanning arrangement (USGS, 1979)

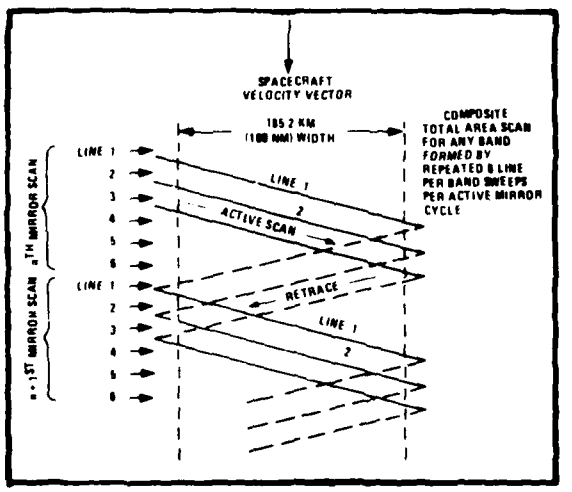

Figure 8. Ground scan pattern for a single MSS detector (USGS, 1979)

because equivalent load resistor noise is best matched by linear quantization. The available ground commandable analog processing options are illustrated in Figure 10. In the high-gain mode applied to Channels 4 and 5, amplifier gain is increased by a factor of four (U.S. Geological Survey, 1976). This increase allows greater use of system dynamic range for those scenes producing low sensor radiant energy, such as for hydrographic applications. The majority of Landsat imagery uses the low-gain linear setting where signals on all four channels have counts between 0 and 63; since some land features (e.g., white sand, concrete) have such high radiant energy levels, the high gain setting would saturate the sensor level. However, for hydrographic applications in which the radiant energy is extremely low from the water features, the high-gain setting enhances the quality of the image.

4. Photographic Outputs

Landsat's photographic products are available in two basic film sizes - 70 mm and 9.5 inch (241 mm nominal). The 70 mm size is primarily used for only bulk products. The 9.5 inch size includes bulk-enlarged images and precision images. Bulk processing uses the spacecraft altitude at "image center time" to scale each 70 mm image to 1:3,369,000. When the image on 70 mm film is enlarged by a factor of 3.369 and is printed on 9.5 inch film, the scale is 1:1,000,000. Landsat MSS images used in the case histories are derived from standard bulk-processed negative and positive transparencies from the U.S. Geological Survey EROS Data Center.

The area and location of the Landsat images used in the case studies are referred to as "scenes". Each scene is approximately 3200 pixels across and 2300 scan lines long, or 100 by 96.3 nautical miles.

Four registration marks are placed beyond the image corners to facilitate alignment of different spectral images of the same scene. The intersection of diagonals drawn through the four registration marks is the format center of the image.

Prior to February 1979, latitude and longitude tick marks were placed outside the edge of the image writing area at intervals of 30 arc minutes (NASA, 1971). Since February 1979, the geodetic tick marks provided on each Landsat product have been annotated with a new coordinate system associated with the Hotine Oblique Mercator (HOM) map projection.

The primary advantage of the HOM tick marks is that they can be interpolated accurately to any location on the image. However, use of this type of annotation does not allow easy correlation of the image with normally available map bases. The map bases used with Landsat imagery are usually polyconic projections and include latitude/longitude indicators.

A fifteen-step gray scale tablet was exposed on every scene as it was produced on the EROS Data Center's Electron Beam Recorder (EBR). This scale is subject to the same copying and processing as the image to which it is attached. The gray scale gives the relationship between a level of gray on the image and the electron beam density used to expose the original image. The gray scale thus illustrated the amount of contrast used in printing and processing the image. High contrast areas will have few gray level steps, while low contrast will have many gray levels. For hydrographic-related interpretation, it is normally desired to have high contrast, since the energy levels within the water are low. However, in bulk processing the contrast levels are preset. It is important that the interpreter uses the gray scale levels on each print to interpret the image correctly. Examples of different contrast levels of Landsat imagery are given in the case histories.

Details of the bulk image annotation block, are located at the bottom of each Landsat image (figure 11).

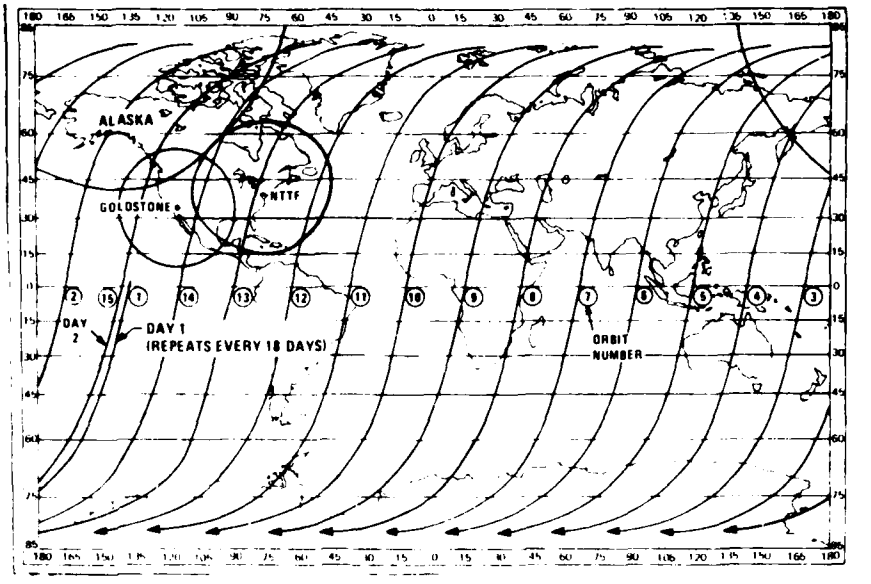

Figure 9. Typical Landsat daily ground trace (daylight passes only) (USGS, 1979)

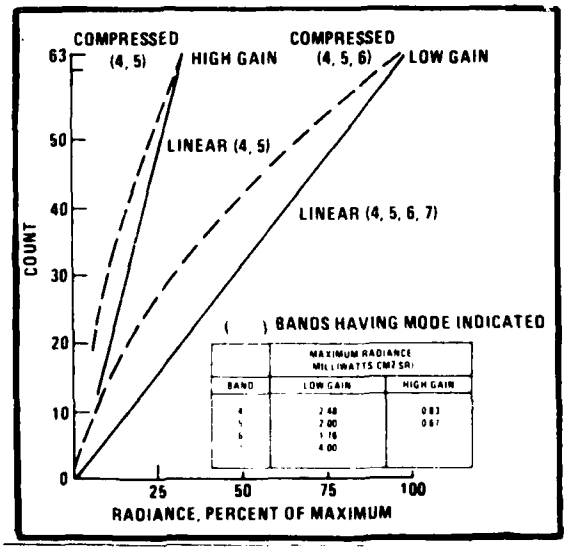

Figure 10. MSS output count versus radiance, compressed and linear modes (USGS, 1979)

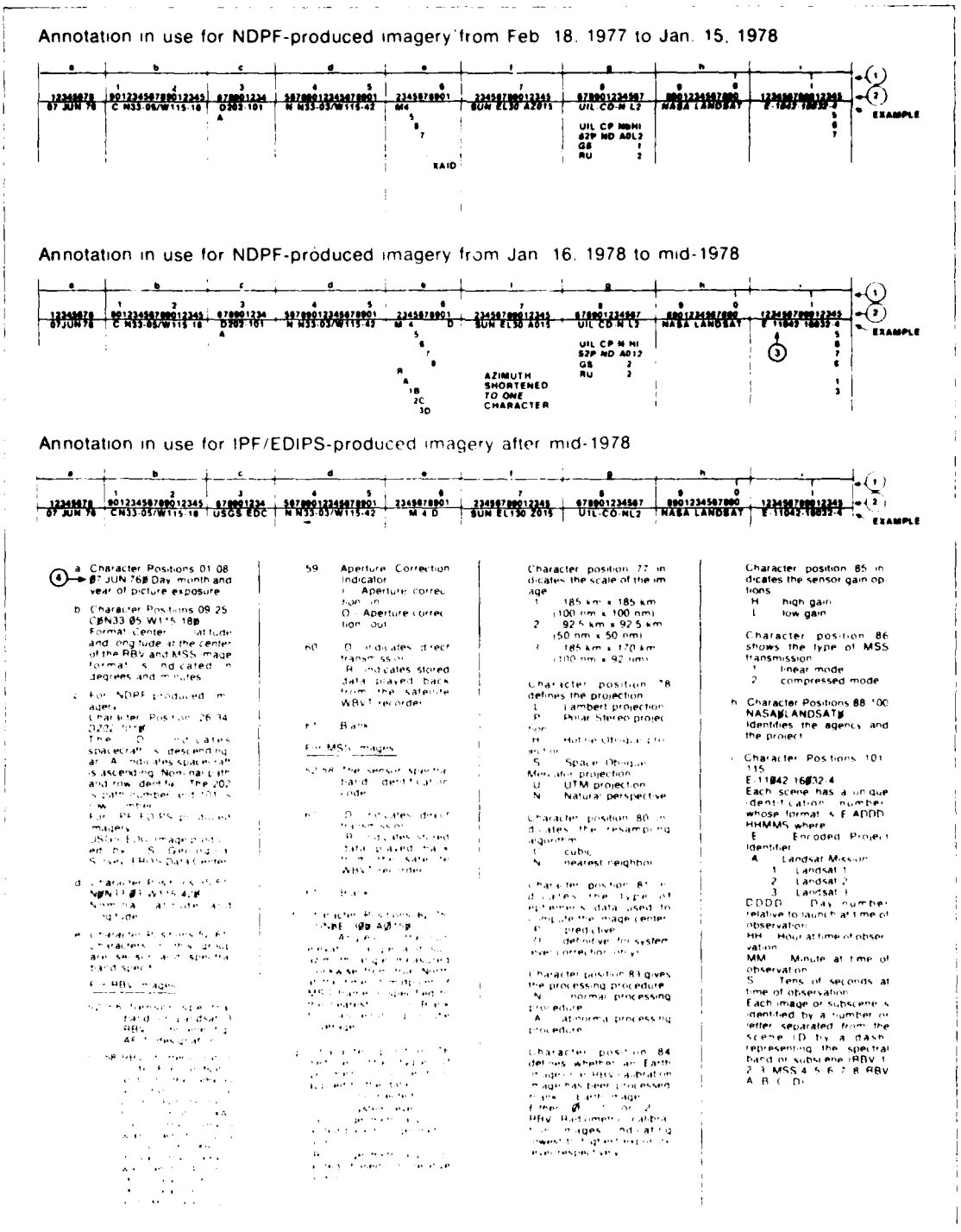

Figure 11. Details of bulk processed image annotation block (USGS, 1979)

IV. CASE HISTORIES

IV. Case Histories

Ten case histories of Landsat imagery are presented to familiarize the analyst with techniques of interpreting hydrographic features. Selection of the case histories was based on presenting diverse hydrographic features within Landsat imagery and numerous techniques used in interpretation. A certain degree of redundancy is contained in the case histories; however, this repetition illustrates the similarities which exist between Landsat scenes and also familiarizes the analyst with characteristic patterns or tones. The case histories are presented to interpret the most predominant hydrographic features; therefore, minor or more subtle hydrographic features may have been overlooked and have not been illustrated in this report. The ten areas for which case histories were selected follow.

1. Cedar Keys, FL
2. Cape Cod, MA
3. Key West, FL
4. Apalachee Bay, FL
5. Palau Islands
6. Gulfport, MS, Approaches
7. Little Bahama Bank
8. Mississippi River Delta
9. Cape Hatteras, NC
10. Cape San Blas, FL

1. Cedar Keys, FL

1. Cedar Keys, FL

The Cedar Keys area is located on the west coast of Florida, north of Tampa Bay. The coastline is somewhat irregular, with numerous offshore sand bars and islands (keys). The ocean bottom is gently sloping and has large, hard, sand reefs (St. Martins Reefs) extending approximately 18 nautical miles offshore. The area is illustrated by the hydrographic chart (figure 1-1). MSS Landsat imagery corresponding to the same approximate area are illustrated for the four channels in Figure 1-2 (Channel 4), Figure 1-3 (Channel 5), Figure 1-4 (Channel 6), and Figure 1-5 (Channel 7). This imagery was derived from a standard bulk processed negative from the EROS Data Center.

It is immediately noted that the visible channels, 4 and 5 (figures 1-2, 1-3), contain extensive information on water color and bathymetry, whereas IR Channels 6 and 7 distinguish mainly land and water. The majority of hydrographic interpretation is provided in the visible channels, although through comparison, the IR Channels will permit distinction between wetlands and submerged sandbars and reefs. This distinction is illustrated in various areas in Figure 1-2 (annotation A) along the complex shoreline where there is little variation in contrast. The difficulty in interpreting the coastline from the highly reflective bottom in Channels 4 and 5 can easily be resolved by comparison with Channels 6 and 7. The dendritic stream pattern also noted at location A is best illustrated in Channel 5 (figure 1-3). These patterns result from rivers draining into the offshore water, and forming channels in the bottom. The subsurface dendritic channels appear darker in Landsat's visible channels as a result of deeper water and lower reflectance bottom. Yet Channel 7 (figure 1-5) fails to detect the submerged dendritic patterns. Channel 4 (figure 1-2) also illustrates a similar pattern, though not as distinctly, since this channel is affected more by atmospheric contamination and a higher degree of scattering within the water column than Channel 5.

Note the highly reflective bottom near the shoreline (B) in Figures 1-2 and 1-3. The mottled appearance in this bottom type results from patches of vegetation or bottom reflectance differences. Vegetation or bottom reflectance differences are also shown at location C, between two dendritic channels. At location C, the IR channels (figures 1-4 and 1-5) display numerous small islands (most likely mangrove islands). Surrounding the islands is an area with a mottled speckled appearance within the white, highly reflectant bottom. Vegetation or bottom reflectance differences are responsible for this appearance, since dramatic changes in depth or turbidity would be unlikely in this low-lying land area and are not characteristic of this pattern.

Submerged bottom reefs/shoals are illustrated in the visible channels (figures 1-2 and 1-3) in numerous locations (D). The extent of these shoals are illustrated better in Channel 4 than in Channel 5, since this channel spectrally penetrates water deeper, as previously discussed in Section III.B on basic water optics. However, caution should be taken not to mistake turbid water for a shoal, as can easily be done in this image. This determination can best be made by viewing the scene on several dates. The striated banding, appearing at location F in Figure 1-2, is related to turbid water. This pattern is typical for dispersion of both turbid and clear water. Aerial photographs (B&W photo from 40,000 ft) of Cedar Keys, illustrated in Figures 1-6 and 1-7 and indexed on the Landsat overlays, depict streaming flows of the turbid water around the keys and subsurface features. This process is further evidenced by

comparison with hydrographic chart overlay. The divergence in the stream patterns (figure 1-7) indicates subsurface features, and is evidenced by comparison with the overlay of the detailed hydrographic chart. (There was no geometric correction between the aerial photography and the hydrographic chart.) Notice that as the turbid water diffuses in deeper ocean water, a striated pattern occurs in a somewhat regular pattern. This similar pattern occurs on a larger scale in Channel 4 (figure 1-2) of Landsat at areas annotated F. Channel 5 (figure 1-3) does not illustrate similar turbidity patterns, since it is not spectrally sensitive to subtle water color changes. It is noted that at the bottom of the aerial photos (figures 1-6 and 1-7) the highly reflective sunglint areas highlight surface patterns. Yet by comparison of the overlap area of the two images, it is very apparent that the sunglint precludes any penetration (see Appendix B - Sunglint).

The visible channels of the LANDSAT image (figures 1-2 and 1-3) illustrate long lenticular striations at locations labeled E on the overlay. These patterns are characteristic of waves breaking over shoals or reefs. The visible channels measure the reflectance from the white foam at the sea surface, water color, and bottom reflectance. Because Channel 4 penetrates water deeper, a greater extent of bottom reflectance is observed in this channel than in Channel 5, and is evidenced by comparison of Figures 1-2 and 1-3, respectively. In the IR channels, sea surface reflection of IR energy occurs only from the white foam that results from breaking waves. Therefore, in Channels 6 and 7 the presence of bright tones in water (usually coinciding with reefs) indicates the presence of breaking waves. These tonal patterns are commonly observed as striations on the IR imagery. However, because striation patterns are not observed on the reefs in Figures 1-4 and 1-5, the interpreter should not conclude the absence of breaking waves. By observing the gray wedge at the bottom of these two figures, it can be noted that low contrast printing and processing was applied to the image. In an outside exercise this scene was analyzed via a Computer Compatible Tape (CCT) on a computer. The contrast was stretched to where the striations were observed on the IR imagery, thus indicating the presence of breaking waves. The interpreter is then able to interpret shallow water locations, since waves break at approximately half their wave length (see Appendix A on Breaking Waves).

Note that the Suwannee River appears dark in all four channels of Landsat. In Figures 1-2, dark areas indicating low reflectance values, which is characteristic of clear water, are shown (H) emptying into brighter areas characterizing more turbid near-shore waters. Note that most inland waters appear dark or clear (less-turbid). Aerial photography (figures 1-6 and 1-7) illustrates similar water clarity for the Suwannee River. Note the darker tone of the water which extends southward from the Suwannee River as it empties into the more turbid bay waters. This tone indicates that the general water flow in the area is to the south.

The lighter gray areas at the shoreline, which are depicted in Figures 1-4 and 1-5 at location I, are characteristic of tidal-influenced wetlands and should not be confused with shoaling or turbid water pattern. The tonal characteristics of wetlands are the result of the vegetation type; in this example, mangroves and water.

Dredge spoils are illustrated in all four channels on Landsat (J). Note the regular spacing and linearity which are characteristics of manmade features. The highly reflected dredge spoils are accumulations of channel deposits and are indicators of the bottom reflectance properties, in this example, sand.

Misinterpretation can easily occur from atmospheric contamination, as noted in Figures 1-2 and 1-3 at annotation K. The lighter tone with gentle dispersion (K) can easily be confused with turbidity patterns, as noted in Figure 1-2 (F). The fog/haze interpretation is identified by the extension of this light tonal area across the land/water interface. This phenomenon can be observed by close examination and comparison of the visible channel (figure 1-2), which is most affected by atmospheric haze, and an IR channel (figure 1-4 or 1-5), which is least affected by haze and essentially images the land/water boundary. Fog and haze commonly accumulate along coastal areas in early morning and dissipate by midmorning. In confined/protected coastal areas, such as shown in this example, fog/haze are more apt to remain later in the morning before dissipation. Landsat overpasses at approximately 0930 local time, and commonly images this phenomenon along protected coastlines.

A selected area of this Cedar Keys case history was examined using computer analysis techniques to illustrate the possible utility of Landsat's capability in hydrographic charting. The full resolution (512 x 512 pixel area) image of the Cedar Key area was illustrated as a color composite. The composite was generated by displaying Channel 7 in the red gun, Channel 5 in the green gun and Channel 4 in the blue gun. The resulting false color composite was then contrast- and brightness-stretched to optimize the hydrographic features.

The false color composite was then warped to overlay a detailed hydrographic chart (11408) by selection of coastline control points. Figure 1-8 illustrates this composite with an overlay of the hydrographic chart showing direct comparison of the location, size, and shape of hydrographic features as depicted by Landsat with a hydrographic chart. This technique provides a rapid means for updating charts. In this example, several important features should be noted. The location and size of the two linear offshore reefs (A, B), which were previously discussed, are observed to overlay the hydrographic chart very closely. Also, the location of Seashore Reef (C) corresponds closely between the chart and Landsat imagery. The shape of the submerged reefs (annotated D's on the composite) does not appear to correspond to the hydrographic chart. Also note that the location of submerged reefs and islands (annotated E) does not correspond with the chart. This application of Landsat imagery, though not an absolute measure of water depth or obstructions to navigation, demonstrates its utility to detect hazards and zones of safe passage for chart revision, and in survey planning.

To fully exploit Landsat for charting purposes, a portion of Figure 1-8 was magnified and a larger scale hydrographic chart (1:40000) of the area overlain. Figure 1-9 illustrates this magnification and the pixel size limitation of Landsat for charting purposes. Each of the rectangular areas compositing this image corresponds to the 79 x 57 meter resolution of Landsat. By comparison with the chart overlay, the location and shape of the island and shoals is quite readily shown. The red-colored pixels (A) corresponding to land features coincide with the position and general shape, as illustrated on the chart. The whitish-toned pixels (B) representing very shallow water have corresponding shoal markings on the chart.

The blue-toned pixels grading from light blue (representing shallow water) to dark blue (representing deep water) show coincident bottom features on the chart. Note that the dark-blue band (D) which flows between North Key and Sea Horse Key coincides with the channel as depicted on the chart. Note also that several of the shallow reef areas are slightly offset or have a slightly different shape than depicted on the chart. Though this is a possible misalignment of Landsat and the chart, a more thorough investigation of

this area is warranted to determine whether a chart revision is required. Note also the gray shading (E- indicating a shoal area) on the chart coinciding with Deadman's Channel. Landsat fails to show the whitish-toned pixels indicating shoals in this area as it does on similar shoaling areas in the vicinity. This omission is an indicator of possibly deeper water that the chart depicts.

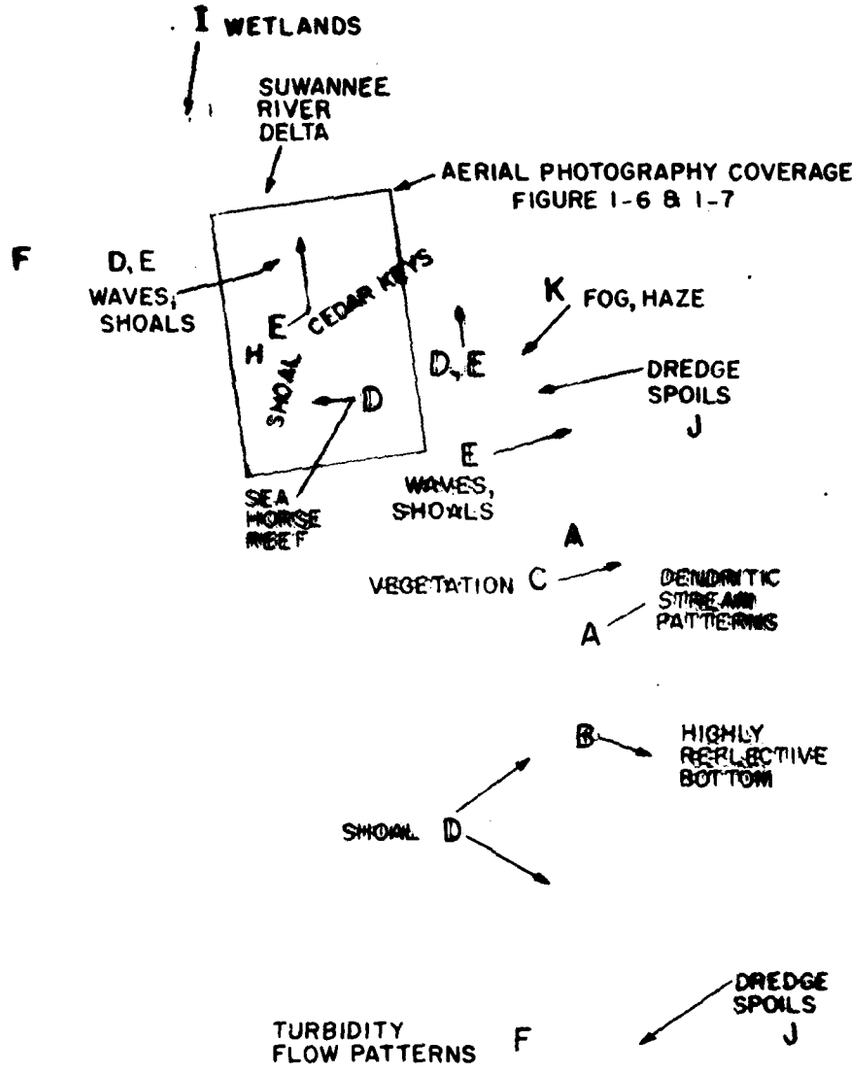

(LANDSAT) CEDAR KEYS 5 NOV 78

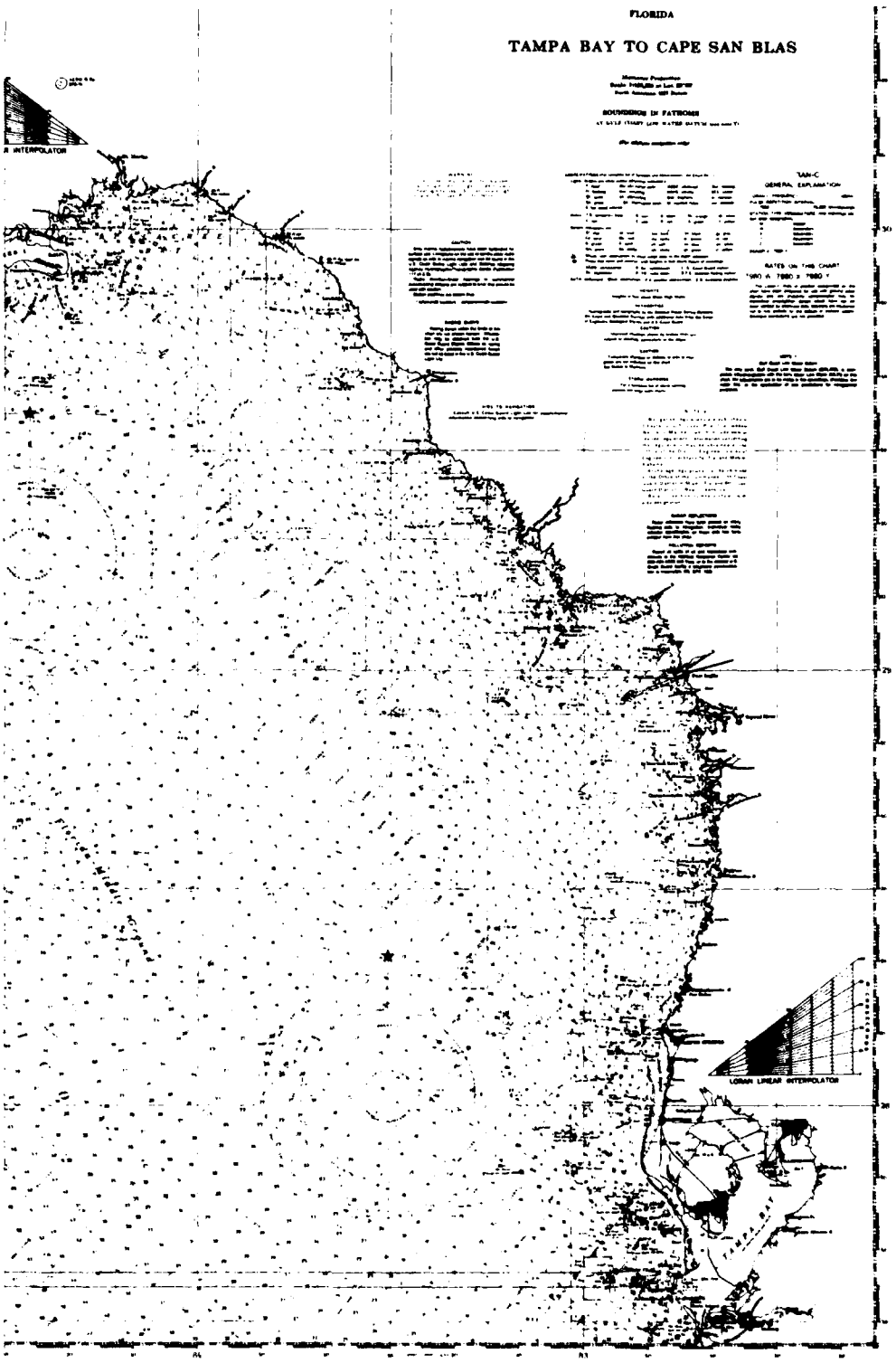

Figure 1-1 Hydrographic chart of Cedar Keys, FL (11400)

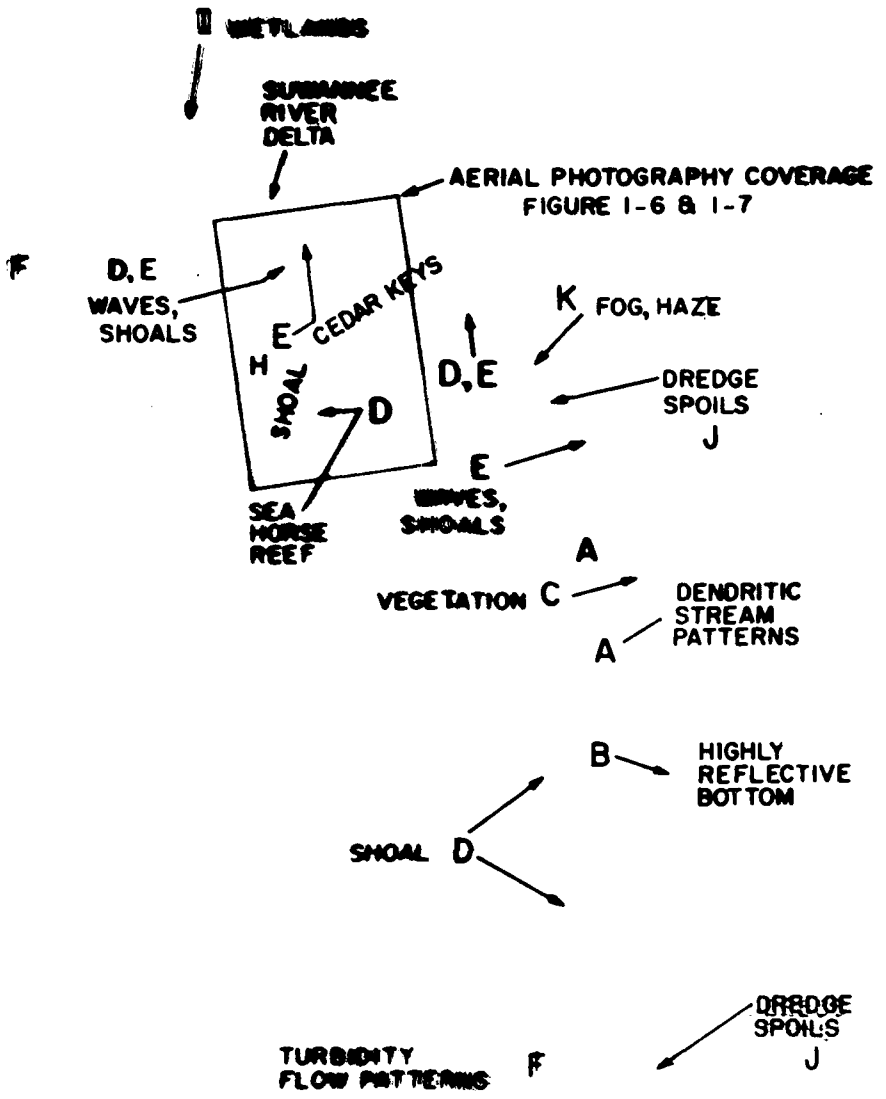

(LANDSAT) CEDAR KEYS 5 NOV 78

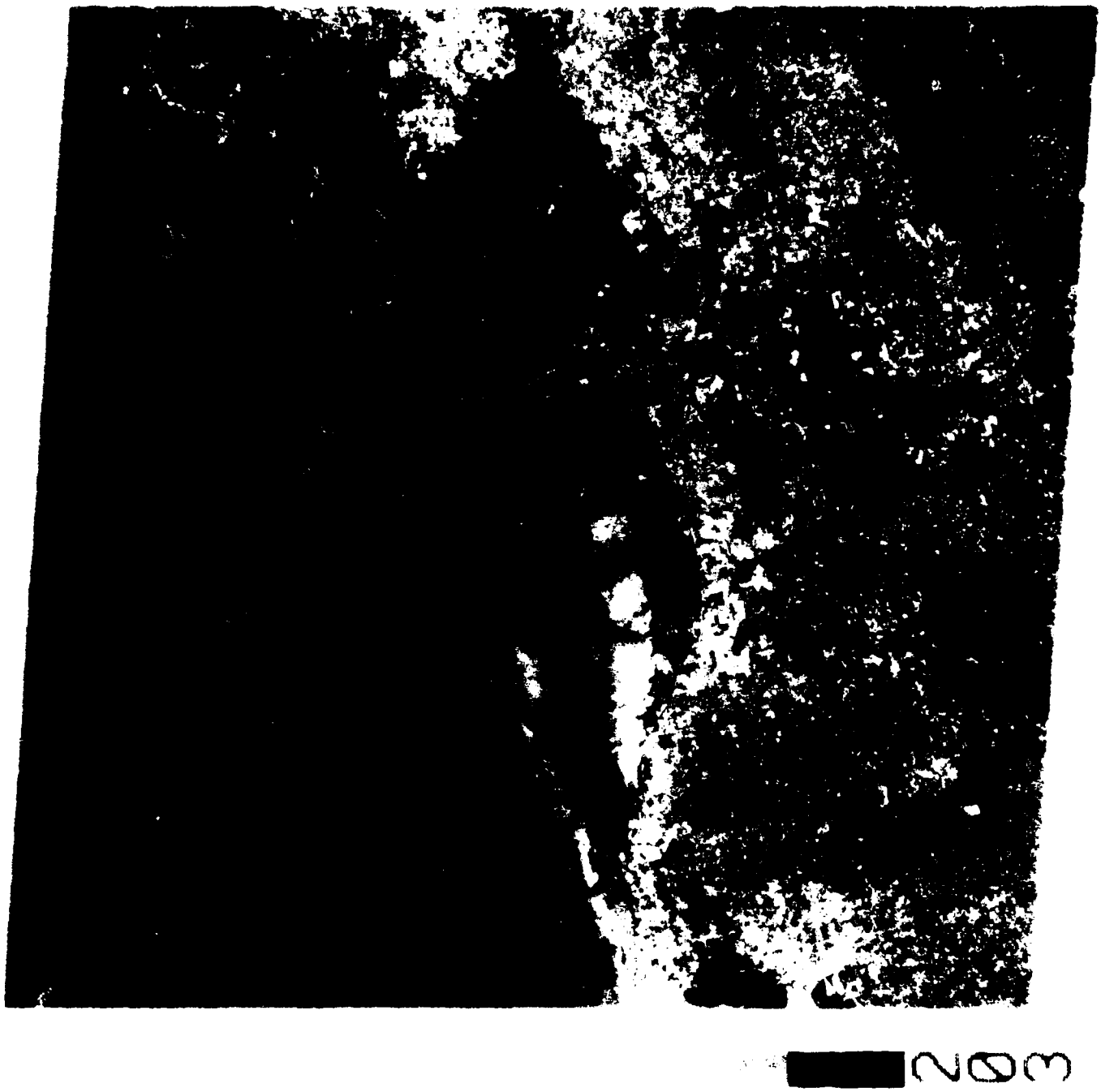

Figure 1-2. Landsat image Cedar Keys, FL (5 Nov 78)

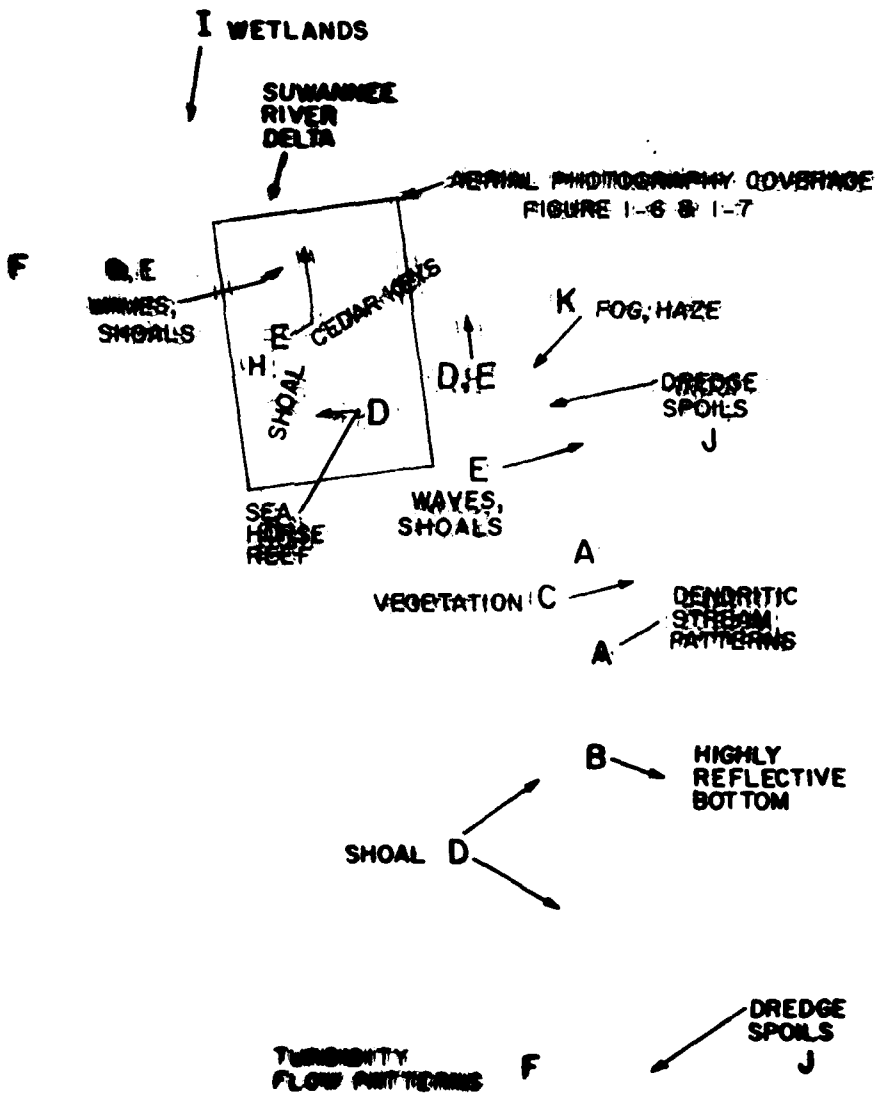

(LANDSAT) CEDAR KEYS 5 NOV 78

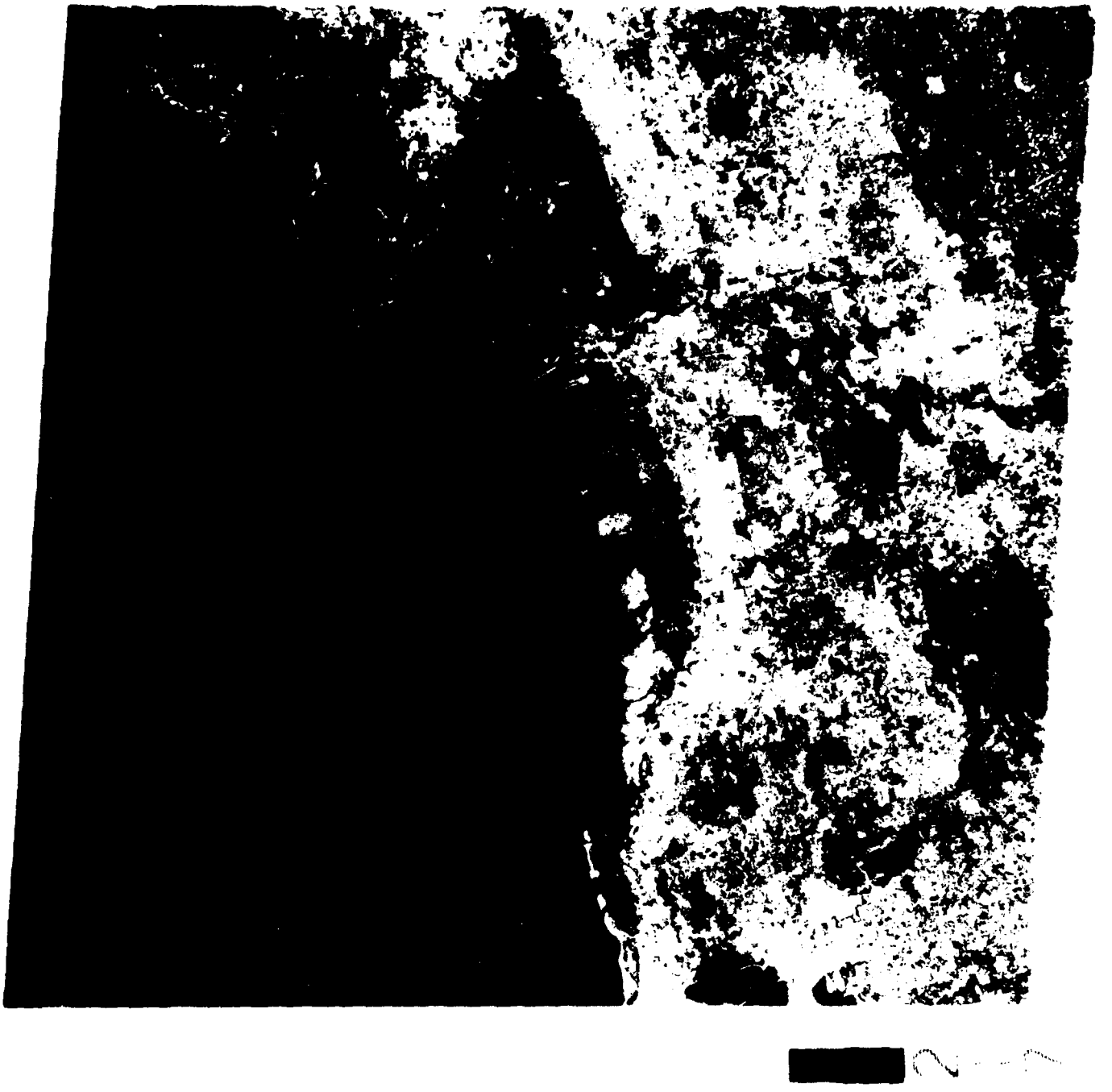

Figure 1-3. Landsat image, Cedar Keys, FL (5 Nov 78)

(LANDSAT) CEDAR KEYS 6 NOV 78

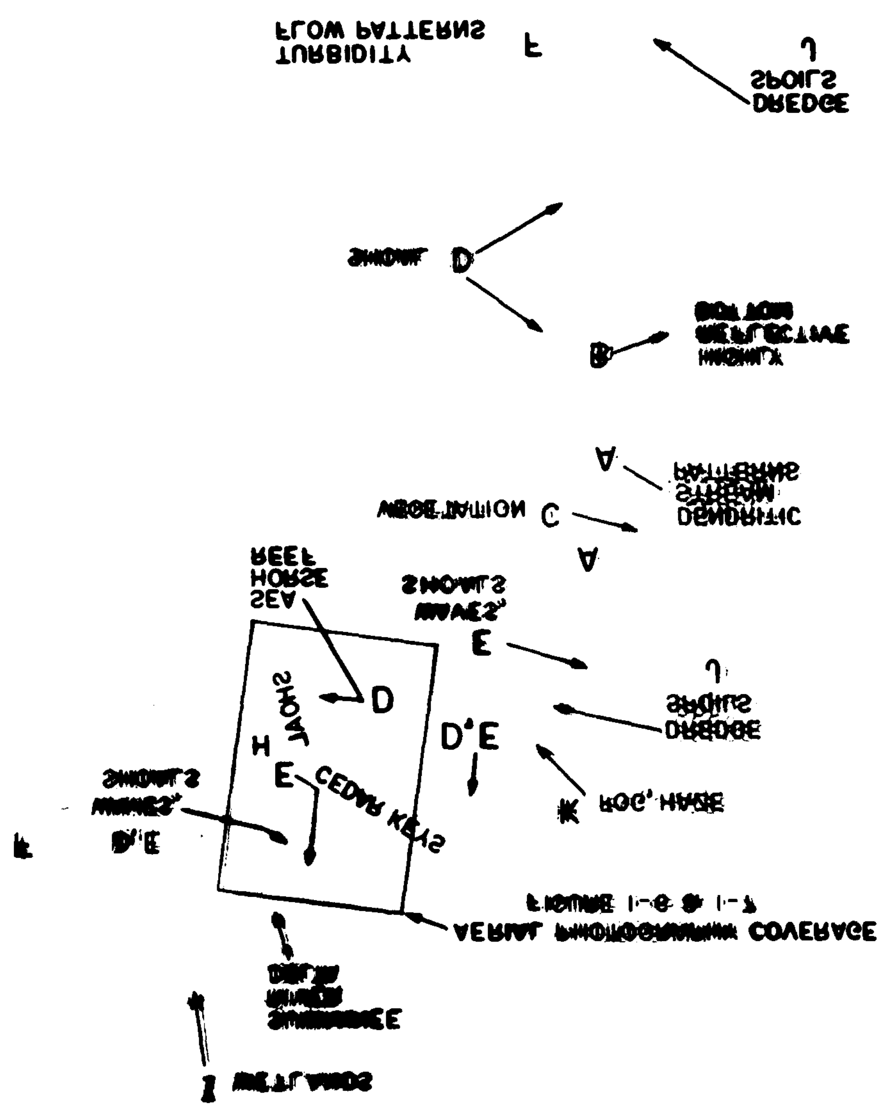

FIGURE 1-6 & 1-7

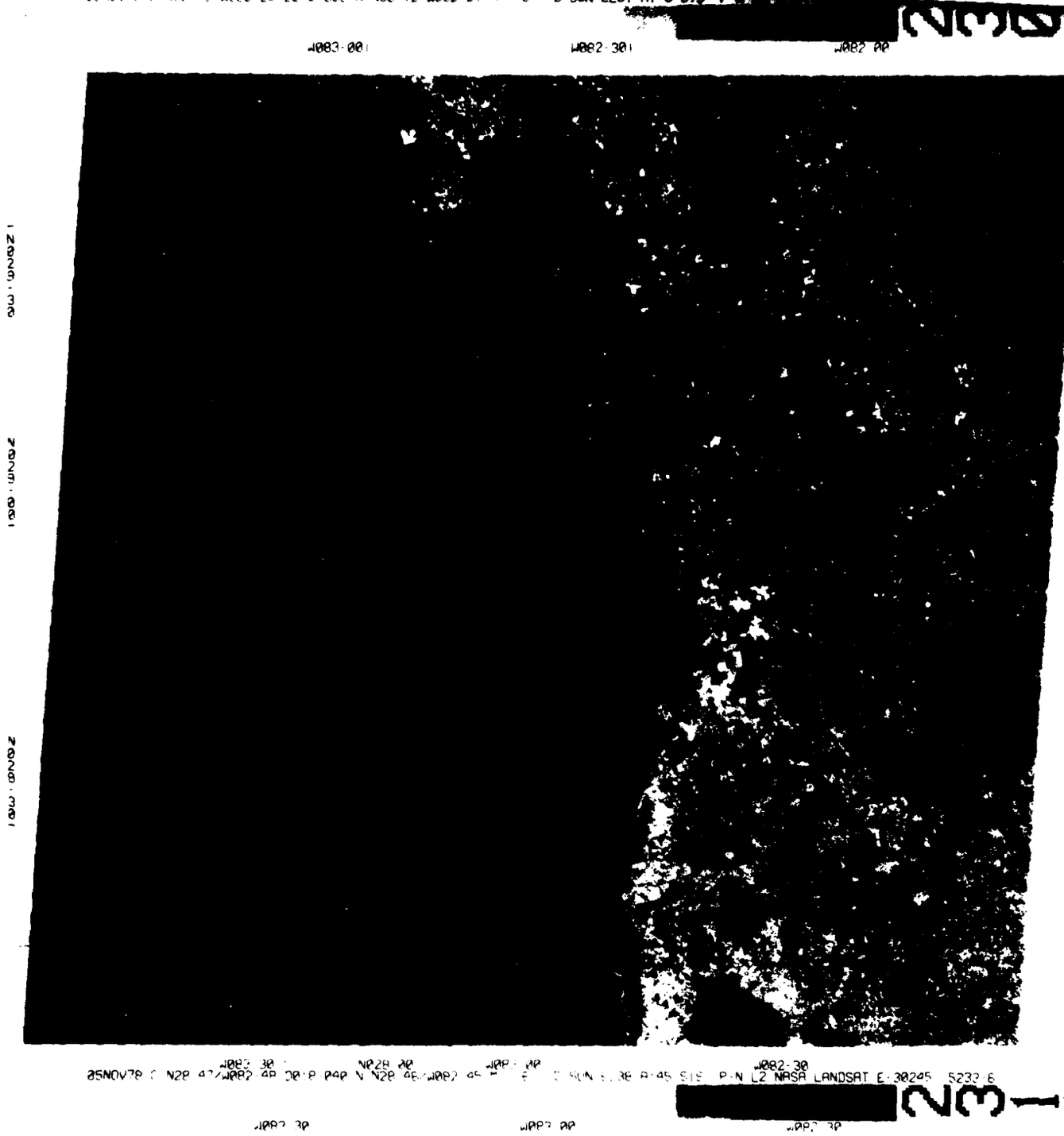

Figure 1-4. Landsat image, Cedar Keys. FL (5 Nov 78)

SUWANNEE RIVER
DELTA

REEF

REEF

DIFFUSION
OF
TURBID
WATER

REEFS

CHANNEL

HIGH
TURBIDITY

REEFS

CHANNELS

TURBIDITY
FLOW PATTERNS

SUNGLINT

(AERIAL PHOTOGRAPHY) CEDAR KEYS, FLA.

Figure 1-5. Landsat image Cedar Keys, FL (5 Nov 78)

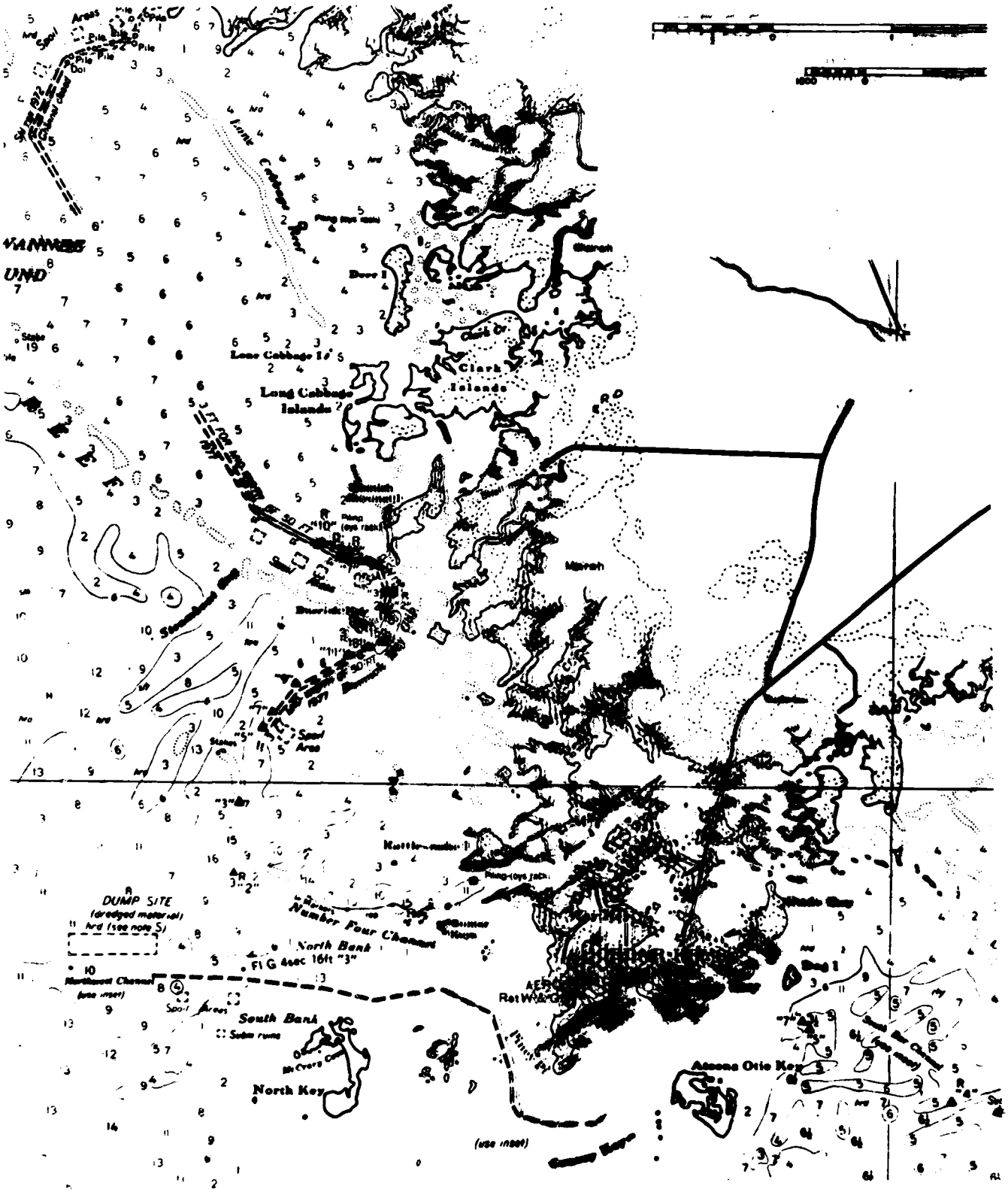
DUMP SITE
(dredged material)
Long Cabbage Islands
Clark Islands
North Bank
South Bank
North Key
Number Four Channel
Marsh
Spoil Area
(use inset)

Figure 1-6. Black and white aerial photograph (1:80,000) Cedar Keys, FL (27 NOV 77)


DUMP SITE
(dredged material)
Four Channel
North Rock
Sombrero Key
(Aband Lt Ho)
Sombrero Channel
DUMP SITE
(dredged material)
SEAWARD

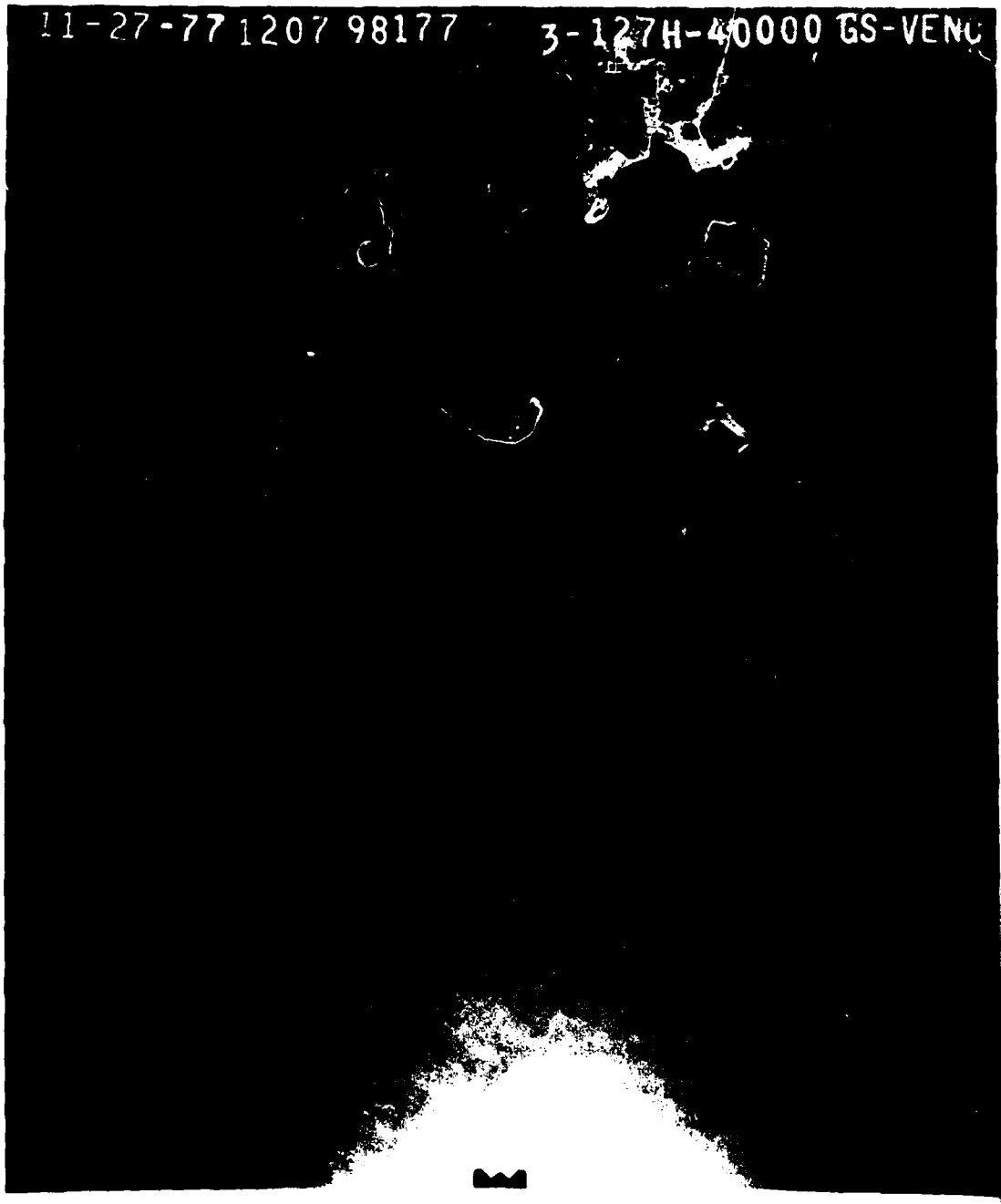

Figure 1-7. Black and white aerial photography (1:80,000), Cedar Keys, FL (27 Nov 77)

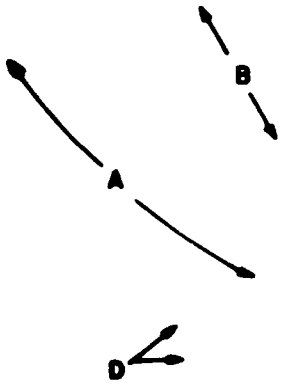

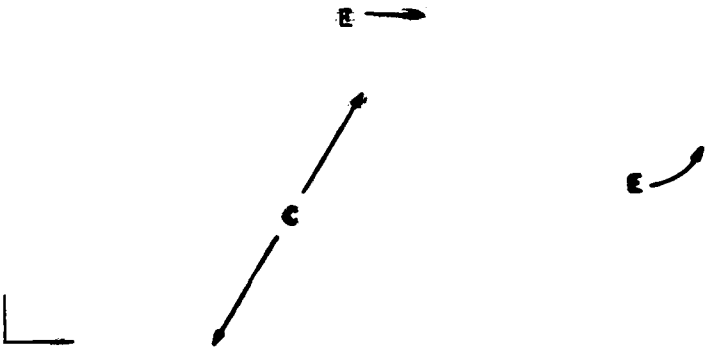

(LANDSAT) CEDAR KEYS 5 NOV 7

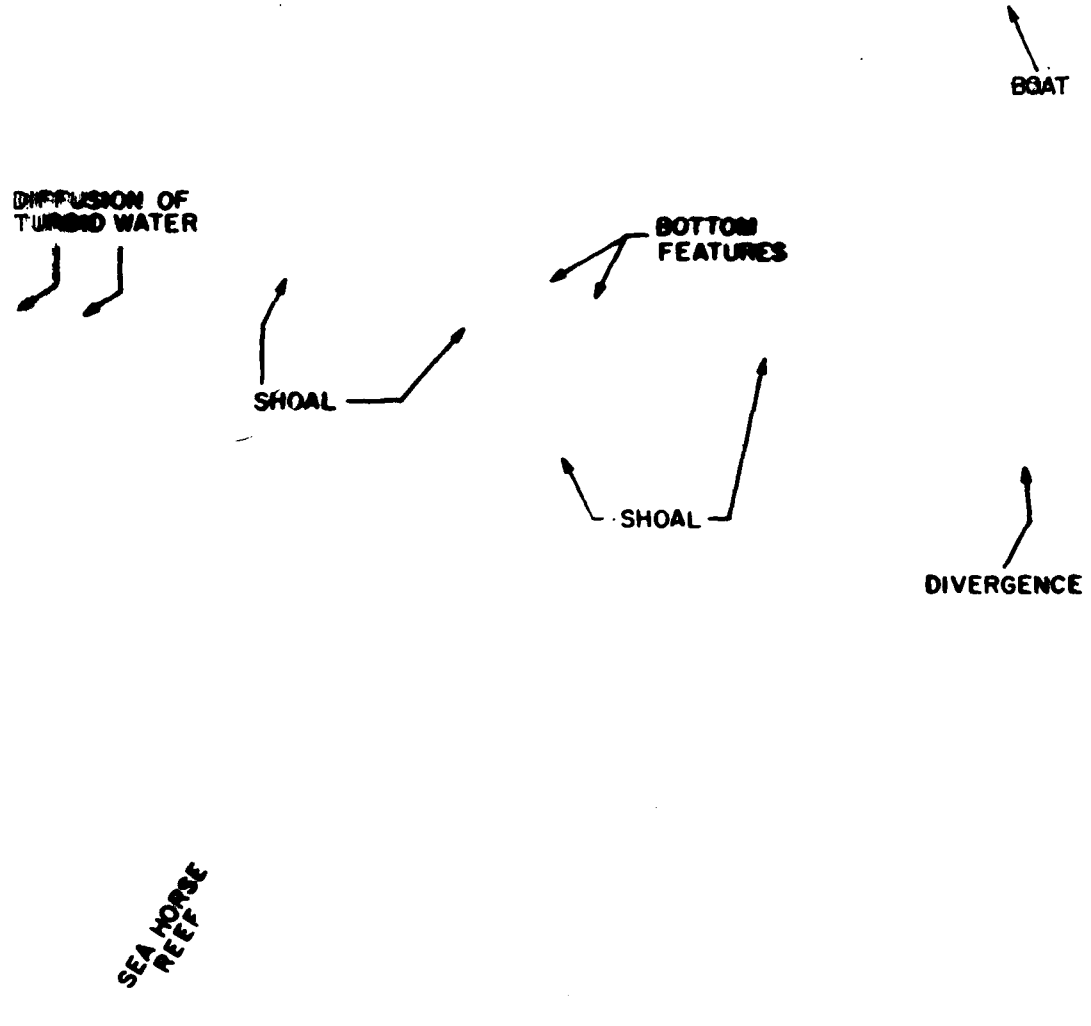

(AERIAL PHOTOGRAPHY) CEDAR KEYS 27 NOV

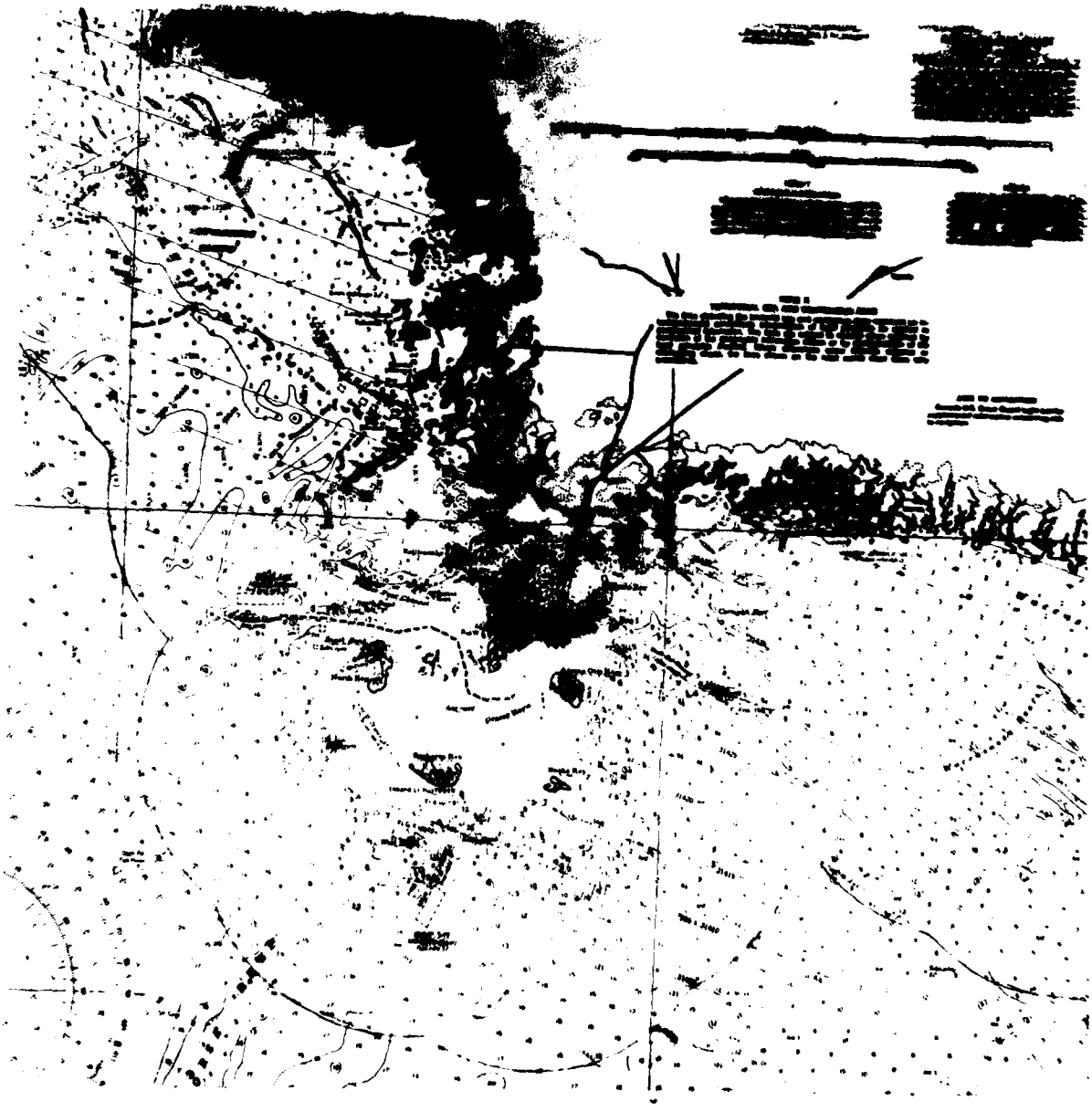

Figure 1-8. Landsat computer generated color composite of channels 4, 5 and 7, Cedar Keys, FL (5 Nov 78)

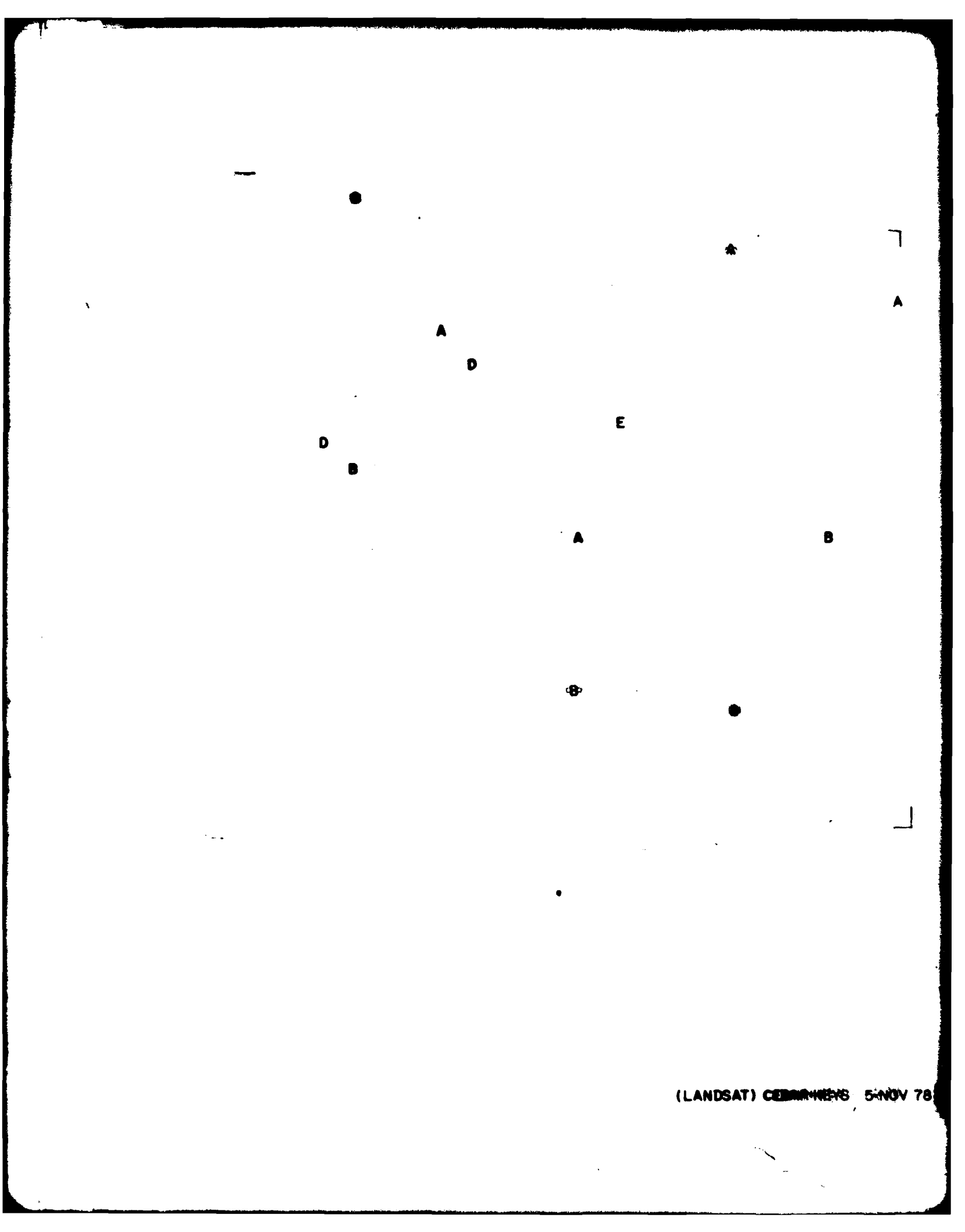

(LANDSAT) [illegible] 5-NOV 78

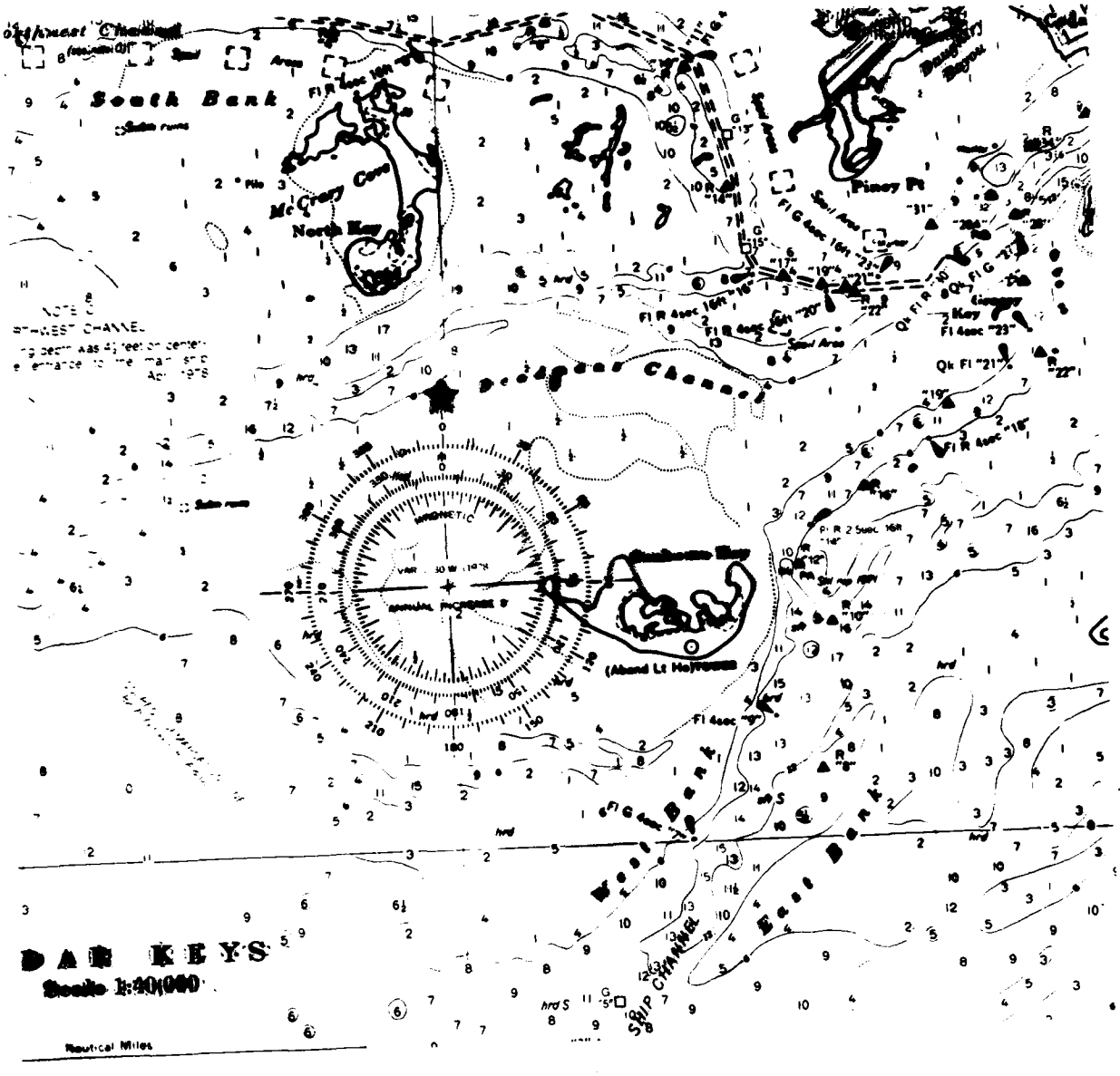
South Bank
McCrory Cove
North Key
Pinoy Pt
Channel
Fl R 4sec 16ft
Fl G 4sec 16ft
Qk Fl "21"
Fl 4sec "23"
Fl R 2.5sec 16ft
Fl 4sec
(Aband Lt Ho)
West Bank
East Bank
SHIP CHANNEL
BAR KEYS
Scale 1:40000
Nautical Miles

Figure 1-9. Landsat computer generated color composite enlargement of channels 4, 5 and 7, Cedar Keys, FL (5 Nov 78)

2. Cape Cod, MA

2. Cape Cod, MA

The Cape Cod case history area is located off the east coast of Massachusetts and extends from Cape Ann (Mass.) in the north to Block Island (N. Y.) in the south. The hydrographic chart corresponding to this area is illustrated in Figure 2-1 (H.O. Chart 13200). A different type of coastline is shown in the Landsat image for this case history. The northern coastlines are characterized by rocky, steep-cliffed beachfronts. The coast is irregular with numerous offshore rock islands. The bottom slope is very steep with little-to-no beaches. Deep water is close to the shore and Landsat imagery would not be expected to be of help in the detection of submerged obstructions to navigation. Numerous protected coves within the rock formations line the northern coastline. Rock obstructions, both above and below the water are definite hazards to navigation, but are generally smaller than the resolution of Landsat. However, high-contrast features, as compared with dark ocean backgrounds, which are smaller than the nominal Landsat resolution, have been noted on the IR bands. The appearance of these features in the same location on several temporal images eliminates the possibility of system noise or whitecaps. Features as small as 20 meters x 40 meters have been detected in this manner. The coastline south of Boston, including the Cape Cod Spit, Martha's Vineyard, and Nantucket Island, is a mixture of a rocky coastline and small sand beachfronts. The location and extent of shoals are determined by the long-shore and offshore current dynamics and local wave dynamics; thus, they are continuously changing in response to this high energy environment.

This set of Landsat images provides an interesting example of a capability for use, not only in coastal processes, but also in oceanographic processes. Figures 2-3, 2-4, 2-5 and 2-6 correspond to Landsat imagery of Channels 4, 5, 6, and 7, respectively.

First impressions of this set of images focus on the long-banded crescent wave forms (A) located 10-20 nautical miles to the east and the northeast of Cape Cod, and are very apparent in the first two visible channels (figures 2-3 and 2-4). The pattern is characteristic of internal waves (see the section on Internal Waves in Appendix A). Appendix A explains that internal waves are remotely sensed by their surface expressions. Surface expressions of internal waves appear as variations in the sea surface roughness. Landsat senses these variations in the sea surface reflectance. A more thorough explanation is provided in Appendices A and B. Appendix B, "Sunglint," contains an explanation on how to interpret sea surface conditions from the sunglint pattern and a more detailed explanation of the location where sunglint is most likely to occur.

Also the relationship of the bottom topography and internal waves is explained in greater detail in Appendix A and is applicable to this image.

To enhance the position and relationship to topography, the internal wave packets were transferred from the Landsat imagery (figure 2-4) and reconstructed as an overlay to the hydrographic chart (figure 2-2). Note that the position of the wave packets generally correlates with the bathymetric features that are at depths of 100 fathoms. The curvature of the packets and the length of the foremost waves are indicative of the bottom slope characteristics, as explained in Appendix A. This effect is most evident to the northeast of Cape Cod (figure 2-4) where internal waves are illustrated to propagate upslope (B) on both sides of the deeper water channel (see hydrographic chart, figure 2-2, for comparison). A similar example is shown for a bottom dome feature at C (figure 2-4). The wave packets approach this feature from different sides. At location D in Figure 2-4 note that the area is surrounded by internal waves. To the west of this feature the wavelengths of the internal

waves indicate an impinging bottom change, to the east the wavelengths indicate the location of another change. Therefore, area D is interpreted as a deep water area, as verified by the hydrographic chart. The refraction of the internal waves in the vicinity of bottom topography changes occurs in a similar method as for gravity waves, and is also explained in Appendix A on wave refraction. The internal wave patterns provide the interpreter a useful technique to interpret position and shape of shoaling features.

Note that the internal wave patterns are most evident in Channel 5 (figure 2-4), which, from Appendices A and B, indicates the presence of sea surface reflectance. The spatial response of sea surface reflectance is dependent on the intensity of the incident solar radiance, as discussed in the section on basic water optics (Section III. B). This case history provides a good example of that discussion. In light of that discussion, the sea surface features in the IR channels are only expected to show reflectance patterns and essentially no water color information. However, the low contrast used in bulk processing of Channel 7, Figure 2-6, fails to reveal this reflectance phenomenon. Higher contrast printing combined with under exposure would reveal surface reflectance patterns in these channels.

From the high amount of sea surface reflectance, which is illustrated in the various bands (especially in bands 5 and 6) of this image, basic interpretation of the sea state conditions can be assumed. (See Appendix B for a more detailed explanation of the following discussion.) The Primary Specular Point (PSP), which is not contained in Landsat imagery, is located to the southeast in this image. The brighter areas in the water are caused by short, wind-generated waves roughing the surface and creating large numbers of facets or point reflectors in any given area which the Landsat integrates into a single bright voltage reading. The smoother the sea surface (often characterized as a slick), the less or minimal reflectance of solar energy occurs, and results in a dark area on the image. A dark area interpreted as a calm sea surface is located at E (figures 2-3, 2-4). Similarly, the dark banding within the internal wave patterns indicates the slicks associated with internal waves. Note the dark, near-shore water on the western side of Cape Cod (H). This darkness illustrates calm, protected waters that increase in roughness (brightness) farther offshore. Sea surface slicks not associated with internal waves, but possibly with a surface current, are seen through careful examination of the high sea surface reflectance area in Figure 2-4 (F, G). Long, striated, sinuous, black patterns among the generally lighter toned area are commonly observed in a surface high reflectance area and may be generally interpreted as slicks. Surface currents and/or surface streaking by surface winds often follow the same direction as these patterns. These slick patterns are observed to intersect internal waves (G) and form a complex pattern (figure 2-4).

The visible channels (figures 2-3 and 2-4) appear to show Nantucket Shoals and other hydrographic features within Nantucket Sound. A more detailed hydrographic chart (figure 2-2) of Nantucket Sound is required for comparison with the Landsat images. Numerous examples of shoals can be correlated to the imagery through comparison with the nautical chart, although only several will be pointed out in this case history. The light tonal area labeled I (figures 2-3, 2-4) is interpreted as Rose and Crown Shoal, based on similarities with the structure on the hydrographic chart (figure 2-2). This is also true for Old Man Shoal (J) and Point Rip (K). The lighter tone characteristic of shoals in this area results from both (1) sea surface reflectance of solar radiance, and/or (2) high bottom reflectance off the shoal; however, the former is believed to be primarily responsible

for the lighter tone, especially in Channel 5 (figure 2-4). Increased reflectance in high/rougher sea states (as previously discussed for sunglint areas and explained in Appendix B) is likely over shallow shoal areas, because of the effects of bottom activvity on surface waves (see Appendix A). Note, however, that Channel 4 (figure 2-3) does locate the position of deeper shoals better than Channel 5. This difference is illustrated by the extent to which Channel 4 shows deltaic-type shoal located south of the Muskaget channel (L), which is not shown in Channel 5 (figure 2-4).

Notice that Landsat imagery can be used to locate channels (L and M) within the shoals. Utilizing Landsat imagery and hydrographic charts, the interpreter is provided a technique of quickly assessing position and changes in the shape or size of the shoal since the last edition of the chart and determining whether additional hydrographic surveys are warranted.

Clouds are observable in the lower left corner of the visible channels of the Landsat image. The extension of this lighter tone area over Block Island eliminates the possibility of a shoal. A ship can be seen to the northwest of Nantucket Island in Figure 2-4. Careful examination reveals the characteristics of a V-shaped wake trailing the ship. The wake is also confirmed as a sea surface expression by the clarity with which it is observed in Channel 5, as opposed to the other Landsat channels.

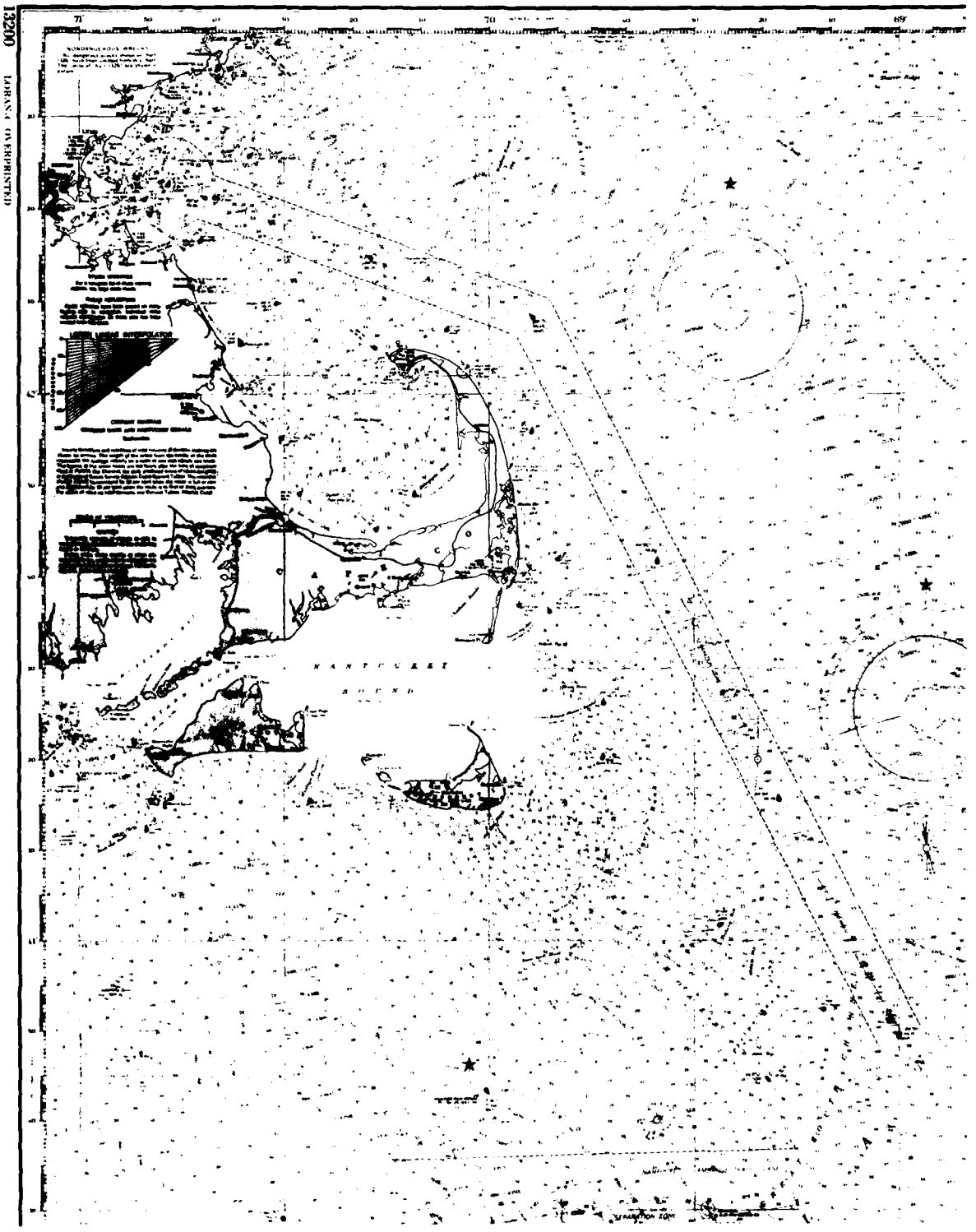

Figure 2-1 Hydrographic chart of Cape Cod, MA (13200)

Figure 2-2. Hydrographic chart of Nantucket Island, MA (13237)

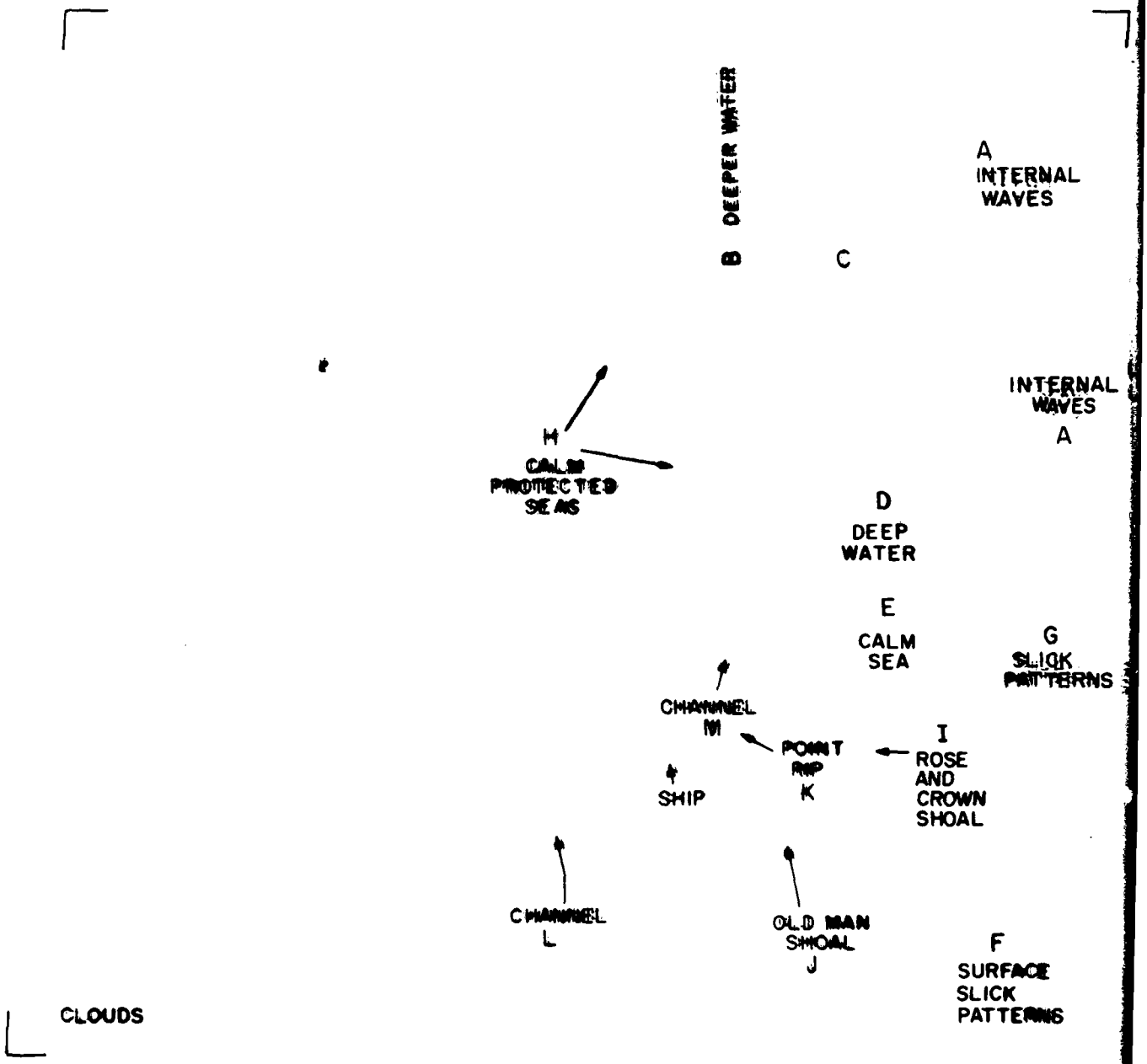

(LANDSAT) CAPE COD 17 JUL 72

(LANDSAT) CAPE COD 17 JUL 74

Figure 2-3. Landsat image, Cape Cod, MA (17 Jul 74)

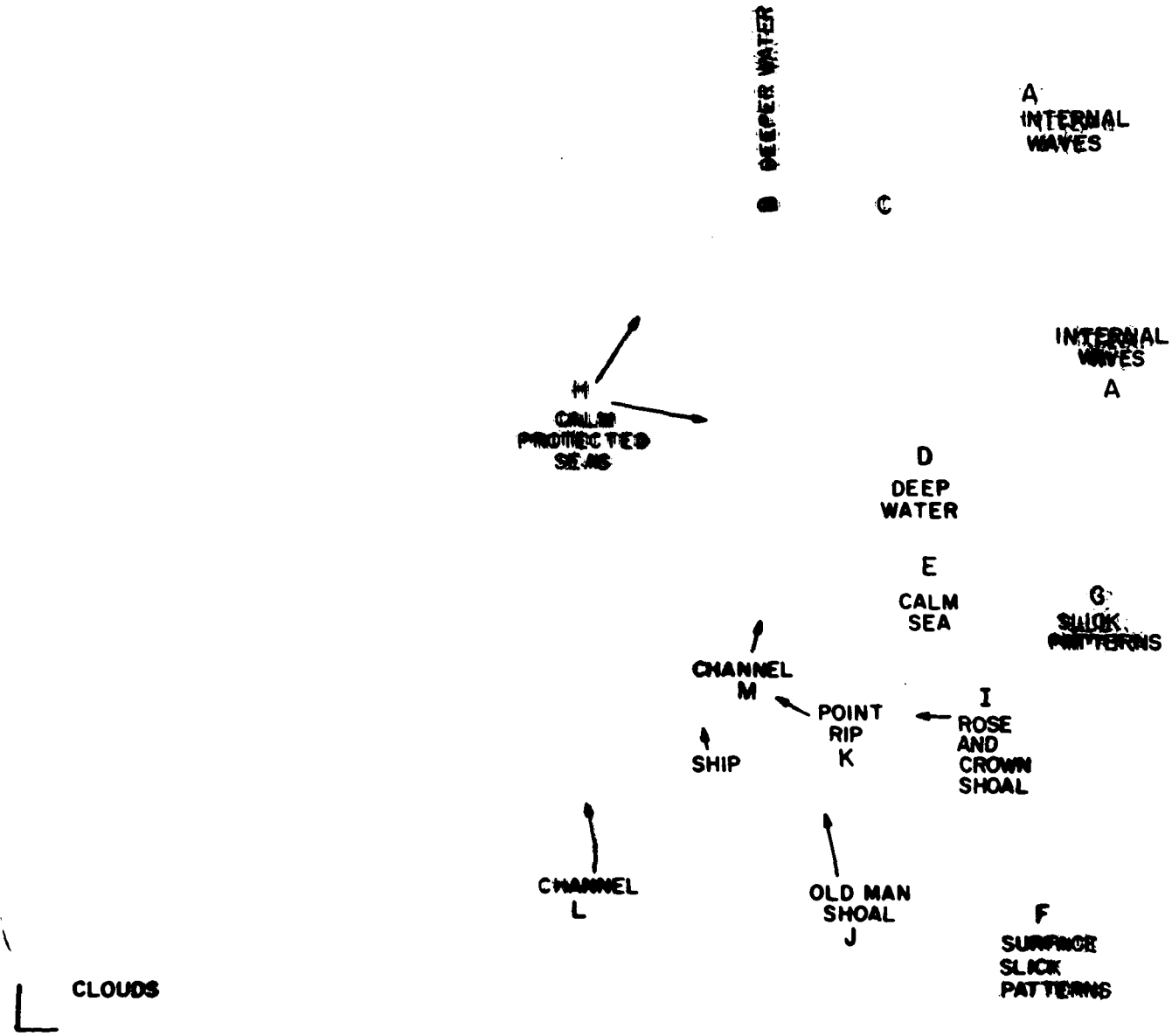

(LANDSAT) CAPE COD 17 JUL 74

Figure 2-4. Landsat image, Cape Code, MA (17 Jul 74)

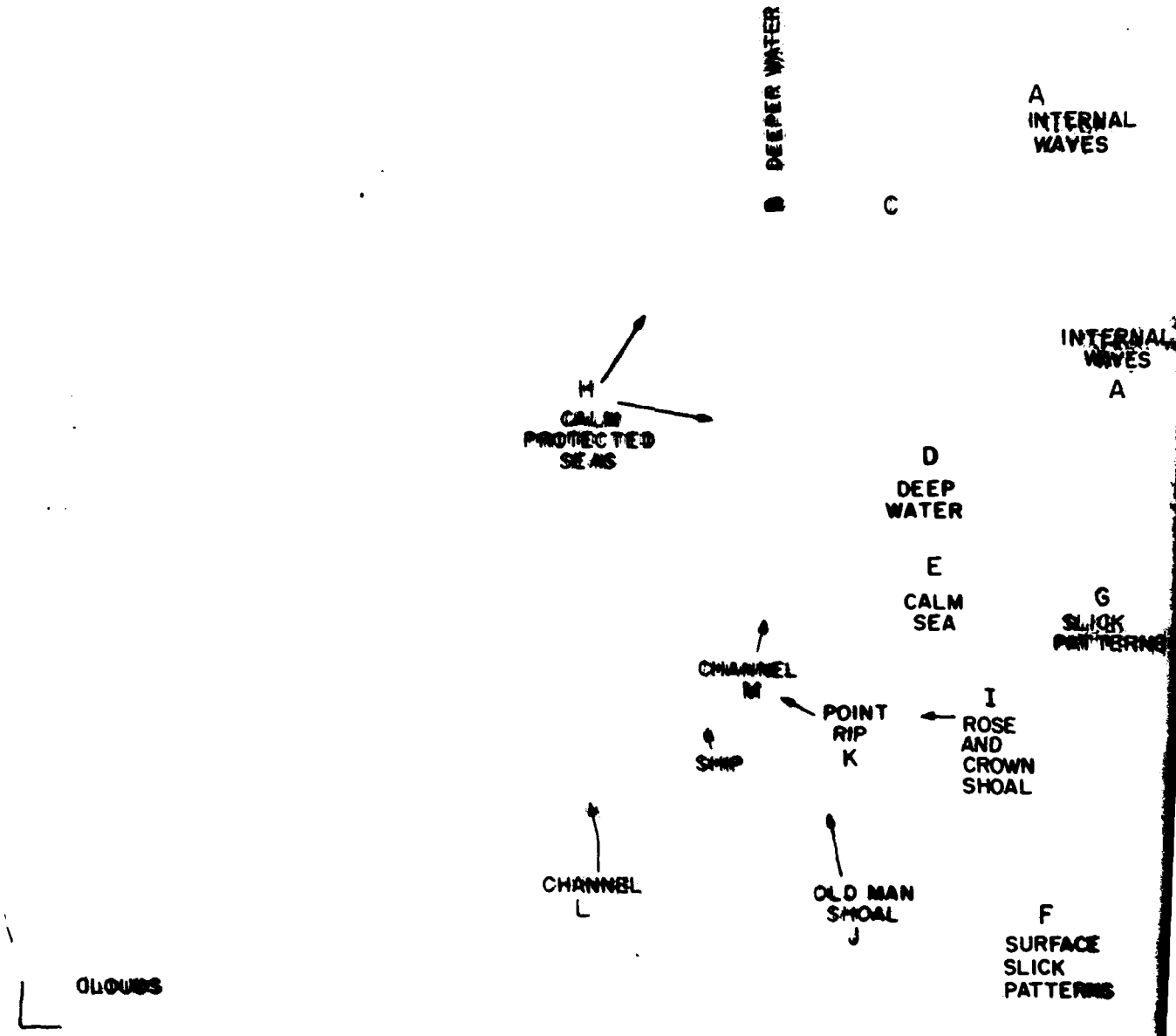

(LANDSAT) CAPE COD 17 JUL 72

Figure 2-5. Landsat image, Cape Cod, MA (17 Jul 74)

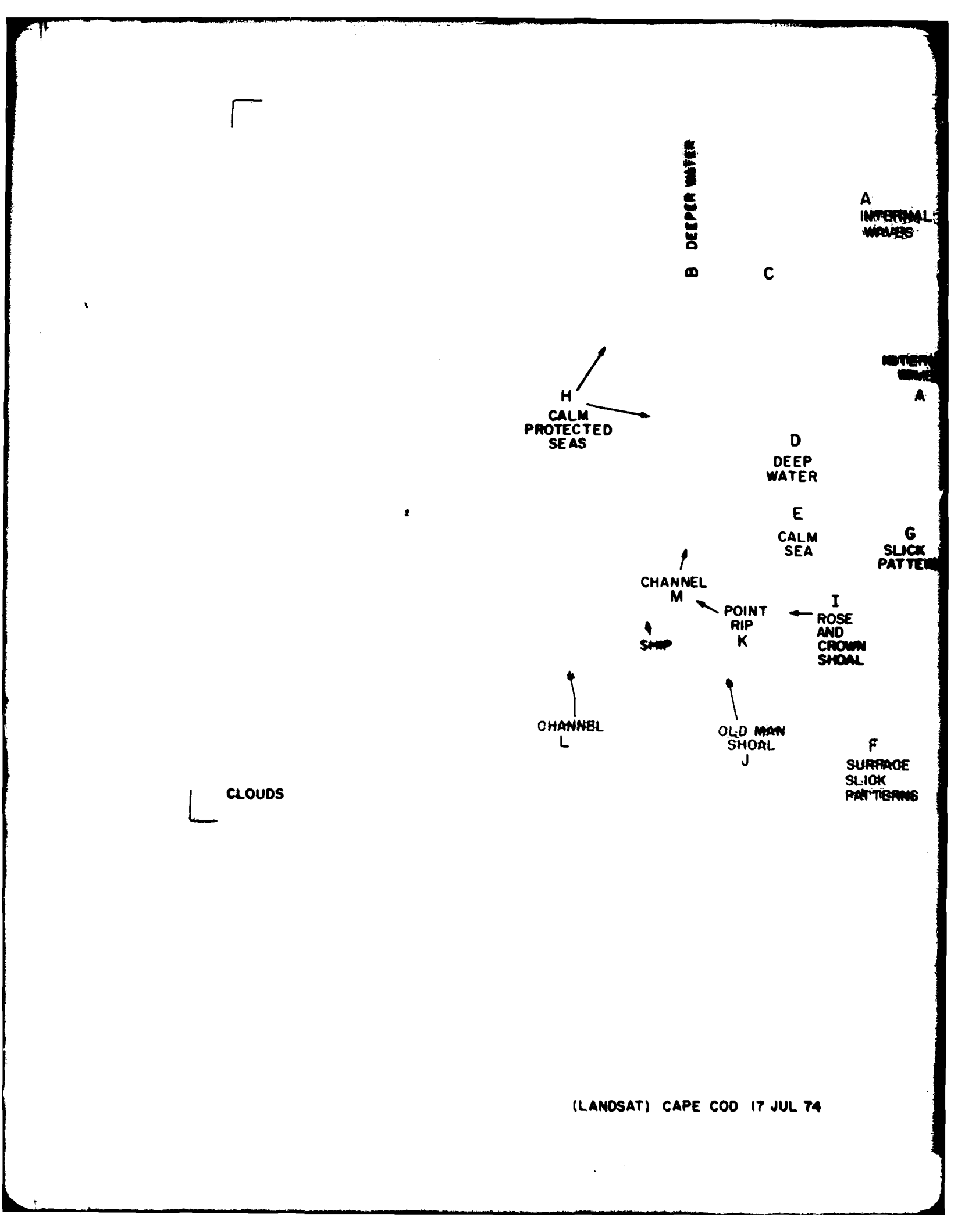

(LANDSAT) CAPE COD 17 JUL 74

Figure 2-6. Landsat image, Cape Code, MA (17 Jul 74)

3. Key West, FL

3. Key West, FL

The Key West case history area is located at the southern tip of the Florida Keys. The Keys area is a calcareous reef system characterized by shifting calcareous sands migrating among the active reef system. The strong Florida Current flows northeast along the southern shelf of the Keys. The Keys themselves have irregular shorelines and form an extremely complex pattern of shoals, channels and land masses. Figures 3-1 and 3-2 illustrate hydrographic charts available for the Florida Keys and Key West area. Note that the water remains quite shallow off the southern shore for about 5 nautical miles, where it quickly drops off to the Straits of Florida. This boundary of deep and shallow waters is represented by such numerous hydrographic obstructions as Sand Key, Marquesas Rock, Coalbin Rock and Western Sambo (see figure 3-1). North of the Florida Keys shoreline, a gradually sloping bottom forms the back waters of the relatively shallow Florida Sound. Landsat imagery of the Key West area are illustrated in figures 3-3 (Channel 4), 3-4 (Channel 5) 3-5 (Channel 6) and 3-5 (Channel 7). The majority of the bottom and left side of this image is cloud covered. The end of the Florida Keys land mass is illustrated in the upper right central section of the image. The hydrographic features surrounding the land masses are best illustrated in Channels 4 and 5. The IR Channels (figures 3-5 and 3-6) best provide discrimination of land and water

The largest extent of the shallow water areas is best characterized by Channel 4 (figure 3-3). The extent of the shallow water surrounding the Key West area is illustrated by the slight density contrast (B) of light to dark water coloration which surrounds Key West and associated Keys. The stream patterns flowing around the tip of the Key West shoal at location C (best illustrated in figure 3-3) are typical of turbid water patterns. Water movement appears to flow from north to south around the Key West tip. Current streamlines associated with the tonal patterns are illustrated in the overlay. Turbid water moving south in this area becomes entrained in the Florida Current and forms streamlines aligned with current direction.

The interpretation of shoals in this image is best illustrated by comparison with a color IR aerial photograph (figure 3-7) and a detailed hydrographic chart (figure 3-2). The color IR aerial photography illustrates the position and shape of the above water/land masses in red and the shoals as a tonal variation of blue. Variations in bottom reflectance characterize the bottom features. Ridge fields and shoaling patterns are easily discernible by their light tone and meandering pattern. Bottom vegetation growth is readily interpreted by the mottled appearance. The long, flowing stream patterns observed in the channel and the offshore areas are associated with dispersion of turbid water. Through comparison, this photograph provides a basic understanding of the coastal processes to be interpreted with Landsat images. Comparable tonal textures and patterns are illustrated between the aerial photograph (figure 3-7) and the Landsat image (figure 3-3). Note similarities in the reef features, bottom vegetation areas, turbid water patterns, and channel entrances.

Another Landsat image of the Florida Keys dated one and one-half years later is illustrated in figure 3-8 (Channel 5). The hydrographic chart (figure 3-1) depicts comparable bathymetry. Temporal differences can be observed in figures 3-4 and 3-8. First note that the gray scales or contrast of the two figures are approximately the same; thus, tonal differences should result mainly from earth reflectance differences; i.e., water color. Note that the ridge fields (D) previously illustrated in figures 3-3, 3-4 and 3-7 are not observed in figure 3-8; turbidity flows are observed instead. High water reflectance characteristic of highly turbid water is observed along the northern shores of Key West. This

high reflection makes interpretation of hydrographic features more difficult in figure 3-8. However, the turbidity patterns do provide an interpretative technique of characterizing the direction and location of surface currents. Notice on figure 3-8 the numerous turbidity flow patterns (E) within the channel entrances between the Keys.

Figure 3-8 also illustrates some nonconclusive physical phenomena. The lighter toned areas (F) in Florida Bay (northeast of Key West) is not specifically known to be turbid water or morning fog patches. The streamlike features in this area are somewhat characteristic of turbid water. Similarly, this lighter toned area appears to cross land in the northern area of the scene, which is characteristic of surface fog. Also note the highly bright tone on the western shore at the beginning of the Keys (Key Largo) (G). High reflectance in this area is believed to result from high concentrations of suspended calcareous sediment in a shallow water (2-39 ft).

Figure 3-1. Hydrographic chart of the Florida Keys (11420)

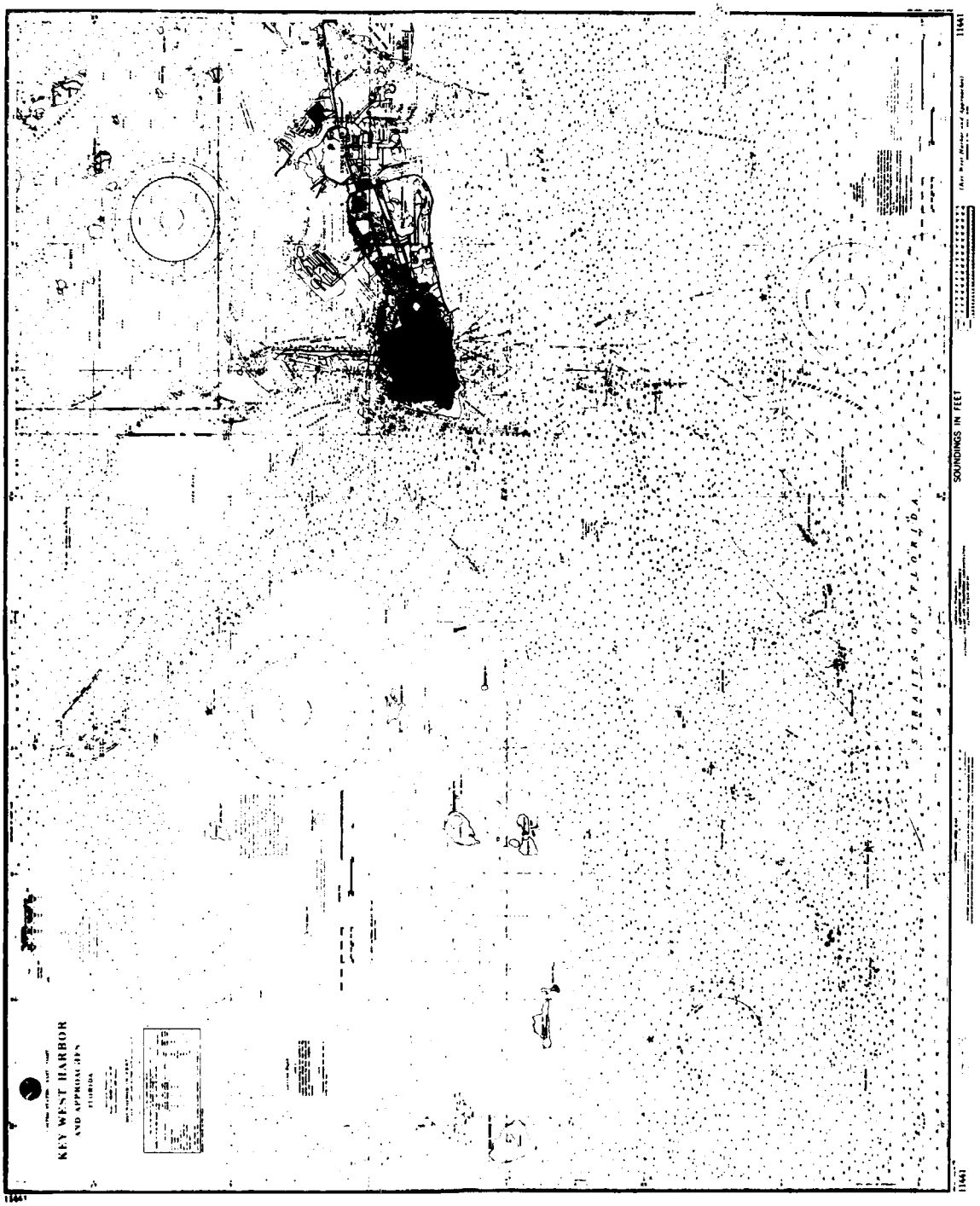

Figure 3-2. Hydrographic chart of Key West, Fl (11441)

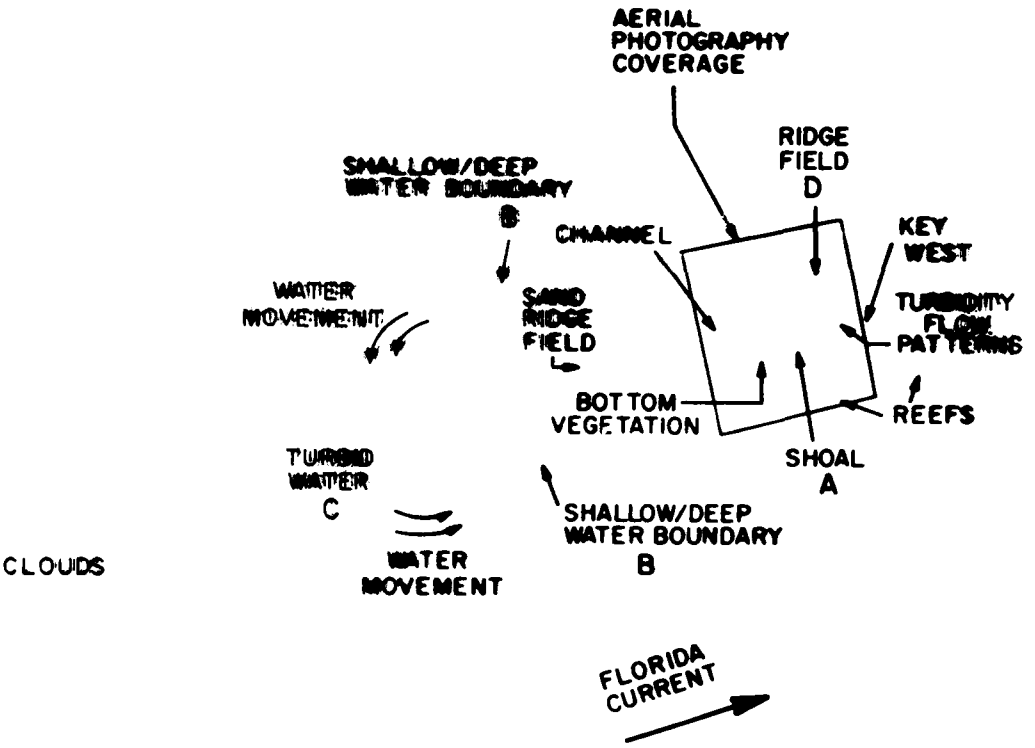

(LANDSAT) KEY WEST 30 OCT 72

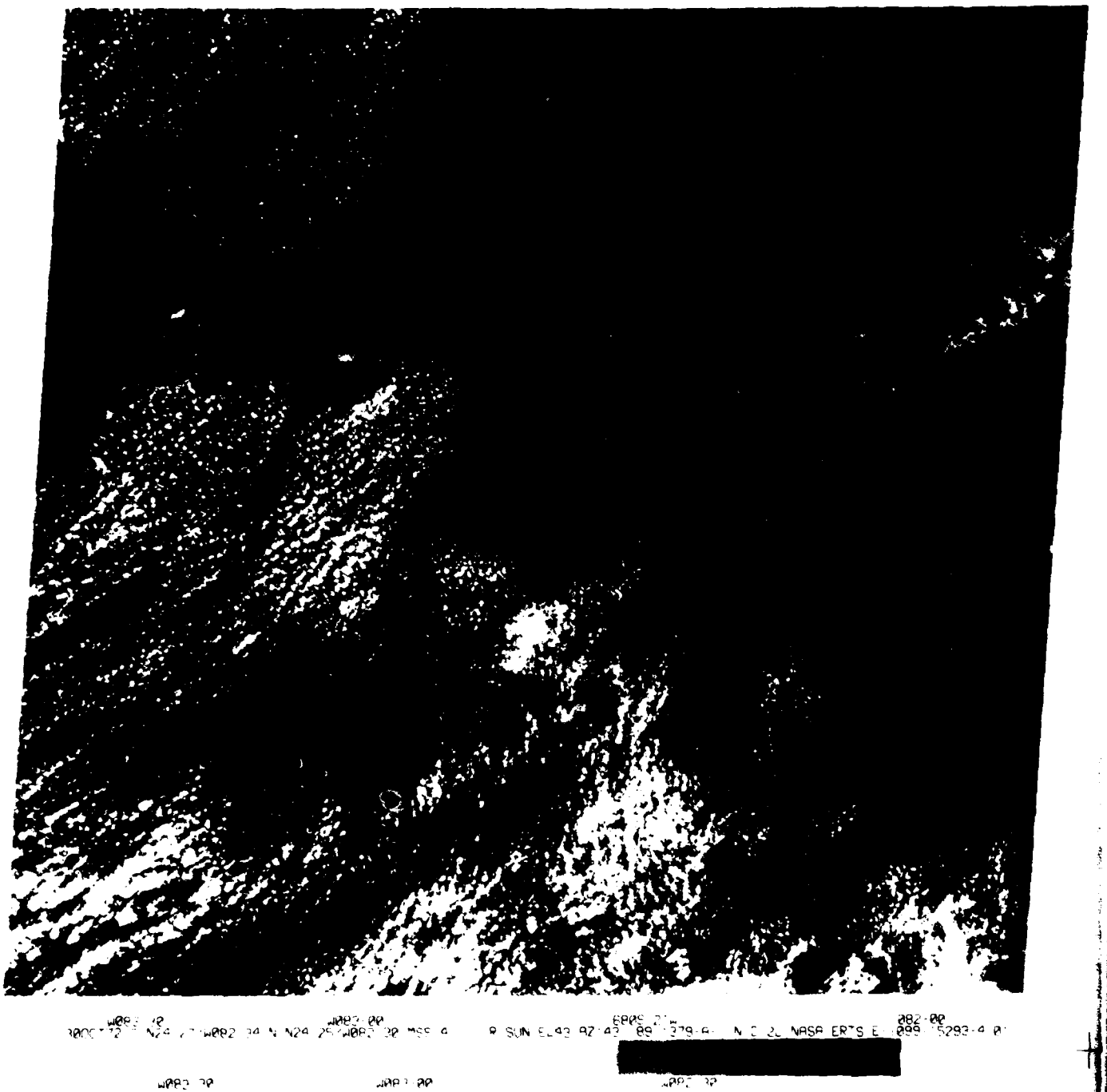

Figure 3-3. Landsat image, Key West, FL (30 Oct 72)

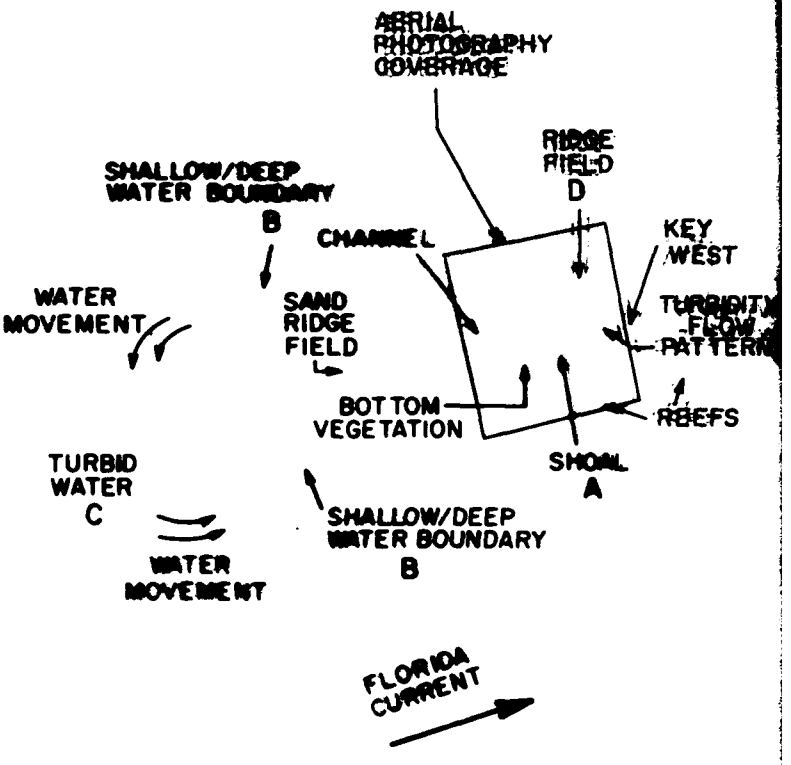

(LANDSAT) KEY WEST 30 OCT 72

Figure 3-4. Landsat image, Key West, FL (30 Oct 72)

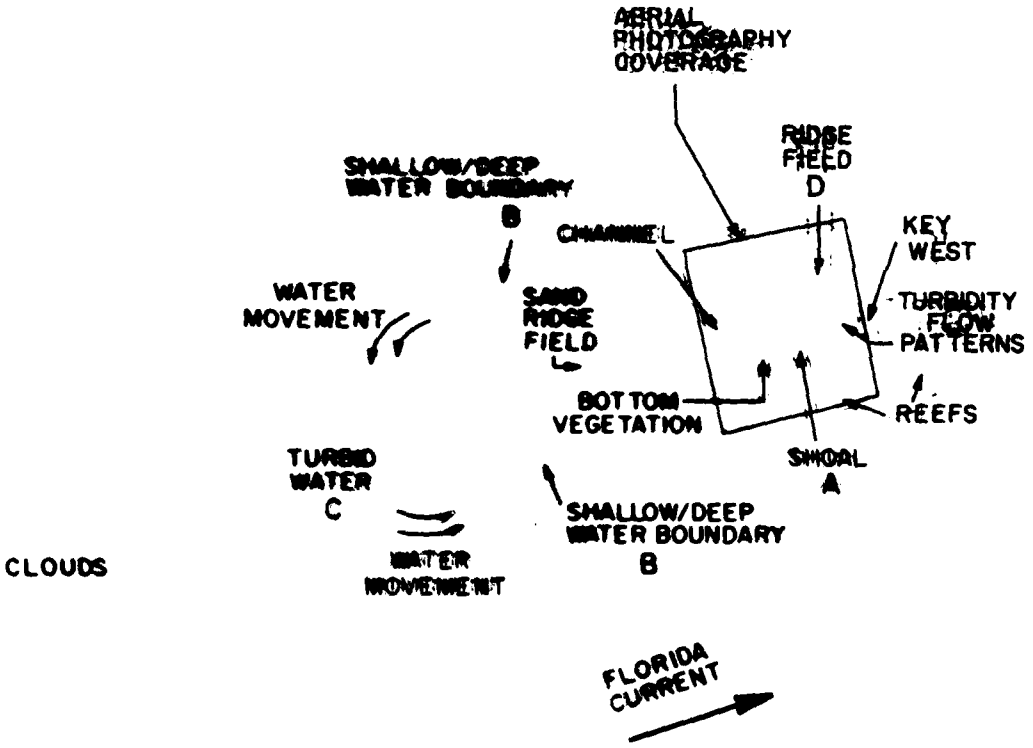

(LANDSAT) KEY WEST 30 OCT 72

Figure 3-5. Landsat image, Key West, FL (30 Oct 72)

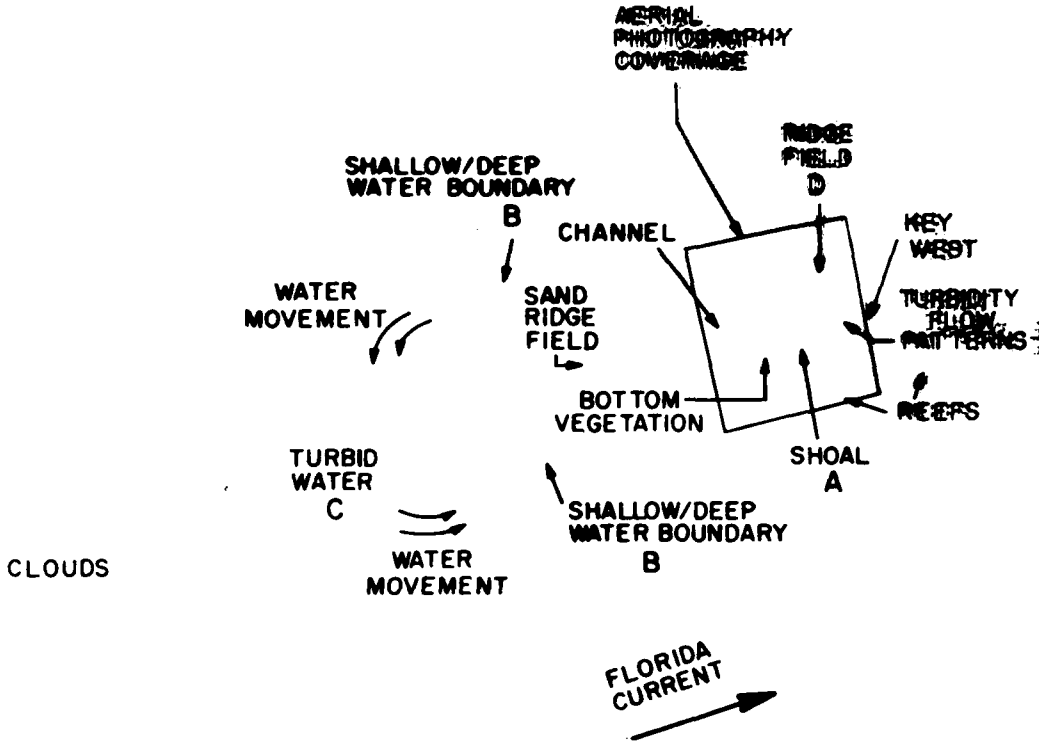

(LANDSAT) KEY WEST 30 OCT 72

Figure 3-6. Landsat image, Key West, FL (30 Oct 72)

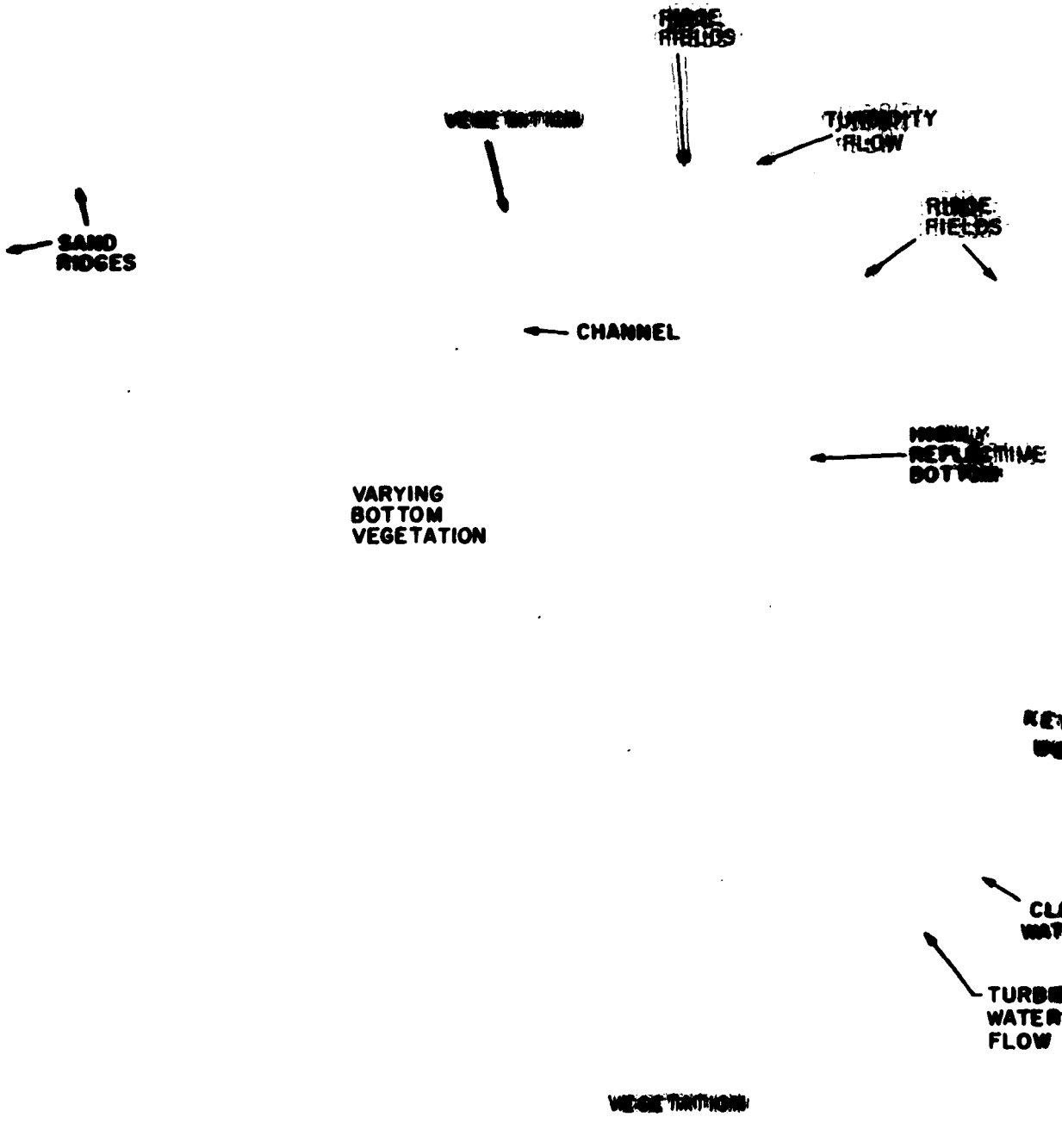

(AERIAL PHOTOGRAPHY) KEY WEST

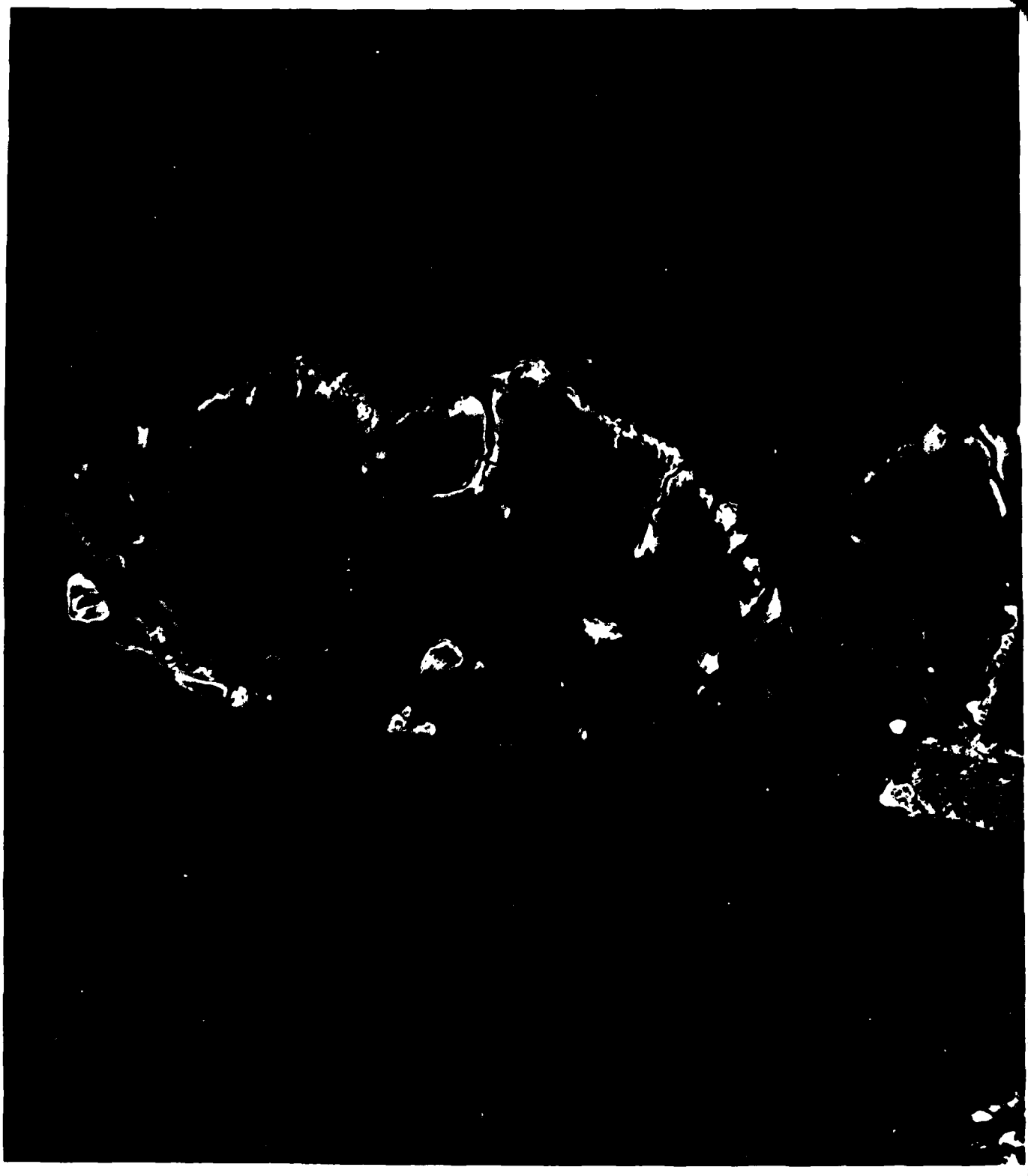

Figure 3-7. Color IR aerial photograph (1:122,000), Key West, FL (15 Oct 69)

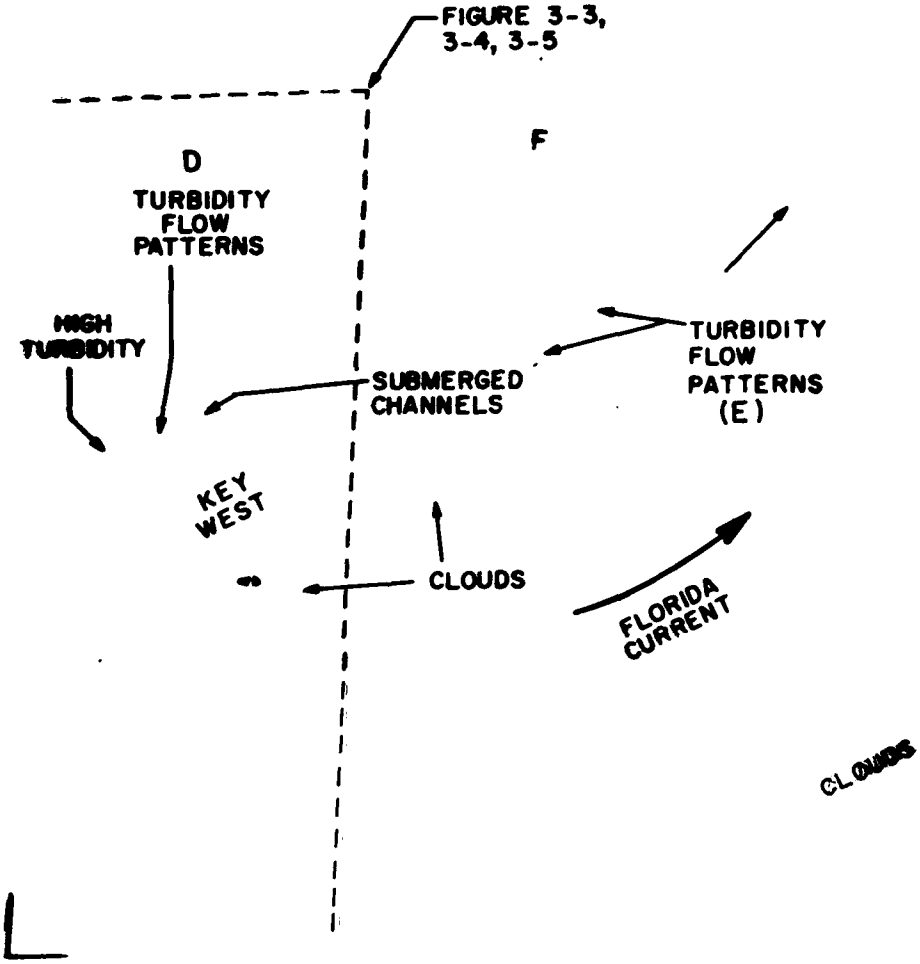

(LANDSAT) FLORIDA KEYS 27 FEB 74

Figure 3-8. Landsat image, Florida Keys (27 Feb 74)

4. Apalachee Bay, FL

4. Apalachee Bay, FL

Apalachee Bay is located on the Florida Gulf Coast at the embayment where the Florida Panhandle and Peninsula join. Apalachi 'a, Florida, is located just west of ' s area. The coastline is low energy with a very gradually sloping bottom. Low-lying, tidal-influenced wetlands form the coastline, with numerous offshore sand shoals present. Figure 4-1 illustrates the hydrographic chart for the corresponding Landsat imagery. Four Landsat images obtained on 12 December 1978 are shown in figures 4-2 (Channel 4), 4-3 (Channel 5), 4-4 (Channel 6) and 4-5 (Channel 7). Low-lying wetlands bordering the coast are illustrated in all four channels by their contrasting tonal differences (depicted by A on the overlay). The bright areas along the coastlines represent highly reflective sand beaches. Numerous shoals are illustrated in the visible channels (figures 4-2 and 4-3). Note the position of Dog Reef, South Shoal, and Ochlockonee Shoal on Landsat as compared with the hydrographic chart, figure 4-1. An atypically shaped shoal having a long lenticular pattern extending perpendicularly from the coastline is located just west of South Shoal. This feature is noted on aerial photography and several Landsat scenes, but is not well-illustrated on the hydrographic chart, figure 4-1.

A color IR aerial photograph of the reference area outlined on the overlay is illustrated in figure 4-6. Notice the bright, highly reflective sand bottom shoals and the complex array of dark-blue-toned channels which migrate inward through the ribbons of oyster reefs throughout the photography. Upon detailed examination, mottled patterns characteristic of bottom vegetation are illustrated. Current regimes can be interpreted by the sand ridge orientation on the shoals. Note the streams emptying into the bay are very dark in color, which is characteristic of the low amount of suspended material in the water. Submerged dredge spoils are located adjacent to the linear dredged channels. Comparison of this photograph with the Landsat images provides a better understanding for interpreting hydrographic features. Many of the features mentioned can also be seen on the Landsat imagery. Bottom vegetation and highly reflective, sandy shoals are illustrated in the visible channels (figures 4-2 and 4-3). These figures also show the complex subsurface channels. The IR channels (particularly Channel 6 because of enhanced contrast used in processing) show the highly reflective oyster reef ribbons and the slightly darker tonal wetlands.

Similarities in shape of the large, highly reflective shoal, which is located in the central position of the aerial photograph and also on the Landsat imagery at (B), are apparent in the visible channels. The aerial photograph (figure 4-6) indicates that the entire shoal is subsurface. For this shoal to show up on the IR channel indicates that either (1) the outgoing tide has exposed the land surface; or (2) waves breaking over the shoal have reflected a significant amount of IR radiation to register on Channel 7 of Landsat. The former conclusion appears to best explain this phenomenon by examining the same scene, but at an earlier date, 6 November 1978. (Tidal fluctuations in this area are on the order of 2-3 feet.) Landsat imagery of Apalachee Bay for this time period are illustrated in figure 4-7 for Channel 5 and figure 4-8 for Channel 7. Comparison of Channel 5 from these two time periods (figures 4-3 and 4-7) indicates that the extent of shoals and the distinction of land forms is better illustrated in figure 4-3 (12 December 1978). Note the clarity with which Dog Reef is illustrated in this figure as opposed to figure 4-7. Similarly, South Shoal is much better depicted in figure 4-3 than in figure 4-7. Higher tide and deeper water are interpreted to be present in the 6 November 1978 time period, and account for the loss of detail in the shoal. A lower tidal level and shallower water in the 12 December 1978 image exposes low-lying coastlines and the extent of the shoal.

This difference is illustrated by comparison of the IR channels, figure 4-5 (12 November) and figure 4-8 (6 November). Note that the extent of Peninsula Point is greater in figure 4-5. Also note that the shoals (C) are present in figure 4-5, but not in figure 4-7. The absence or presence of shoals strongly suggests tidal differences.

Cloud streaks can be observed inland and along the coastline on figure 4-7. Cloud streaking patterns such as these are typically associated preceding cold fronts. The interpreter must be careful of misinterpreting these light streaked patterns over water areas as turbid flow patterns.

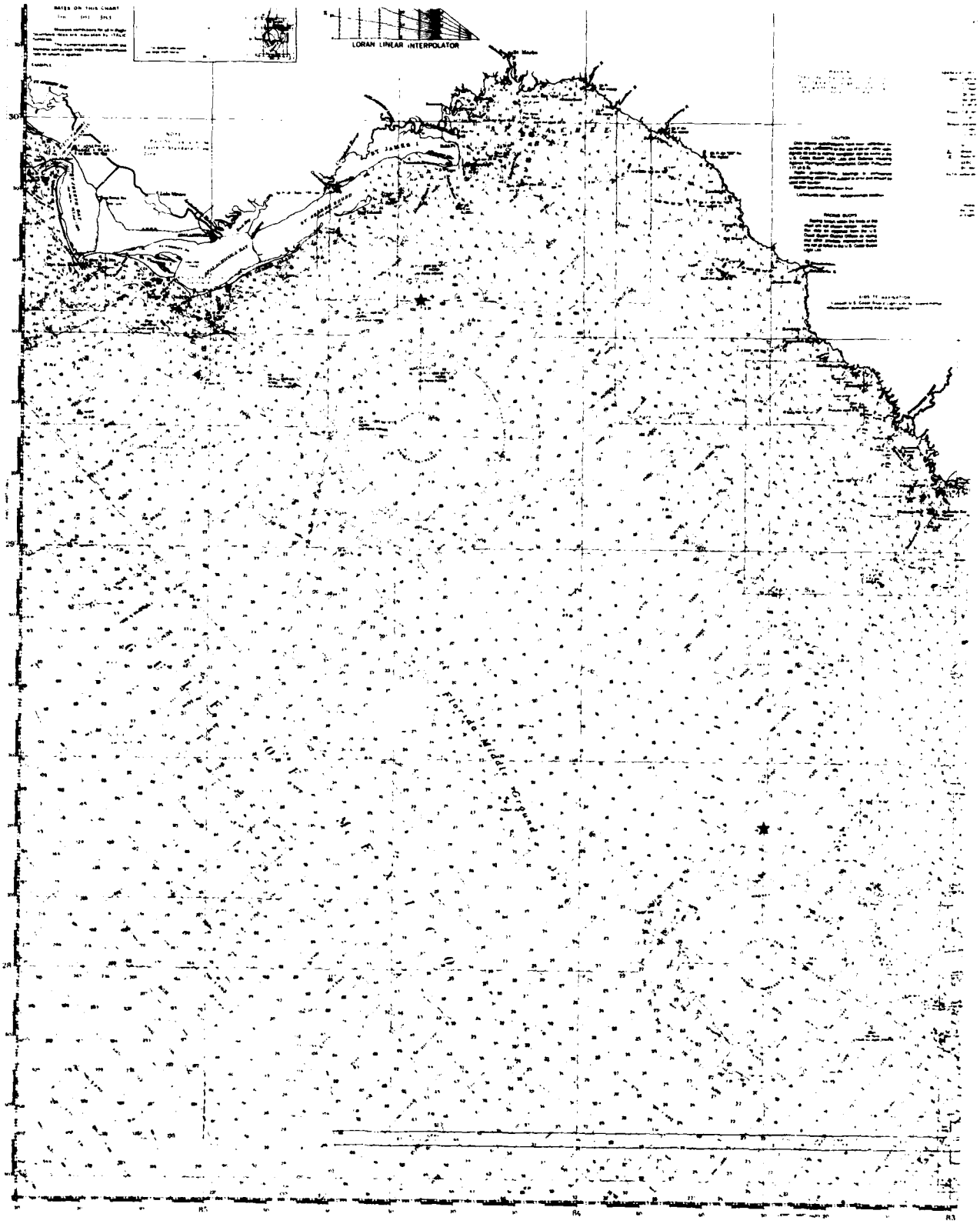

Figure 4-1. Hydrographic chart of Apalachee Bay, FL (11400)

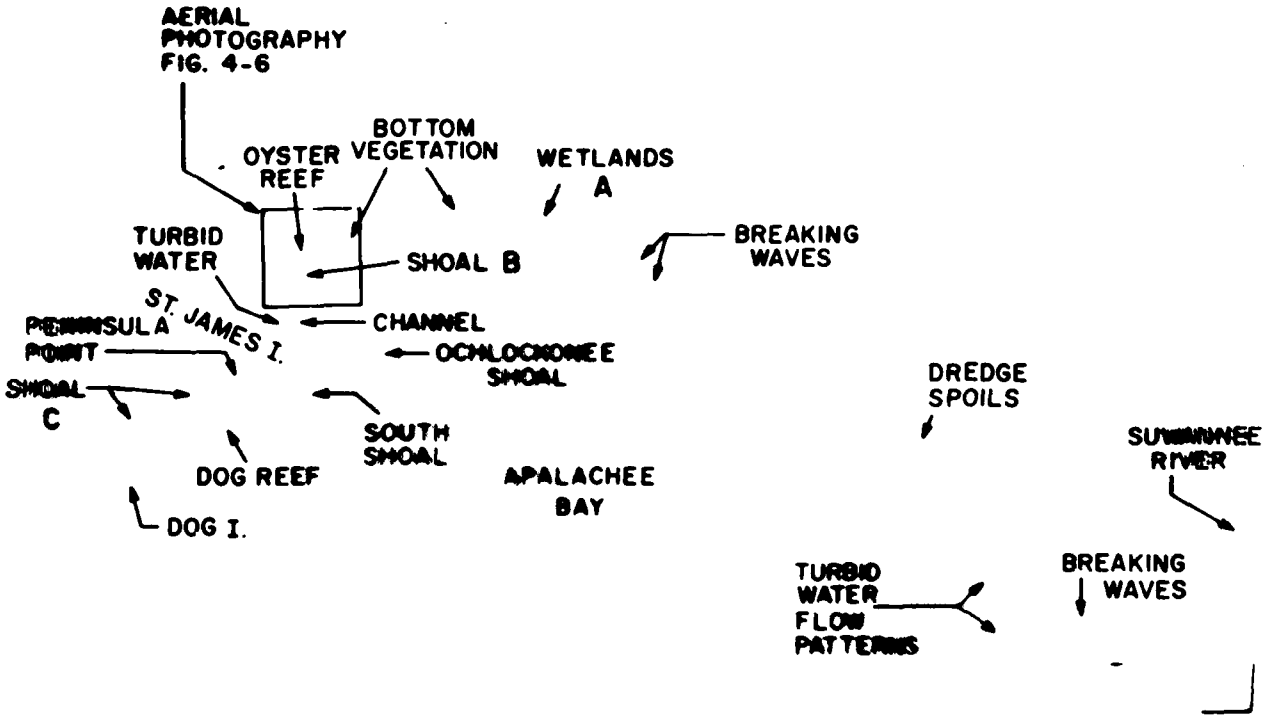

(LANDSAT) APALACHEE BAY 12 DEC 78

AD-A125 760 INTERPRETATION OF HYDROGRAPHIC FEATURES USING LANDSAT IMAGES(U) NAVAL OCEAN RESEARCH AND DEVELOPMENT ACTIVITY NSTL STATION MS R A. ARNONE ET AL. JUN 81 NORDA-39 F/G 8/10 NL 2/3

UNCLASSIFIED

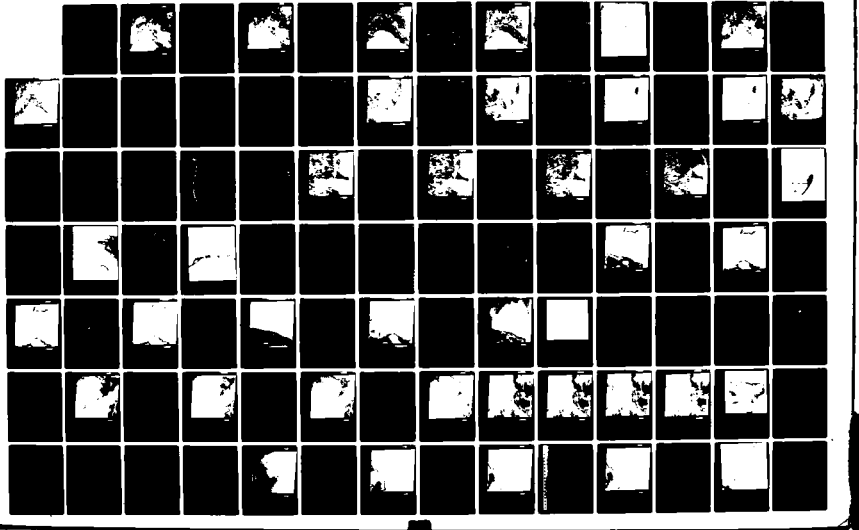

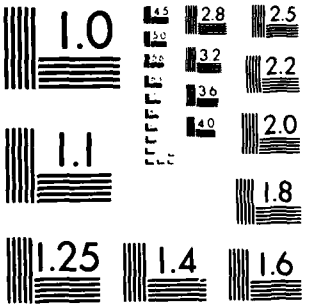

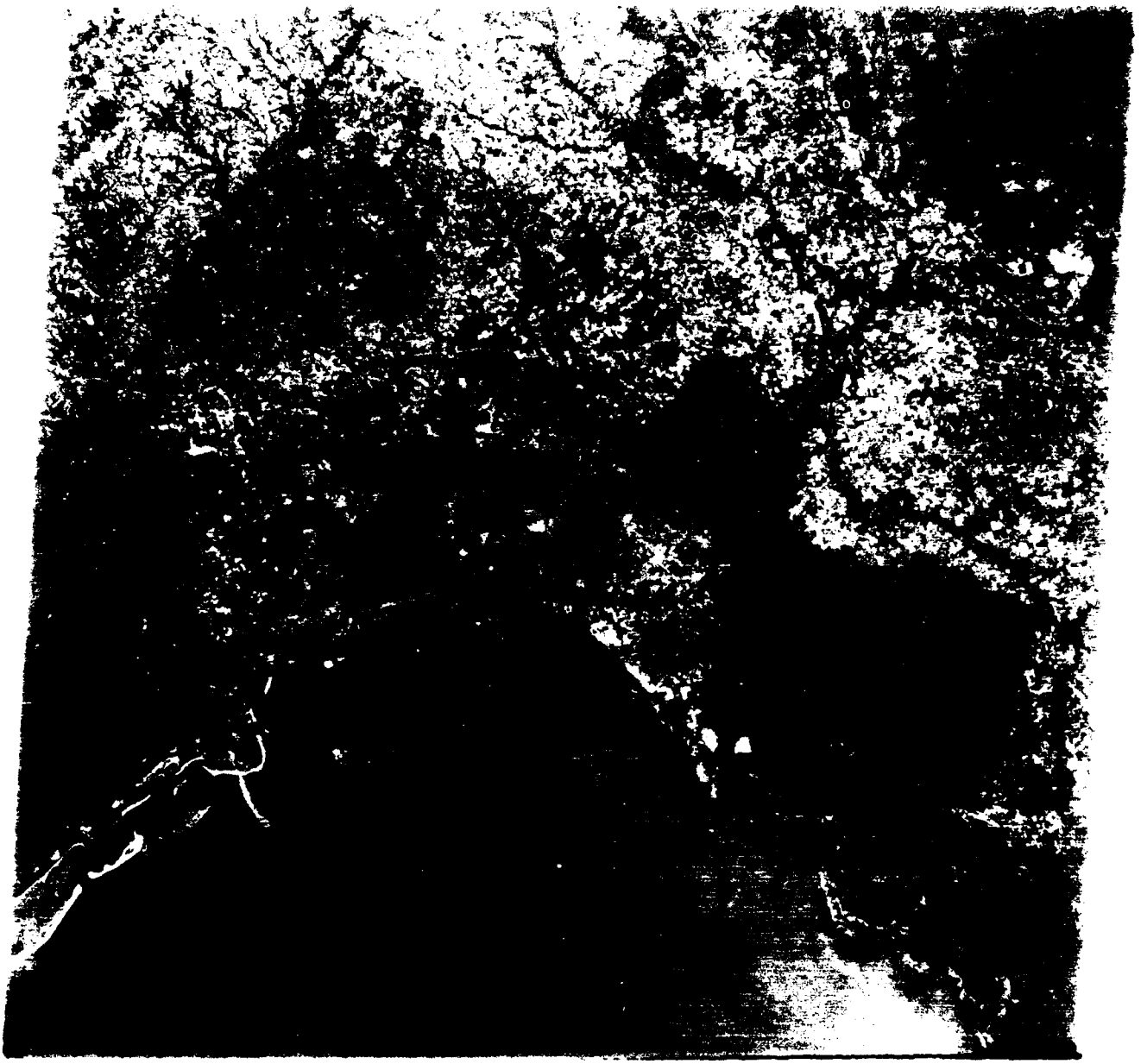

Figure 4-2. Landsat image, Apalachee Bay, FL (12 Dec 78)

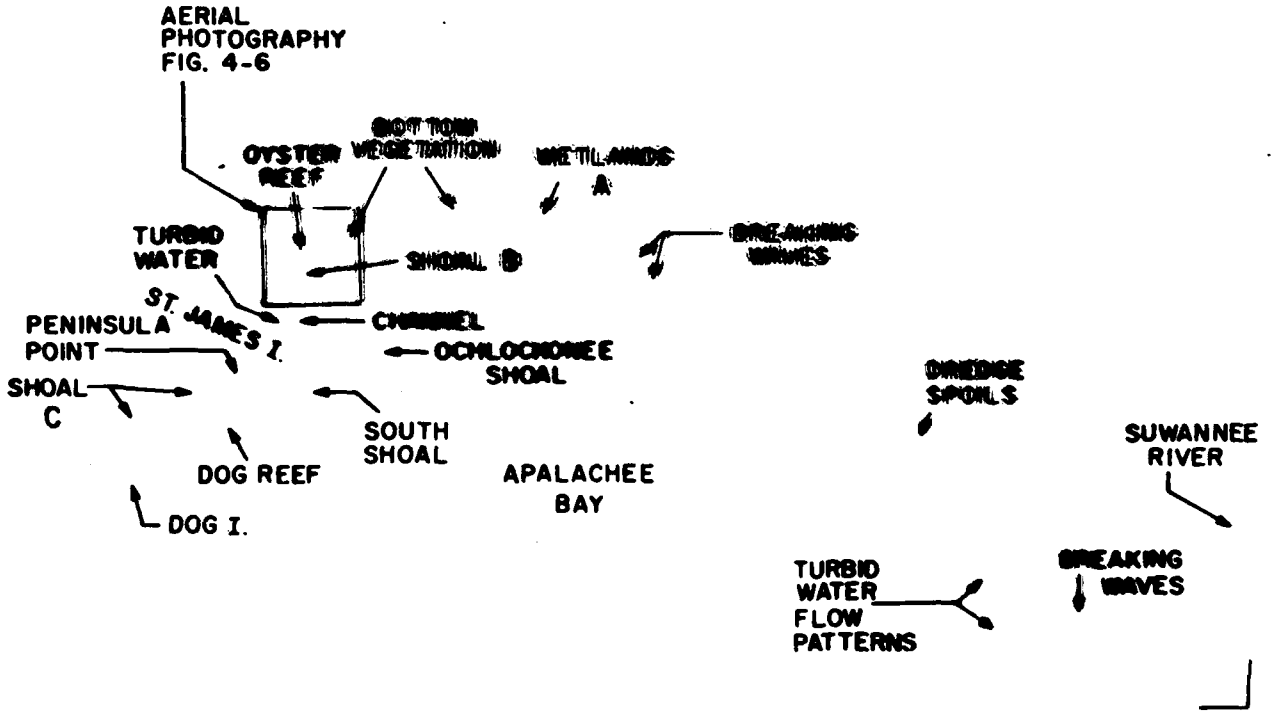

(LANDSAT) APALACHEE BAY 12 DEC 78

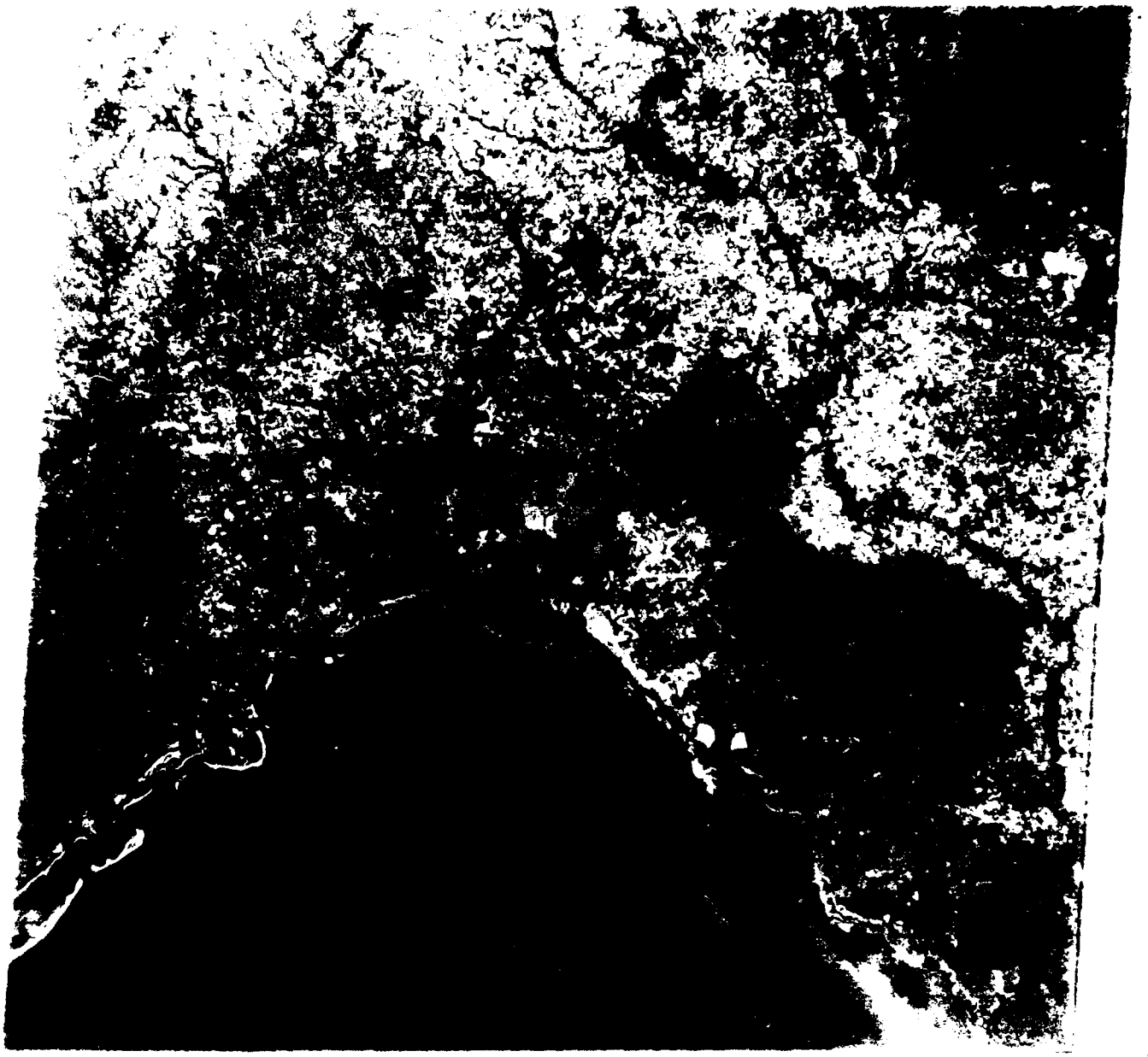

Figure 4-3. Landsat image, Apalachee Bay, FL (12 Dec 78)

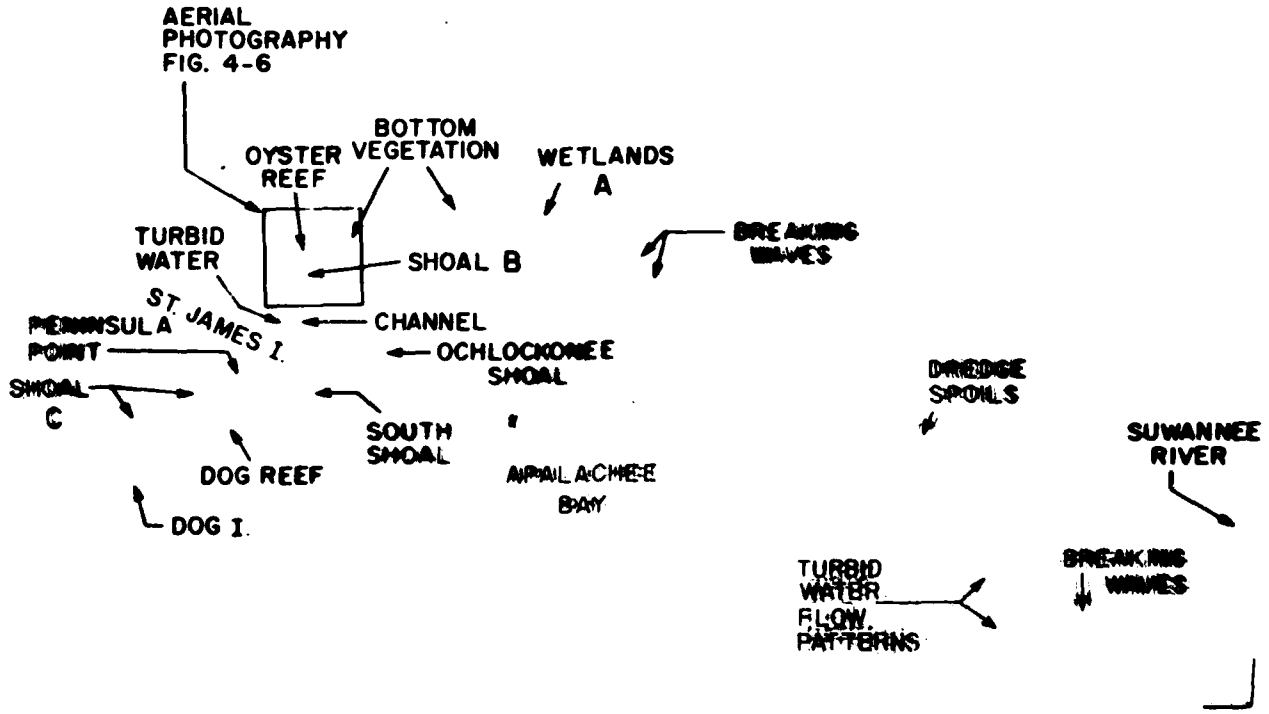

(LANDSAT) APALACHEE BAY 12 DEC 78

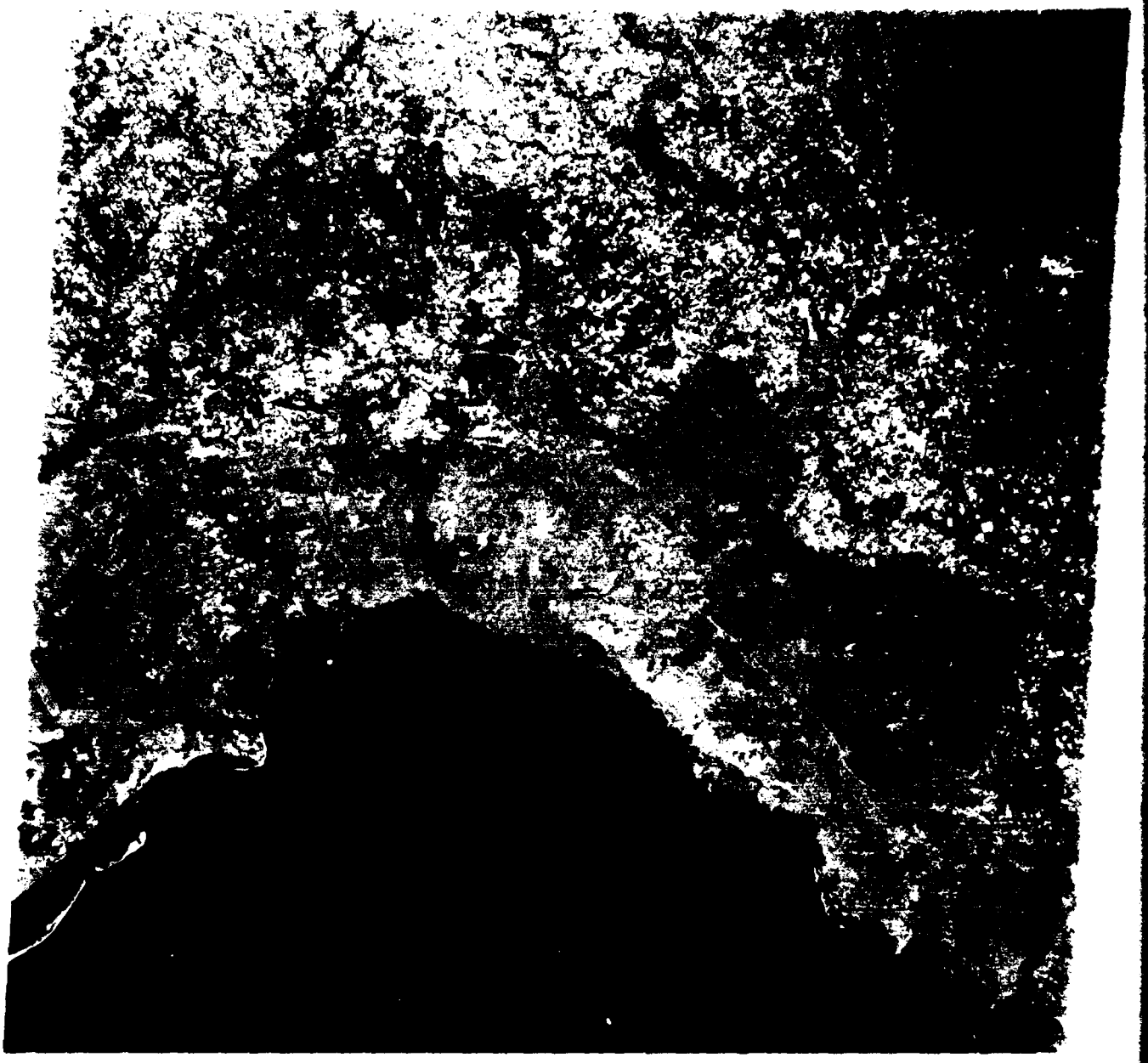

Figure 4-4. Landsat image, Apalachee Bay, FL (12 Dec 78)

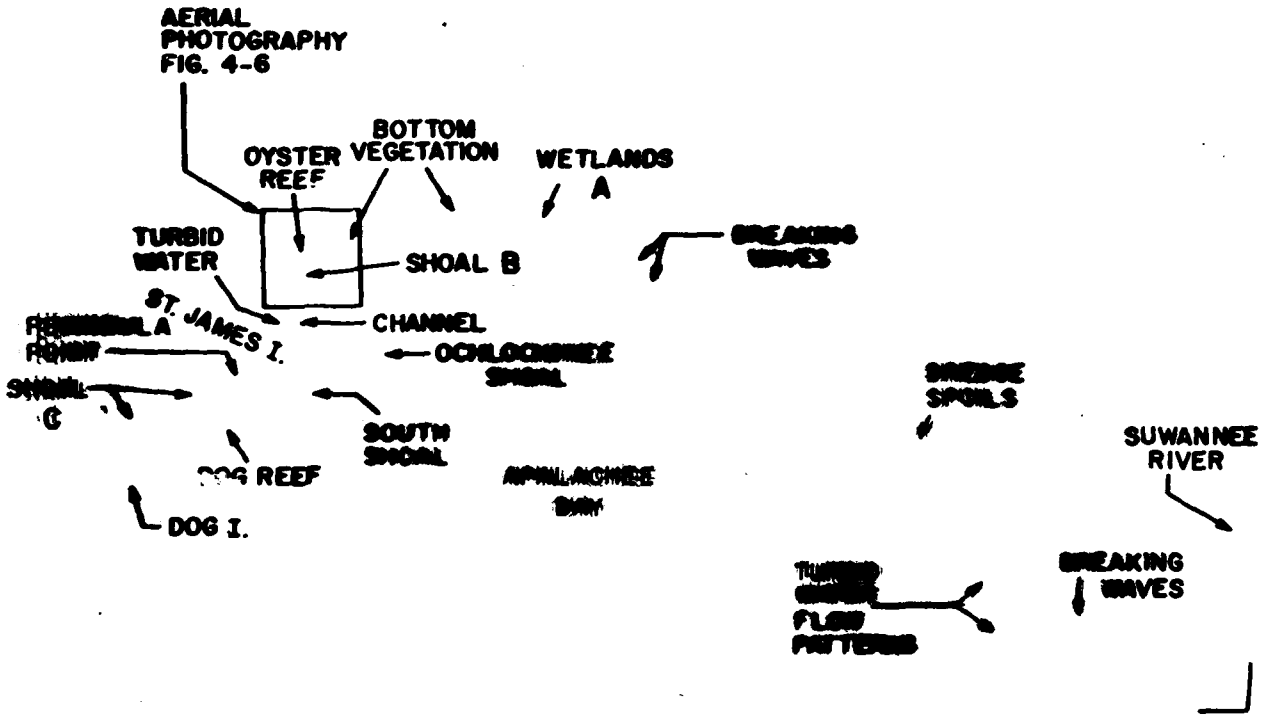

(LANDSAT) APALACHEE BAY 12 DEC 78

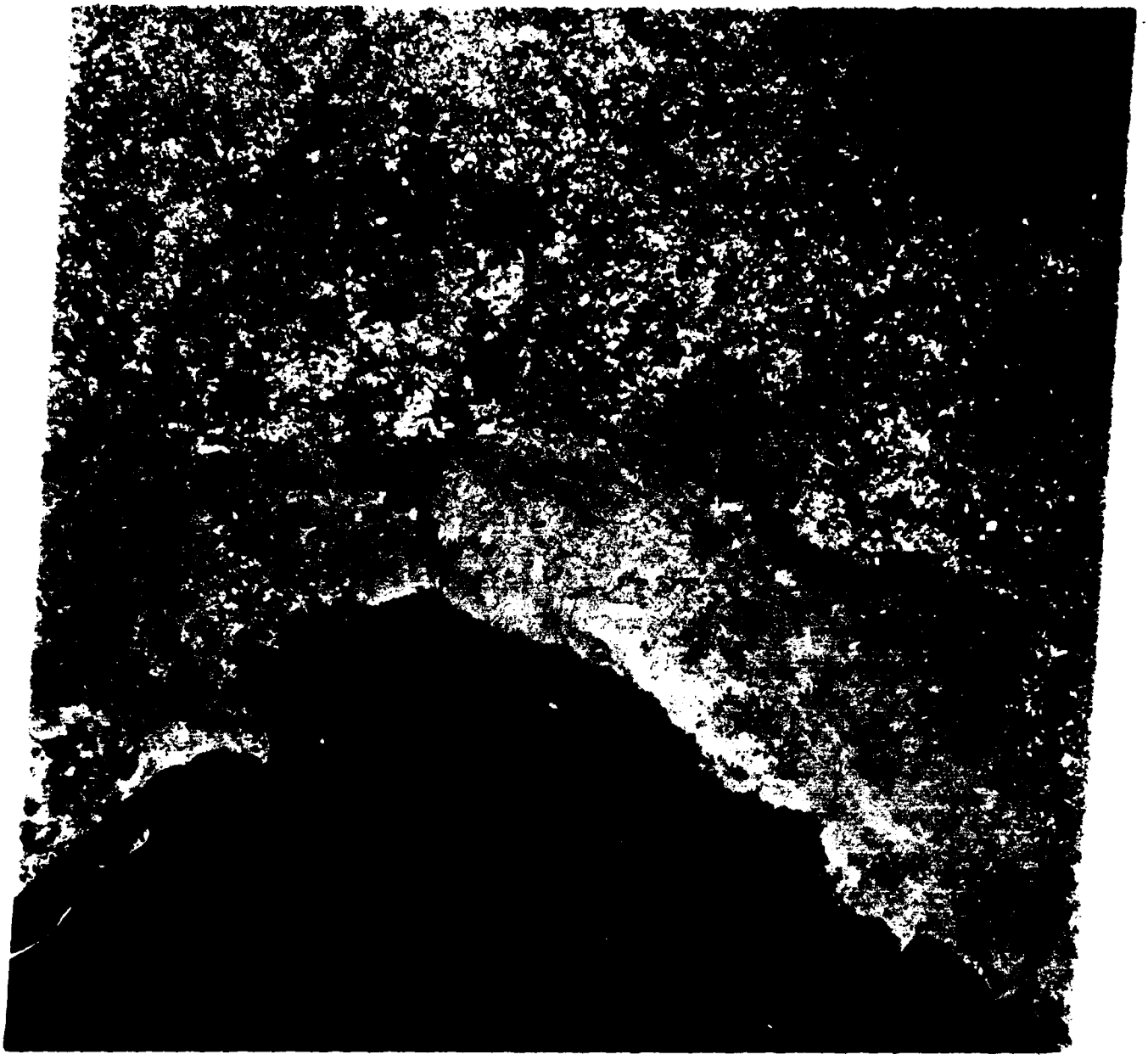

Figure 4-5. Landsat image, Apalachee Bay, FL (12 Dec 78)

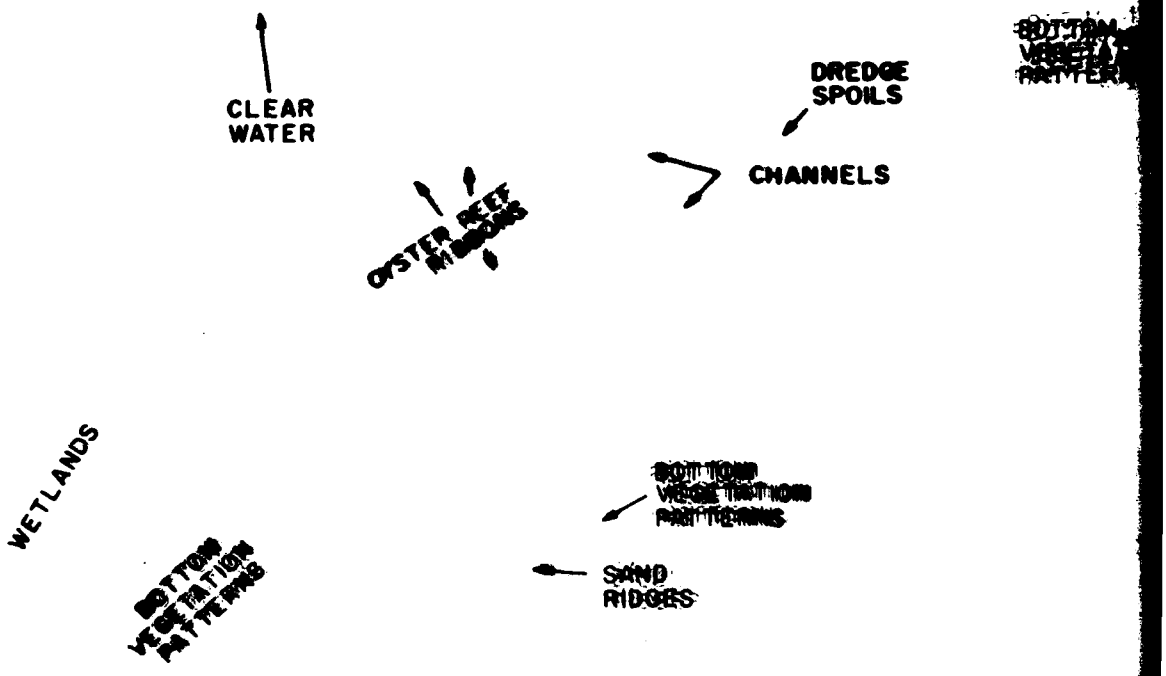

(AERIAL PHOTOGRAPHY) APALACHEE BAY
15 NOV 79

Figure 4-6. Color IR aerial photograph (1:130,000), Apalachee Bay, FL (15 Nov 79)

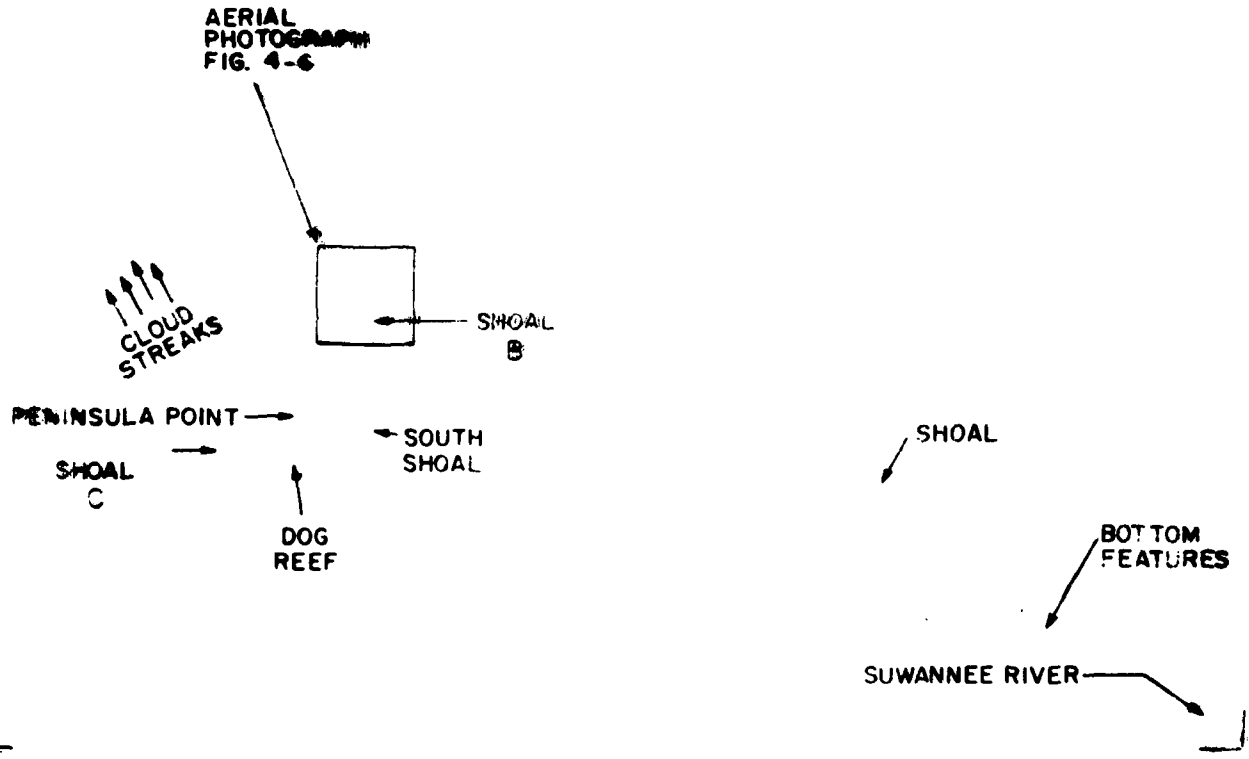

(LANDSAT) APALACHEE BAY 6 NOV 78

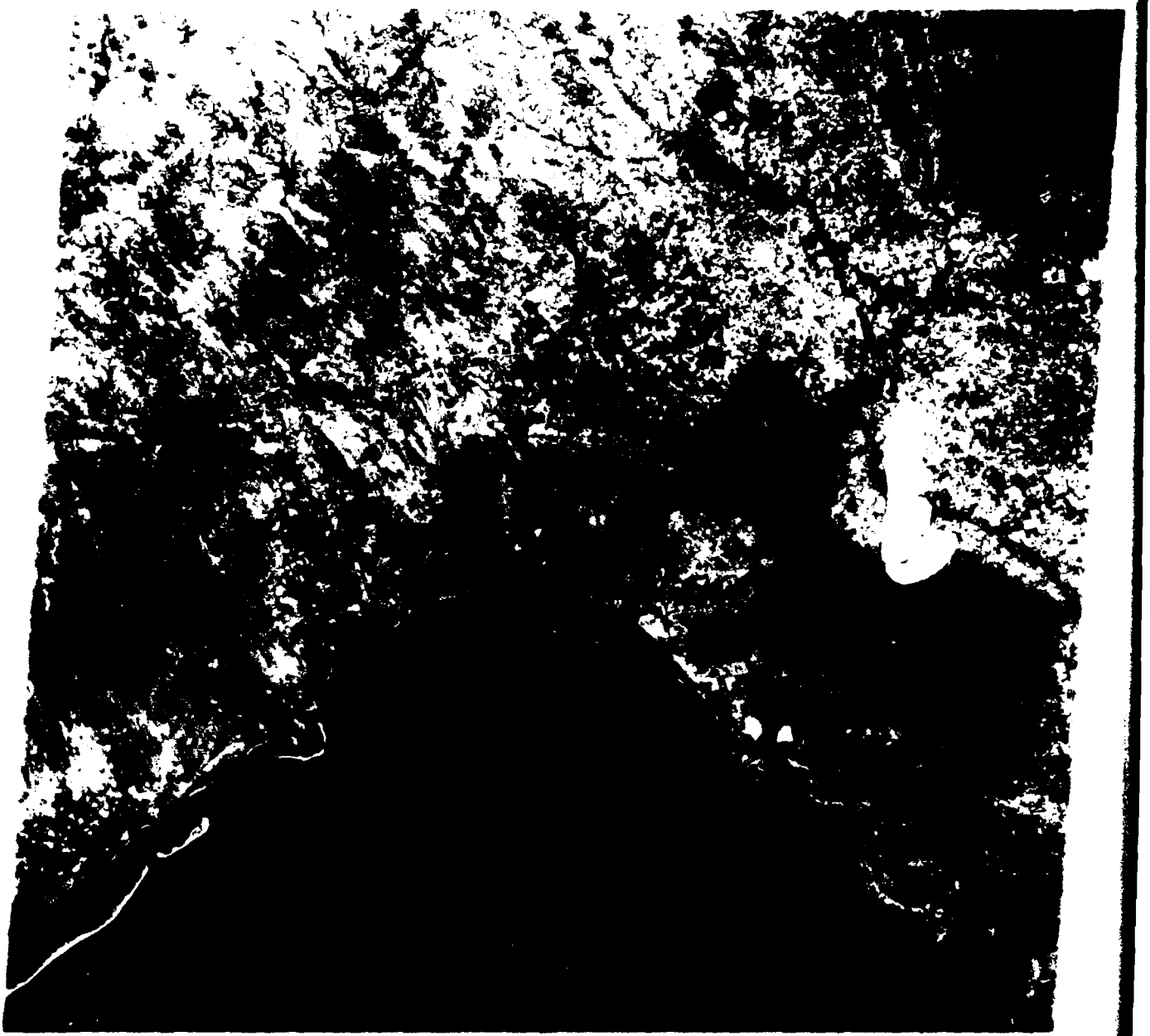

Figure 4-7. Landsat image, Apalachee Bay, FL (6 Nov 78)

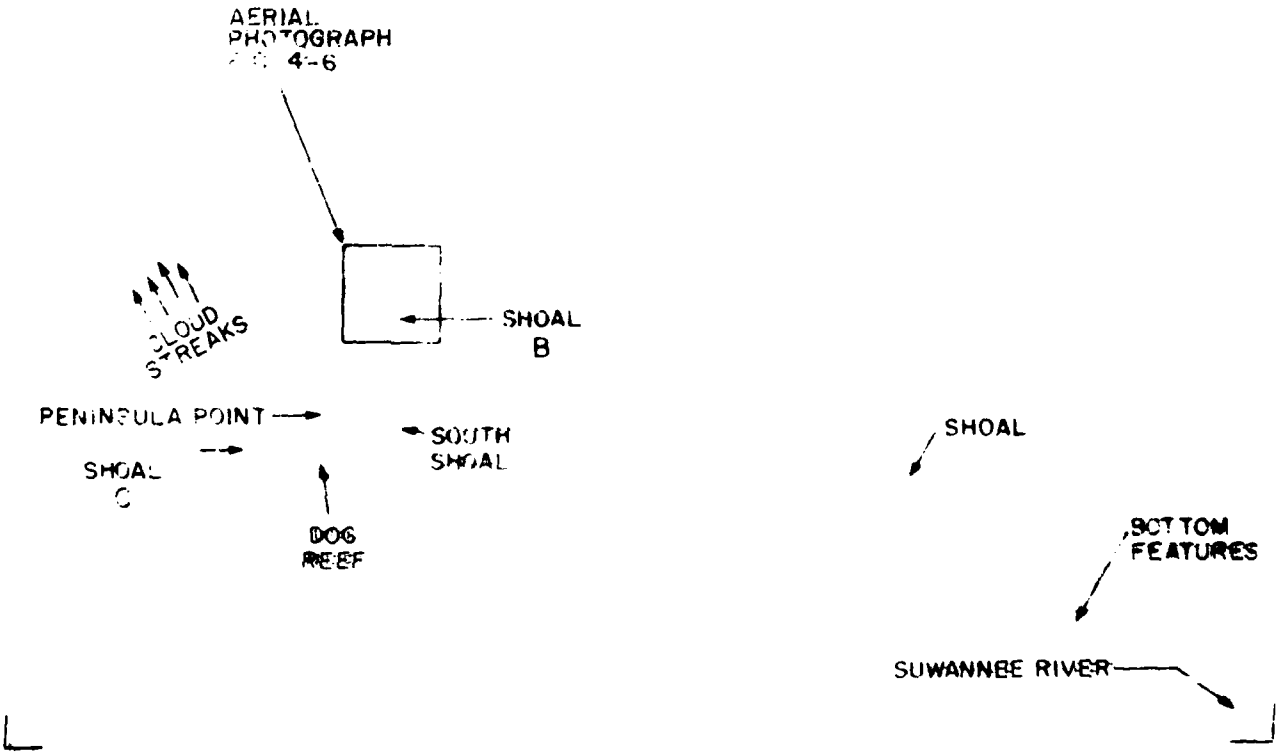

(LANDSAT) APALACHEE BAY 6 NOV 78

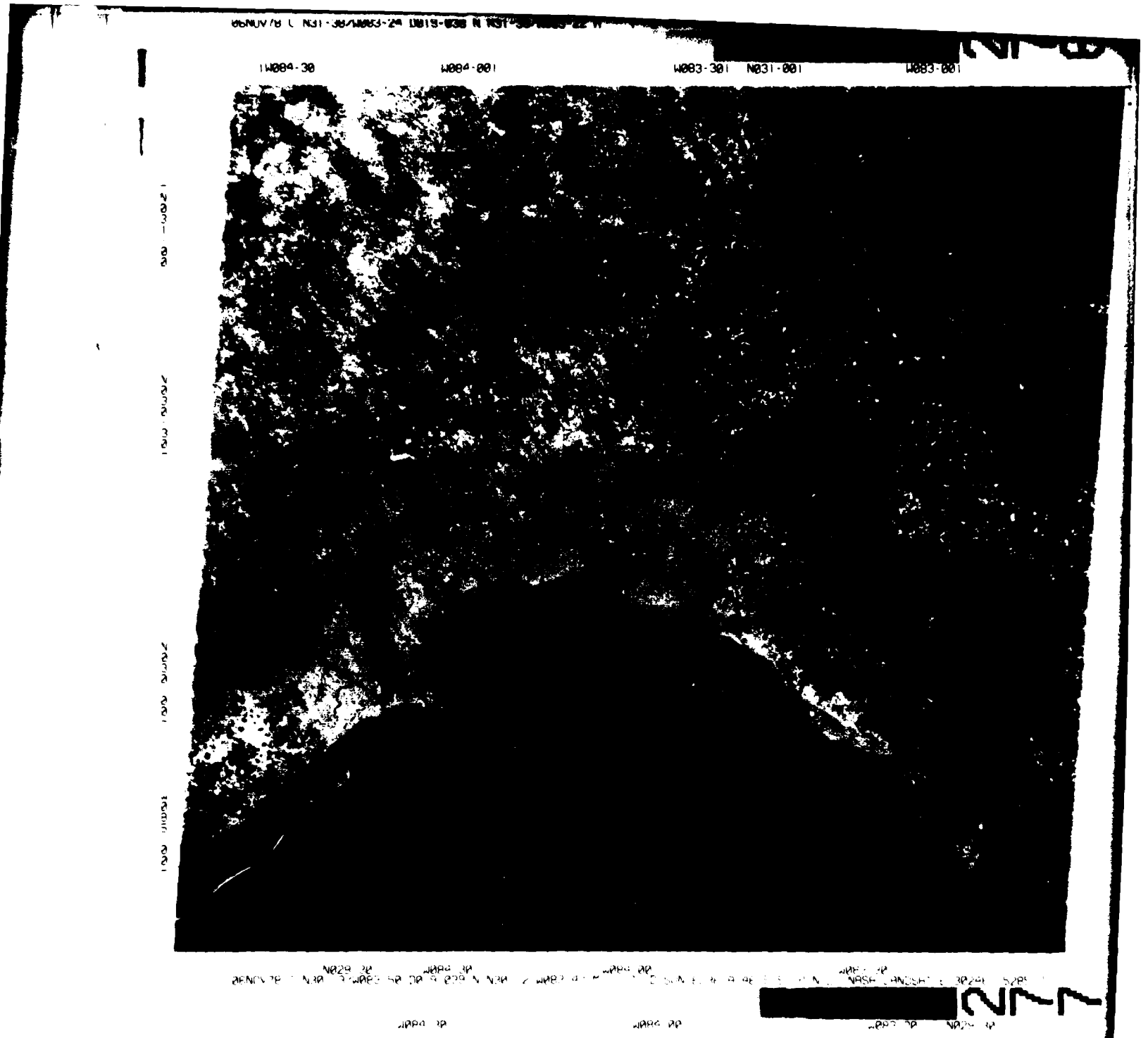

Figure 4-8. Landsat image, Apalachee Bay, FL (6 Nov 78)

5. Palau Islands

5. Palau Islands

The Palau Islands are located in the southern Philippine Sea in the southern Caroline Island Chain (7°N, 134°E). This atoll is surrounded by deep clear oceanic water and illustrated by hydrographic chart 81141 (figure 5-1). Note the limited amount of hydrographic data available on this chart.

The coral atoll surrounding the islands has several channel entrances. The backwater behind the atoll is scattered with numerous coral heads and shoal features, all of which present hazards to navigation.

Landsat imagery of the Palau Islands was taken 23 July 1977, and is presented in Figures 5-2 (Channel 4), 5-3 (Channel 5), 5-4 (Channel 6) and 5-5 (Channel 7). The visible channels are high gain mode, which are optimum for Landsat water penetration.

Through comparison of these four images, it is immediately noticeable that the atoll is readily observed surrounding the island in the visible channels, and is not in the IR channels. The high gain in the visible channel enhances the subsurface features extremely well. The complex shape of the surrounding atoll can be quickly compared with the hydrographic chart (figure 5-1) as a technique for updating charts. Figures 5-2 and 5-3 illustrate the entrance passages through the atoll. Notice that Channel 4 has increased water penetration over the other channels and that a greater extent of the shoals can be observed. By careful comparison, the detailed location and shape of the shoals/reefs seen in Channel 4 imagery in most instances coincide with that observed on the hydrographic chart. Only at several locations can differences be observed. At the entrance channel (depicted as A on the overlay), a shoal not indicated on the hydrographic chart appears to have formed across the channel. Also note that the offshore reef (B), as shown in Channel 4, is more extensive than indicated by the hydrographic chart. It becomes difficult for the interpreter/analyst to discern minute differences in imagery and hydrographic charts by viewing each separately. A rapid technique is required to overlay the bathymetric charts and Landsat imagery; but this technique also requires correction for geometric distortion in the image. Such a technique will provide the analyst a more powerful tool for exploitation of Landsat imagery for updating hydrographic charts. Instruments such as reflecting projectors, transfer scopes and plotters are available for performing this task. However, loss of detail and image contrast can possibly occur with use of reflection projectors.

Techniques are being developed with the Navy's research community (NORDA) for chart information to be digitized for input to a computer for correlation and comparison with Landsat digital data. To date the technique is not streamlined and requires a moderate amount of time.

In the early 1960's the Defense Mapping Agency Topographic Center (DMATC) developed the Digital Graphics Recorder (DGR) system that introduced new digitizing techniques and processing methods into the field of three-dimensional mapping. The DGR system consisted of an automatic digitzing table and a computer system that recorded a grid of terrain elevations from traces of the contour lines on standard 1:250,000 topographic maps. A sequence of computer accuracy checks were performed, and then the elevations of grid points not intersected by contour lines were interpolated. The DGR system produced computer magnetic tapes which controlled the carving of plaster forms used to mold raised relief maps.

It was realized almost immediately that this relatively simple tool for carving plaster molds had enormous potential for storing, manipulating, and selectively displaying (either graphically or numerically) a vast number of terrain elevations. As the demand for the digital terrain tapes increased, DMATC began developing increasingly advanced

digitizing systems and now operates the Digital Topographic Data Collection System (DTDCS). With DTDCS, two types of data--elevations as contour lines and points, and stream and ridge lines--are sorted, matched, and resorted to obtain a grid of elevation values. Undefined points on the grid are found by either linear or planar interpolation. It is believed that this technique can be developed to the level that hydrographic data can be extracted from hydrographic charts on a digital base and used for comparison and correlation with Landsat data for the compilation of future charts.

As an aside, in order to demonstrate an alternative technique to fully exploit Landsat imagery, a simple photographic processing technique is illustrated. The contrast used in printing Channel 6, Figure 5-4, is the same as the standard product from EROS. However, by changing the density in printing this scene (figure 5-6), increased detail of hydrographic features is observed as is illustrated in this figure. Notice that for Channel 6 the atoll that was not observed in Figure 5-4 is observed in Figure 5-6. This detail is a strong indicator that very shallow (< 1/2 m) water lies over the reef.

Because of increased latitude in contrast densitites, film positive transparencies offer the interpreter even greater detail and resolution of Landsat imagery. The interpreter is able to extract available information from the image without special processing as for photographic prints.

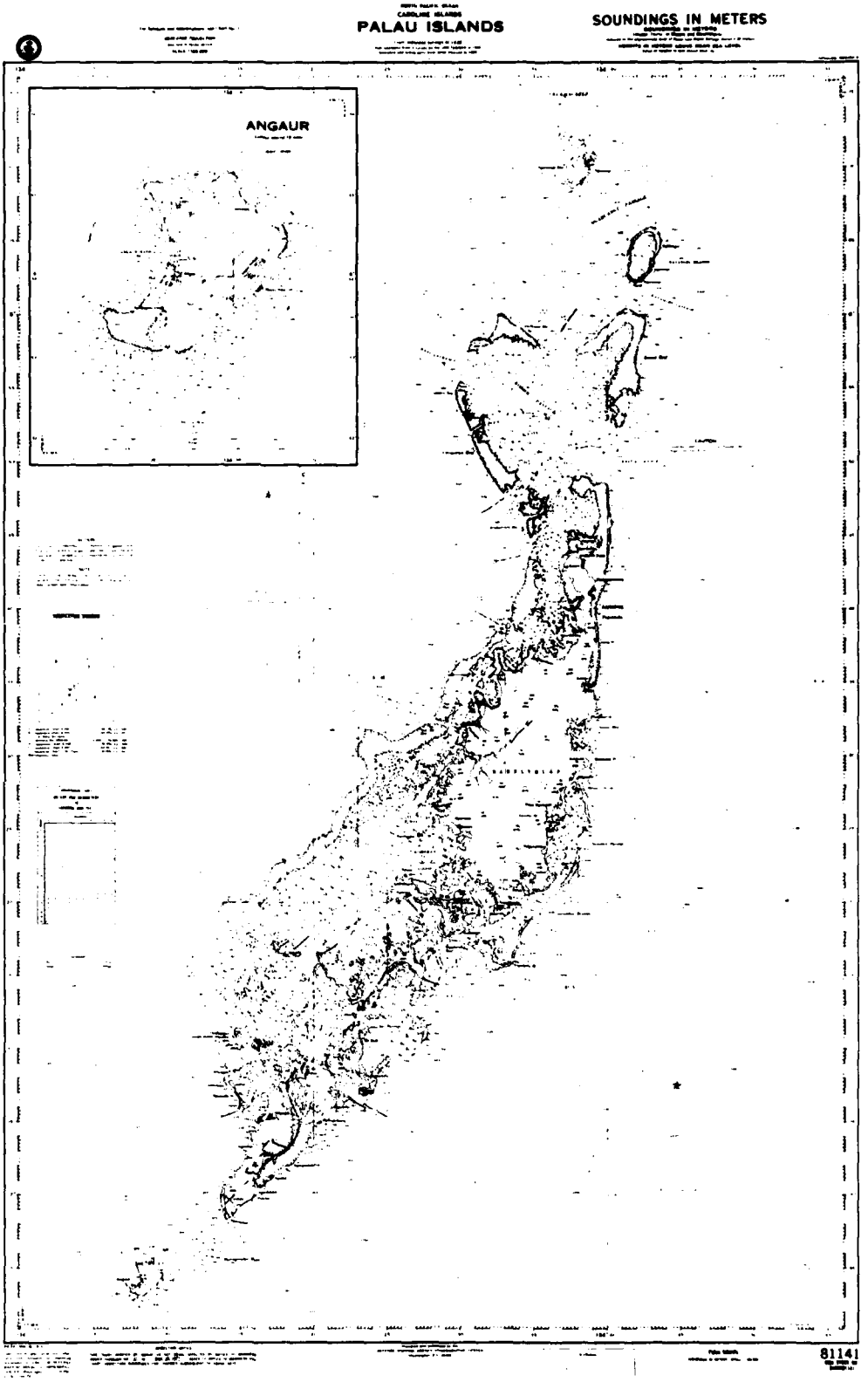

Figure 5-1. Hydrographic chart of Palau Islands (81141)

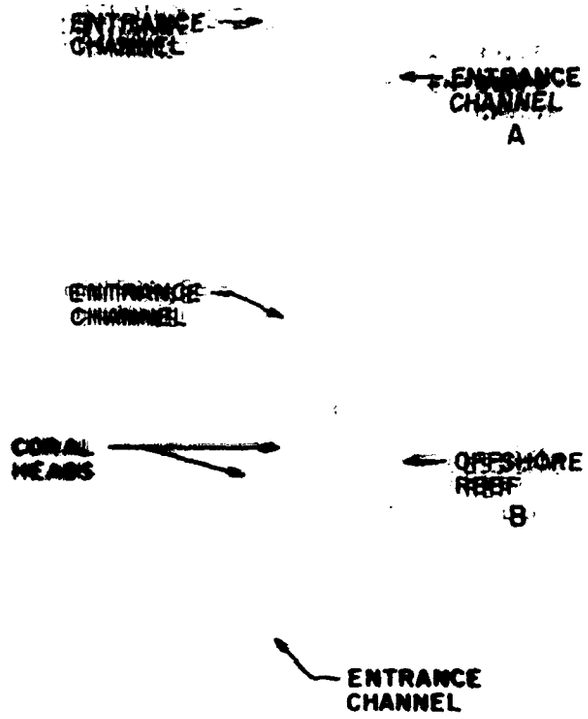

(LANDSAT) PALAU ISLANDS 23 JUL 77

Figure 5-2. Landsat image of Palau Islands (23 Jul 77)

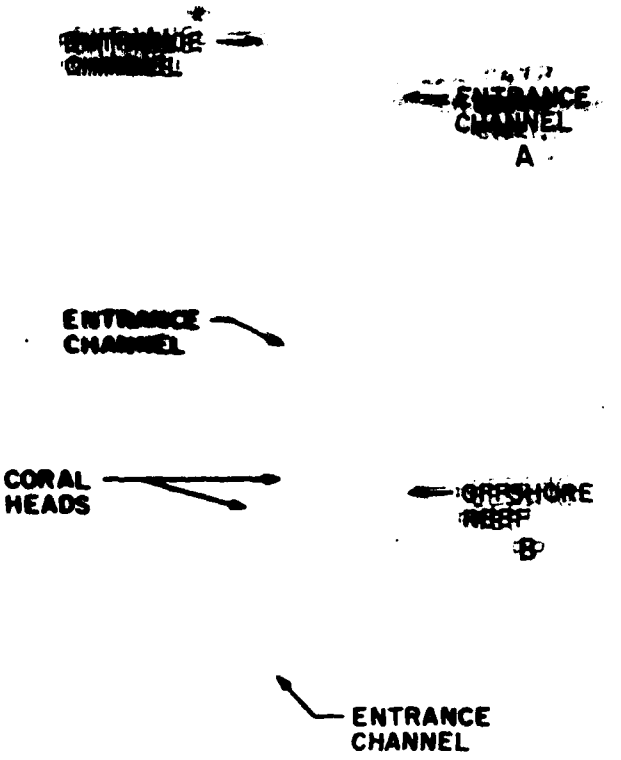

(LANDSAT) PALAU ISLANDS 23 JUL 77

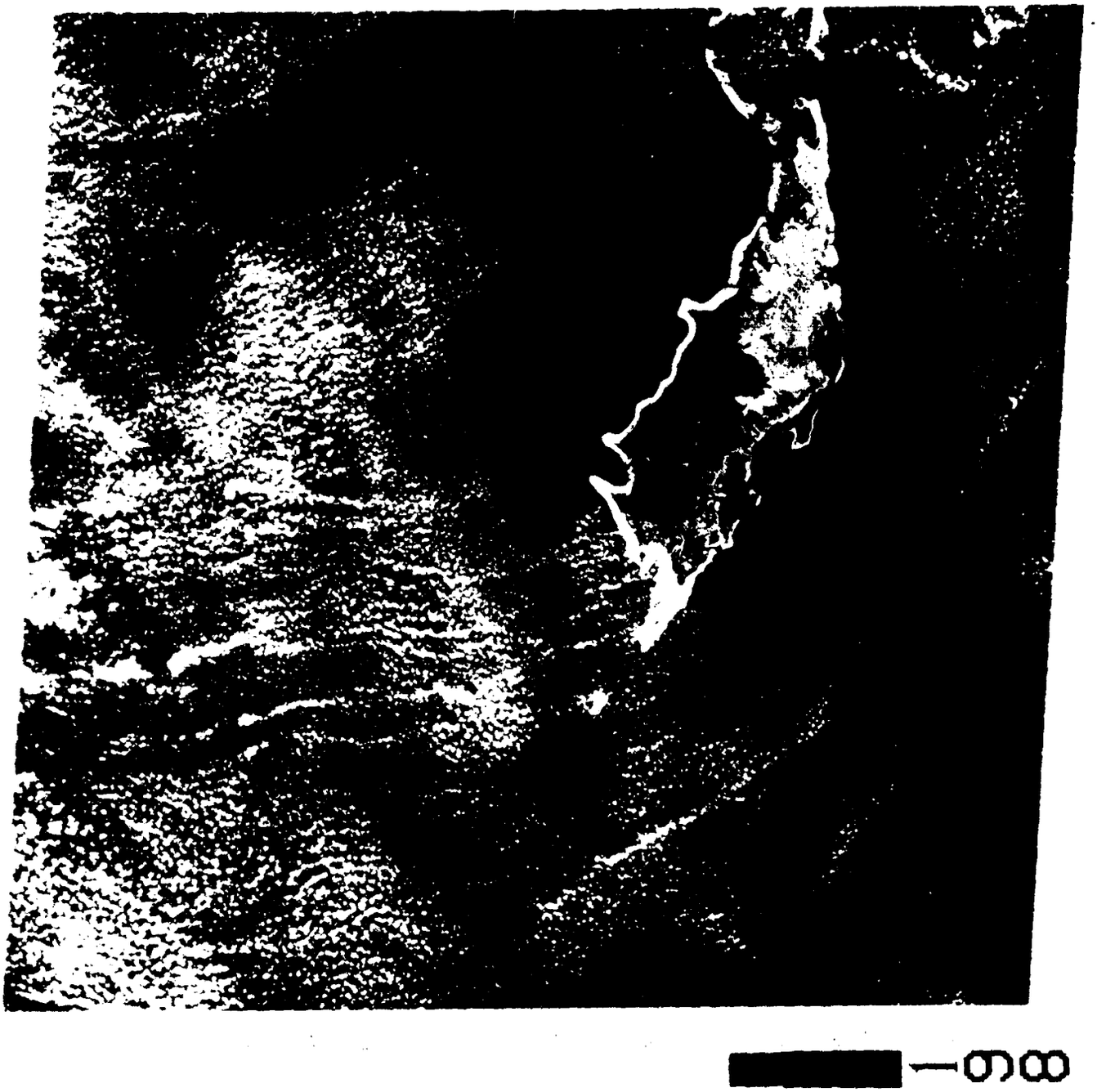

Figure 5-3. Landsat image of Palau Islands (23 Jul 77)

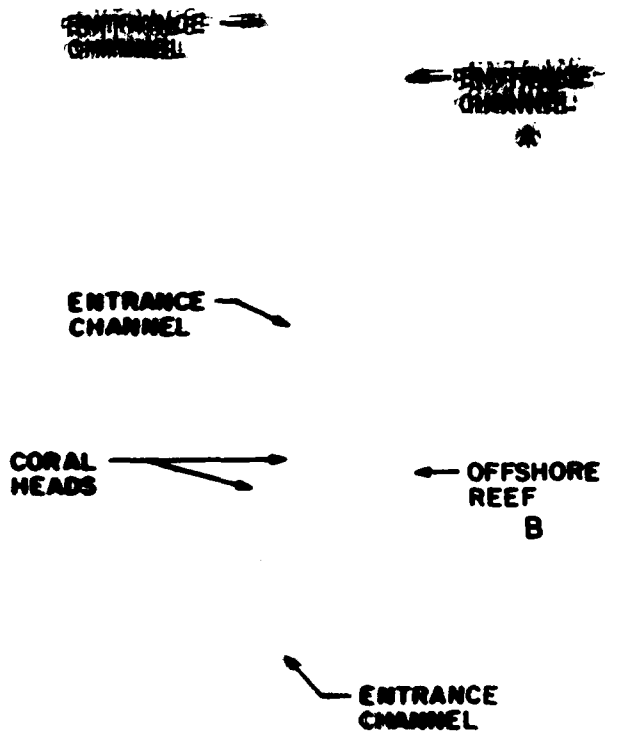

(LANDSAT) PALAU ISLANDS 23 JUL 77

Figure 5-4. Landsat image of Palau Islands (23 Jul 77)

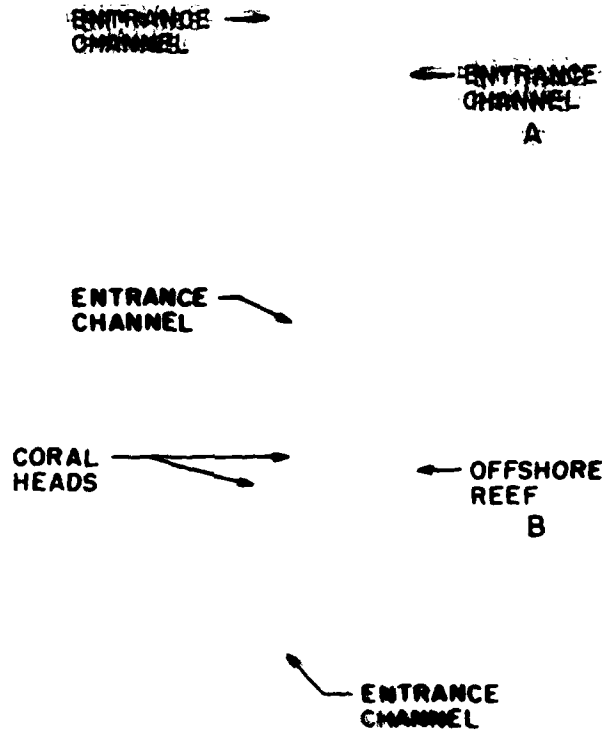

(LANDSAT) PALAU ISLANDS 2[illegible] JUL 77

Figure 5-5. Landsat image of Palau Islands (23 Jul 77)

Figure 5-6. Landsat image of Palau Islands (23 July 77) density controlled enhancement (underexposed)

6. Gulfport, MS, Approaches

6. Gulfport, MS, Approaches

The Gulfport, MS, approaches are located off the coast of Mississippi in the Gulf of Mexico and include Cat and Ship Islands and the Chandeleur Islands. The coastline in this area is low-lying, with a very gradually sloping bottom. A small quartz sand beach forms the coast, but nearshore bottom sediments consist of soft clay from the Mississippi Embayment. Because water turbidity is quite high and is coupled with the dark clay bottom, penetration of the water column for aircraft photography or Landsat imagery is quite limited. Offshore from the coastline, several islands form the Mississippi Sound (see hydrographic chart, figure 6-1), and turbid water flow patterns are commonly observed within this area. Resuspension of bottom sediments resulting from wave action occurs readily in this shallow sound. The right half of Landsat imagery 15514, 10 November 1978, illustrates this case history. Figures 6-2, 6-3, 6-4, and 6-5 correspond to Landsat imagery of Channels 4, 5, 6, and 7, respectively.

A large white cloud is observed in the central portion of the area of interest, yet the Mississippi Sound and offshore islands are cloud-free. For comparison, a color infrared aerial photograph of Cat Island taken at 60,000 ft and a color aerial photograph taken at 12,000 ft are illustrated in Figures 6-6 and 6-7, respectively. Figure 6-8 is a color infrared aerial photograph of Dog Keys Pass east of Ship Island. The coverage of the aerial photography on the Landsat imagery is illustrated on the overlays.

In the Landsat images the position and extent of Cat Island (A) are best seen in the IR channels, Figures 6-4 and 6-5. In the visible channels (figures 6-2 and 6-3), it is somewhat difficult to discriminate between land and water. The color IR aerial photograph (figure 6-6) illustrates the extent of shoals, wetlands, and turbidity patterns surrounding Cat Island. The extent of shoals in this photograph corresponds with those shown on the hydrographic chart (figure 6-1), although the chart does not contain as much detail. A finer detailed (lower altitude) photograph of the northern tip of Cat Island is illustrated in Figure 6-7. Note, through comparison with Figure 6-6 and the hydrographic chart (figure 6-1), the breaking surf on Raccoon Spit. This surf can also be seen on Figure 6-2, and provides an interpretative technique for location of shoals. Wave refraction patterns observed in the aerial photography are clearly observed in the sunglint areas in Figure 6-6. Figure 6-7 also illustrates in more detail the wave refraction surrounding the tip of Cat Island. The refraction patterns provide an important interpretative technique for inferring bottom shape and depth. This effect is explained in greater detail in Appendix A. Figure 6-7 also illustrates a mottled surface texture of a series of light textures typical of numerous cloud shadows. The turbid flow patterns around land and shoals are also illustrated in the aerial photographs, as depicted in the overlays of Figures 6-6 and 6-7.

Landsat imagery does not show the detail observed in these aerial photographs; however, some similarities are noted. The visible channels (figures 6-2 and 6-3) of Landsat show the extent and position of shoals surrounding Cat Island and the turbid water flow patterns within the Mississippi Sound. The color IR aerial photography (figure 6-8) taken at 60,000 ft illustrates the positions of shoals and channels in Dog Keys Pass. The positions correspond with relative accuracy to the hydrographic chart (figure 6-1), though differences can be seen in the distribution of shoals. Note the sharp water mass boundaries depicted by different water colors in this photograph. Also illustrated are the localized concentration of irregular boat patterns, which are typical of shrimp boats resuspending bottom sediments with their nets, resulting in turbid water boat wakes. The dispersion of this

pattern permits an interpretation of the current magnitude and direction. Through a careful comparison of the aerial photography (figure 6-8) and Channel 4 of the Landsat image (figure 6-2), similarities in the extent and position of the light tones corresponding to shoals can be observed. Similarities in the darker tones in the area of the shoals which correspond to channel entrances can also be observed.

Exploitation of Landsat imagery in interpretation of hydrographic features in turbid water is difficult. Problems exist in discrimination of turbid water versus shoals. Presently with the standard bulk-processed paper products that the EROS Data Center produces, little can be done to aid the interpreter. However, the use of contrast enhancement and digital analysis of Landsat data through computer processing techniques may prove to be an invaluable interpretive tool for the analyst.

Figure 6-1. Hydrographic chart of the Gulfport approaches (11371, 11373)

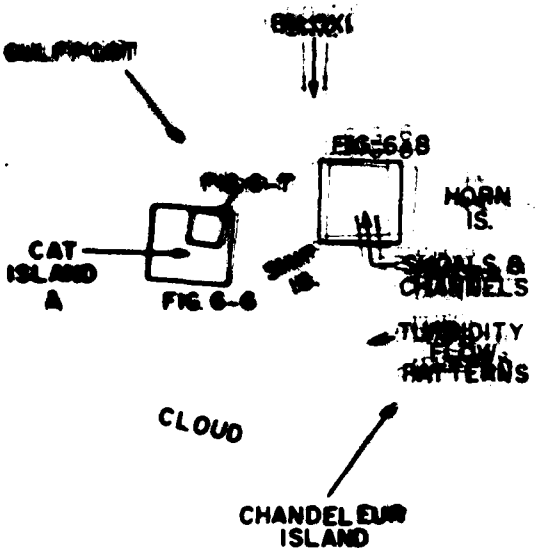

(LANDSAT) GULFPORT APPROACHES 10 NOV 78

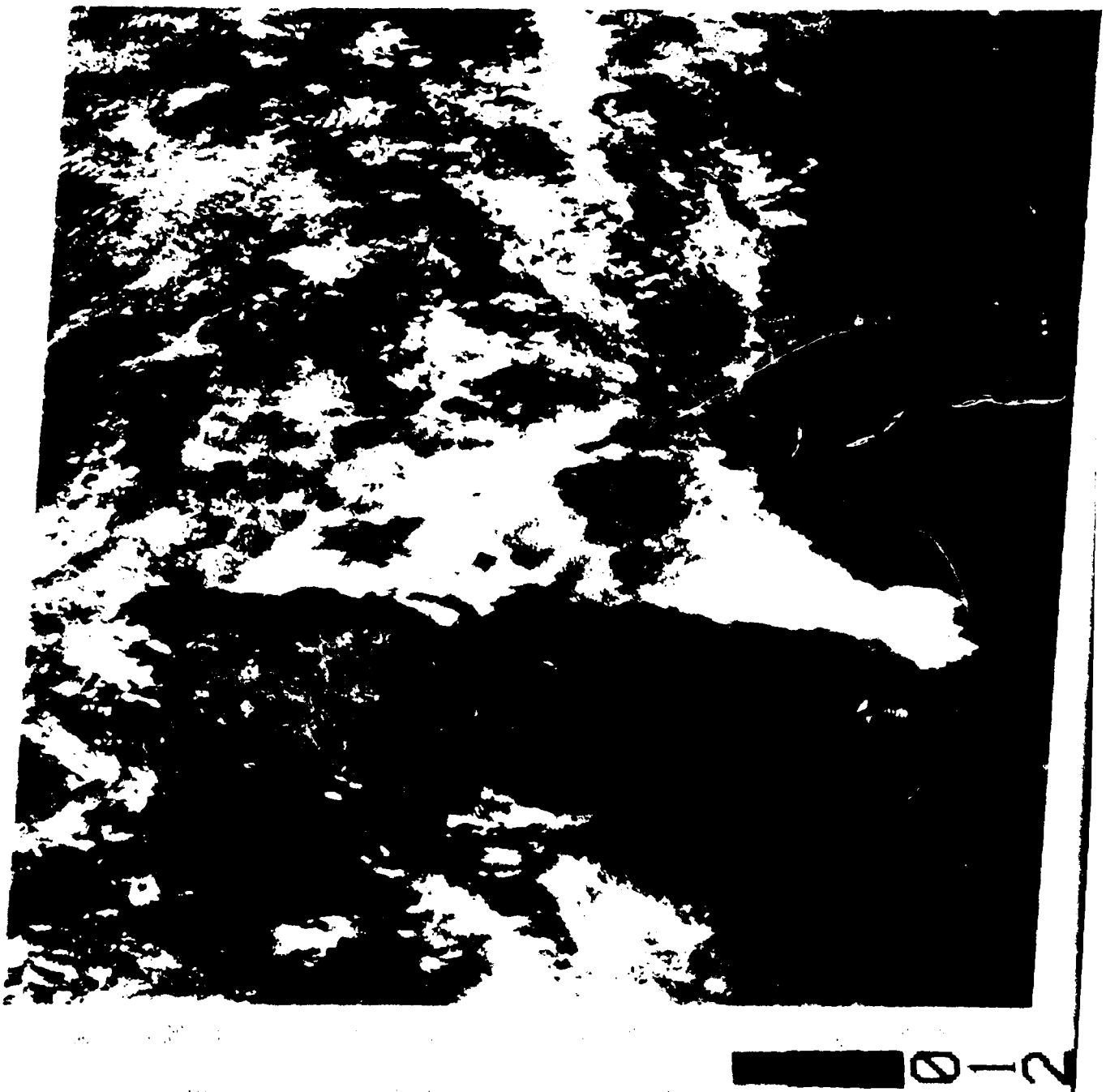

Figure 6-2. Landsat image, Gulfport approaches (10 Nov 78)

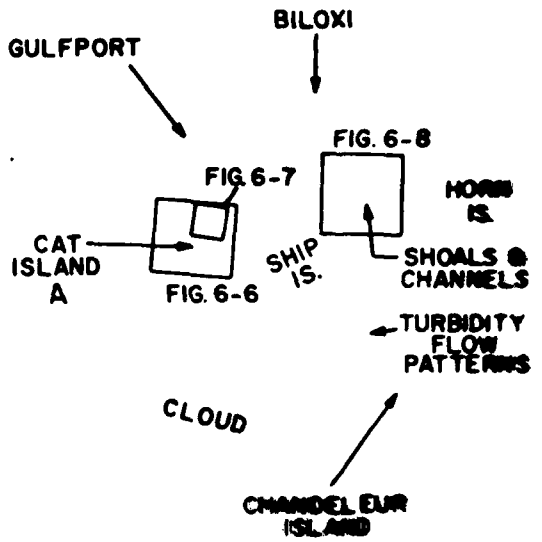

(LANDSAT) GULFPORT APPROACHES 10 NOV 78

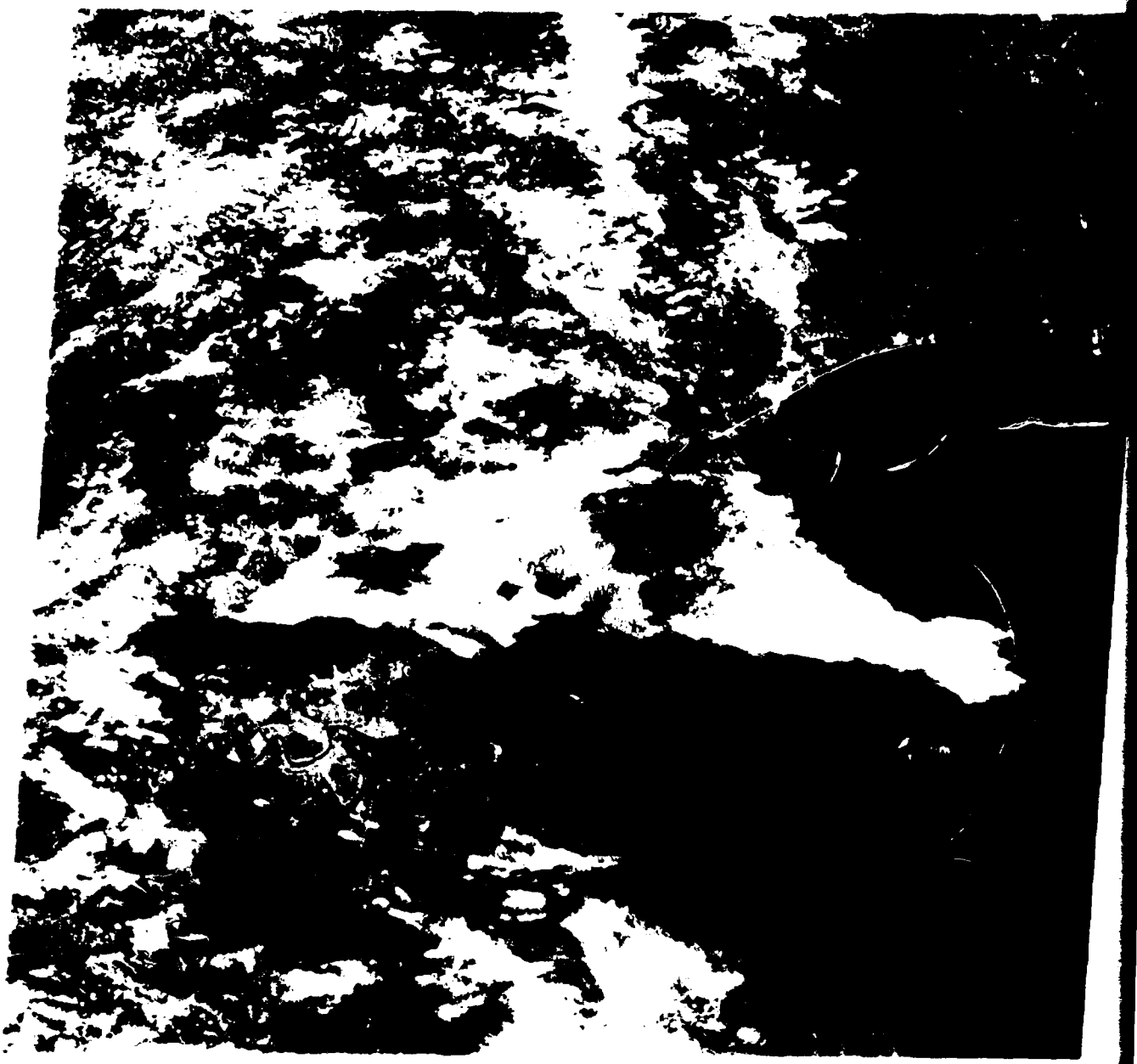

Figure 6-3. Landsat image, Gulfport approaches (10 Nov 78)

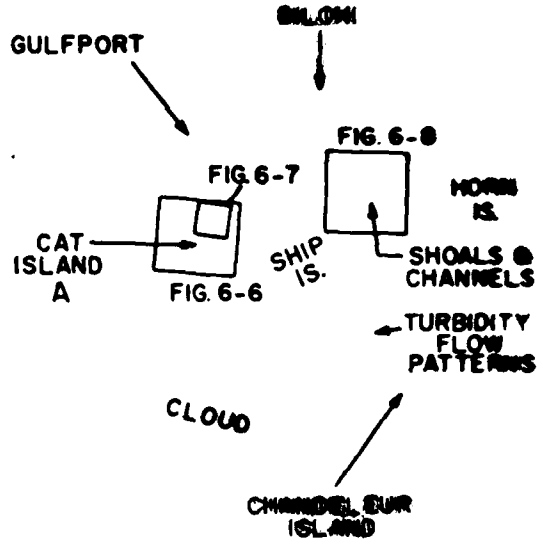

(LANDSAT) GULFPORT APPROACHES 10 NOV 78

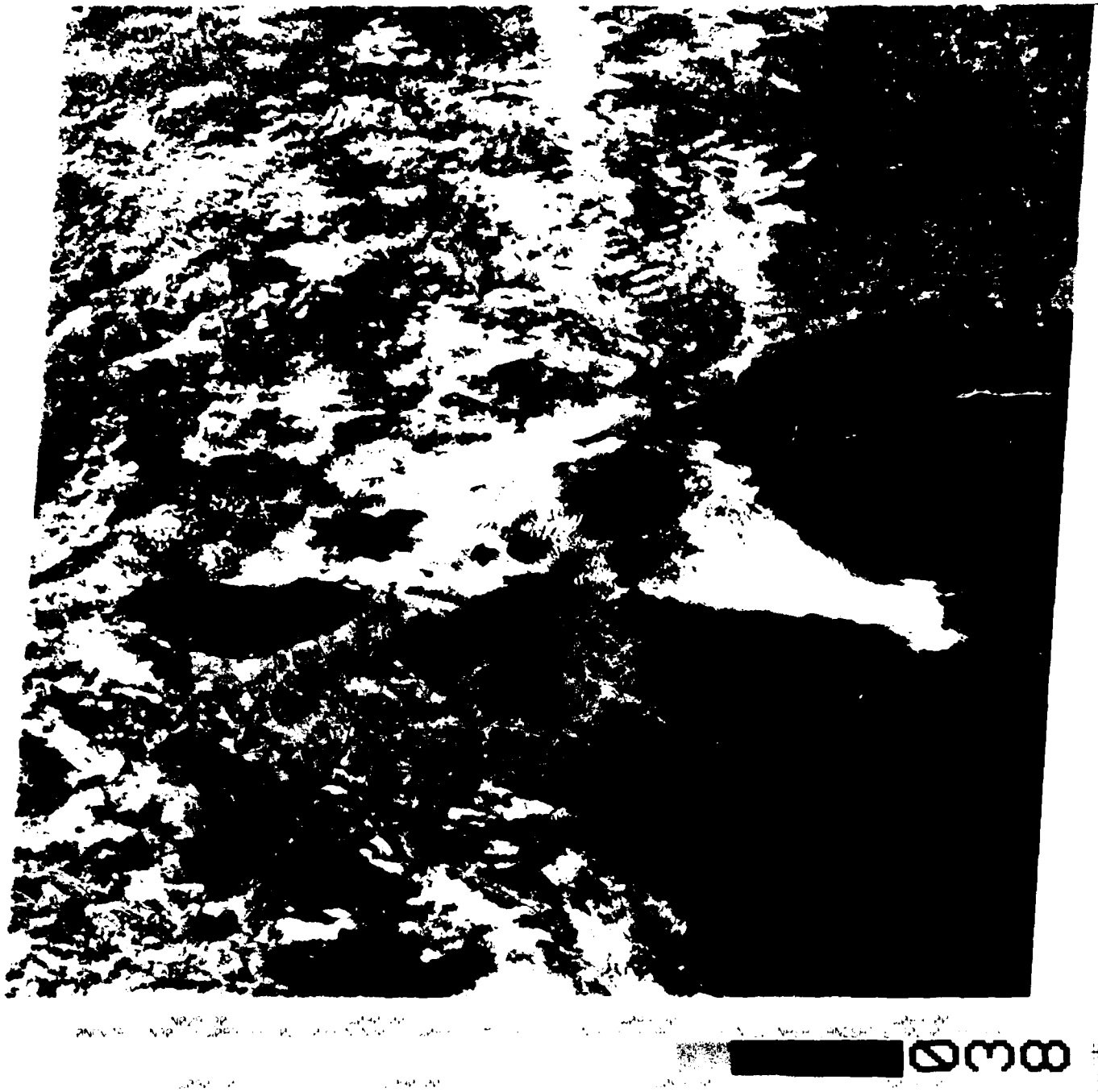

Figure 6-4. Landsat image, Gulfport approaches (10 Nov 78)

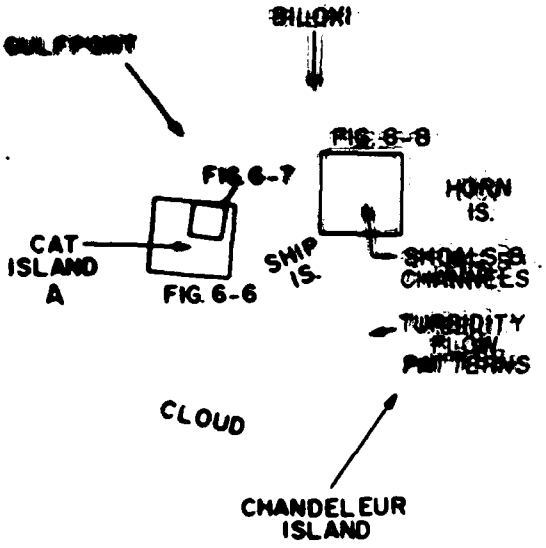

(LANDSAT) GULFPORT APPROACHES 10 NOV 78

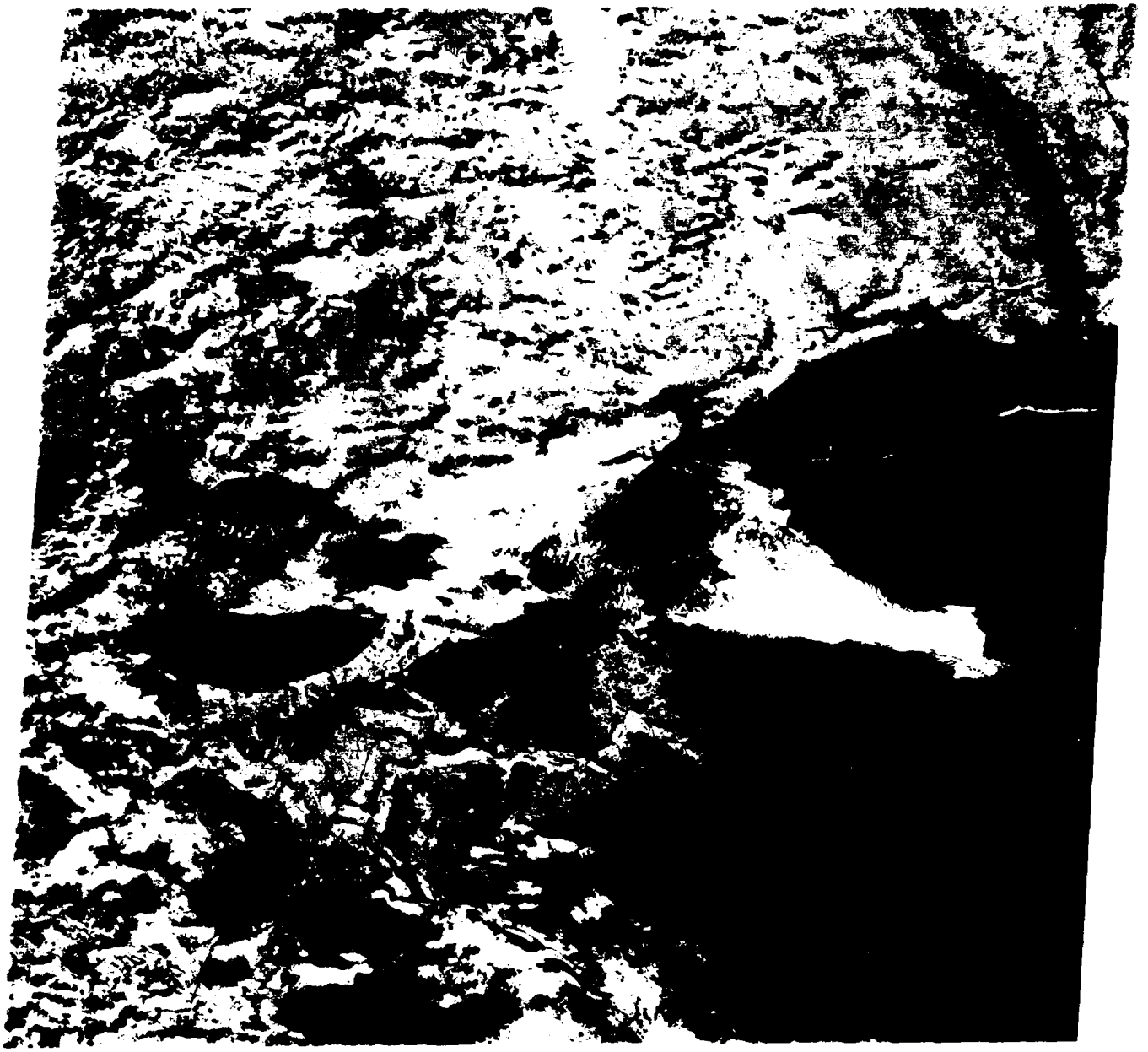

Figure 6-5. Landsat image, Gulfport approaches (10 Nov 78)

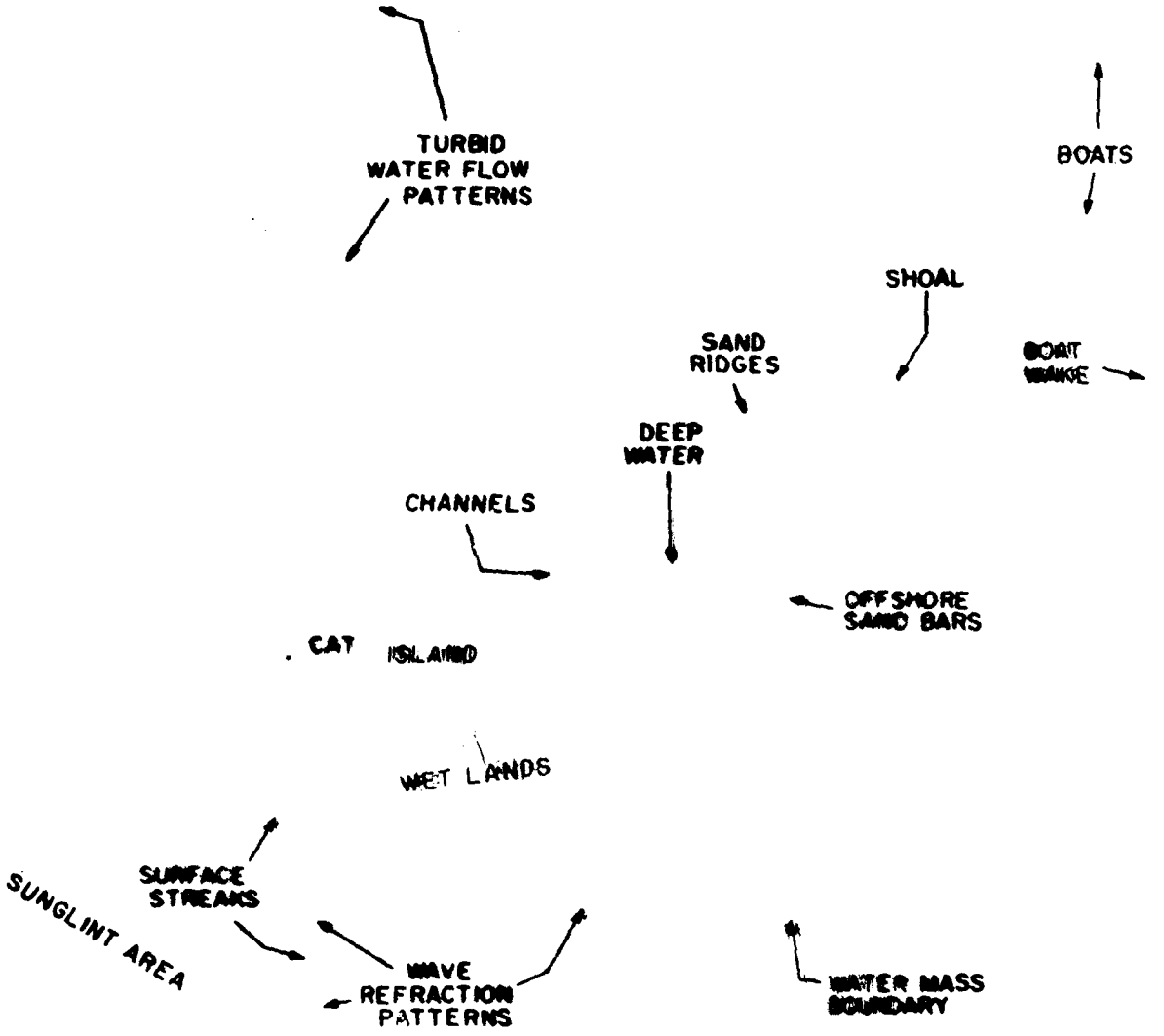

(AERIAL PHOTOGRAPH) CAT ISLAND 8-OCT-78

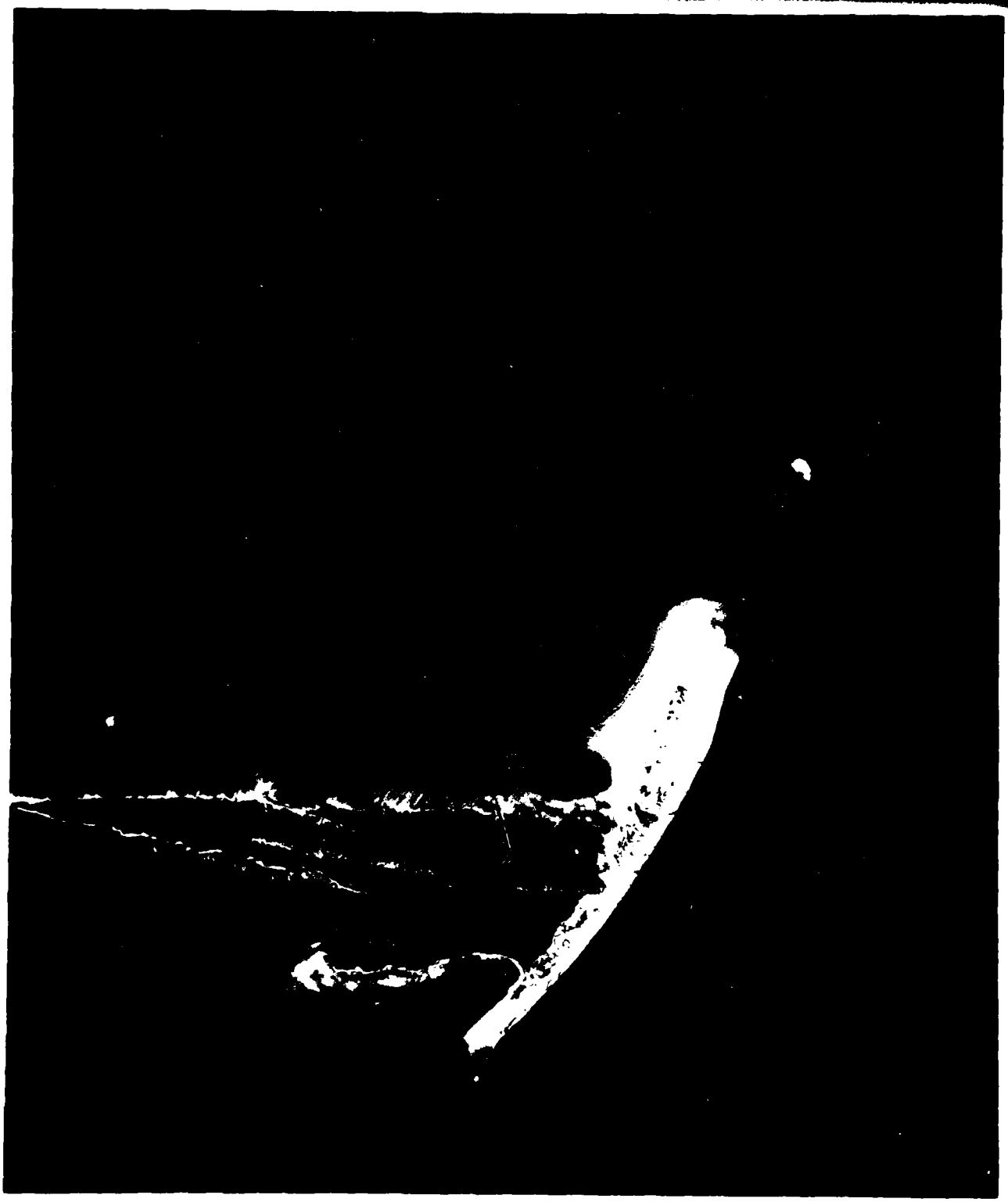

Figure 6-6. Color IR aerial photograph (1:122,000), Cat Island (8 Oct 78)

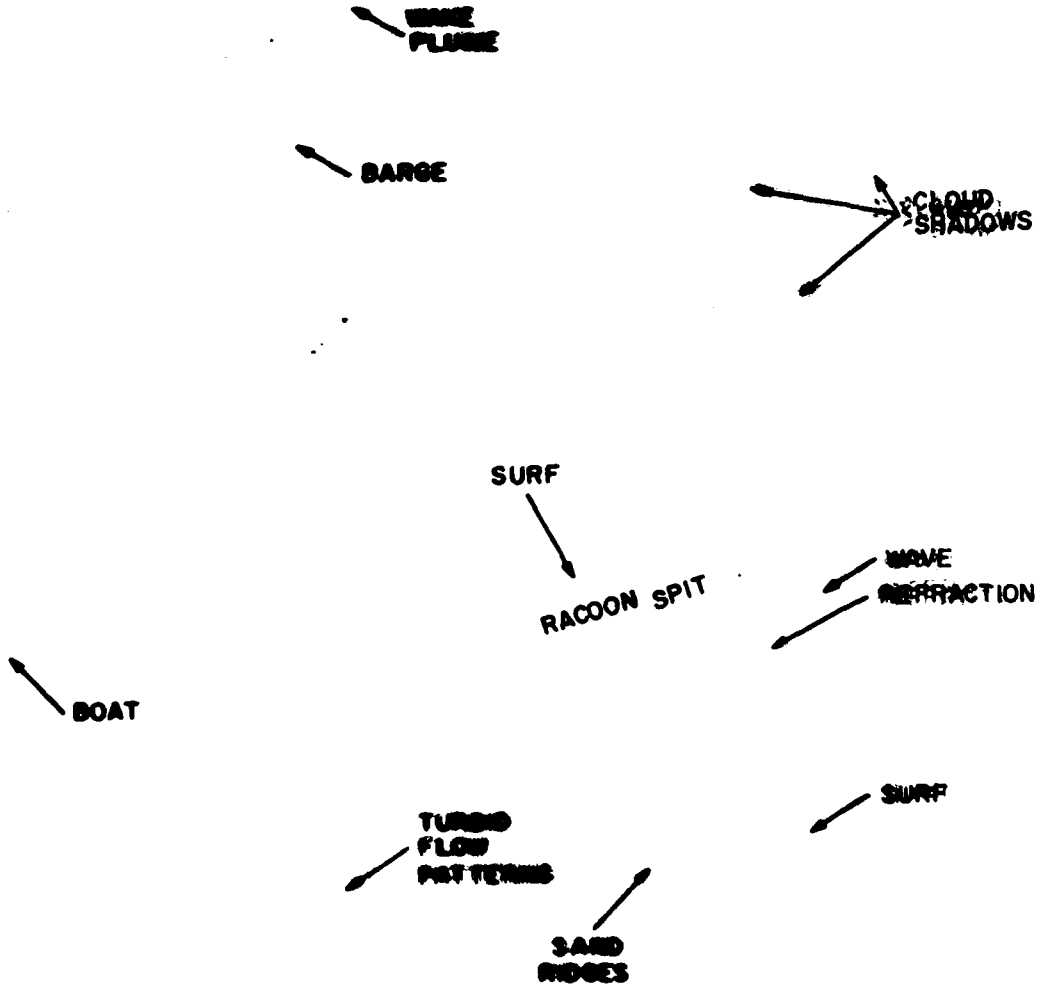

(AERIAL PHOTOGRAPHY) CAT ISLAND
14 DEC 78

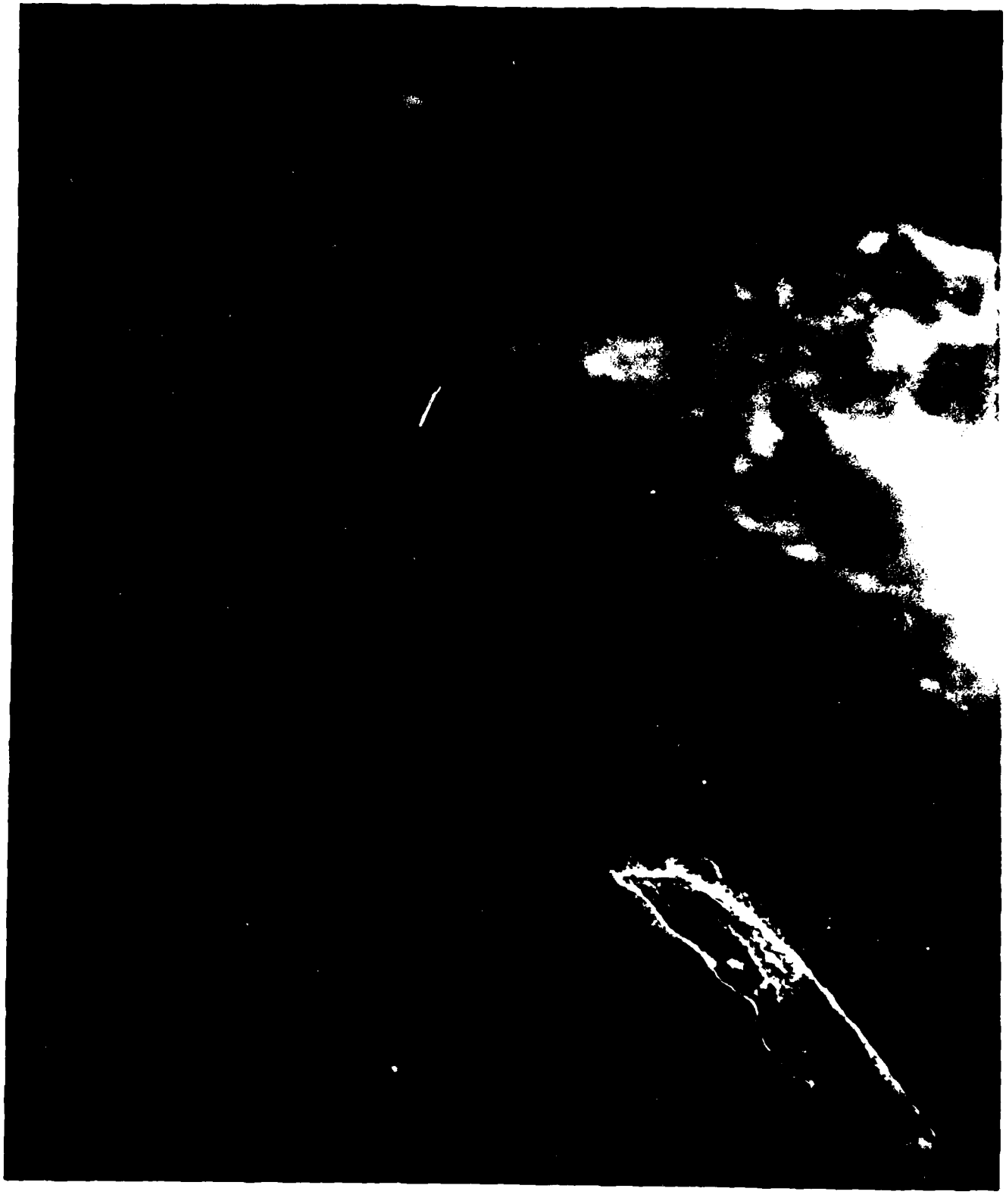

Figure 6-7. Color aerial photograph (1:12.000), Cat Island (14 Dec 78)

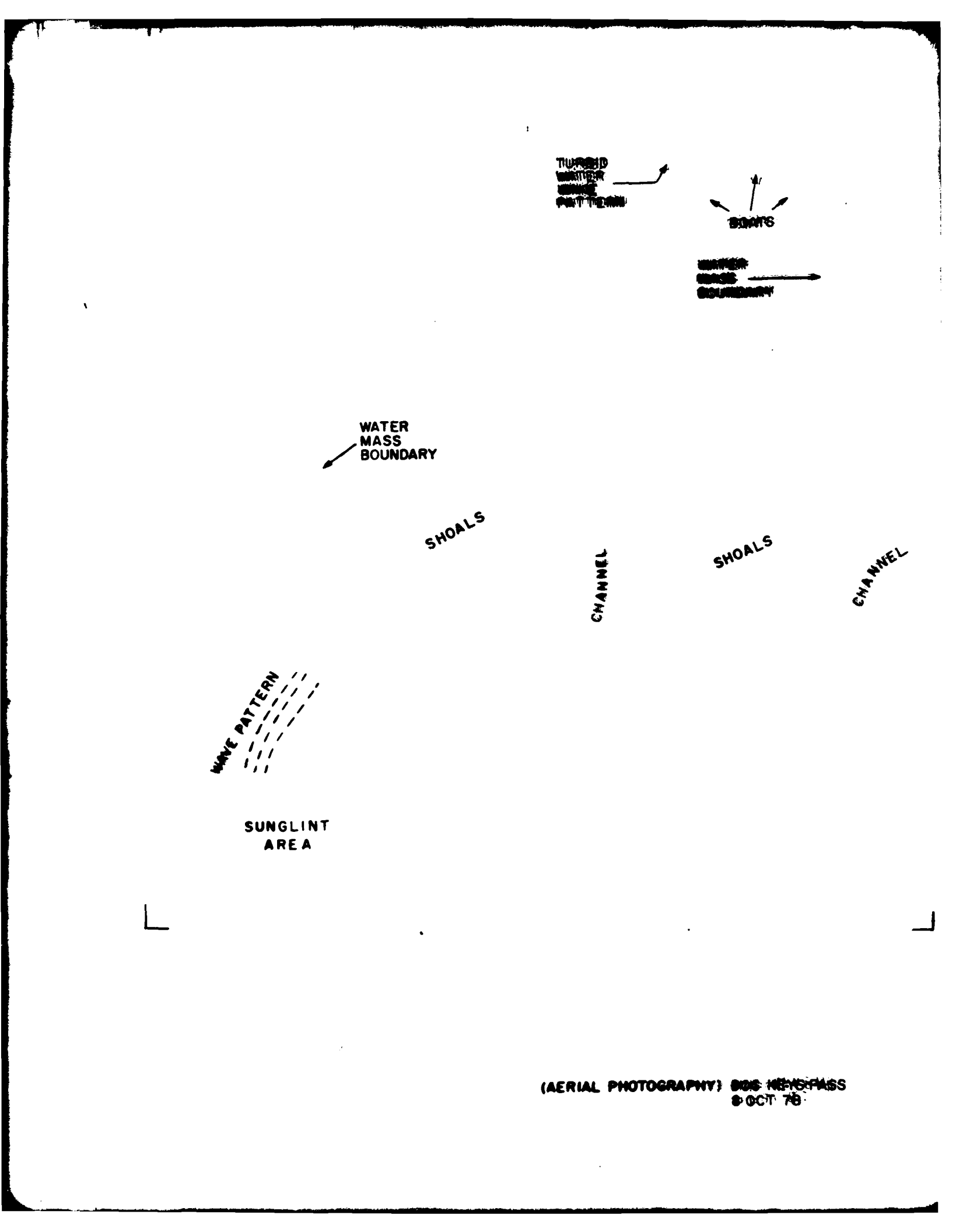

(AERIAL PHOTOGRAPHY) [redacted]
9 OCT 78

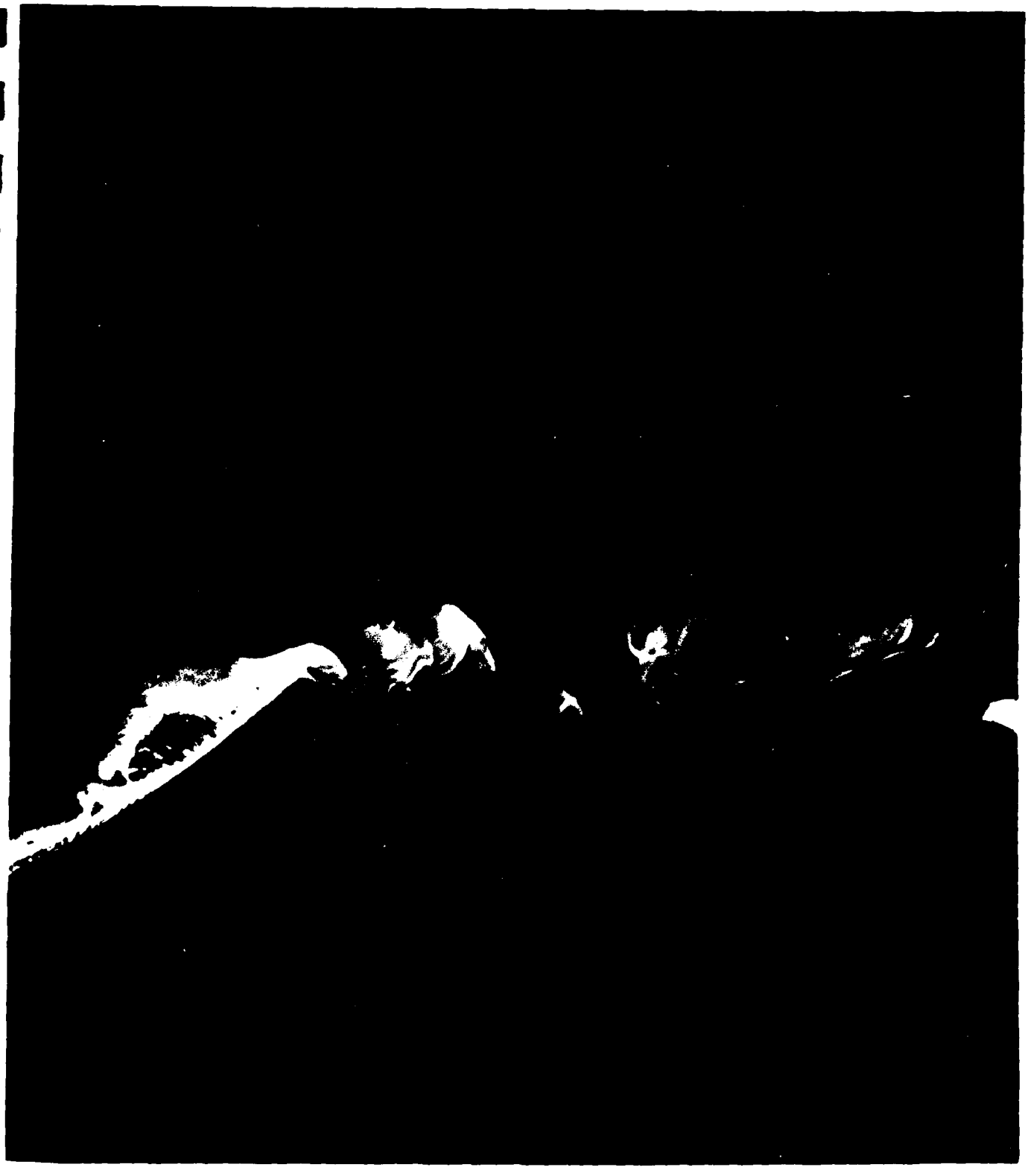

Figure 6-8. Color IR aerial photograph (1:122,000), Dog Keys Pass (8 Oct 78)

7. Little Bahama Bank

7. Little Bahama Bank

The Little Bahama Bank case history area is located off the east coast of Florida in the northern Bahama Islands. Grand Bahama Island forms the southern border, and the northern tip of Little Abaco Island forms the northern border. Numerous small cays are located throughout the Bank. The Gulf Stream is located to the west. The bank is characterized as a calcareous reef, and migrating calcareous sand ridges/fields form numerous changing bottom features. The periphery of the Bahama Bank is observed to be a relatively slow changing hydrographic feature; however, the movements within the bank change as a direct result of local winds, waves, and tidal currents.

Figure 7-1 illustrates the hydrographic chart (26320) corresponding to this case history area. Note the very deep water which occurs close offshore from the outer islands and reef. Also note that the northern border of the bank is irregular and has relic coral outcrops.

Several Landsat images of this area will be presented to illustrate not only the interpretation of hydrographic features, but also the temporal changes which occur on this bank. Exploitation of Landsat as a technique for chart revision and change detection will become evident. Through comparison of these images with the hydrographic chart, it will be seen that differences have occurred since the collection of soundings used in compilation of the chart. However, distinct differences are also shown to exist between images taken several weeks apart. It is, therefore, difficult to keep current, accurate, reliable charts in these areas of changing hydrographic features. The first set of Landsat images was taken on 8 April 1978 and is illustrated in Figures 7-2, 7-3, 7-4 and 7-5 for Channels 4, 5, 6, and 7, respectively. Channel 4 (figure 7-2) best characterizes the hydrographic features. The degree of subsurface detail shown in the shallow waters in this figure is much greater than that shown on the hydrographic (see overlay for feature or recognition) chart (figure 7-1). The numerous mixtures of tones on the image in the area of the reef can be associated with channels, local currents and, to a certain extent, the water depth. Note the highly reflectant sand bottoms (depicted as light tones) surrounding the cays and the sharp tonal borders delineating various hydrographic features (sand spits, fans, channels, sand ridge fields and bottom variations).

Highly reflective "fish whites" are seen scattered throughout the shallows of the bank (figures 7-1 and 7-3). "Fish whites" are localized areas where waters supersaturated with calcium carbonate precipitate out, forming a milky white water mass with highly reduced underwater visibility. This phenomenon is known to occur mainly at the surface (as a result of high evaporatic rates), although the entire water column has been known to be affected. "Fish whites" commonly occur in tropical regions and are most common in the Bahamian/Caribbean locale in areas of shallow waters. Their lenticular shape and tonal appearance aligns with the current direction. Misinterpretation of "fish whites" and the highly reflective bottom shoals is resolved through comparison of temporal variations in the scene. The rapid change of location in a light tonal area in a brief time period is a strong indication of "fish white." Care must be taken not to mistake this feature with a shoal that is temporally changing shape. This dramatic temporal change in the location of "fish whites" will be illustrated in the temporal illustrations to follow.

Upon careful examination, a lightly mottled pattern can be observed in certain areas in Channel 4 (figure 7-2). A similar pattern for patches of bottom vegetation was illustrated earlier in the Key West and Cedar Key case histories.

Figure 7-3 (Channel 5), although it does not illustrate the deeply submerged hydrographic features, does delineate the shallow, highly reflective bottoms. Intricate subsurface channel patterns on the highly reflective bottoms of sand shoals are shown in this figure, as depicted by the overlay.

Channel 5 provides the interpreter with a rapid survey technique of eliminating the detail and complexity of the bottom features illustrated in Channel 4 (figure 7-2). The highly reflective bottoms and/or very shallow areas can be rapidly delineated. Also note that comparison of figure 7-3 with the hydrographic chart (figure 7-1) shows the increased detail present in the imagery. The location and extent of the numerous channel patterns that are readily discernible in Channel 5 do not have a comparable feature on the hydrographic chart. Landsat provides greater detail in this area than on the chart.

The IR Channels 6 and 7 (figures 7-4 and 7-5) illustrate the locations of the land features. The tonal differences in the coastlines result from wetland or tidal differences, as described in previous case histories. Note the location of the clouds in all four channels/figures and that they often occur directly over land features. This occurrence is characteristic of low velocity winds and calm sea conditions within the scene. Over the bank the interpreter must take care not to misinterpret a cloud as a shallow sand reef or "fish white" (look for cloud shadows.)

A second set of Landsat imagery for this same location was obtained on 26 March 1977 and is illustrated in Figure 7-6 (Channel 4) and Figure 7-7 (Channel 5). (Imagery of the IR channels for this date are not illustrated, since they are essentially identical to Channels 6 and 7 of the previous date; figure 7-4 and 7-5.) This data set consists of high-gain imagery, as can be noted by the high exposure of the highly reflective bottoms of shallow water. (Annotation H2 in the image legend also indicates high gain.) Note the similarities between these images and the images of 8 April 1978 (figures 7-2 and 7-3) as shown on the overlays. Channel 4 (figure 7-6) in the high-gain mode shows hydrographic detail from a deeper water depth, while the detail of the shallow hydrographic features is lost from saturation or overexposure in processing. (In the Bahamas, white sand bottoms that extend to a depth of about 1.5 m will usually saturate high-gain imagery.) Channel 5 (figure 7-7) provides a better image for comparison with the low gain imagery on 8 April 1978. The majority of similar shallow water features are detectable on both dates. However, notice that the light speckled pattern in the central bank is more numerous and does not coincide with those observed on the 8 April 1978 (figure 7-2) image. This phenomenon we interpreted as "fish whites," since they are such a transitory feature. Be careful not to confuse white clouds, which also are over the bank, with the "fish whites." Look for cloud shadows to interpret clouds.

Notice that a bright linear feature which follows the northern coral shoreline (figures 7-6 and 7-7) is not distinctly observed in the 8 April 1978 scene. Strong northeast winds resulted in large breaking waves on the northern reef. Increased sea surface reflectance from the sea foam is imaged in all four channels and appears as an elongated pattern following the reef. The IR Channels illustrate this pattern if the contrast is enhanced. The general mottled appearance of the northern offshore deep water, which is observed in Figures 7-6 and 7-7, is characteristic of a highly wind stressed sea surface. Digital enhancement will illustrate this pattern more vividly, though Figure 7-6 shows the general pattern. Notice that the southern shoreline of the land masses appear to be less reflective and have calmer sea conditions than the northern shores. Interpretation of this area as the leeshore indicates that high winds are prevailing from the northeast.

A third temporal Landsat scene of this area obtained on 13 February 1978 (two months prior to the first data set) is illustrated in Figure 7-8 (Channel 4). This image is suited for the interpretation of hydrographic features, since the "fish whites" have essentially vanished. Comparison of this image with the previous data sets immediately shows the discrimination of shoals and "fish whites." All lighter toned areas, which are relocatable through comparison of figures 7-2, 7-7 and 7-8, are interpreted as bottom features or as resulting from bottom reflectance. This temporal comparison technique eliminates misinterpretation of the lighter tones as turbid flow patterns (water color), surface roughness, or atmospheric phenomenon. Several specific examples of coincident shoals on all three images are illustrated on the overlays. Through comparison of these three data sets, this interpretation technique will become clearer and more useful.

Other hydrographic features which can be interpreted through comparison of these three data sets are indicated on the overlay of Figure 7-8. At numerous channel entrances in the coral reefs between the shallow bank and the deep water, bright-toned sand fields are observed as alluvial fan shaped features. The features' characteristic shape and close association with channel entrance are repeatedly illustrated in this image along the northern shoreline of the bank. Not only do these features indicate the dominant tidal current directions, but they also indicate a complex and changing water depth expected to occur in this area. By careful examination of these fan-shaped features in figures 7-6 and 7-8 (which are separated by approximately one year's time), slight modifications in these features are noticeable. The hydrographic chart of this area (figure 7-1) does not illustrate the detailed bathymetry associated with these features.

Hydrographic obstructions are also illustrated by careful examination of Figure 7-8 and comparison of the hydrographic chart. These lighter toned features, which correspond to rock and coral shoals as illustrated on the hydrographic chart, probably result from Landsat sensing reflectance of the surf associated with the obstructions.

Figure 7-9 illustrates a 512 x 512 pixel subsection of the Little Bahama Bank data. The MSS digital data taken 26 March 1977 is a subsection of the second data set, which is high-gain imagery. A color composite using Channels 4, 5 and 7 of this subsection was computer-generated. A similar technique was used in the Cedar Keys, FL, case history to generate a color image from MSS digital data. The color composite, which was contrast stretched by computer processing, illustrates increased detail of the bottom features than was previously described. Features such as the surfline, "fish whites," bottom channels, shoal patterns around cays, and land boundaries can be distinguished more readily than by resorting to simple comparisons of individual spectral channels. This example was illustrated to indicate future techniques available to the interpreter so that interpretation can be made more rapidly and more accurately.

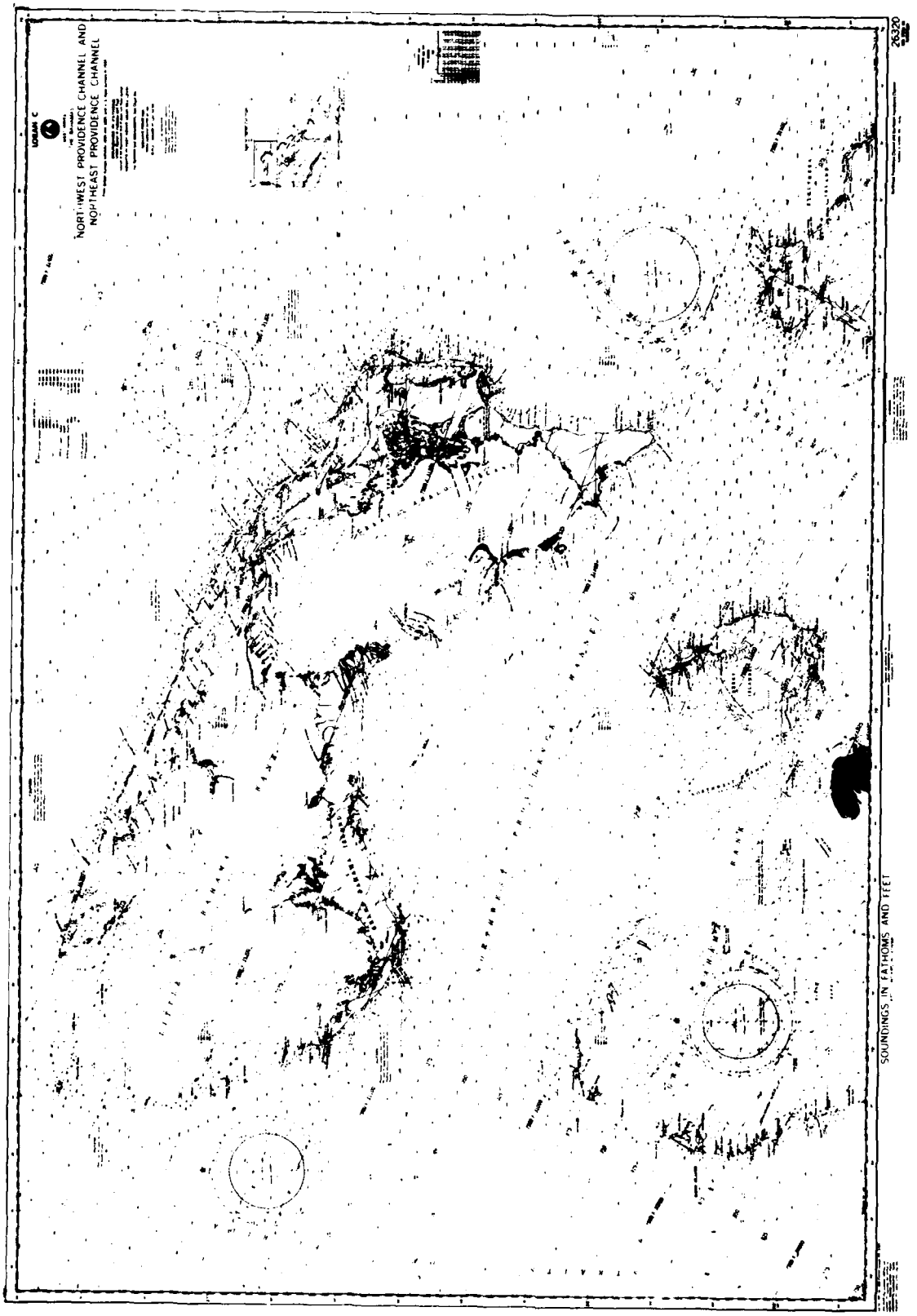

Figure 7-1. Hydrographic chart of Little Bahama Bank (26320)

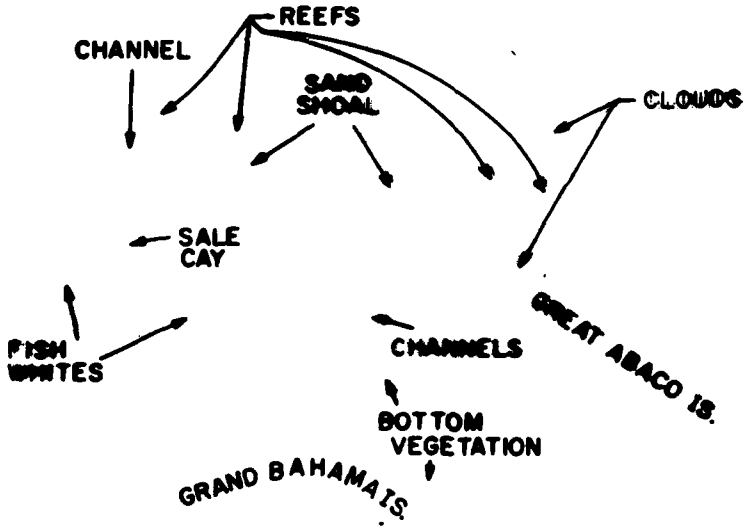

(LANDSAT) LITTLE BAHAMA BANK 8 APR 78

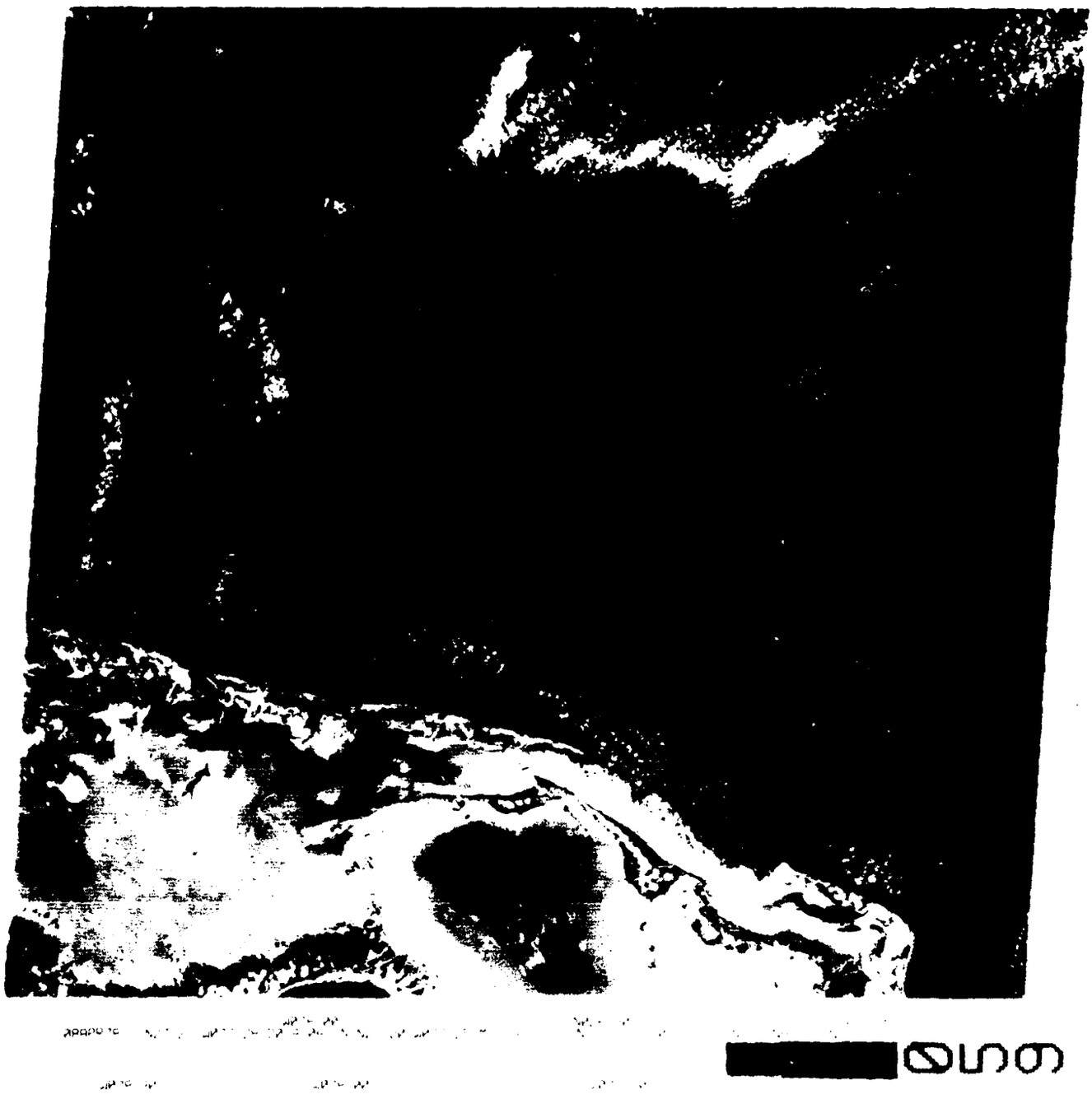

Figure 7-2. Landsat image, Little Bahama Bank (8 Apr 76)

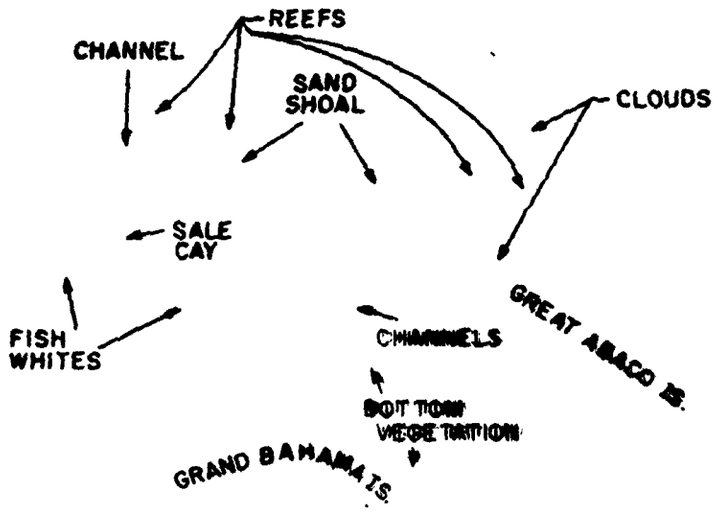

(LANDSAT) LITTLE BAHAMA BANK 8 APR 72

Figure 7-3. Landsat image, Little Bahama Bank (8 Apr 78)

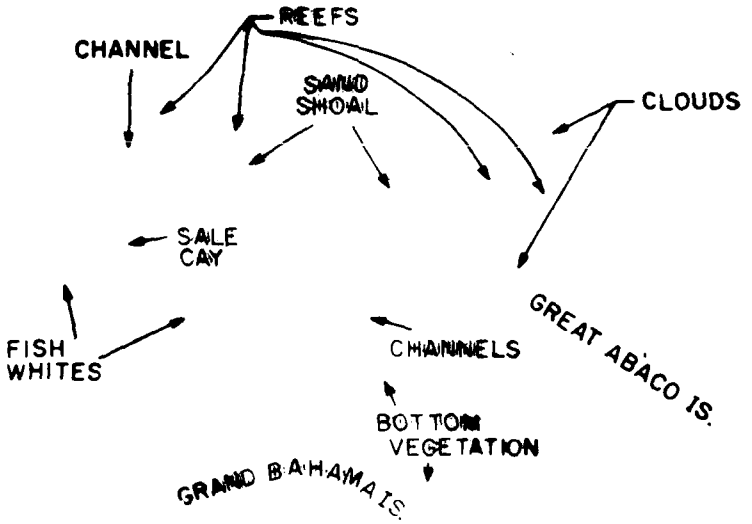

(LANDSAT) LITTLE BAHAMA BANK 8 APR 76

Figure 7-4. Landsat image, Little Bahama Bank (8 Apr 78)

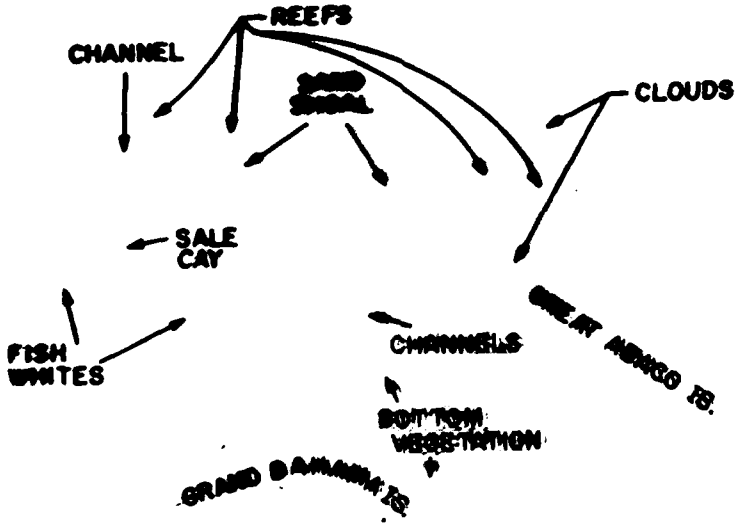

(LANDSAT) LITTLE BAHAMA BANK 8 APR

Figure 7-5. Landsat image, Little Bahama Bank (8 Apr 78)

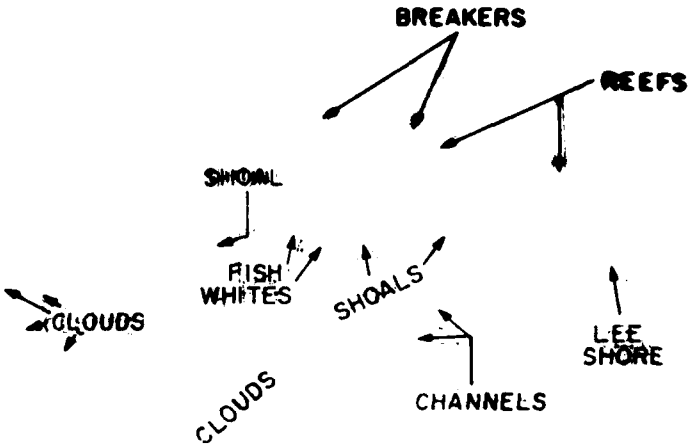

(LANDSAT) LITTLE BAHAMA BANK 26 MAR 77

Figure 7-6. Landsat image, Little Bahama Bank (26 Mar 77)

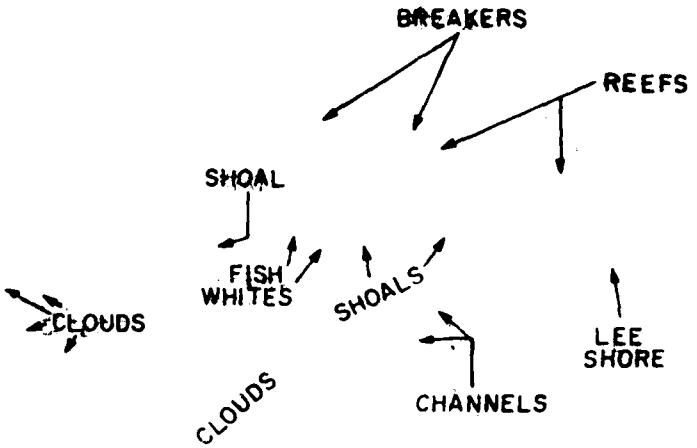

(LANDSAT) LITTLE BAHAMA BANK 26 MAR 77

Figure 7-7. Landsat image, Little Bahama Bank (26 Mar 77)

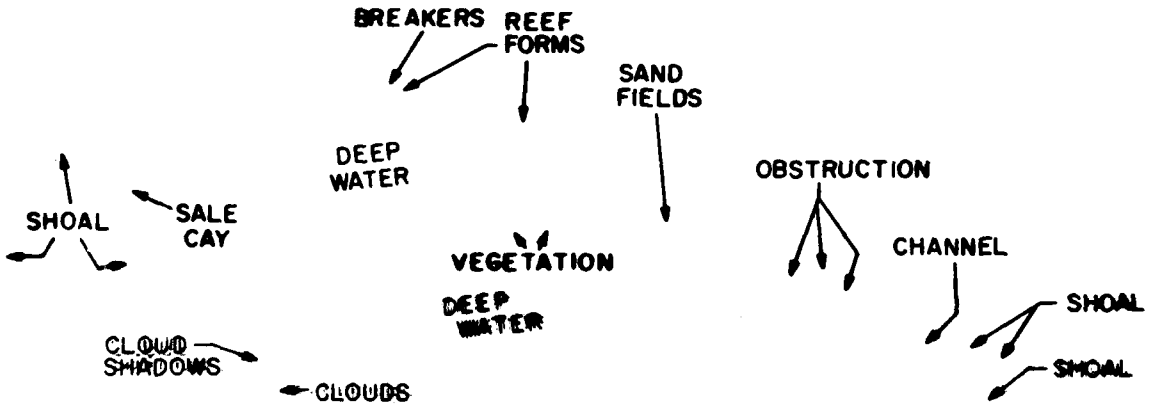

(LANDSAT) LITTLE BAHAMA BANK 13 FEB 78

Figure 7-8. Landsat image, Little Bahama Bank (13 Feb 78)

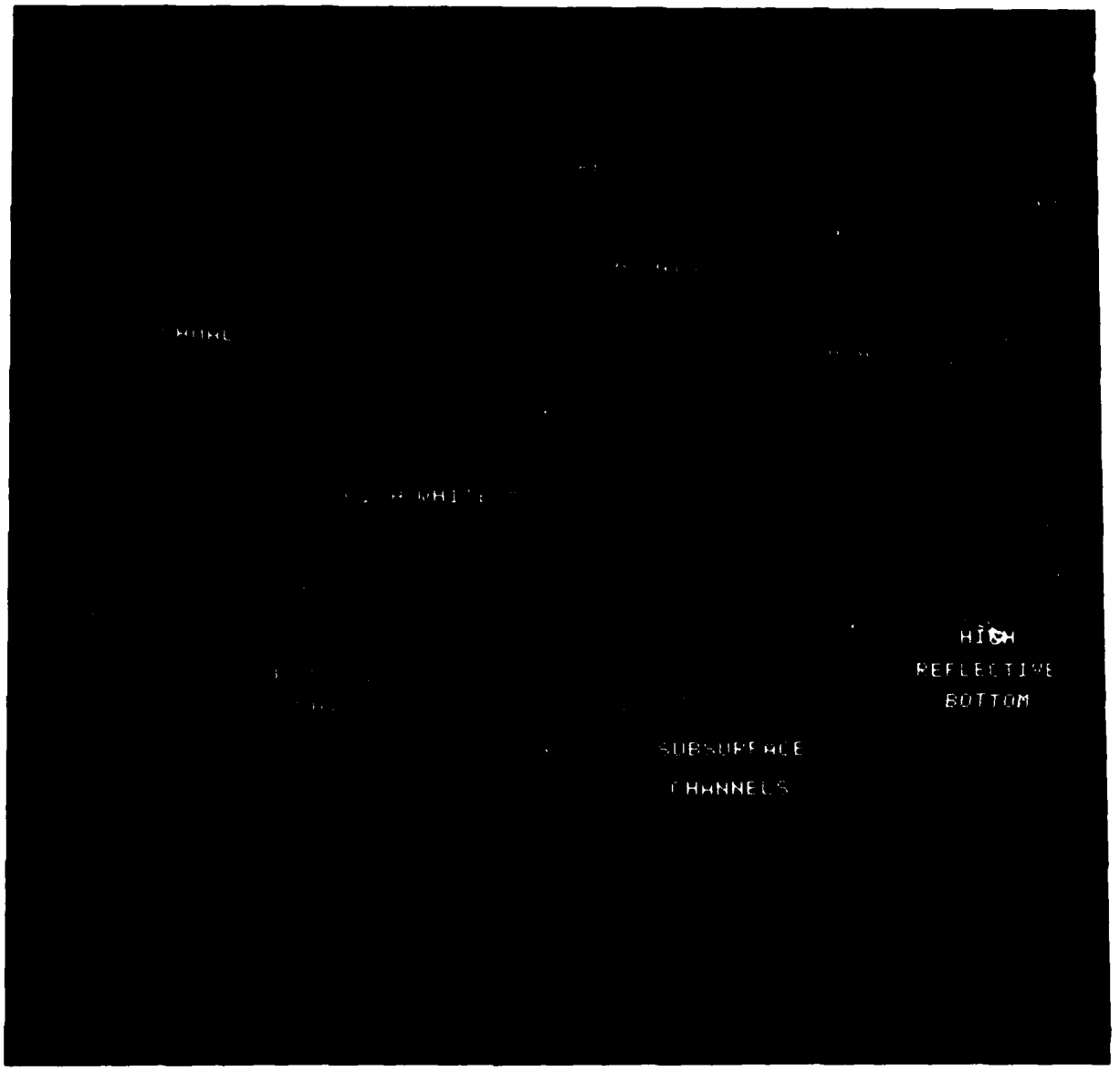

Figure 7-9. Landsat computer generated color composite of channels 4, 5 and 7, Little Bahama Bank (26 Mar 77)

8. Mississippi River Delta

8. Mississippi River Delta

The bird-foot-shaped Mississippi River Delta, which is located in the northern Gulf of Mexico, is a dynamically changing land feature. Accurate and recently updated charts are required on a frequent basis for this area. The discharge of the Mississippi River is very high in suspended sediment; therefore, water clarity is very poor for direct detection of bottom features through aerial photography or satellite imaging. The turbid flow patterns, which are detectable through remote sensing techniques, allow interpretation of the surface currents and, to a certain extent, submerged features.

A hydrographic chart (figure 8-1) of the Mississippi River Delta is presented for comparison with Landsat imagery. Landsat imagery of the delta dated 16 December 1978 is illustrated in Figures 8-2, 8-3, 8-4, and 8-5 for Channels 4, 5, 6, and 7, respectively. Imagery dated 9 November 1978 is illustrated in Figures 8-6 (Channel 4), 8-7 (Channel 5), 8-8 (Channel 6) and 8-9 (Channel 7). In these data sets the sediment plumes associated with the river discharge are well-defined as gradations of gray shades extending offshore.

The first data set (16 December 1978) displays a highly contrasting discharge pattern of turbid water flows, which is especially noticeable in the visible channels (figures 8-2 and 8-3). Notice that the turbid water flow patterns are also illustrated in Channel 6 (figure 8-4) and faintly in Channel 7 (figure 8-5). These flow patterns, which are imaged as differences in water turbidity, result from the mixing of water masses by the local currents. High turbidity waters result in high reflectance (light colors) on Landsat imagery. Note the bright tone of the highly turbid Mississippi River in relation to the dark tone of the clear offshore waters. Other discharge plumes along the Louisiana coast are also illustrated. The Mississippi River Delta discharge plume and associated flow patterns indicate general westward movement of surface currents, which is typical in this region. Turbidity flows are observed migrating around the delta toward the west; therefore, the currents at the southwest pass appear to move in a southwest direction. (Clouds in this area mask much of the flow patterns.)

Note that in Channel 5 (figure 8-3), the sediment plumes along the Barataria Bay coastlines are streaming to the northwest. Water movements in this embayment just west of the delta have been reported as moving clockwise, a counter current to this westward offshore movement. This imagery confirms the reported current measurements. Superimposed on the overlays of this data set are the approximate locations of the 10 and 40 fathom contours. Note the general relationships (figures 8-2, 8-3) of the turbid flow patterns with the bathymetry. In Figure 8-2, the approximate location of the deep water canyon can be observed by a general darker tone that is characteristic of a clear water area.

The second data set (9 November 1978) images the end of the bird-foot-shaped delta. The majority of this image is cloud cover over the Gulf of Mexico. Similar westward-flowing, turbid stream patterns around the delta are illustrated in Figures 8-6 and 8-7, yet the gray tonal patterns are suppressed and are not as vividly illustrated as compared with the previous data set (figures 8-2, 8-3). Also, the IR Channels 6 and 7 (figures 8-8, 8-9) do not show any of the turbid water flow patterns as do the previous IR images (figures 8-4 and 8-5). The interpreter might erroneously conclude that the water sediment concentrations were higher on 16 December 1978 than 9 November 1978, which would account for the brighter tones or enhanced turbid water patterns observed in the visible and the IR channels. The comparison of these data illustrates limitations of interpretation of hydrographic features which result from suppressed contrast. By comparison of the gray wedges at the

bottom of images for corresponding channels (figures 8-2, and 8-6, 8-3 and 8-7, 8-4 and 8-8, 8-5 and 8-9) it is evident that higher contrast was used in printing images in the first data set, thereby enhancing the water. Because a lower contrast was used in printing the second set of images the water tones are highly suppressed. This suppression is a drawback in bulk processing Landsat imagery, since the amount of contrast selected may not be optimal for hydrographic interpretation. When comparing temporal images, the interpreter should first compare the gray wedge to observe any differences in the bulk processing (beware of high- versus low-gain differences). Misinterpretation of changing surface reflectance patterns in the images can be eliminated by comparing the contrast enhancements used in printing.

From this example it is evident that estimating the turbidity of the water can only be done on an image-by-image basis. The variability of the bulk processing makes estimates between images impossible. By eliminating the bulk processing and going directly to the digital MSS tape and computer processing the data, a better estimate of the water turbidity can be obtained. Still, it is difficult to relate temporal images through computer processing, since different sun elevations, atmospheric conditions, and other effects will change the reflectance of turbid water. Density slicing on the 16 December 1978 image (Channel 5) was performed through computer processing. Results are illustrated in Figure 8-10. Black areas are land and clouds. Relative water clarity is color-coded in the figure.

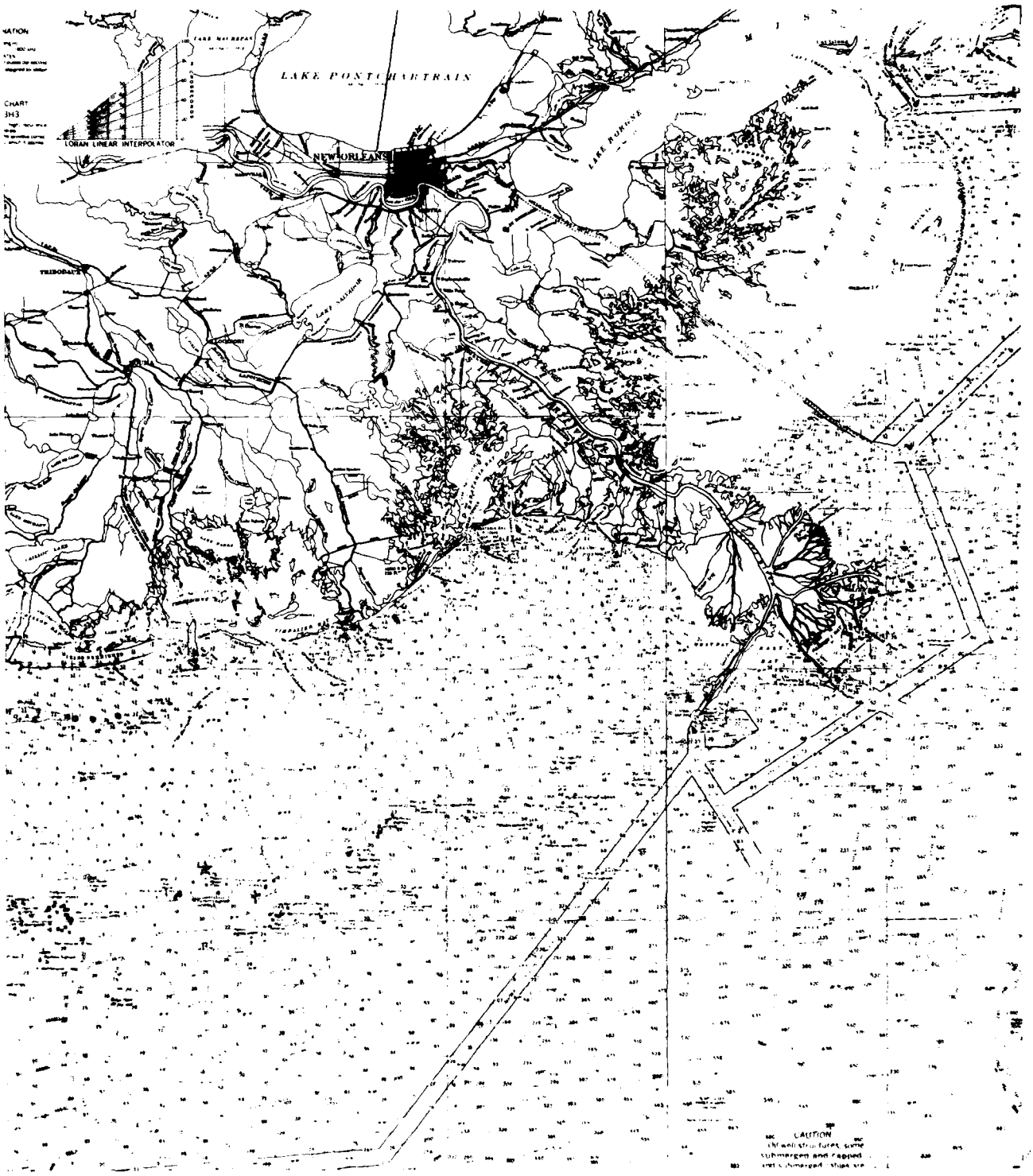

Figure 8-1. Hydrographic chart of the Mississippi River Delta (11371, 11373)

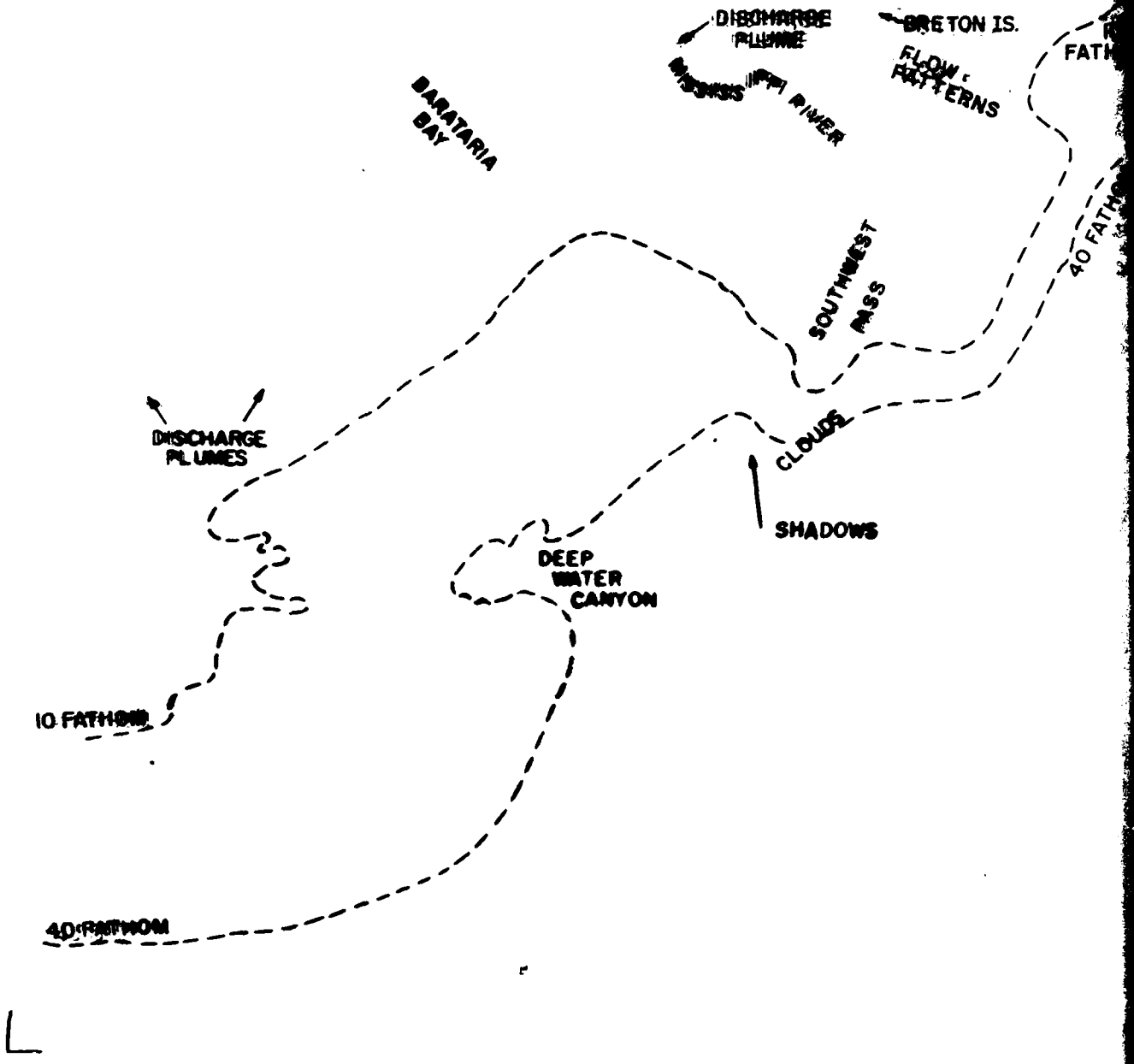

(LANDSAT) MISSISSIPPI RIVER DELTA 18-DEC 78

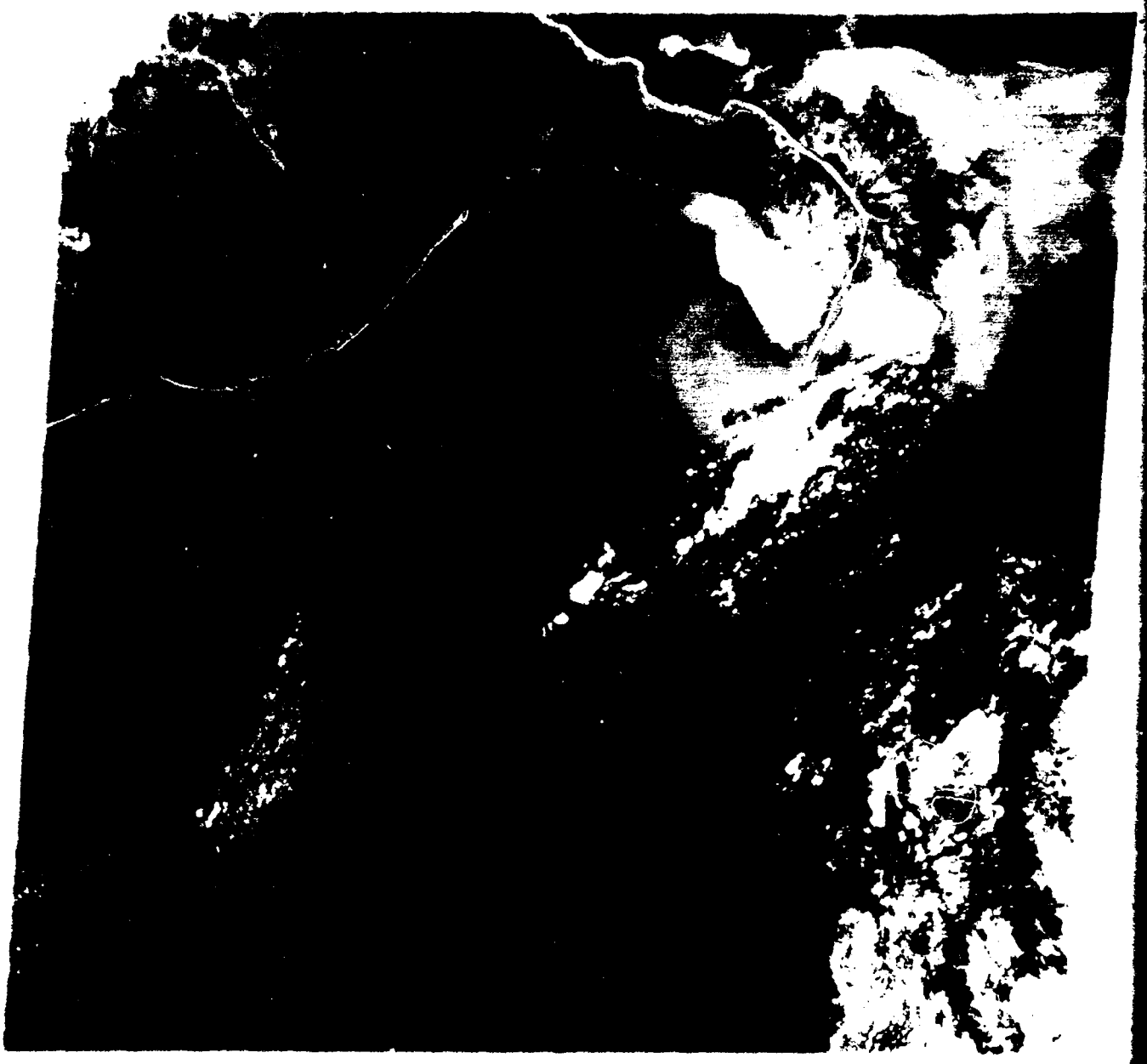

Figure 8-2. Landsat image, Mississippi River Delta (16 Dec 78)

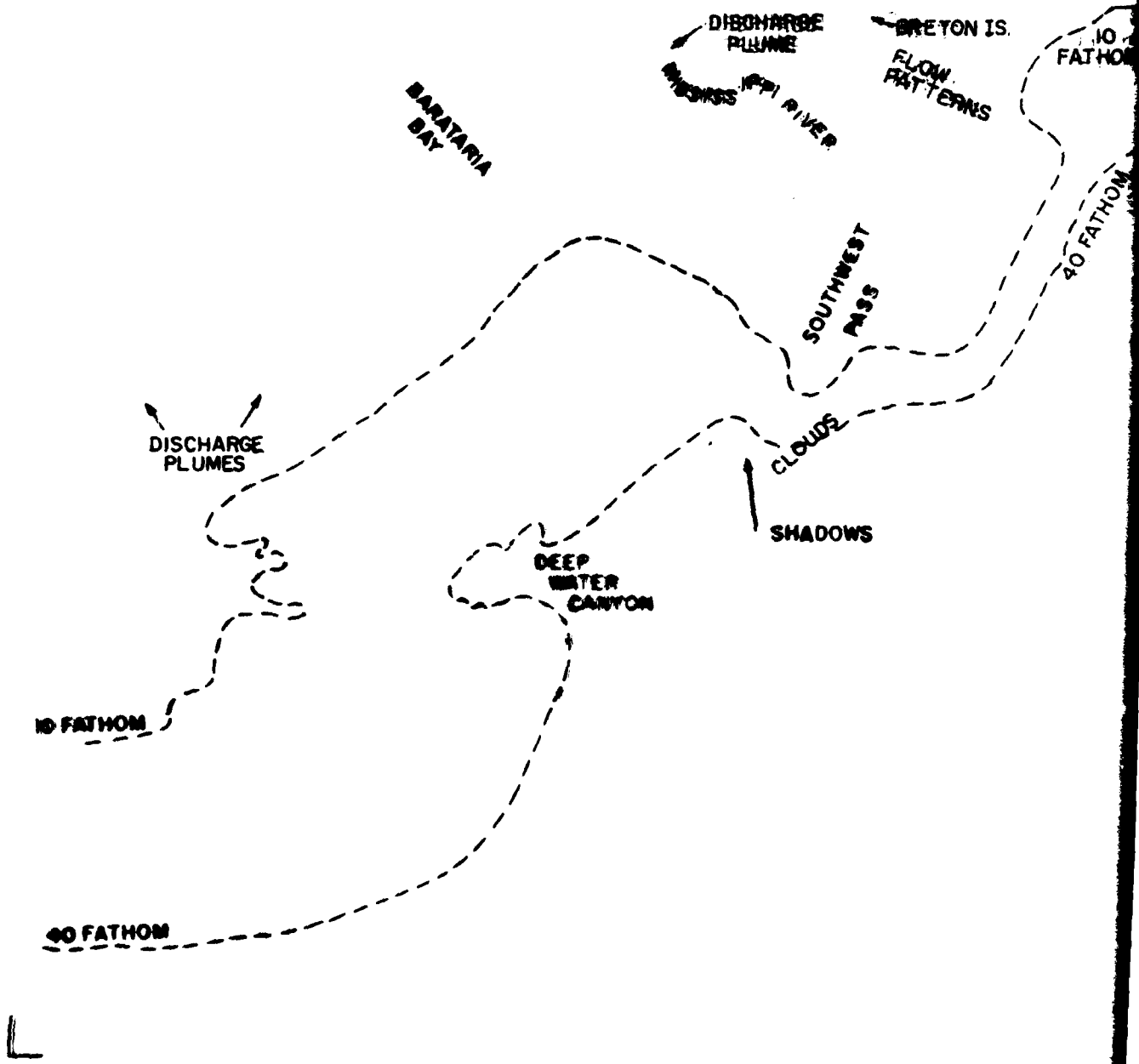

(LANDSAT) MISSISSIPPI RIVER DELTA 16 DEC 78

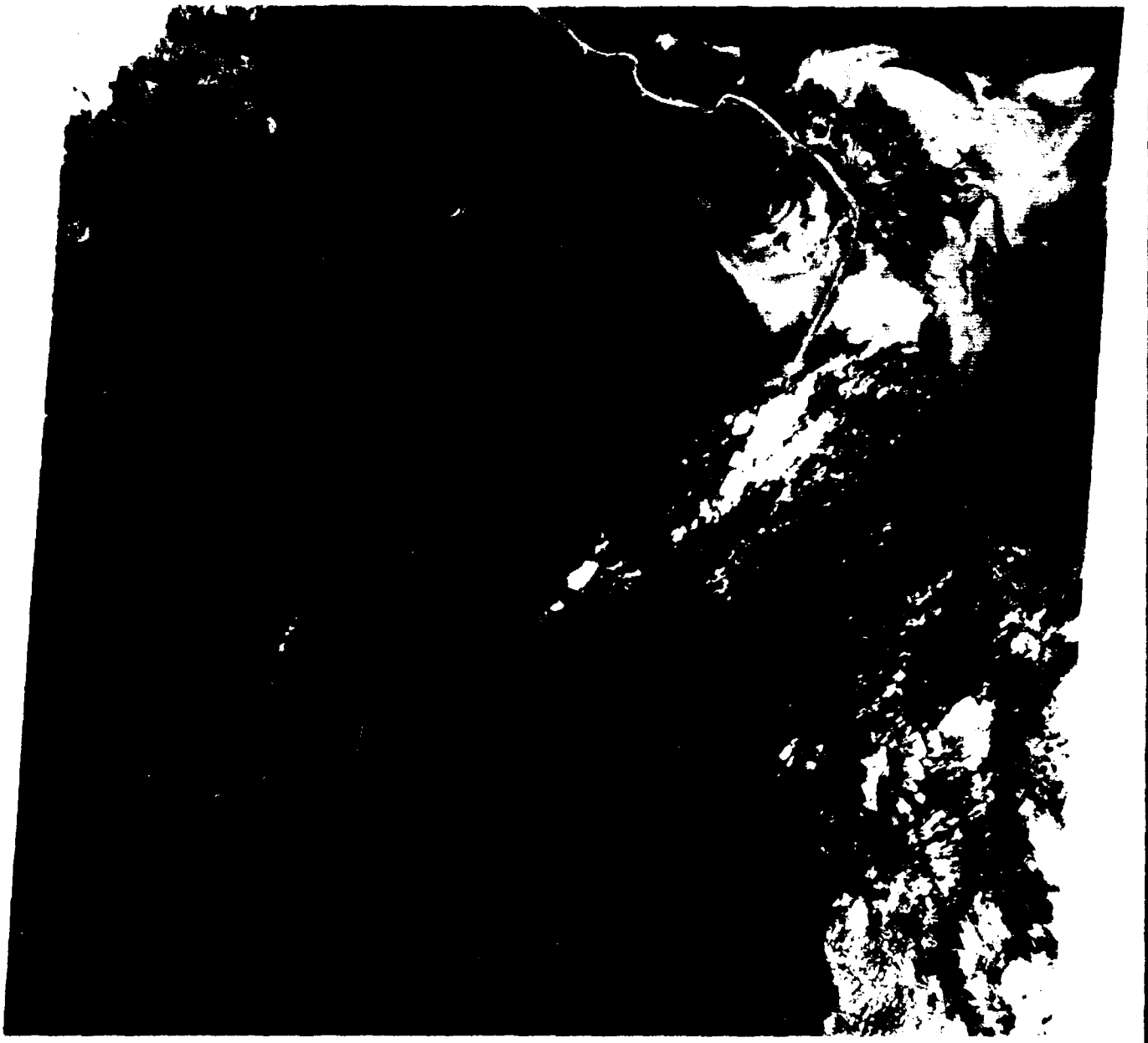

Figure 8-3. Landsat image, Mississippi River Delta (16 Dec 78)

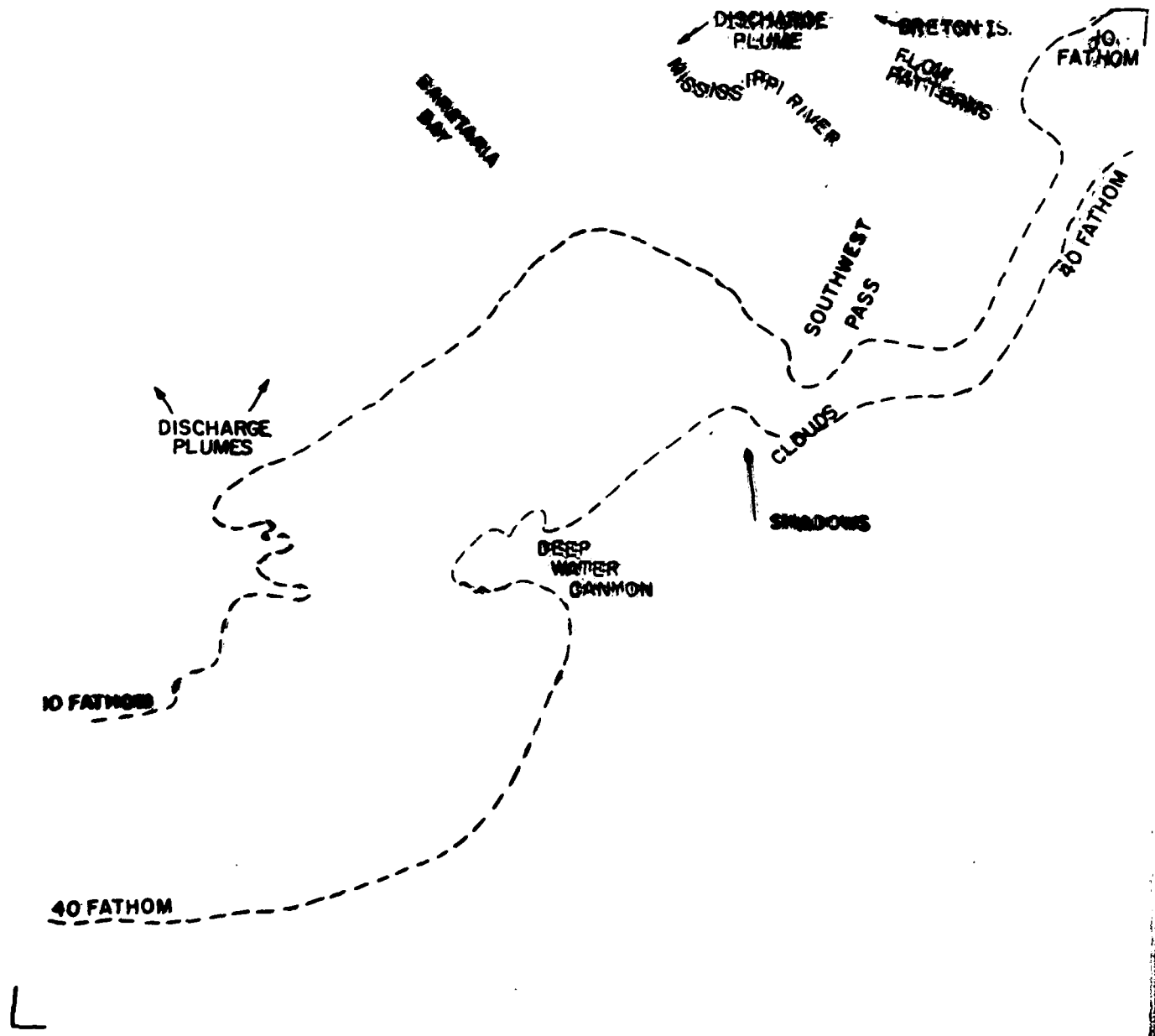

(LANDSAT) MISSISSIPPI RIVER DELTA 16 DEC 78

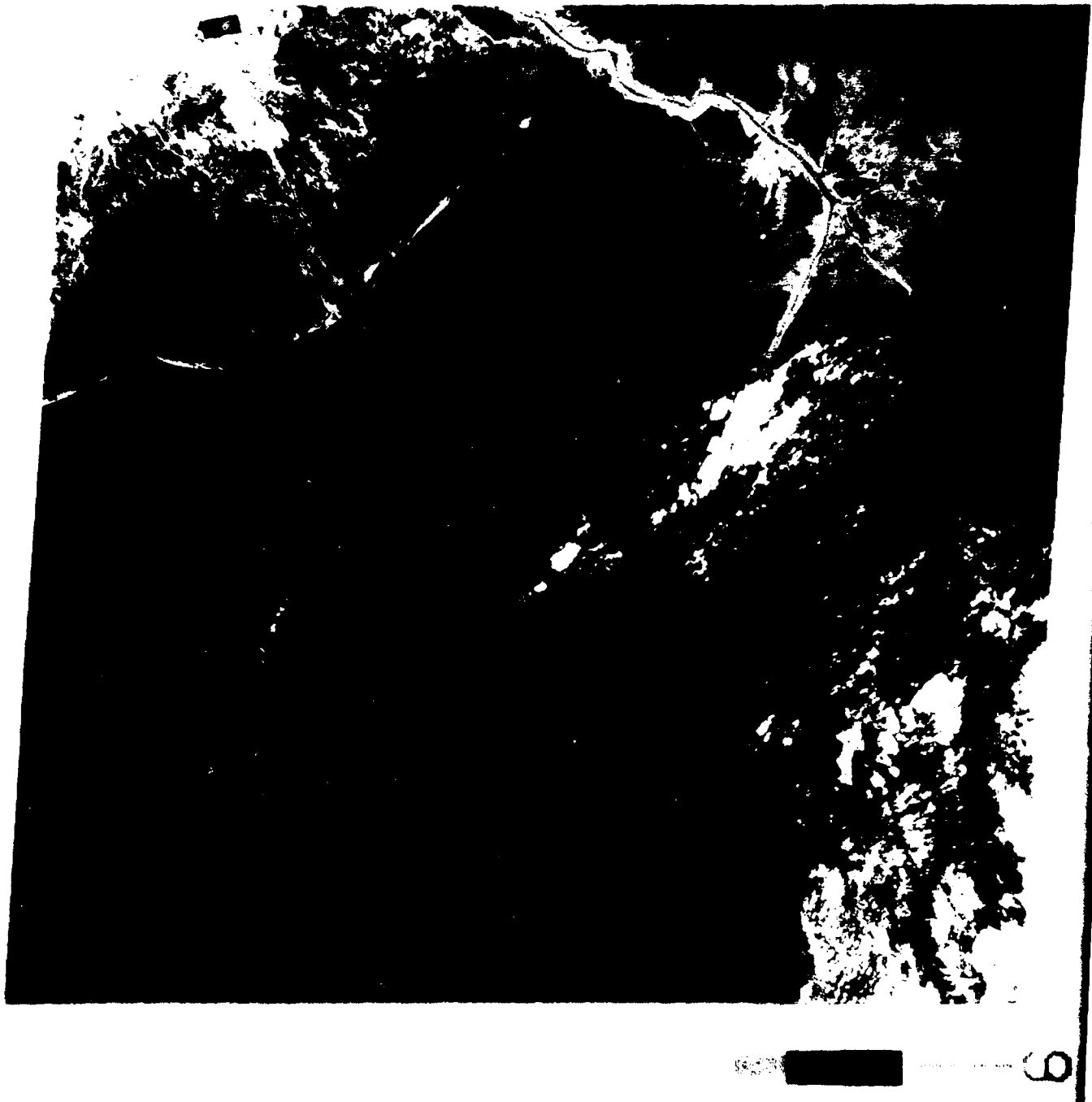

Figure 3-4. Landsat image, Mississippi River Delta (16 Dec 78)

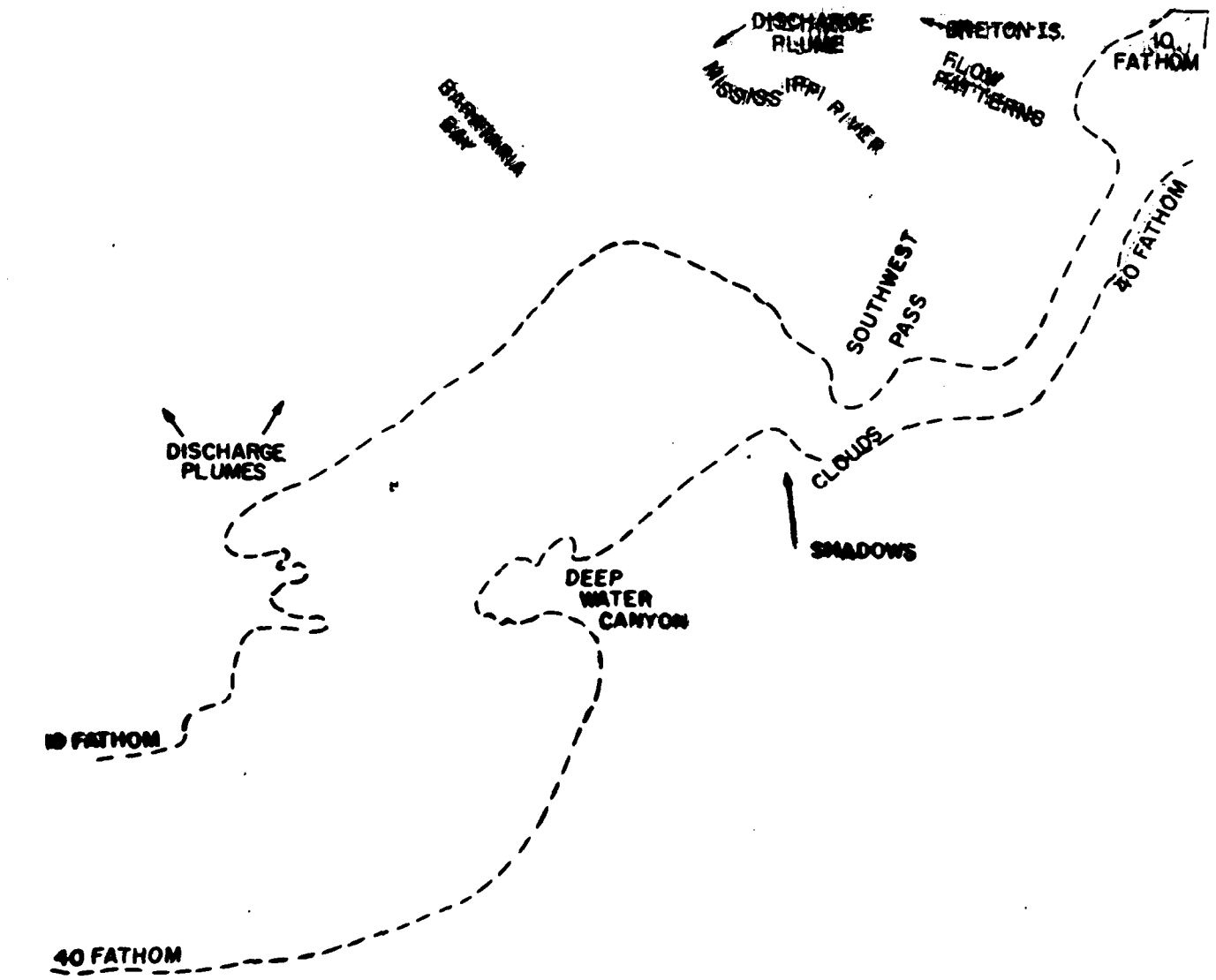

(LANDSAT) MISSISSIPPI RIVER DELTA 16 DEC 78

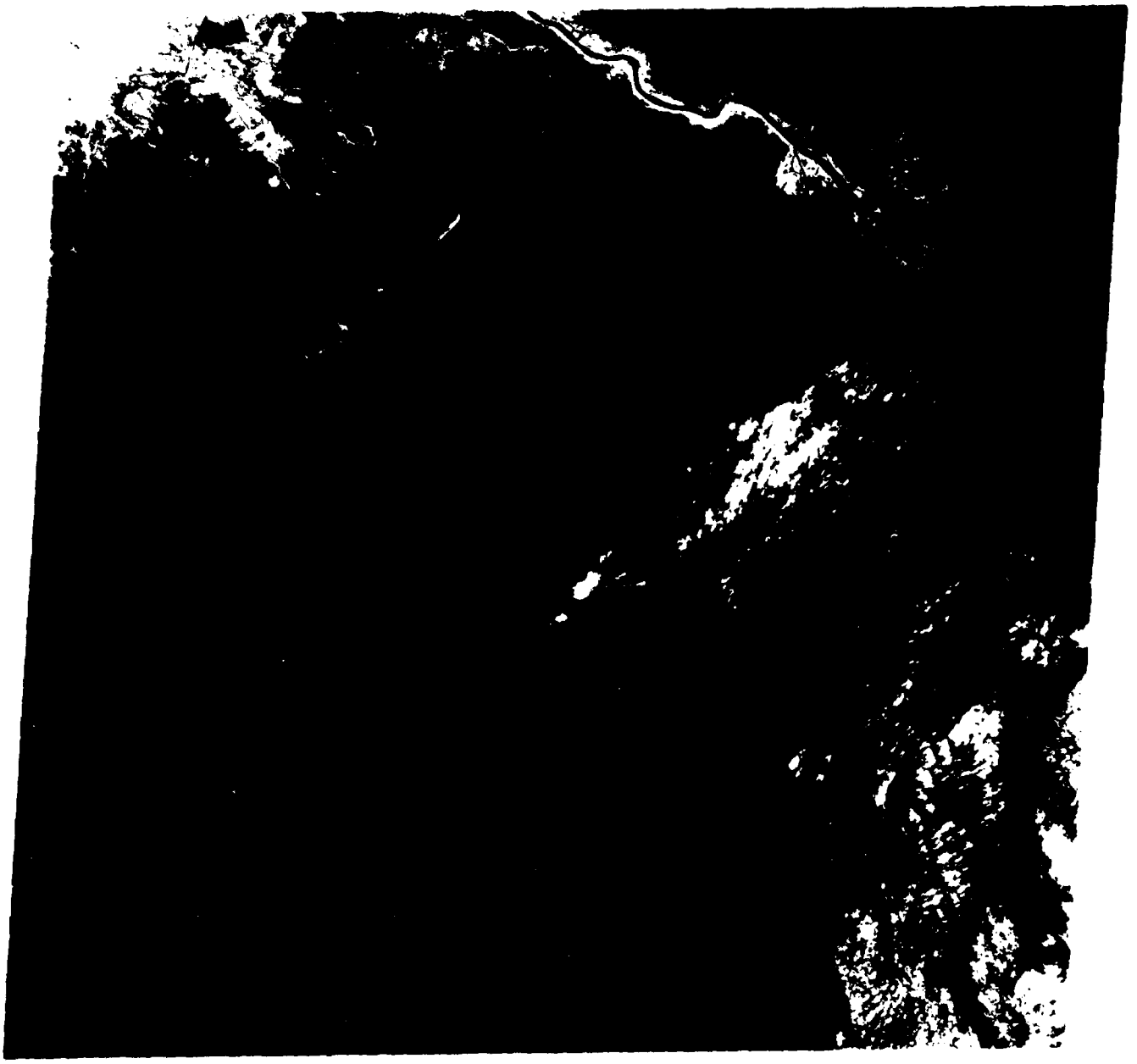

Figure 8-5. Landsat image, Mississippi River Delta (16 Dec 78)

Figure 8-6. Landsat image, Mississippi River Delta (9 Nov 78)

Figure 8-7. Landsat image, Mississippi River Delta (9 Nov 78)

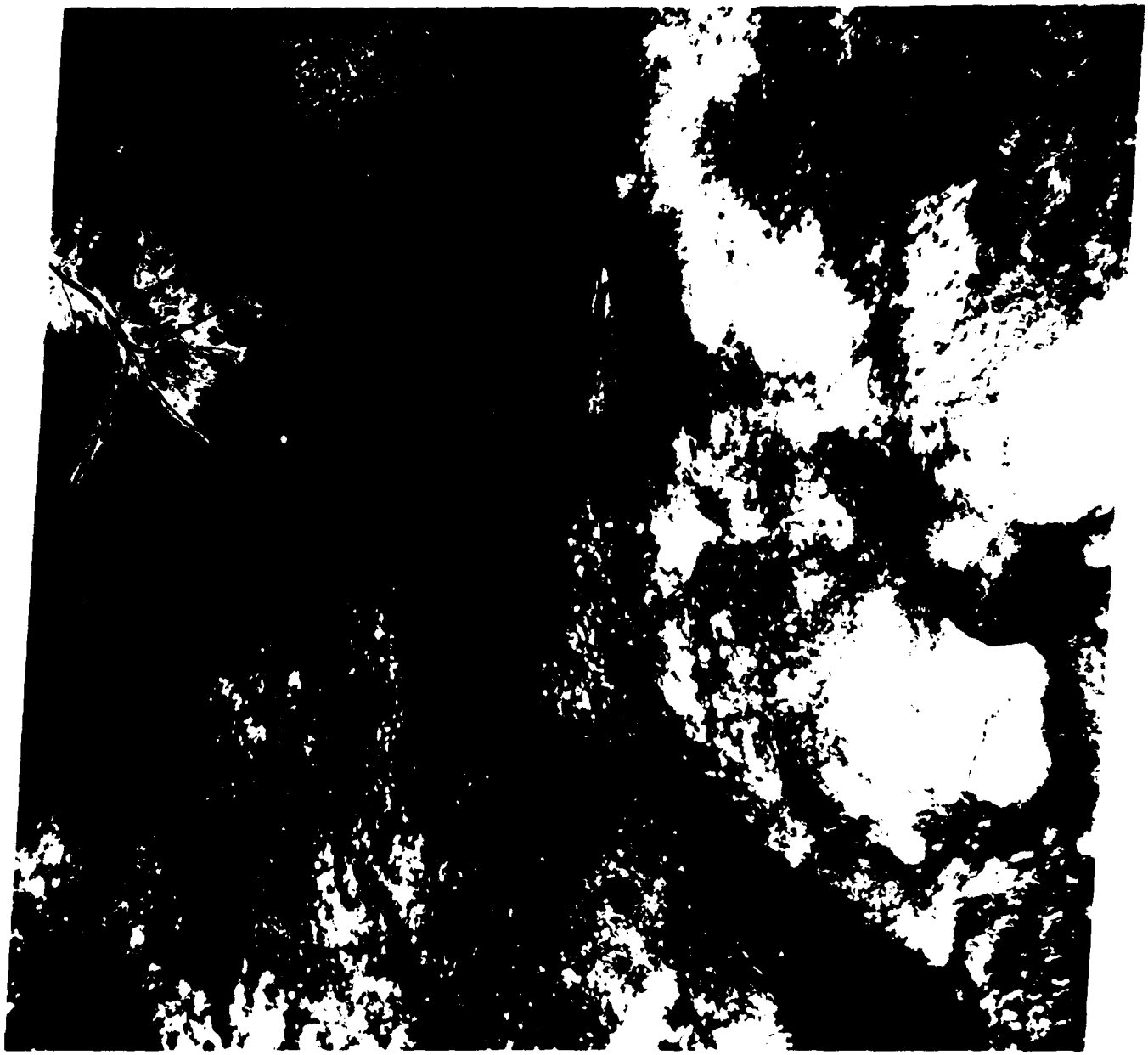

Figure 8-8. Landsat image, Mississippi River Delta (9 Nov 78)

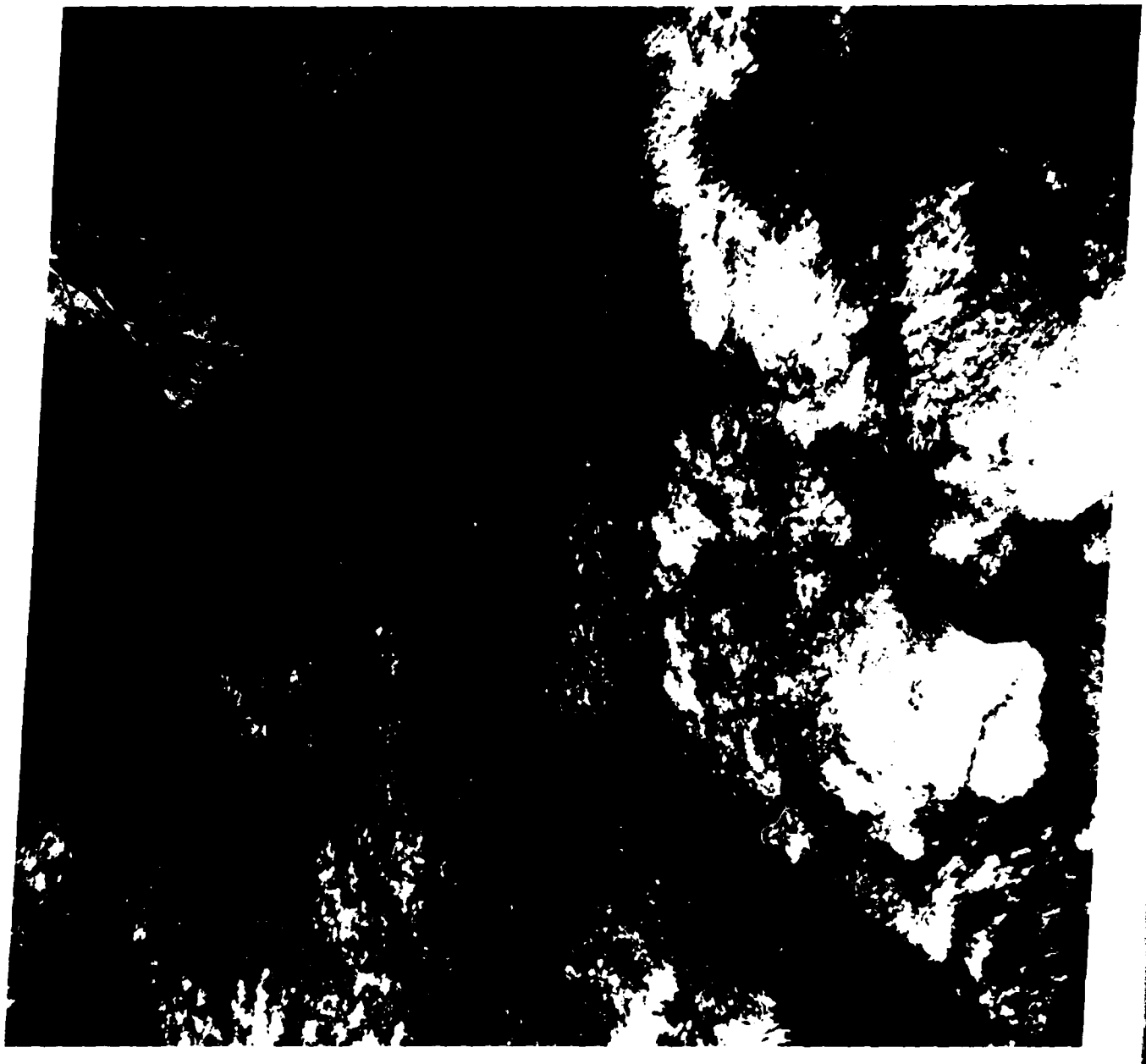

Figure 8-9. Landsat image, Mississippi River Delta (9 Nov 78)

Figure 8-10. Landsat computer derived water clarity classification Mississippi River Delta (16 Dec 78)

9. Cape Hatteras, NC

9. Cape Hatteras, NC

Cape Hatteras is located on the east coast of North Carolina. A barrier island chain extends the length of the coastline in this area. A series of shallow water sounds, which are located behind the barrier island chain, are characterized by turbid water flow patterns and by an intricate series of shoals and channels. Seaward of the barrier islands the water depth slopes rapidly offshore. The continental shelf along the east coast of the United States is most narrow directly off Cape Hatteras. The westward divergence of the Gulf Stream commonly occurs directly off the Cape Hatteras coast. (Appendix C illustrates the major ocean currents.) A hydrographic chart of this area is shown in Figure 9-1. Landsat imagery (2 December 1972) for Channel 4 (figure 9-2), Channel 5 (figure 9-3), and Channel 7 (figure 9-4) is also shown for the corresponding area. (Channel 4, figure 9-2 represents extremely noisy, poor quality Landsat data for this pass.)

Note the light-colored ocean frontal boundary shown propagating to the northeast in Channels 4 and 5. Clear Gulf Stream waters are located south of the boundary and higher turbidity coastal waters comprise the northern boundary waters. As the Gulf Stream interacts with the bottom in the Cape Hatteras area, it is diverted to the northeast. The more turbid coastal waters located north of Cape Hatteras become entrained in the Gulf Stream's offshore movement and are observed as a sharply defined ocean color boundary. The boundary delineates the east side of the Gulf Stream and illustrates the meandering patterns that occur along this boundary as it extends offshore.

The current movements are to the south along the northern coastline north of Cape Hatteras. Northerly long-shore currents dominate along the coastlines south of Cape Hatteras as a direct result of the Gulf Stream. The sediments associated with longshore transport have possibly resulted in the development of an eastward-extending shoal off Cape Hatteras.

Surf on the shoal is observed in Channel 5 (figure 9-3) of the Landsat image and aids the interpreter in detecting the shoal's presence. The extent and position of the shoal should be observed better in Channel 4, but poor quality data in this channel make Channel 5 the better image. Through comparison of Figure 9-3 with the hydrographic chart (figure 9-1), the tonal and brightness differences in the image can be associated with local bathymetric features.

Figure 9-5 is a color IR aerial photograph of Cape Hatteras taken at 60,000 ft. This photograph provides a better understanding of Landsat imagery through comparison. Figure 9-5 illustrates a series of shoals and channels in Pamlico Sound. The water clarity appears good at the time the photograph was taken, since the bottom in Pamlico Sound is distinguishable. Breaking surf is also detectable at the Cape Hatteras point and northward along the barrier island coast. The amount of surf on the day the photograph was taken appears to be less than when the Landsat imagery was observed. Note also the sand ridges and vegetation patches in the photograph and the similarities in texture and pattern observed in the Landsat imagery (Channel 5). A "halo" feature surrounding the seaward (eastward) shoal off Cape Hatteras is observed in the photo and similarly in the Landsat image. This feature results from a difference in water color or water turbidity. Also present in the photograph are sunglint, clouds, and cloud shadows.

Waters behind the barrier island chain in Pamlico Sound create a variety of bottom features and water flow features. Figure 9-2 (Channel 4) illustrates the mixture of light-toned patterns characteristic of turbid flow patterns. Shoals and channel features are also illustrated within Pamlico

Sound. Off the west side of the barrier islands, relatively clear, shallow water permits Landsat to image the bottom. The lighter tones represent a highly reflective bottom (sand), and the mottled patterns within these areas are representative of vegetation patterns (also illustrated in previous case histories of Key West and Cedar Keys). The linear dark tones (figures 9-2 and 9-3) bordered by light features are characteristic of channel and dredge spoils. The discrimination of the bottom features and land is illustrated by the IR Channel 7, Figure 9-4. The light gray coastline bordering the highly reflective land is representative of wetlands and salt marshes (in this locale, SPARTINA salt marshes are common).

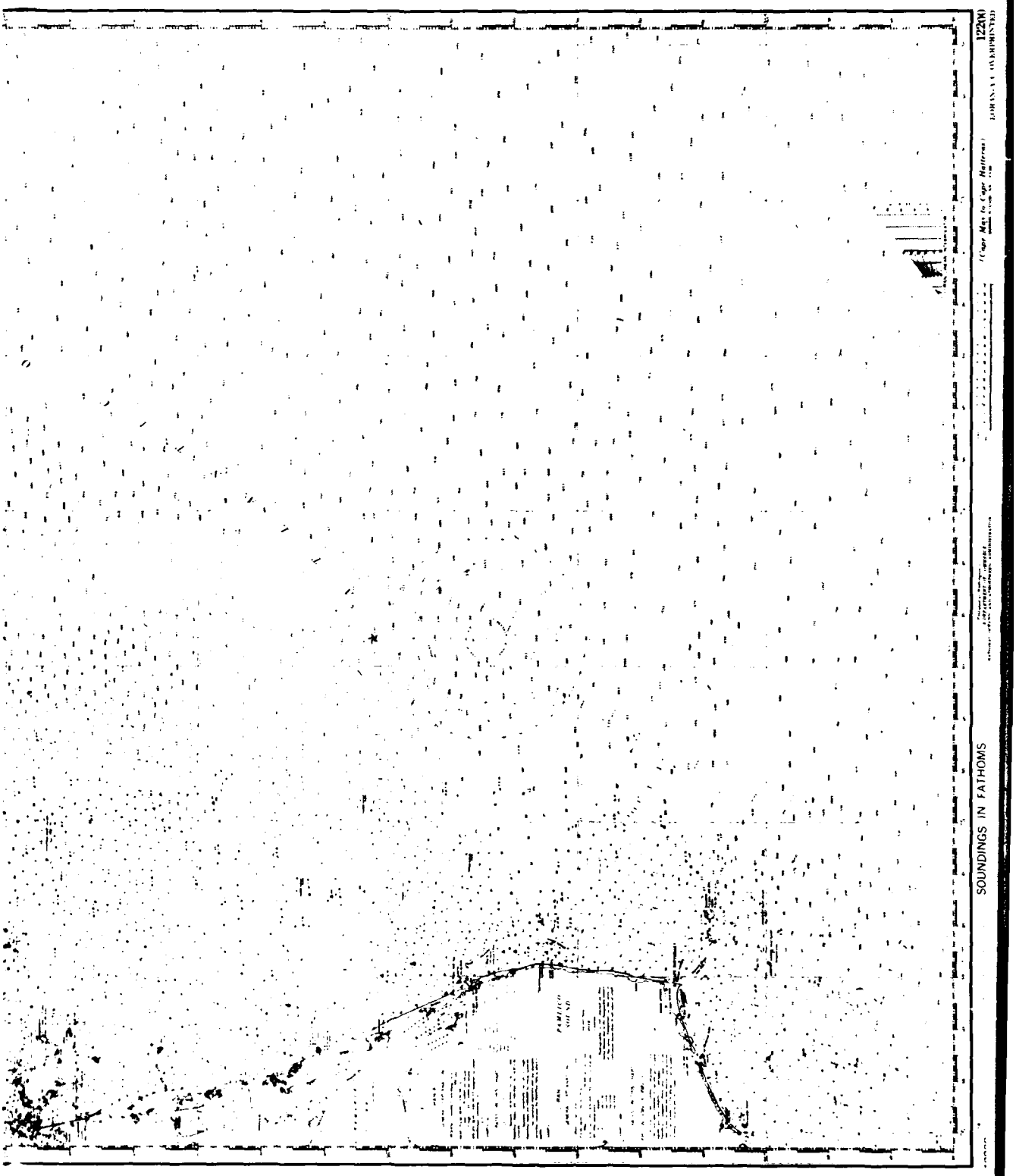

Figure 9-1. Hydrographic chart of Cape Hatteras, NC (12200)

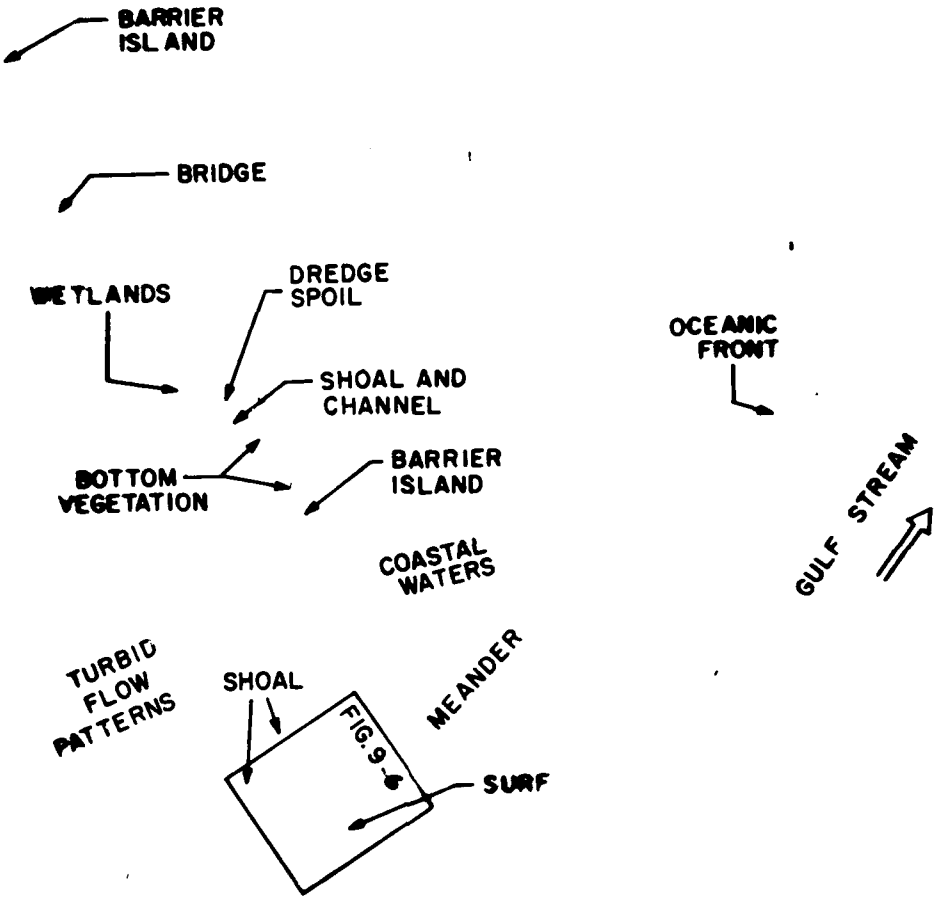

(LANDSAT) CAPE HATTERAS 2 DEC 72

Figure 9-2. Landsat image, Cape Hatteras, NC (2 Dec 72)

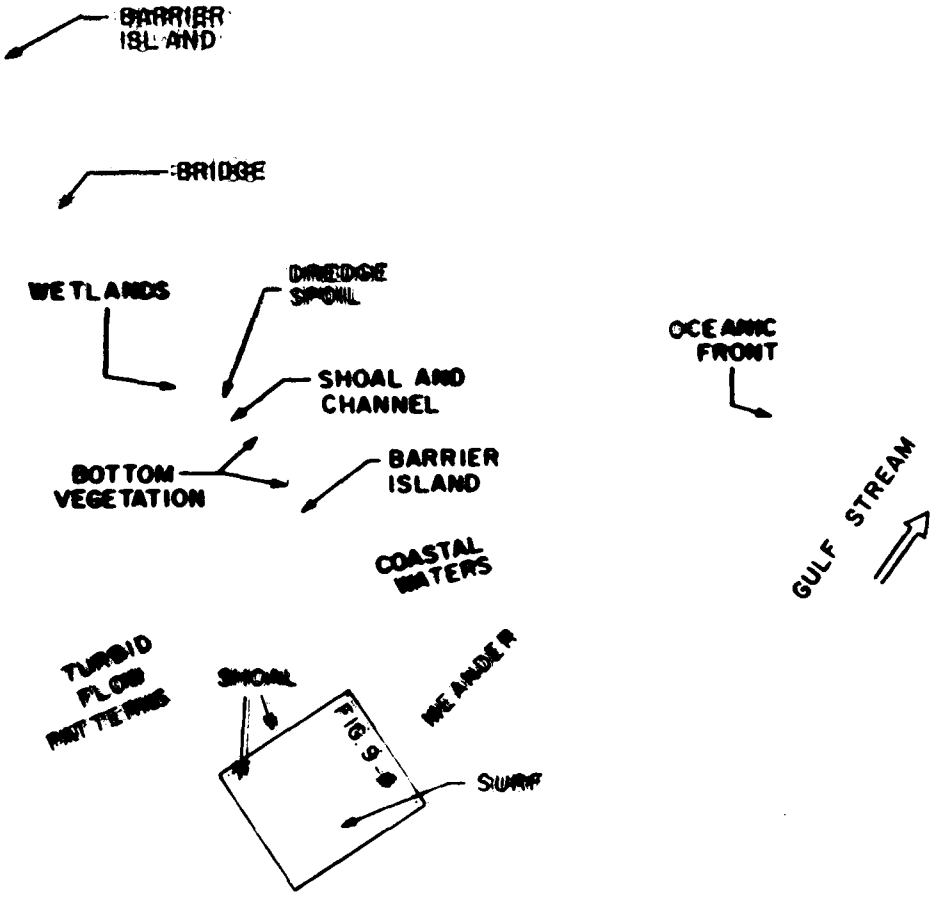

(LANDSAT) CAPE HATTERAS 2 DEC 72

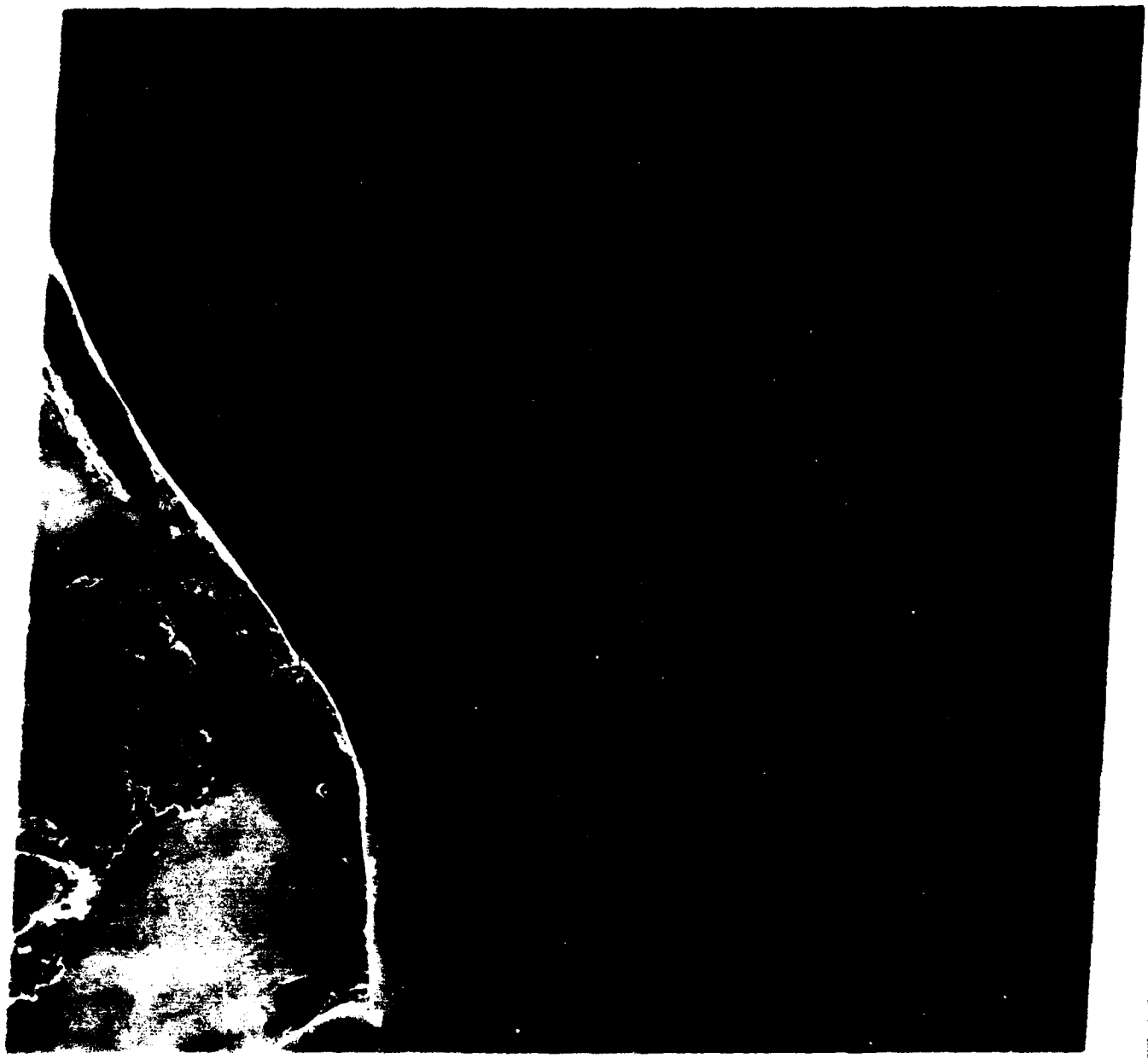

Figure 9-3. Landsat image, Cape Hatteras, NC (2 Dec 72)

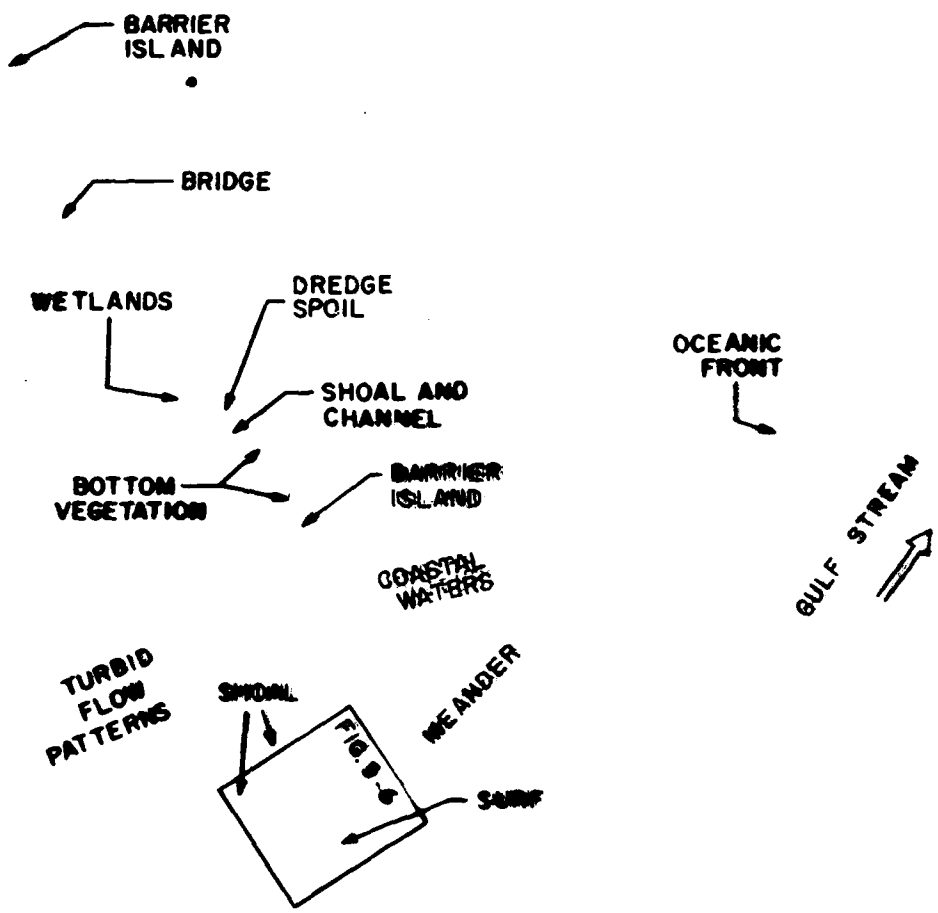

(LANDSAT) CAPE HATTERAS 2 DEC 72

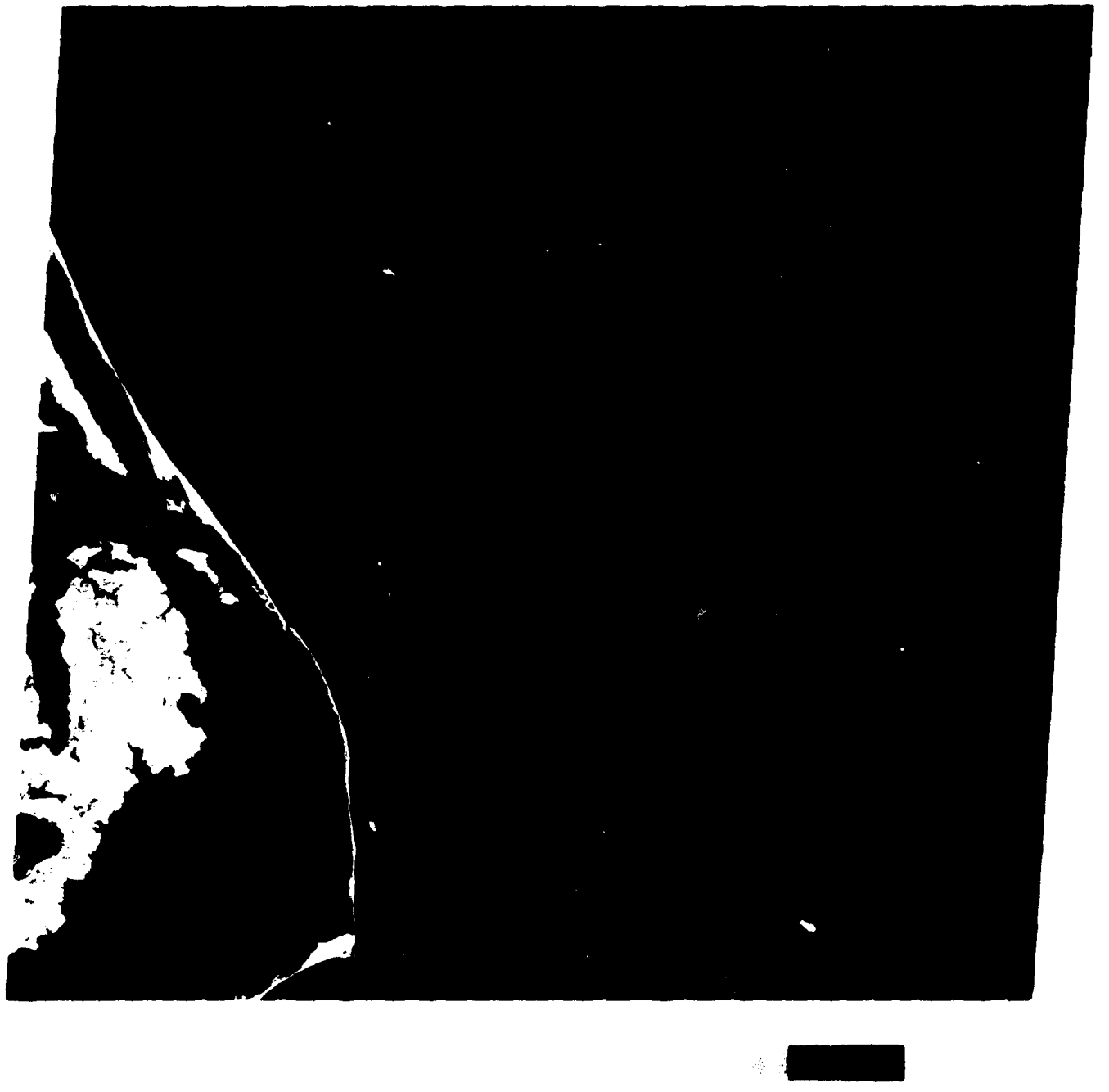

Figure 9-4. Landsat image, Cape Hatteras, NC (2 Dec 72)

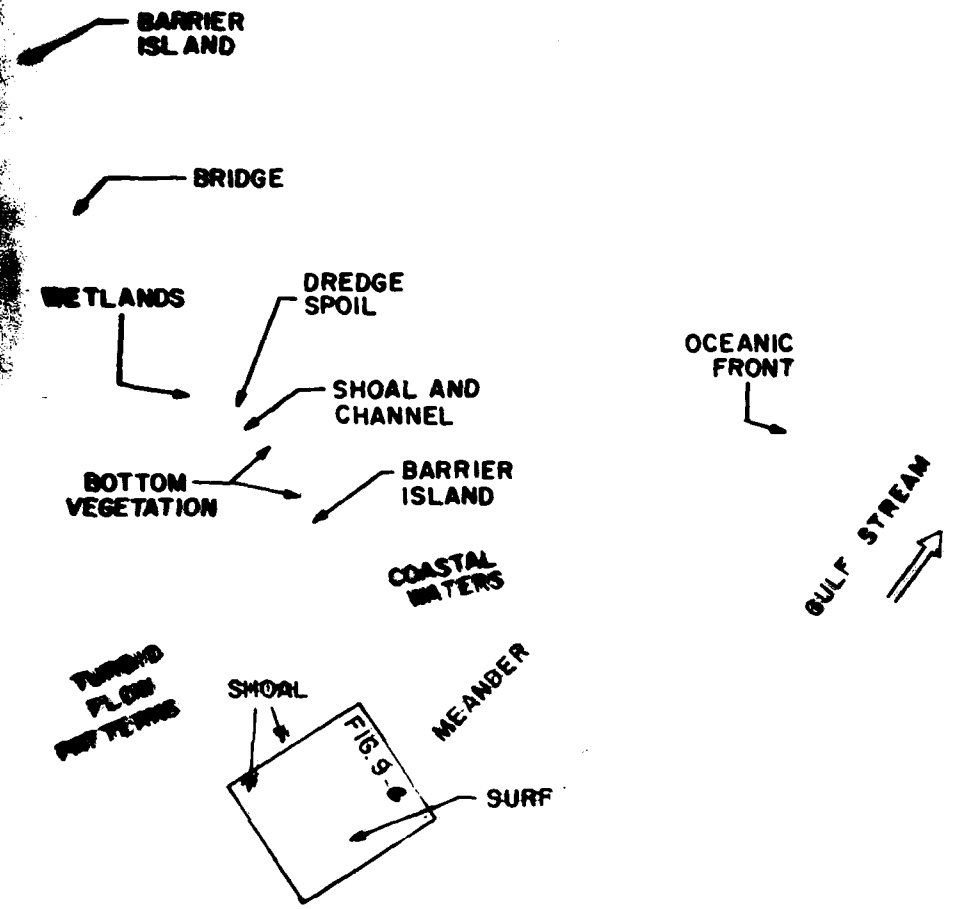

(LANDSAT) CAPE HATTERAS 2 DEC 72

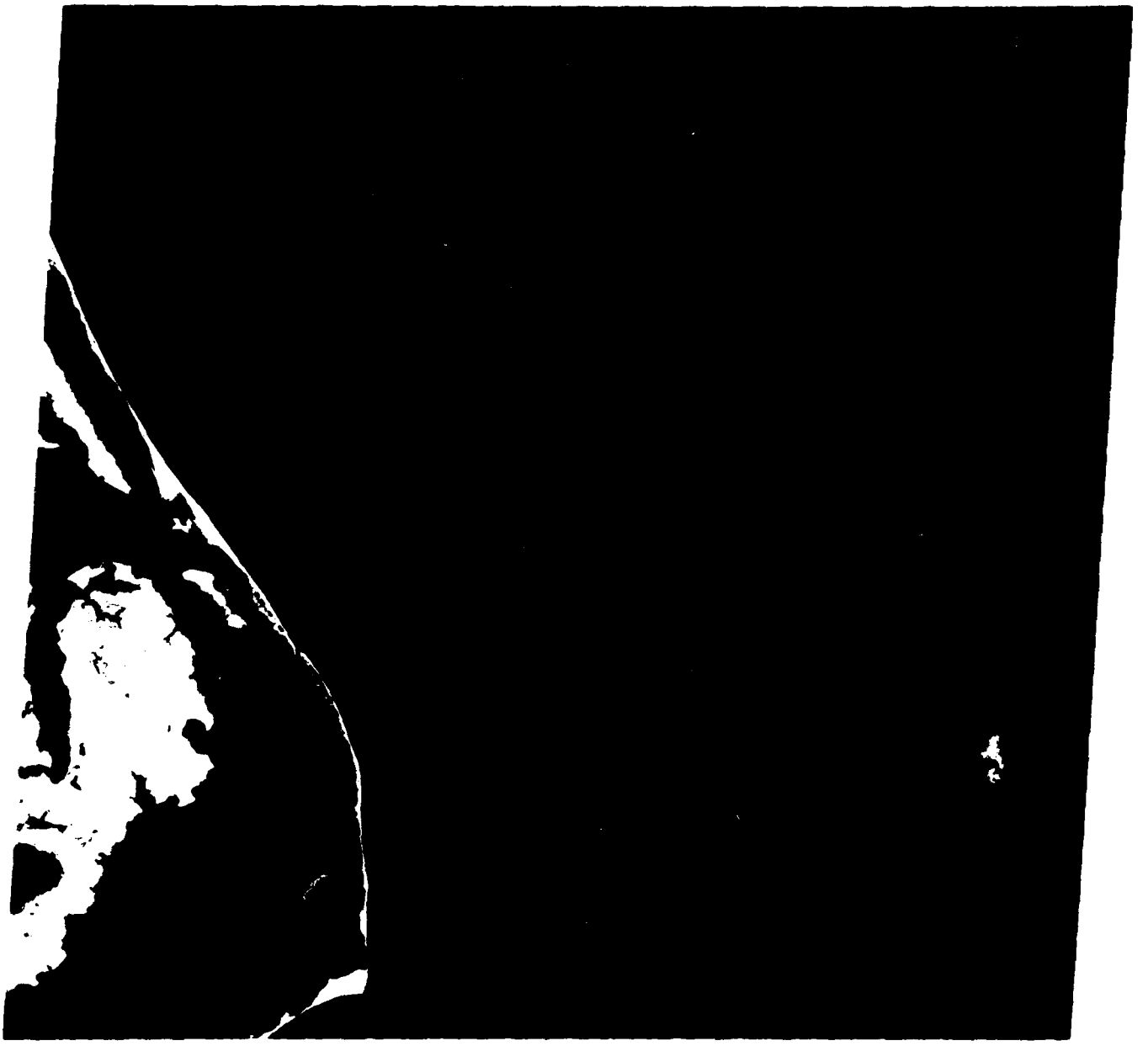

Figure 9-5. Landsat image, Cape Hatteras, NC (2 Dec 72)

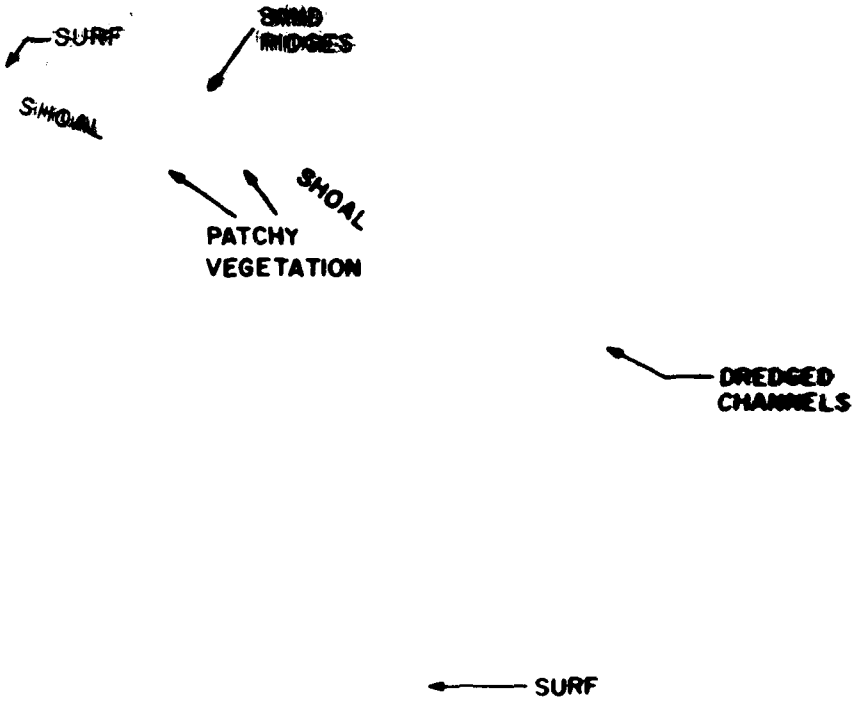

(AERIAL PHOTOGRAPHY) CAPE HATTERAS N

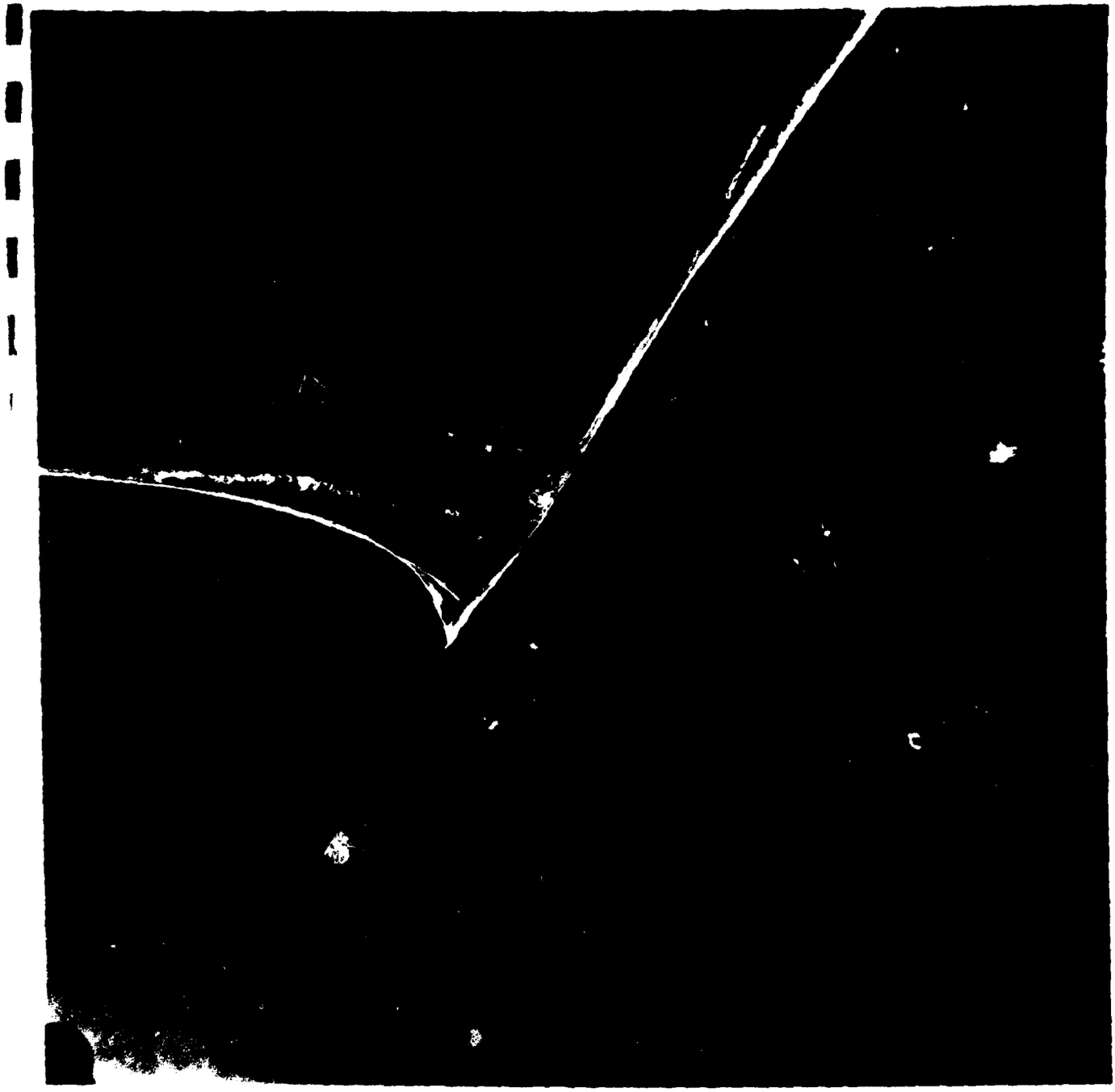

Figure 9-6. Color IR aerial photograph (1:135,000), Cape Hatteras, NC (Nov 1970)

10. Cape San Blas, FL

AD-A125 760 INTERPRETATION OF HYDROGRAPHIC FEATURES USING LANDSAT IMAGES(U) NAVAL OCEAN RESEARCH AND DEVELOPMENT ACTIVITY NSTL STATION MS R A ARNONE ET AL. JUN 81 NORDA-39 3/3

UNCLASSIFIED F/G 8/10 NL

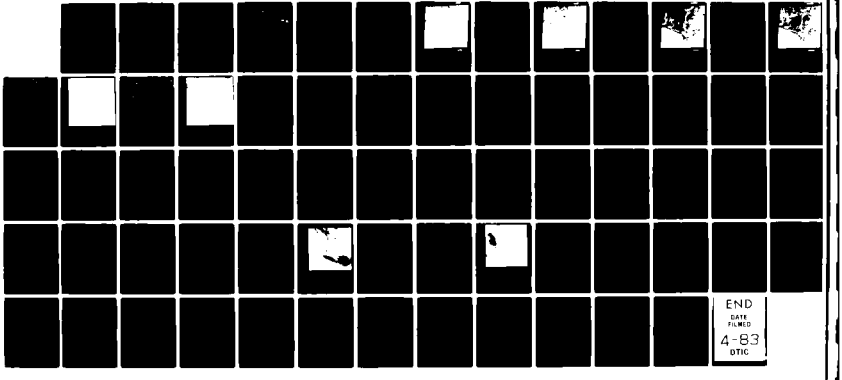

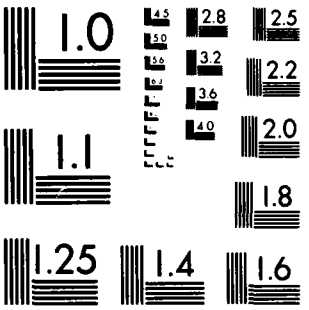

10. Cape San Blas, FL

The Cape San Blas area is located in the southern Florida panhandle on the Gulf of Mexico. The protrusion of the cape into the Gulf is the result of an ancient deltaic formation of the Apalachicola River. Present river discharge is not sufficient to continue an active prodeltaic formation, and the shoreline is presently controlled mainly by near-shore processes. The shoreline is actively changing as a result of the local long and offshore currents. A series of barrier islands and spits have formed and are under continual modification by these coastal processes. The Apalachicola Bay, located behind the barrier islands, receives the discharge of the Apalachicola River. Waters within this area are turbid as compared to the exceptionally clear coastal waters located offshore to the West (Panama City) and to the east (Apachee Bay). A hydrographic chart of this area is illustrated in figure 10-1 (11360). A more detailed hydrographic chart (11401) of the Apalachicola Bay is illustrated in Figure 10-2.

Seaward of Apalachicola Bay (south of Cape San Blas) extensive sand shoals are present. Local currents within these shoals are treacherous to shipping. Migration and shifting of the shoals are constant problems when updating nautical charts. Currents in this region occur in response to tidal cycles. Farther offshore in the Gulf of Mexico, movements of the Loop Current (Appendix C) when near the Florida Panhandle coast, influence the mass movement of coastal water along shore. A general easterly flow of offshore waters in the Panama City area meets the general westerly flow of the Apalachicola delta waters. The combining of these opposing flows which occurs south of Cape San Blas Shoals probably resulted in the formation of Cape San Blas shoals.

Gently sloping sand bottoms extending offshore are characteristic of the area. The Continental Shelf extends the farthest offshore in this area than anywhere in the Northern Hemisphere. reflective, white, fine-grained quartz sand and has little coral outcropping. Near shore and in the bays and inlets, the bottom is composed of mixtures of sands and dark clays, with patches of vegetation outlining the bottom. These variable vegetation patches consisting of turtle grass are poorly reflective and vary considerably in thickness. Vegetation is limited to depths less than approximately 10 ft.

Landsat imagery of 13 December 1977, is illustrated in Figures 10-3, 10-4, 10-5, and 10-6 for Channels 4, 5, 6, and 7, respectively. Color IR aerial photographs (taken at 60,000 ft) of this area are illustrated in Figures 10-7 and 10-8. Channel 4 of Landsat (figure 10-3) shows a generally darker water tone (clear water) off the Panama City coastline than in the lighter toned waters (more turbid and shallower) off Cape San Blas and within Apalachicola Bay. Through comparison of Landsat's visible channels (figures 10-3 and 10-4) with the hydrographic chart (figure 10-1), the images' lighter tones, which extend offshore from the coastline, correspond to the location of Cape San Blas shoals and St. George shoal as depicted on the chart.

These tones result from reflectance of both the bottom and turbid water, and it is difficult for the interpreter to distinguish between them. By comparison of the Cape San Blas shoal in Landsat (figures 10-3 and 10-4) and in the aerial photography (figures 10-7, 10-8) general similarities can be seen. In the color IR photograph, the Cape San Blas shoals are illustrated as variable tonal shades of blue. The majority of these tonal variations have patterns associated with flow features and are interpreted as resulting from turbid water. There are also areas within the aerial photos where shoals are directly detectable by their high bottom reflectance (see overlay for figures 10-7 and 10-8). Similar patterns and features are illustrated on

the Landsat Channel 5 imagery (figure 10-4). The location of the Cape San Blas Shoal corresponds with that on the hydrographic chart (figure 10-2). Also observed on the aerial photo (figure 10-7) are the variety of bottom types/ ottom reflectances within St. Joseph Bay. The mottled dark patterns, characteristic of vegetation patches and the highly reflective sand bottoms, are clearly illustrated, as depicted on the overlay. Similar bottom features can be observed in the visible channels of Landsat; however, it is difficult to distinguish land from the bottom. The IR channels of Landsat (figures 10-5 and 10-6) provide the interpreter a different perspective when attempting to make this distinction.

Figure 10-8 is a color IR aerial photograph of the area adjacent to the photo illustrating St. Vincent Island and western Apalachicola Bay. Numerous boat wakes and water color fronts between clear and turbid water are illustrated. Surrounding the seaward entrance to Indian Pass, numerous shoals are illustrated which are also observed on the more detailed hydrographic chart (figure 10-2). Similar shoal features are also observed in Landsat imagery (figure 10-4) after close examination. Within Apalachicola Bay the numerous white ribbons of oyster reefs, which are readily distinguishable on the aerial photography (figure 10-8), cannot be readily observed on the Landsat imagery. Through close examination of Channel 5 (figure 10-4), several of the larger oyster reefs can be distinguished as lighter toned bright ribbons similar to that observed in the aerial photograph.

Since many of the water features on the aerial photographs are constantly changing (such as water fronts, boat wakes, and turbid water flow patterns), direct comparison of these features between the photographs and Landsat imagery is not possible. However, the general trends and patterns are similar and provide for interpretation of coastal processes through the correlation of Landsat imagery and aerial photography.

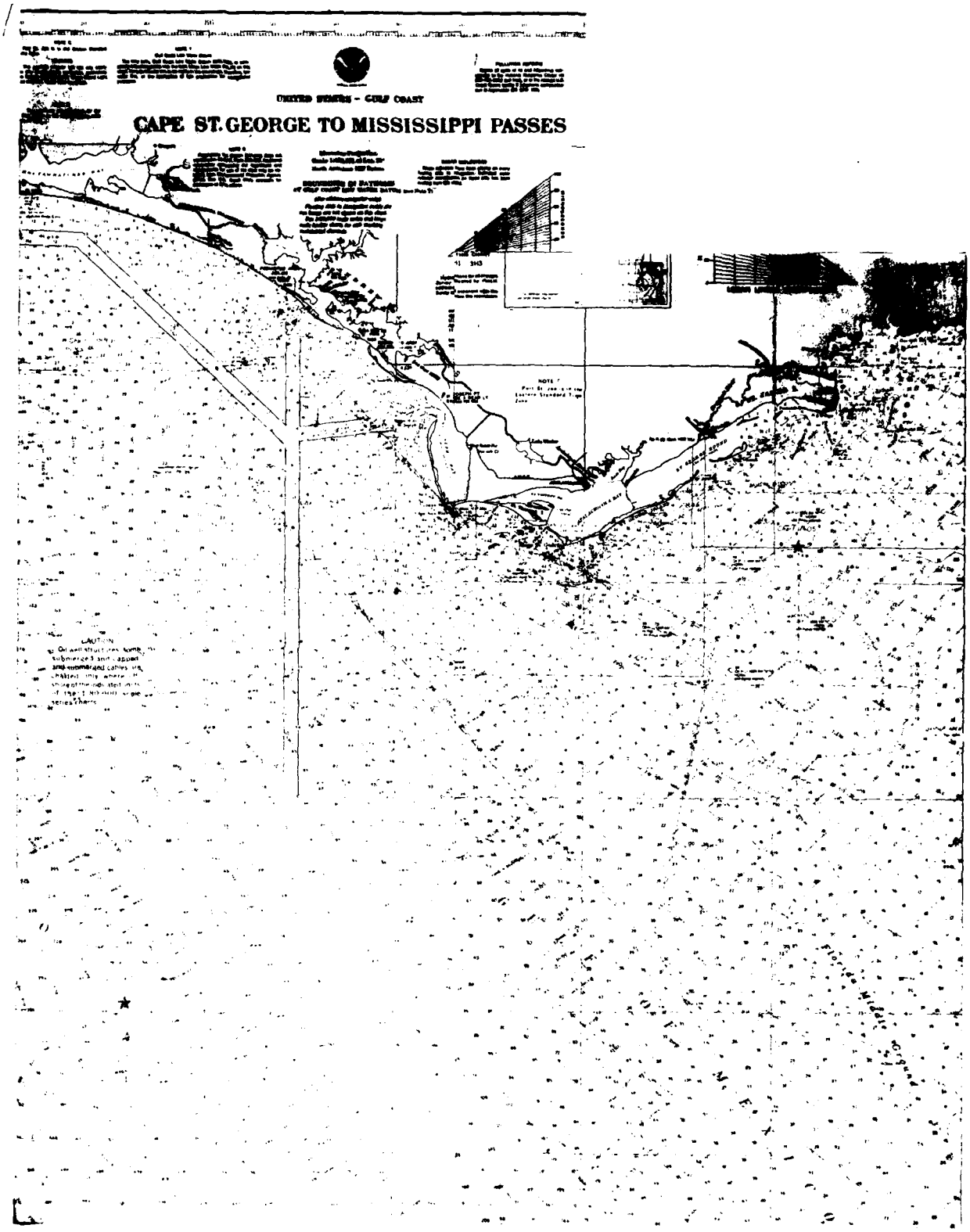

Figure 10-1. Hydrographic chart of Cape San Blas, FL (11360, 11340)

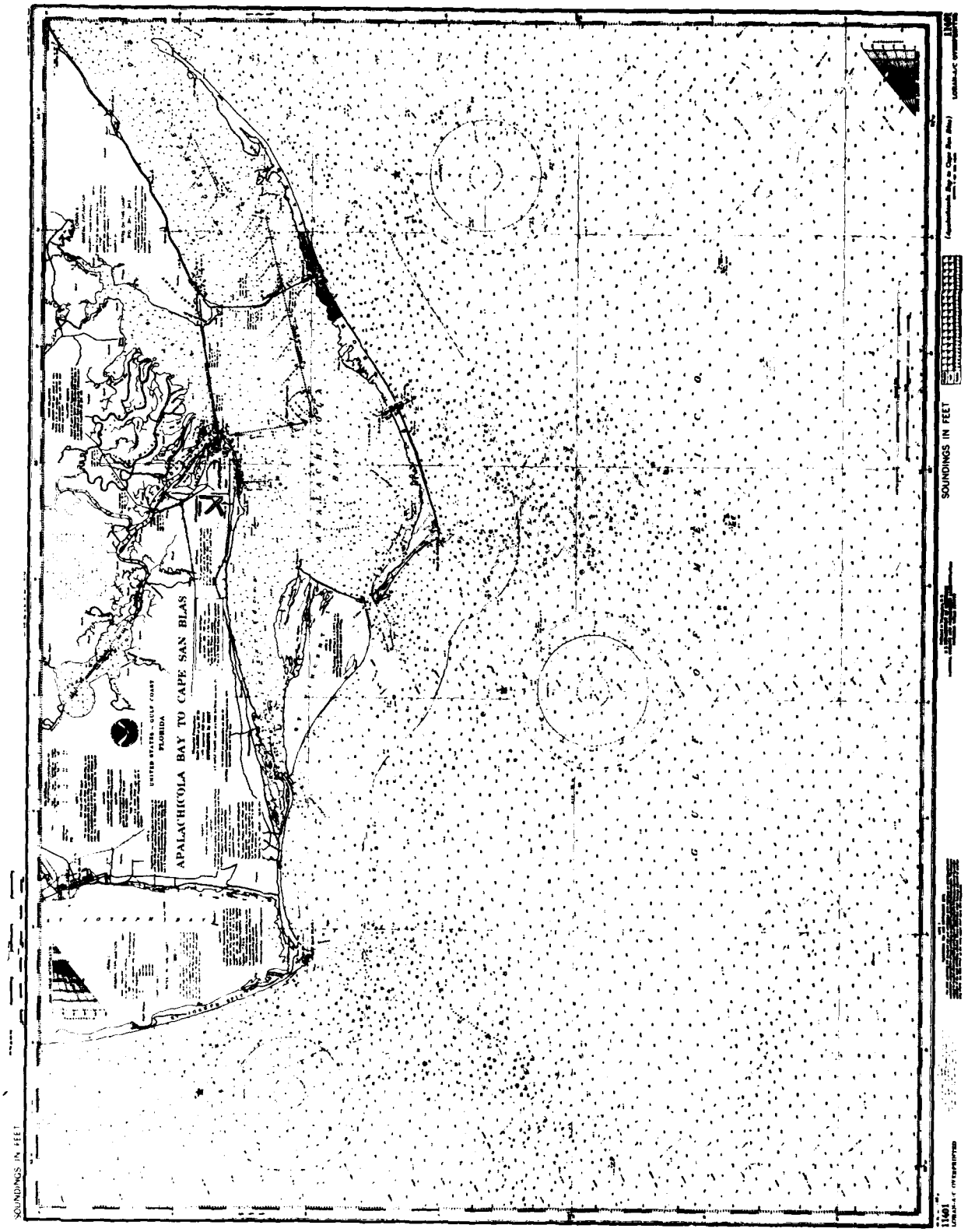

Figure 10-2. Hydrographic chart of Cape San Blas, FL (11401)

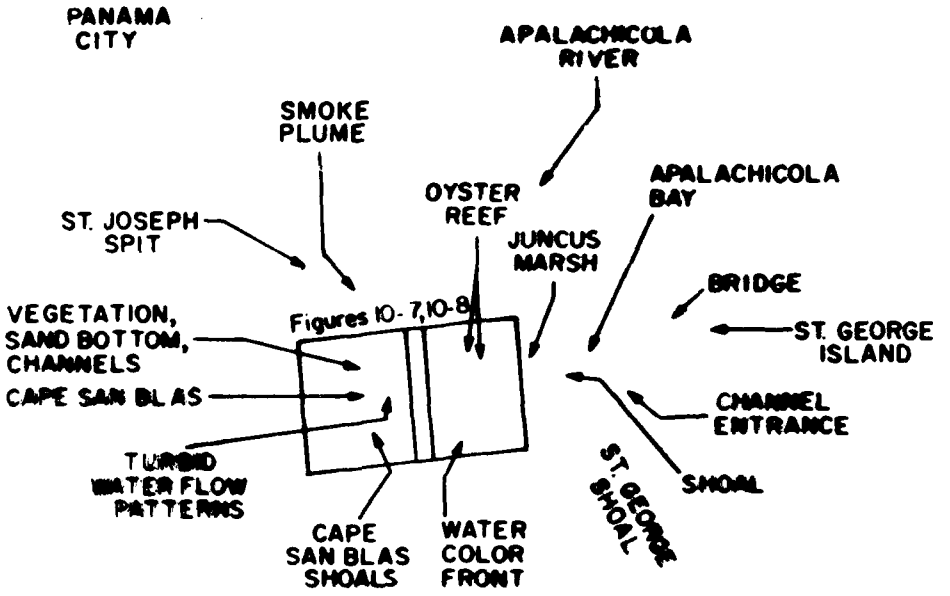

(LANDSAT) CAPE SAN BLAS 13 DEC 78

Figure 10-3. Landsat image, Cape San Blas, FL (13 Dec 78)

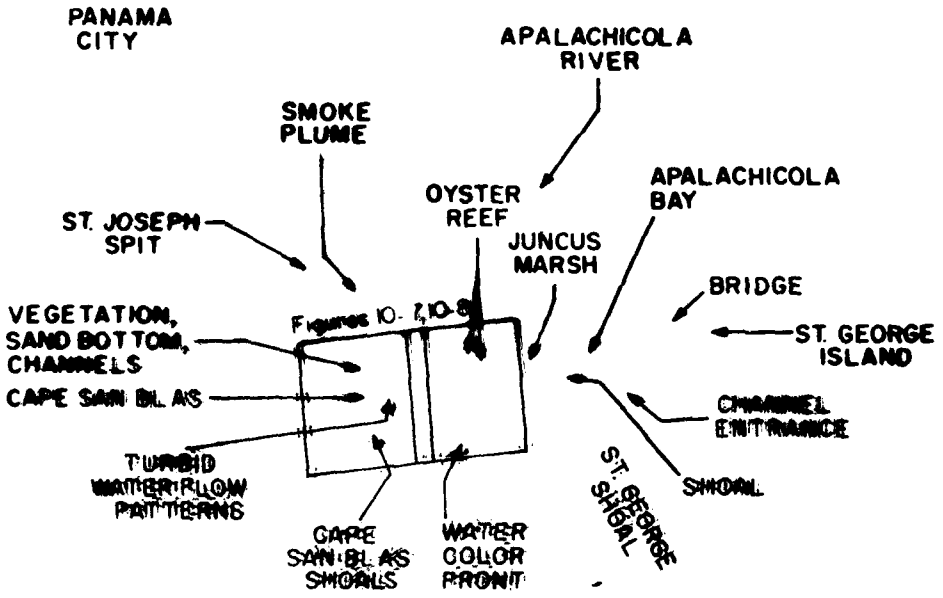

(LANDSAT) CAPE SAN BLAS 13 DEC 78

Figure 10-4. Landsat image, Cape San Blas, FL (13 Dec 78)

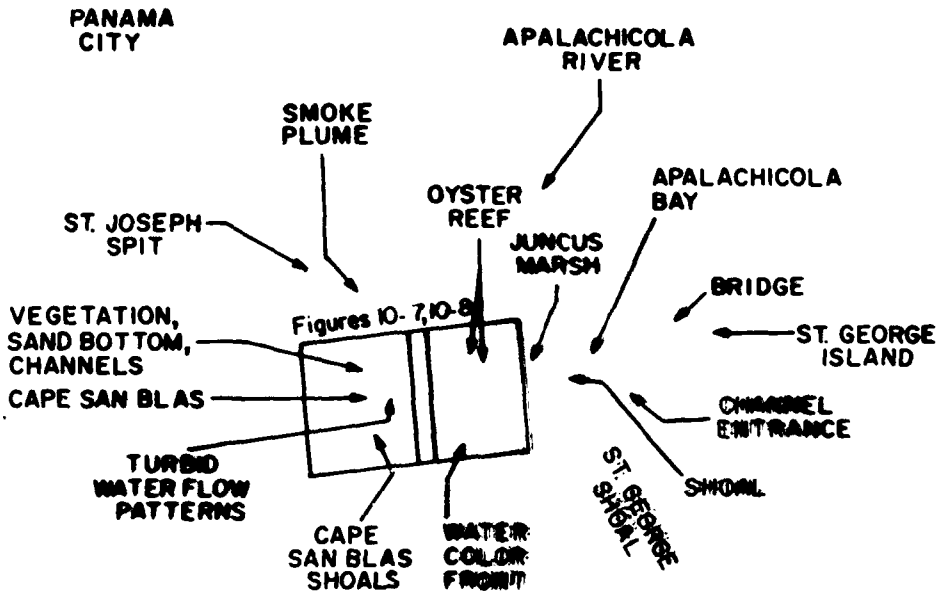

(LANDSAT) CAPE SAN BLAS 13 DEC 78

Figure 10-5. Landsat image, Cape San Blas, FL (13 Dec 78)

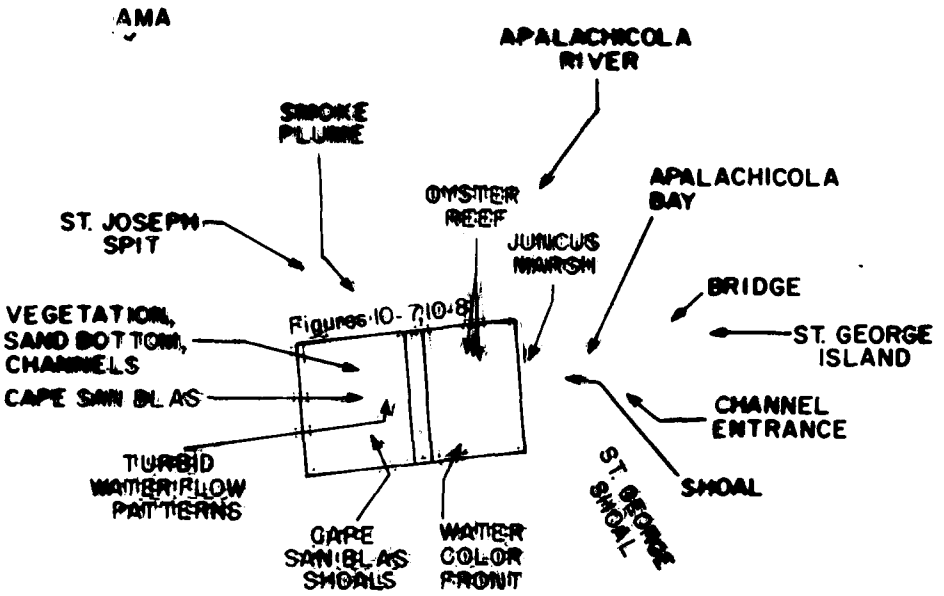

(LANDSAT) CAPE SAN BLAS 13 DEC 78

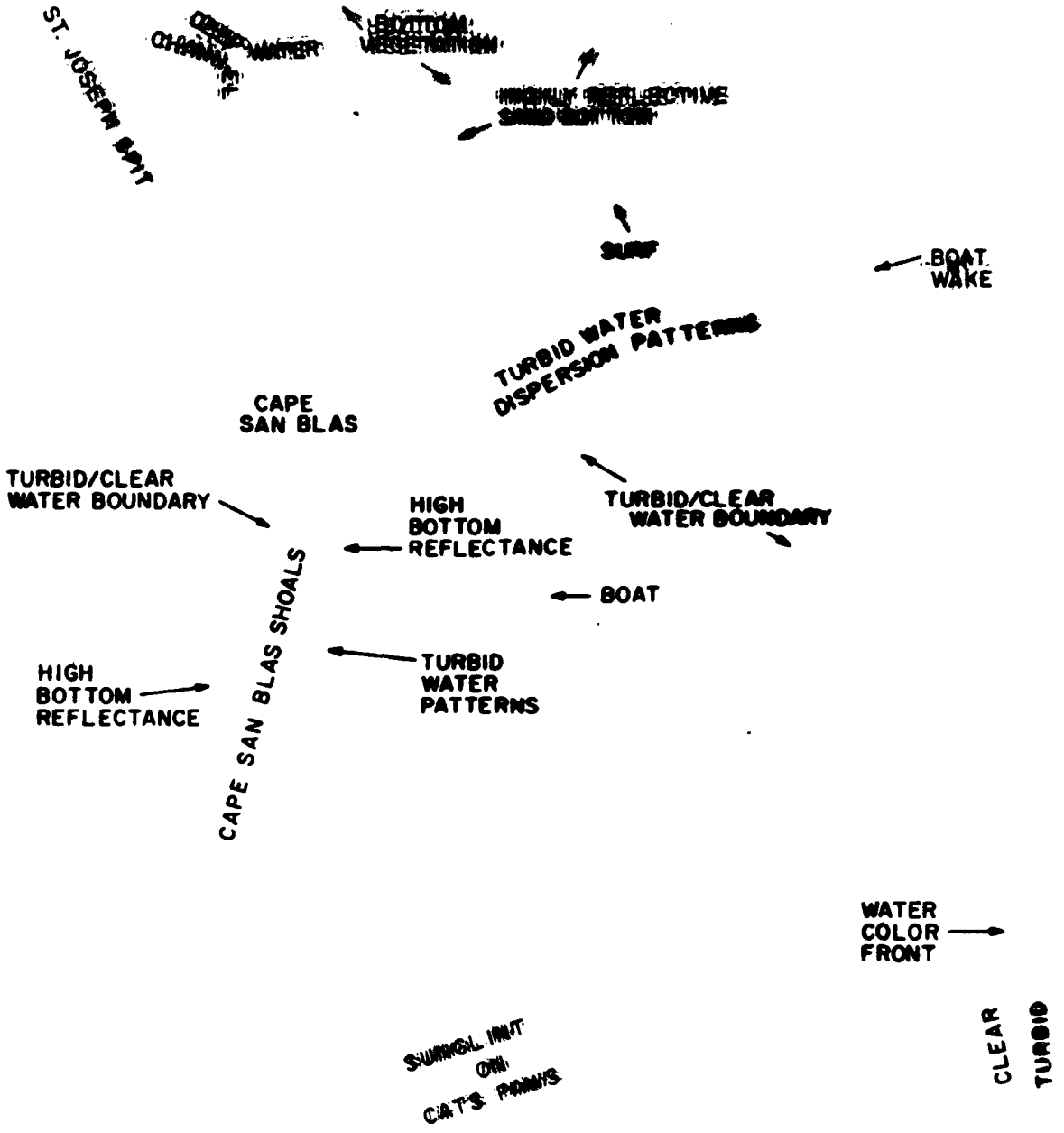

(AERIAL PHOTOGRAPHY) CAPE SAN BLAS
15 NOV 79

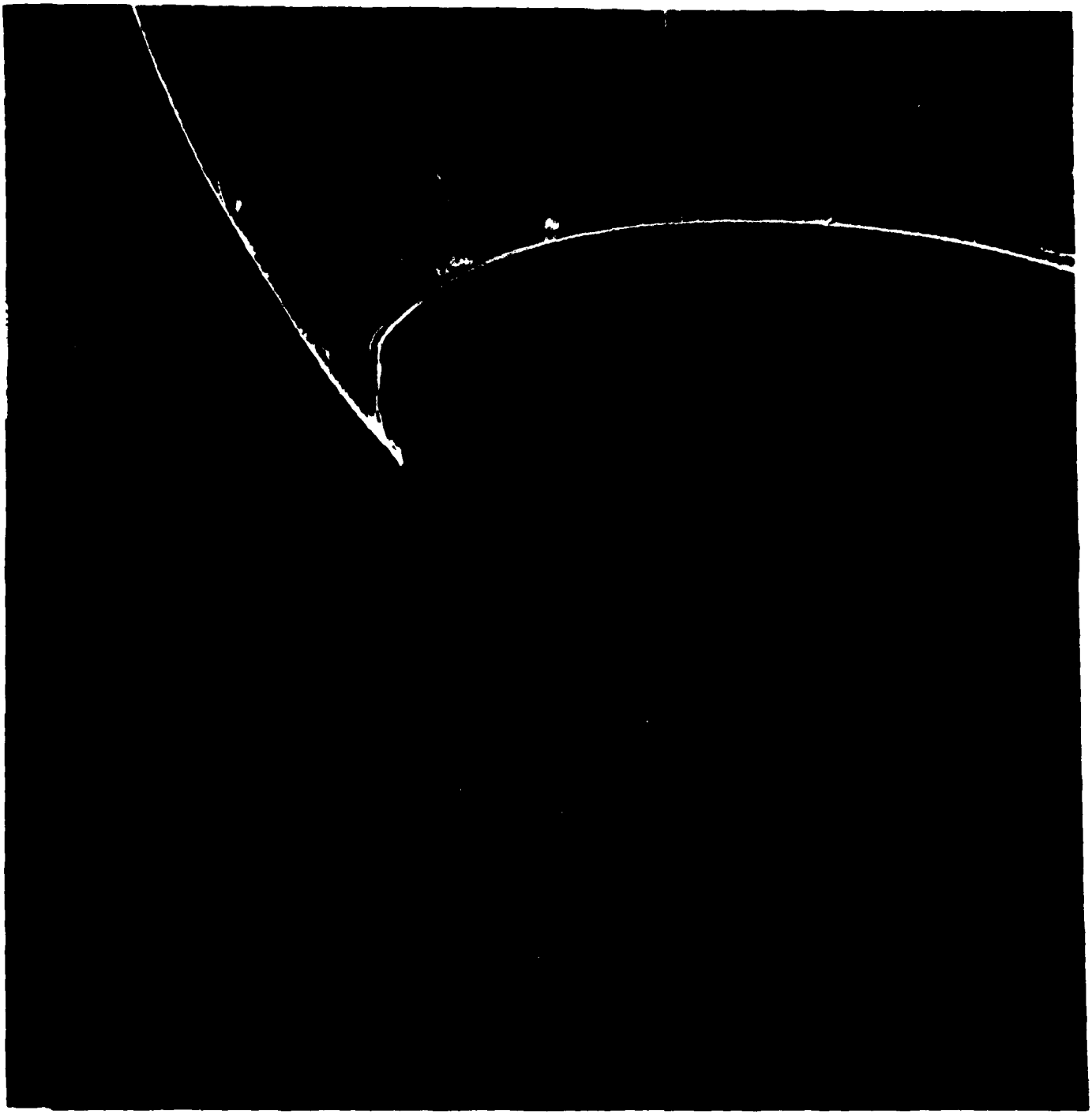

Figure 10-7. Color IR aerial photograph (1:135,000), Cape San Blas, FL (15 Nov 79)

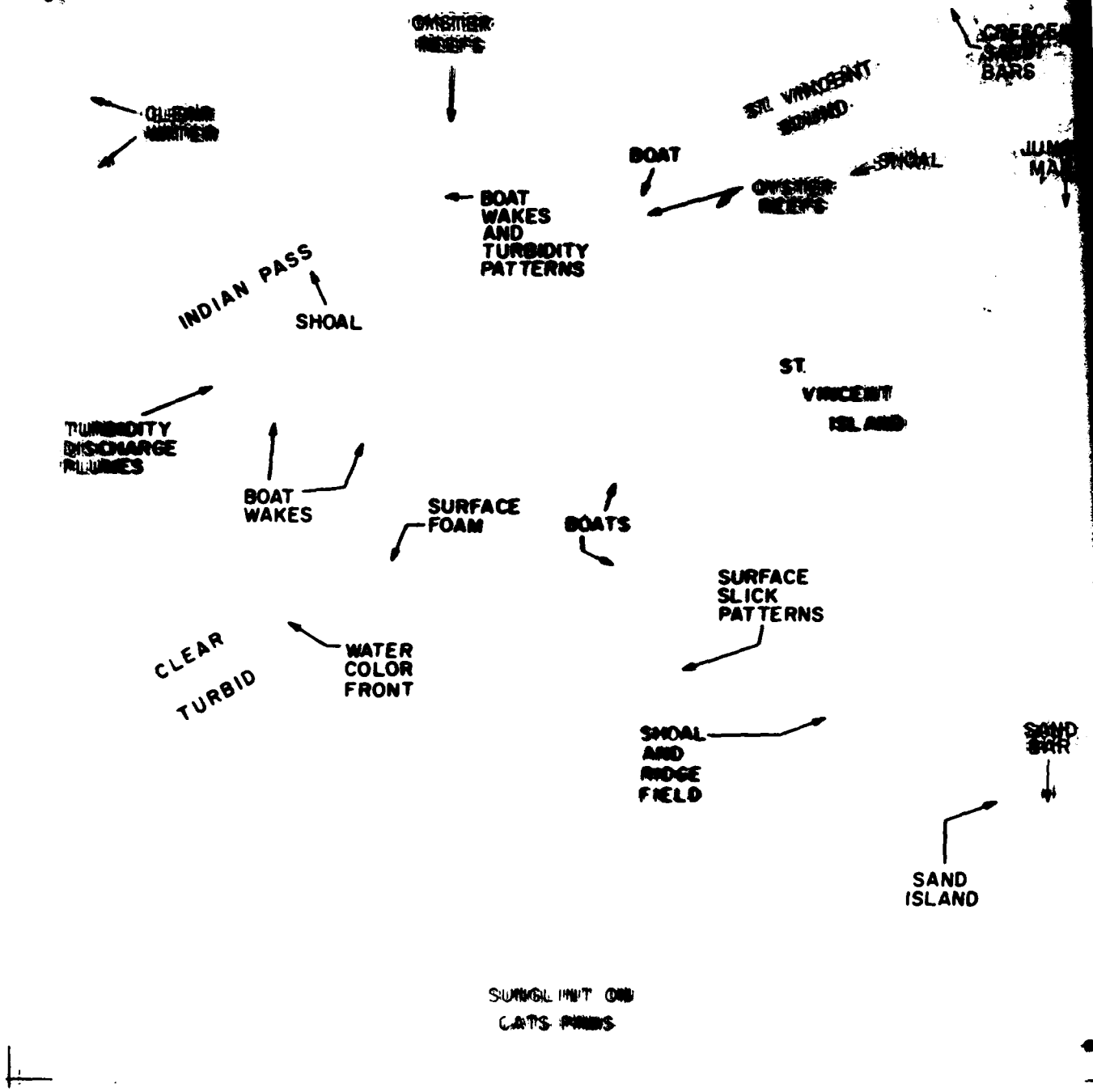

(AERIAL PHOTOGRAPHY) ST. VINCENT ISLAND
15 NOV 79

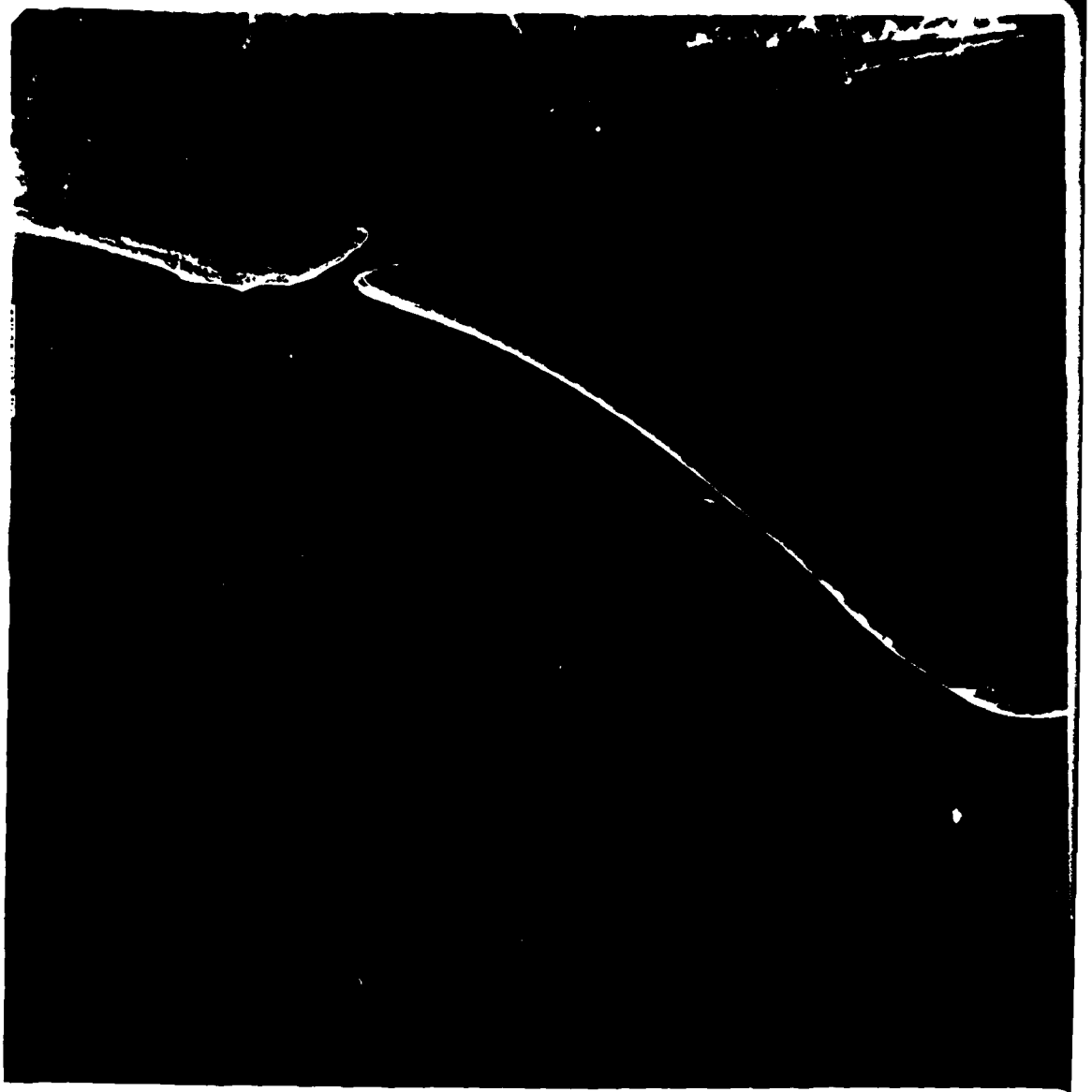

Figure 10-8. Color IR aerial photograph (1:135,000), Apalachicola Bay, FL (15 Nov 79)

V. FUTURE CONSIDERATIONS

V. Future Considerations

Landsat imagery has been shown to provide useful data for updating hydrographic charts. This report was directed toward interpretation techniques of the bulk-processed imagery as received from EROS Data Center. Use of enhancement techniques were only mentioned and were not fully demonstrated as to improving Landsat's exploitation for hydrographic charting.

Several simple techniques in photographic proccessing of the Landsat image, which were used to enhance the appearance of hydrographic features, demonstrate how to appreciably aid in interpretation. Instrumentation is available at the EROS data facilities (and commercially) to increase contrast, magnify and simultaneously superimpose different channels of Landsat scenes. These facilities and techniques have not been demonstrated in this report, yet the analyst should become familiar with these instruments which can aid him in interpretation.

Transfer scopes used to superimpose hydrographic charts on Landsat imagery provide an expedient technique for revising hydrographic charts by rapidly comparing temporal changes in hydrographic features. However, loss of contrast and resolution also occur and make it difficult to fully exploit Landsat imagery.

In many of these techniques, however, the analyst is dependent on the quality of the film original. In order for optimum enhancement, optimum exploitation of the multispectral data, and comparison of temporal variability, the imagery is best exploited by computer analyses of the digital MSS data.

Computer processing for image enhancement is a rapidly advancing technology. Various filter techniques minimize scan line noise and increase the quality of the imagery. Other computer processing techniques/algorithms, such as atmospheric corrections, cloud removal, correction of geometric distortion, magnification and contrast stretching, will increase the use of Landsat in interpretation of hydrographic features and processes. Computer processing of the digital data also permits determination of temporal variability. The original values of the digital data can be directly compared as opposed to the variable film densities inherent in photographic products. The methodology for rapid and efficient computer enhancement techniques for relating hydrographic charts and MSS Landsat imagery has not been established. Future considerations should address this requirement, since this method would optimumly exploit Landsat (and other remotely sensed data) for interpretation and applications to hydrographic charting. It should also be noted that additional remotely sensed data used in conjunction with Landsat greatly improves the value of the hydrographic interpretation. The use of multisensor data for hydrographic charting provides a greater data base for interpretation, and therefore increases the reliability and the accuracy of interpretation.

As evidenced by analyses of the ten case histories, the analyst will grow to rely on experience for a large percentage of his interpretation ability. As the analyst becomes more familiar with specific regimes of the world, he also will understand better the local coastal and near-shore processes, thus be able to provide experienced interpretation of hydrographic features more reliably and rapidly. This capability will promote rapid updating of hydrographic charts.

VI. REFERENCES

VI. References

[1] Avery, T. E. (1977). Interpretation of Aerial Photographs, Burgess Publishing Co., Minneapolis, MN.

[2] El-Ashry, M. T. (1977). Air Photography and Coastal Problems. Benchmark Papers in Geology 38, Dowden, Hutchinson and Ross, Inc., Stroudsburg, Penn.

[3] Gibbs, R. S. (1974). Interpretation of Aerial Photographs. Burgess Publishing Co., Minneapolis, MN.

[4] Holz, R. L. (1973). Surveillant Science, Remote Sensing of the Environment, Houghton Miffin Co., Boston, MA.

[5] Jerlov, N. G. (1976). Marine Optics. Elsevier Oceanography Series No. 5, Elsevier Scientific Publishing Co., New York, NY

[6] Jerlov, N. G. and E. S. Nielsen (1974). Optical Aspects of Oceanography, Academic Press, New York, NY.

[7] LARS (1976). Remote Sensing Technology and Applications Short Course Notes, Purdue University, Laboratory for Applications of Remote Sensing.

[8] Lillesand, T. M. and R. W. Kiefer (1979). Remote Sensing and Image Interpretation. John Wiley and Sons, N.Y., NY.

[9] Porter, R. W. (1977). The Versatile Satellite. Oxford University Press, Oxford.

[10] Reeves, R. G. (1975). Manual of Remote Sensing, V. I and II. American Society of Photogrammetry, Falls Church, VA.

[11] Sabins, F., Jr. (1978). Remote Sensing Principles and Interpretation. W. H. Freeman and Co., San Francisco, CA.

[12] Short, N. M., P. D. Lowman, S. C. Freden, and W. A. Finch (1976). Mission To Earth. Landsat Views the World NASA-SP-360, Englewood Cliffs, NJ

[13] Sverdrup, H. U., M. W. Johnson, and R. H. Fleming (1942). The Oceans. Prentice Hall, Inc.

[14] U.S. Geological Survey (1979). Landsat Data Users Handbook.

[15] Williams, R. S., Jr., and W. D. Carter (1976). ERTS-1 A New Window on Our Planet. Geological Survey Professional Paper 929, U. S. Govt. Print. Off., Washington, DC.

APPENDIX A.

Appendix A. Ocean Waves

A. Some General Characteristics of Waves

Assuming that the waves on the sea surface are simple sine waves (in vertical section), some terms that we will use are illustrated in Figure A1. The quantity (H), called the height of a wave (the vertical distance from trough to crest), is twice what the physicist calls the "amplitude" (A) of the vertical oscillatory motion of the surface (the maximum displacement above or below the mean water level). For all waves, the speed C = L/T, where L is the wavelength (distance from crest to crest or trough to trough) and T is the period (time between successive crest to pass a fixed point); the height H is basically independent of C, L or T.

For convenience in referring to surface waves, it is common to classify them according to their periods, as shown in Table A.1.

In all these surface waves, gravity is the primary restoring force allowing oscillations to occur. If water is lifted up and allowed to fall back under action of gravity, its inertia will cause it to overshoot the equilibrium position; pressure forces will then push it back up and oscillations will occur.

Ripples or capillary waves (L < 5 cm) are affected mainly by surface tension, and the effects of gravity are minimal. Ripples can be generated by wind blowing over the sea surface or by instabilities in wave slopes of larger wind waves. Because of the importance of surface tension, the position and generation of capillary waves is dependent on sea surface distribution of surface tension. This variability is complex and will not be covered in detail in this text (see Neuman and Pierson, 1966).

When capillary waves interact with longer period gravity waves, the capillary waves appear to be concentrated in the forward face of the gravity wave just before the crest. Longuet-Higgins (1963), through modeling the surface tension on surface waves, has shown reason for this occurrence. Ripples

Table A.1 Waves classified by period (after Pond et al., 1978)

Period	Wavelength	Name
0-0.2 s	Centimeters	Ripples
0.2 - 9 s	To about 130 m	Wind waves
9 - 15 s	Hundreds of meters	Swell
15 - 30 s	Many hundreds of meters	Long swell or forerunners
0.5 min - hours	To thousands of km	Long period wave including Tsunamis
12.5, 25 hours, etc.	Thousands of km	Tides

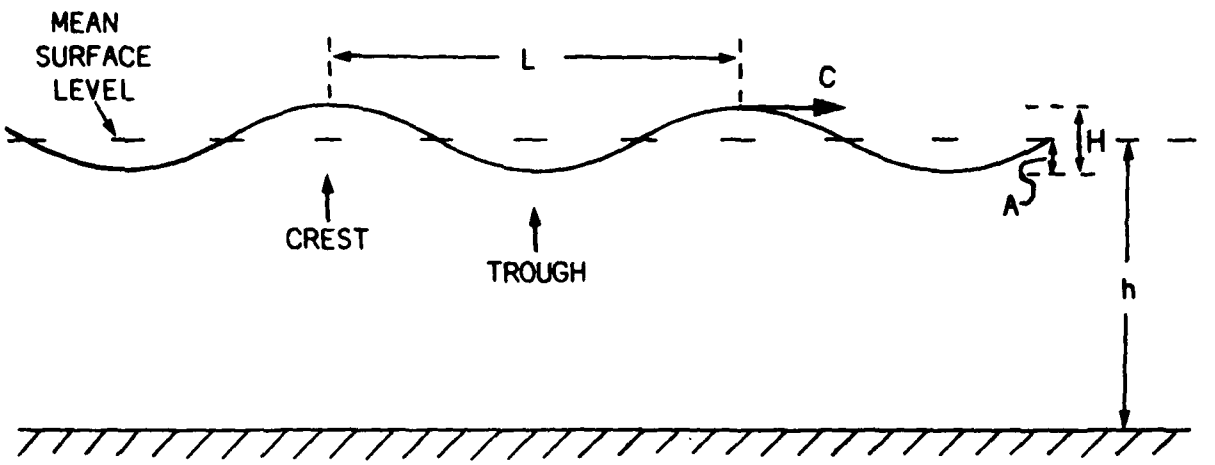

L - WAVELENGTH
T - PERIOD (TIME BETWEEN SUCCESSIVE CRESTS PASSING A FIXED POINT
C - SPEED (CELERITY) RELATIVE TO WATER (C = L/T)
H - WAVE HEIGHT = 2 x AMPLITUDE (A)
h - DEPTH OF WATER BELOW MEAN SURFACE LEVEL

N.B. In this figure, H is exaggerated relative to L for clarity.

Figure A1. Terms related to ideal (sine) waves. (Pond et al., 1978)

are important to remote sensing of the sea surface because they act as multi-facets which reflect sun and skylight. Further explanation of the reflectance properties of ripples will be explained in Appendix B, Sunglint.

The ranges of periods of wind waves and swell actually overlap considerably; wind waves may have periods up to 15 seconds or so if the wind speed is very large, while swell with periods of only a few seconds is possible. Wind waves are the locally generated waves. Since they have a fairly wide range of directions, the sea surface can be quite irregular. Swell is the term for waves which have been generated elsewhere; it travels in one direction and is much more regular. Also, as we shall show, longer waves travel faster than shorter ones; therefore, at some distance from the source area, at any one time, the swell has a narrow range of periods, which also makes it more regular than wind waves.

Wavelength, period, and velocity are directly related: the longer the period the longer the wave, and the longer the wave the greater its velocity. Since wave height has no relationship to either wavelength, period or velocity, the period and height comprise the description of a wave. Figure A2 illustrates the relationships of wavelength, velocity and period.

In a low-height, deep-water wave the water particles' motion approximates a circle (See figure A3). Particles complete one revolution of the circle in the time corresponding to the period of the wave. A water particle at the surface remains at the surface throughout its orbit. The movement of the water particles is greatest at the surface and is minimal at depth. Figure A3 illustrates the particle motion and the progressive direction of wave motion.

Waves of very small height are those for which the ratio of height to length is 1/100 or less. The simplest wave theory deals with such waves, the form of which can be represented by a sine curve. In water of constant depth h, such waves travel with the speed:

$$C = \left(g \frac{L}{2\pi} \tanh 2\pi \frac{h}{L} \right)^{1/2} \qquad (1)$$

where g is the acceleration of gravity and L is the wavelength.

If h/L is large (> 1/2), that is, if the wavelength is small compared to the depth, tanh $2\pi h/L$ approaches 1 and

$$C_d = \left(g \frac{L}{2} \right)^{1/2} \qquad (2)$$

is obtained. These waves are called deep-water waves.

If h/L is small (< 1/25), that is, if the wavelength is large compared to the depth, tanh $2\pi h/L$ approaches $2\pi h/L$ and one obtains:

$$C_s = (gh)^{1/2} \qquad (3)$$

These waves are called shallow-water waves.

In general, waves have the character of deep-water waves when the depth to the bottom is greater than one-half the wavelength (h > 1/2). However, for shallow-water waves the depth must be less than one twenty-fifth of the wave length (h < 1/25). At intermediate depths equation 1 must be used (NOO Pub 604).

Figure A4 shows plots of equation 1 wave speed (C) versus water depth (h) for a selection of wavelengths from 10 m to 10 km. The left-hand (straight) line is the plot of $C_S = (gh)^{1/2}$ (shallow-water wave speed). Then the line for L = 200 m (for example) shows that the speed follows the shallow water line up to about 10 m water depth (h = 1/20) where it commences to curve to lower values, eventually reaching its constant value of $C_d = 17.7\ ms^{-1}$ at about 100 m water depth (h = 1/2). The zone on the graph to the right of the dashed line

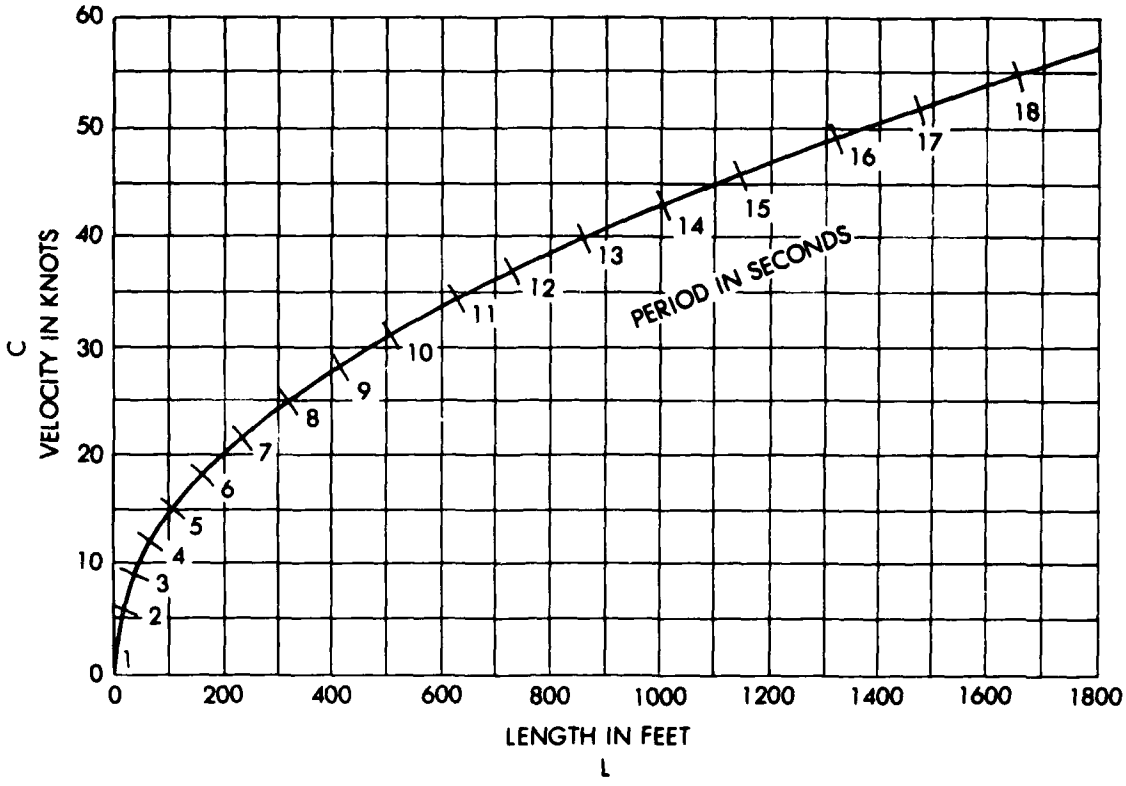

Figure A2. Graphic representation of the theoretical relationship between wave lengths, velocities and period in deep water. A working rule is that the period (in seconds) multiplied by three gives the velocity in knots. The length is approximately equal to the period multiplied by 5.12. Wave velocity is equal to the length divided by the period. (After Bigelow and Edmundson)

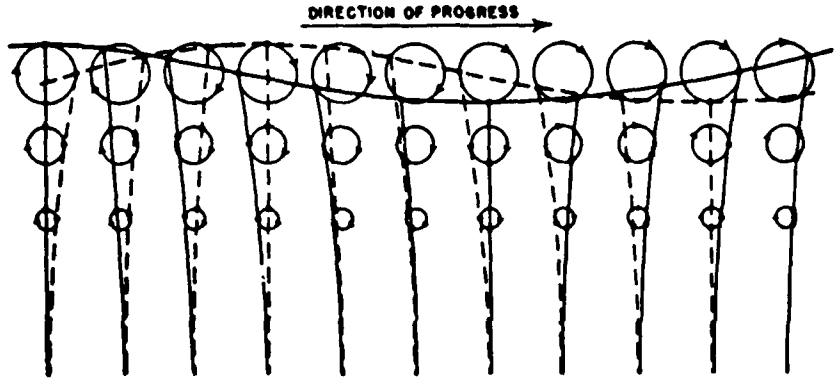

Figure A3. Movement of water particles in a deep-water wave of very small h
The circles show the paths in which the water particles move. T
wave profiles and the positions of a series of water particles a
shown at two instants which are one-fourth of a period apart. T
solid, nearly vertical lines indicate the relative positions of
particles which lie exactly on vertical lines when the crest or
of the wave passes and the dashed lines show the relative posit
of the same particles one-fourth of a period later. (HO PUB 60

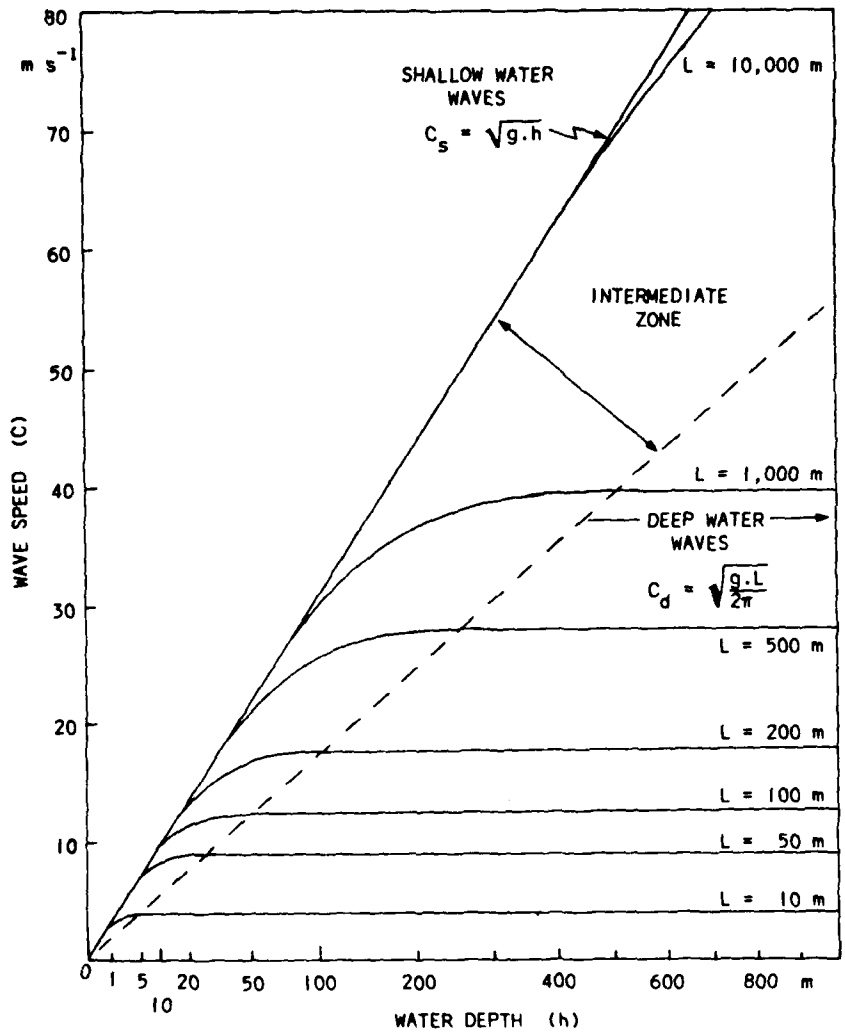

Figure A4. Wave speed versus water depth for various wavelengths, (L). (Pond et al., 1978)

is where the deep-water speed approximation holds, and the intermediate zone between the shallow-water speed line and the dashed line is where the full expression of equation 1 must be used to calculate the speed. In practice, the shallow and deep water approximations find most use; the intermediate zone applies chiefly in studies of the surf zone (Pond et al., 1978).

Notice that the speed of deep-water waves depends on their wavelength and thus on their period, i.e., they are dispersive waves. This term refers to separation in speed along their direction of travel, and not to separation in direction, although it also occurs. The speed of the longer deep-water waves is greater than that of the shorter ones. Therefore, if a number of waves of different wavelengths (a spectrum of wavelengths) are generated simultaneously, the longer ones will move ahead of the shorter ones and be observed first at a distant point (hence the term "forerunners" for the longer period, i.e., longer wavelength, waves generated by the wind). Also, shorter waves tend to lose their energy by frictional effects somewhat faster and die out sooner than longer ones, and therefore do not travel as far (Pond et al., 1978).

A consequence of this dispersion is that by observing the swell for a few days at one location, it is often possible to determine how far away the storm was that generated the waves. If the spectrum of swell periods is determined at intervals of a few hours at the wave recording station (in relatively deep water), it will be observed that the mean period decreases steadily with time. Because the speed of travel of deep-water waves is proportional to their period, the difference between the times of arrival of the longer period (early arrival) and the shorter period (late arrival) swell is due to their different speeds. It is then possible to calculate the distance the swell must have traveled from the observed time separation at the wave station. The reader should note that in practice the wave records will provide information about mean periods for groups of waves, not waves of a single period, and the calculation is a little more complicated than might appear at first sight. For a group of waves it is necessary to use the "group speed," C_g, not the "phase speed" (which was discussed previously as C_d and C_s). For deep-water waves, it can be shown that the group speed is one-half the phase speed ($C_g = C_d/2$), while for shallow-water waves it is the same as the phase speed ($C_g = C_s$) (Pond et al., 1978).

The observations give only the distance to the point of generation, not the direction; but if observations are available at two separate wave stations for the same generation event, then the intersection of the two radial distances from the stations will indicate the location of generation (Pond et al., 1978).

B. The Generation of Waves

Wind waves are started by a wind blowing for some hours duration over a sea surface many miles long (called a "fetch"). Fitful gusts of wind generate a choppy and irregular sea. These oscillations, once reaching a specific size, continue to run across the surface of the sea far beyond the direct influence of the wind. Under these conditions they are called swell. Swell consists of uniform wave trains with a broad sideways extent of the individual crests. Swell can be characterized by numerically measuring the height and period of the wave. Because longer wavelength waves travel faster than the smaller wavelength waves, as the distance from the wind field increases so does the wave period. Similarly, energy within the waves decays and dissipates with increasing distance from where it was created and this results in a corresponding decrease in waveheight. As the swell enters shallow water it touches bottom and a rejuvenation takes place. The wave speed and length decrease and the height increases, but the period remains constant. The swell

information on the generation of waves, see the references listed at the end of this appendix.

The interaction of wind speed, fetch, and waves is illustrated in Figures A5 and A6. Figure A5 illustrates typical oceanographic nomenclature as it applies to forecasting wave conditions. Figure A6 is a useful chart for forecasting the "significant wave height" with the wind speed and fetch over the sea surface as input. Because of the variety of heights present in most real wave conditions, it is common to quote the mean height of the highest one-third of the waves (i.e., "significant wave height").

C. Refraction in Shallow Water

All shallow water waves travel at the same speed, $C_S = (gh)^{1/2}$, in water of a given depth, (h), and therefore do not show dispersion of speed; but where the bottom depth is changing, their direction of travel may change. More generally, as waves move into shallow water, their period remains constant, but C decreases and, therefore, L decreases. As an example, Table A.2 shows the decrease in speed and wavelength for waves of an 8-second period on entering shoaling water.

Hence, if a series of parallel crested waves approach at an angle to a straight shoreline (Figure A7) over a smooth sea bottom that shoals gradually, they progressively change direction as the end of the wave nearer the shore (A in Figure A7) slows down earlier than that farther away (B in Figure A7). As a result, the waves become nearly parallel to the shore by the time that they pile up as surf. The change of direction associated with change of speed is called refraction. The same phenomenon of refraction occurs abruptly to light waves traveling from air to water. Similarly, gradual refraction occurs for light waves coming from the sun and entering the upper atmosphere at an angle to the vertical.

If the sea bottom does not have a uniform slope along the full length of the shore, the refraction may be more complicated. Two examples are where an underwater ridge is running out at right angles to the shore, and an underwater valley. The refraction pattern for waves coming straight in from offshore would then be as that shown in Figure A8. In this figure the wave crests are not shown; instead the wave orthogonals which indicate the direction of travel of the waves, as do the arrows in Figure A7 (Pond et al., 1978) are shown.

Refraction of waves around a headland, for instance, occurs if the water deepens gradually to seaward from the land, but not if the water is of relatively uniform depth off the headland. Wave are often observed to be refracted around islands, and one can sometimes see an interference pattern set up where the waves refracted around the two sides of a small island meet behind it. Similarly, submerged rocks or navigational obstructions will produce refraction patterns.

Table A.2. Decrease in speed and wavelength in shoaling water for deep-water waves of period 8 seconds and length 100 meters (Pond et al., 1978)

h meters	C meters/sec	L meters
50+	12.5	100
10	8.9	71
5	6.6	53
2	4.3	35

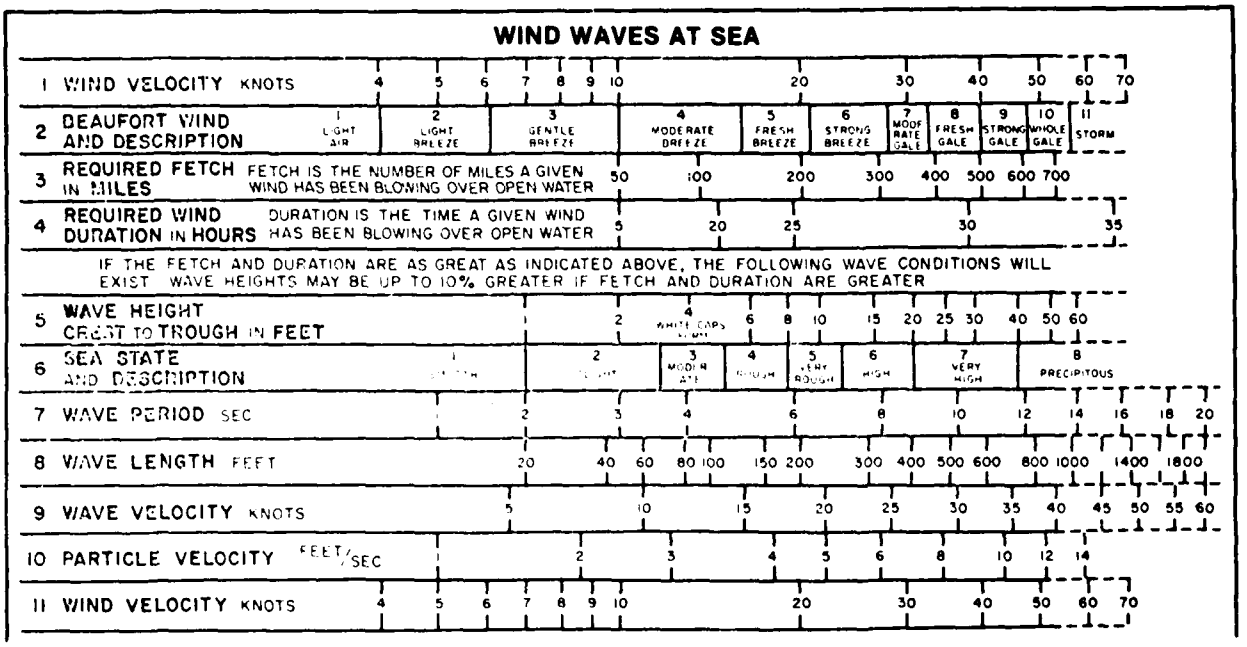

Figure A5. Wind waves at sea

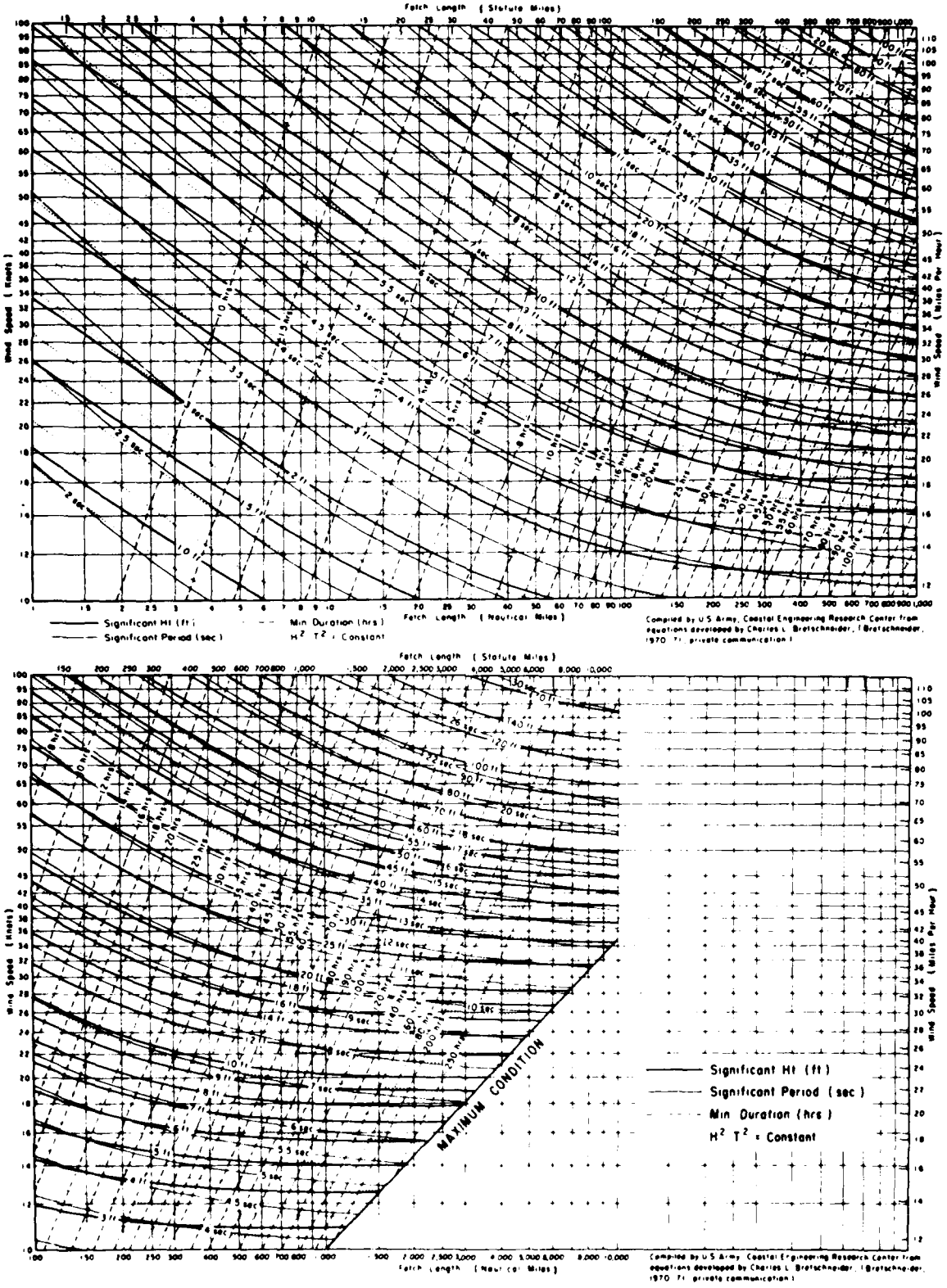

Figure A6. Deep-water wave-forecasting curves, based on Bretschneider (1959), relating the storm conditions to the generated significant wave height and period. (From Coastal Engineering Research Center, 1973)

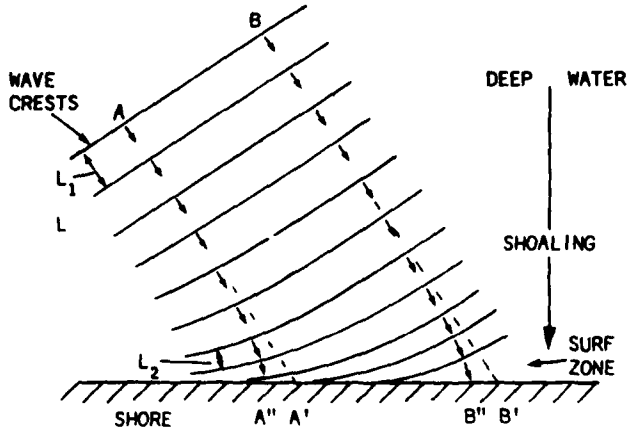

Figure A7. Refraction of waves approaching a smoothly shelving beach. (Pond et al., 1978)

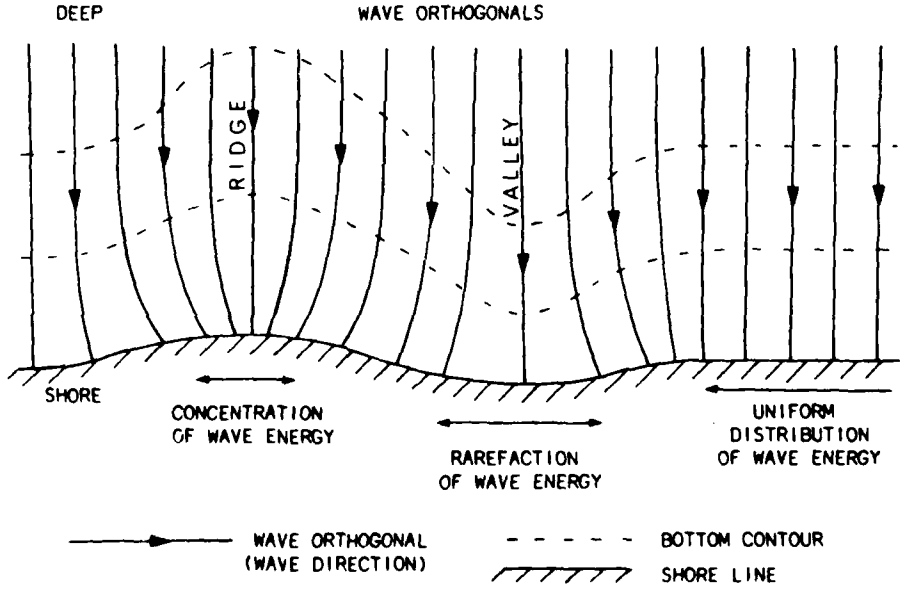

Figure A8. Wave refraction on approaching an underwater ridge (left) and a valley (center). Dashed lines represent depth contours, solid lines represent wave orthogonals (directions of travel of waves). (Pond et al., 1978)

The utility of wave refraction in interpreting bottom features is an important analysis technique for aerial and satellite images. The technique can be used for interpreting abrupt bottom features, such as a rock ledge or a more gently sloping bottom. Wave refraction patterns enable the interpreter to locate positions of channels in entrances to bays or shallow water. Examples of the techniques are best shown in aerial photography, although Landsat does illustrate refraction patterns of extremely long period waves.

D. Breaking Waves

When waves reach the beach and enter water approximately as deep as the waves are high, they break; the crest throws itself forward or disintegrates into bubbles and foam. A common notion is that waves break because they drag on the bottom until they trip and the crest topples forward. This assumption is incorrect; experiments have shown friction to be negligible. Instead, a wave breaks because it becomes overly steep, especially near the wave crest peak, and because the velocity of water particle motion in the crest exceeds the phase velocity of the wave form and, so, surges ahead.

As a swell approaches a beach, the subtle effects of a shoaling bottom become suddenly exaggerated. Wavelength and velocity rapidly decrease as wave steepness increases. At a depth of about twice the offshore height, the crest suddenly peaks, which further increases wave steepness and instability. Finally, at an average depth of 1.3 times the wave height, the amount of water in the trough becomes insufficient to support the crest. The result is surf.

If the waves are initially long (e.g., tsunamis), $C_g = C_s$, the speed decreases and the height increases as shoaling occurs. However, if the waves are initially short, at first C_g increases as shoaling occurs and reaches a maximum value of 1.2 times the deep-water speed. This occurs when $h/L \simeq 0.19$, where L is the local value, not the deep-water value. In this zone, when C_g is maximum, wave height, H, decreases to a minimum of about 90% of the deep-water wave height. The wave steepness (H/L) is mainly constant at first, but begins to increase before $h/L \simeq 0.19$ because L decreases faster than H. At $h/L = 0.19$ the steepness (H/L) is about 10% greater than the deep-water value of steepness. As the waves move further inshore C_g decreases; therefore, H must increase. However, the decrease in L dominates H/L changes. In the example given in Table A.2, when h = 2 m, L is about 35% of the deep-water value, but the increase in H is only about 25%. For initially long waves, L decreases proportionally to $C_s = (gh)^{1/2}$, while H increases proportionally to $(C_s)^{-1/2}$. There is a limit to how much H/L may increase. Theory puts this limit at $H/L = 1/7$, but in practice it is rare for waves to get steeper than H/L 1/12. When the wave steepness approaches this limit the waves tend to change from a symmetrical sine shape (figure A9a) to a more peaked shape (figure A9b) and, finally, as $H/L \simeq$ approaches 1/12 the waves become unstable and break as surf (figure A9c). In shallow water, breaking does not usually occur until the wave height is comparable to the water depth or until $H/L \simeq 1/12$, whichever occurs first (Pond et al., 1987).

Three types of breakers are commonly recognized: spilling, plunging, and surging (figure 10). In spilling breakers the wave gradually peaks until the crest becomes unstable and cascades down as "white water" (bubbles and foam). In plunging breakers the shoreward face of the wave becomes vertical, curls over, and plunges downward as an intact mass of water. Surging breakers peak as if to plunge, but then the base of the wave surges up the beach face so that the crest collapses and disappears. A continuum of breaker types actually grades from one type to the next, so that application of these classifications is not always easy. In general, spilling breakers tend to occur on beaches of very low slope with waves of high steepness values;

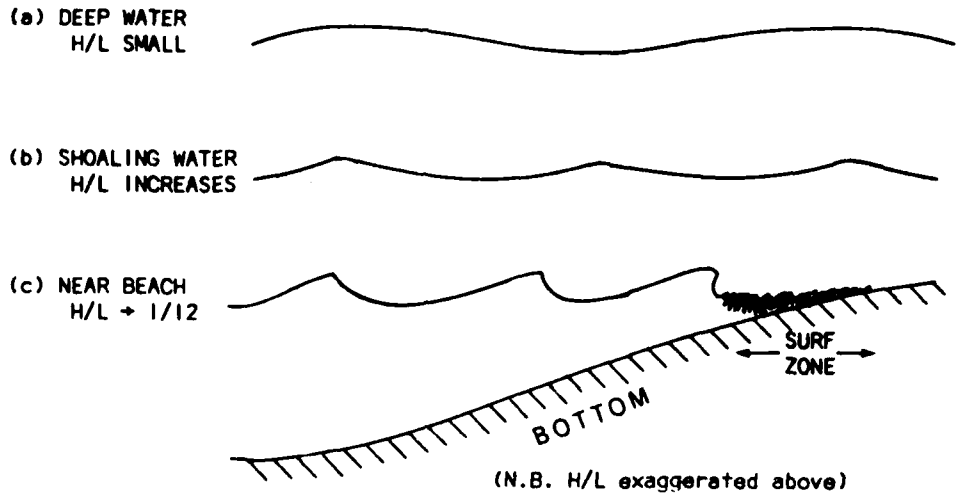

Figure A9. Shape of waves. (a) in deep water, (b) in shoaling water, (c) close to beach. (Pond et al., 1978)

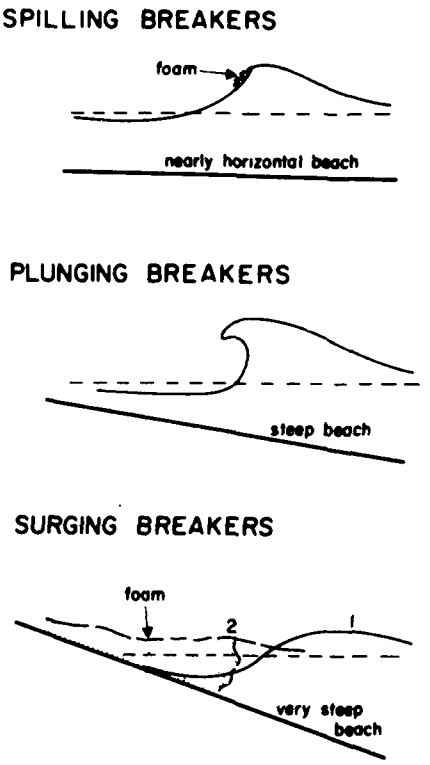

Figure A10. The three types of breaking waves that occur at the beach. (Komar, 1976)

plunging waves are associated with steeper beaches and waves of intermediate steepness; surging occurs on high-gradient beaches with waves of low steepness (Komar, 1976).

In the open ocean, waves can break without the effects of the bottom. Whitecapping is thought to be the major sink for wave energy at work in the deep ocean. Whitecapping occurs when the wave slope near the crest of a wave exceeds a critical angle of 30°. This "peaking" is due to the superposition of wave trains moving at different phase speeds and/or directions. The percentage of the ocean surface covered by foam at any one time ranges from 1% at a wind velocity of 16 knots to about 7% for wind speeds of 35 knots or greater. The threshold wind velocity for whitecap production is about 14 knots. Within 400 km of a lee shore the whitecap coverage becomes fetch-dependent.

E. Internal Waves in the Ocean (taken from Fett et al., 1979)

Internal waves are a wave phenomenon in the ocean that form between subsurface water layers of varying density; the density differences may be due to either temperature or salinity, or both. In the open ocean, internal waves are frequently found along the main thermocline (i.e., in the layer of strong vertical temperature gradient below the surface mixed layer). Recently, surface wave manifestations of internal waves have been observed in satellite imagery, notably in sunglint areas under calm wind and sea conditions (Apel and Charnell, 1974; Fett and Rabe, 1977). Internal waves can have a disruptive influence on underwater sound propagation and, as a result, they are an oceanic phenomeon which must be identified, located, and interpreted for effects on naval undersea operations.

Internal waves in the ocean may be generated in a number of ways. The generating mechanisms include: (1) tidal action, which creates a semi-diurnal or diurnal vertical oscillation of the internal wave, (2) flow impinging on a continental shelf, (3) flow over irregular topography (sill) or around a topographic obstacle (island), (4) along water mass boundaries between two adjacent flows (less dense water over denser water), (5) variations in atmospheric pressure and strong winds, such as found in areas of severe tropical cyclones, and (6) seismic disturbances. Although the amplitudes of internal waves may exceed those of surface waves, internal waves usually propagate at slower speeds. Internal waves on a thermocline in the ocean are progressive waves, and water particles move in alternate clockwise and counter-clockwise vertical orbital planes in response to the amplitude, period, and direction of propagation of the waves (figure A11). In this idealized case, described by LaFond and Cox (1962), the waves are sinusoidal (i.e., with a regular alternate crest and trough pattern), and the amplitude of the waves vanishes at the sea surface. Note that the vertical motion produced between the thermocline and the surface is: (1) downward ahead of the trough due to convergency of the flow between adjacent circulation cells, and (2) upward behind the trough due to divergence of the flow between adjacent circulation cells.

The sea surface features in this idealized schematic are based primarily on visual observations from ships and aircraft. The rough zone at the surface is assumed to be caused by an increase in the speed of the flow just below the surface as a ridge replaces a trough and the water is forced to pass through the constricted region between the surface and the raised thermocline. (The speed of the flow in the horizontal direction is inversely proportional to the thickness of the layer between the thermocline for orbital oscillations limited to the vertical plane, as in this idealized schematic.) The smooth area, or surface slick, occurs in the convergence zone above the adjacent downward-flowing cells.

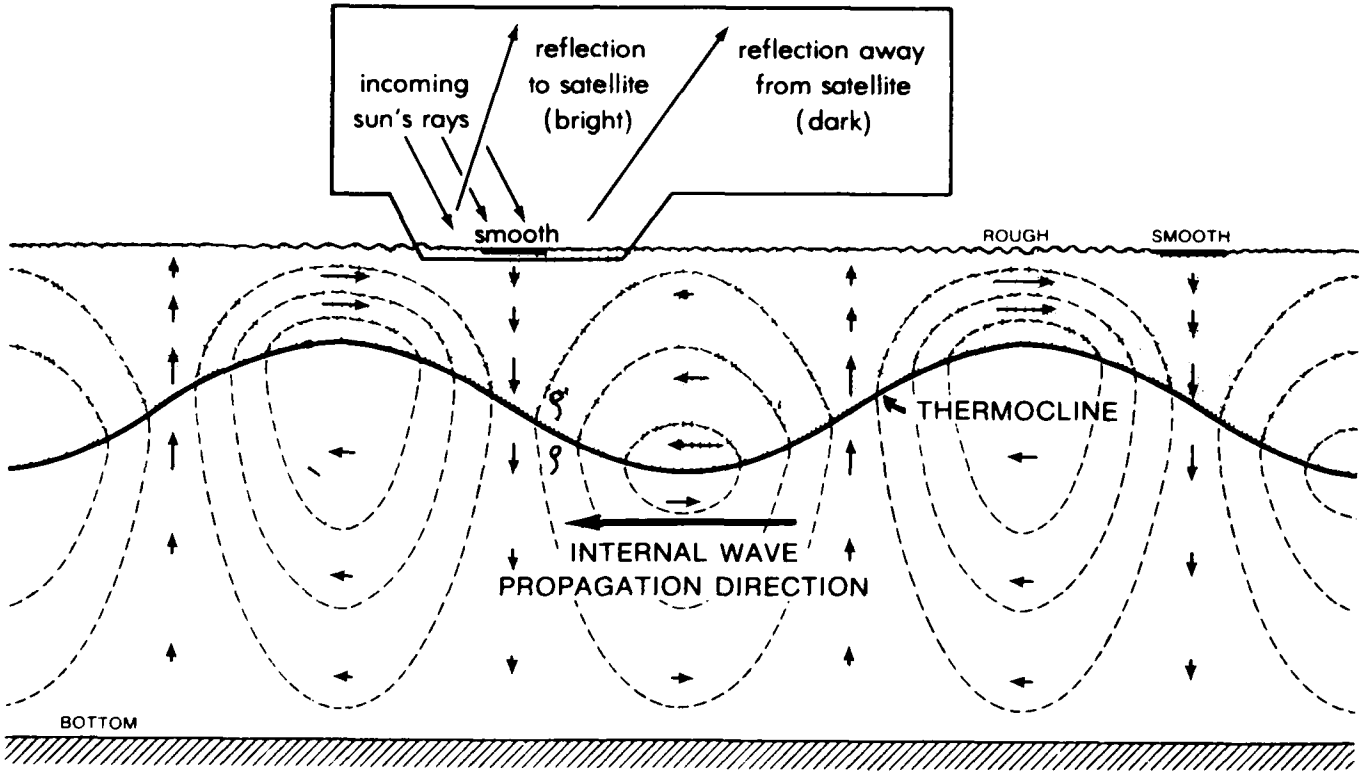

Figure A11. Schematic of the structure of progressive internal wave motion along a sharp thermocline. The small arrows represent streamlines of particle flow (after LaFond and Cox, 1962)

The occurrence of internal waves along the thermocline has a direct influence on underwater sound transmission (Katz, 1967). This influence is due to refractive effects which depend on the temperature gradient within the thermocline and the angle of intersection of the sound waves with the thermocline. When the thermocline undulates, the sound waves intersect at varying angles resulting in a disruption of the acoustical wave propagation. Thus, the use of sonar may be adversely affected within and through an area of internal waves. In addition, sound refraction and condensation effects can suggest false targets, while permitting actual targets to pass undetected.

Internal waves in the ocean cannot be directly observed from satellite platforms. However, surface manifestations of internal waves can be detected in visible, polar-orbiting satellite data when they occur in areas of nearly calm winds and sea conditions, and where sunglint patterns are also present (see Appendix B). The surface manifestations appear as distinctive alternate bright and dark bands in the sunglint area that reveal the internal wave front patterns below the ocean surface.

Several concepts proposed to describe the characteristic appearance of the alternate bright and dark bands observed on the surface in areas of internal waves. LaFond and Cox (1962) suggest that the orbital motions induced by internal waves sweep together surface oil and debris to form a slick in the regions of surface water convergence (see figure A2). According to this concept, brilliant reflection would be observed in a sequence of bands at or near the Primary Specular Point (PSP)--with each of the bright bands (slicks) separated by a darker band of slightly rougher seas. The effect would be reversed at large distances to the north or south of the PSP. Apel et al. (1976) suggest that "small waves are concentrated in the convergency regions due to wave-current stresses," with intervening smoother regions. In this case, dark bands separated by brighter bands would be observed near the PSP.

If it is assumed that the internal waves are nonvanishing at the sea surface, as is indicated in Figure A11, and that small, sea-surface oscillations are caused by internal waves (seismograms recorded on Arctic ice show oscillations with periods characteristic of internal waves; Monin, Kamenkovich, and Kort, 1974), the reflective pattern from these surface waves (swell) would produce the alternately banded structure observed. At the crest of each surface wave, contiguous bright and dark bands would be produced, with intervening bright areas between the bands, as shown schematically in Figure A11. It is important to note that although many cases of internal waves have been documented showing areas of rough water alternating with surface slicks, these features have not been noted in all cases and are not necessary to produce the reflective effects often observed in visible satellite imagery.

A line drawing (Apel et al., 1976) of a set of internal wave packets was interpreted from a computer-enhanced, Landsat 1 image of the Long Island, New York, area and is illustrated in Figure A12. The figure also shows bottom bathymetry to illustrate the general orientation of the lines of constant wave phase with the isobaths, as well as the concentration of wave activity near the Hudson Valley on the continental shelf. A detailed analysis shows several characteristics (Apel et al., 1976) which are worthy of note and are illustrated in Figure A13:

(1) the waves occur in groups or packets with widths (L) from 3 to 5 km, usually landward of the continental slope and separated by distances (D) which are of the order of either 15 or 30 km; taken together with both the observed and calculated phase velocities, these facts suggest a semidiurnal or a diurnal origin;

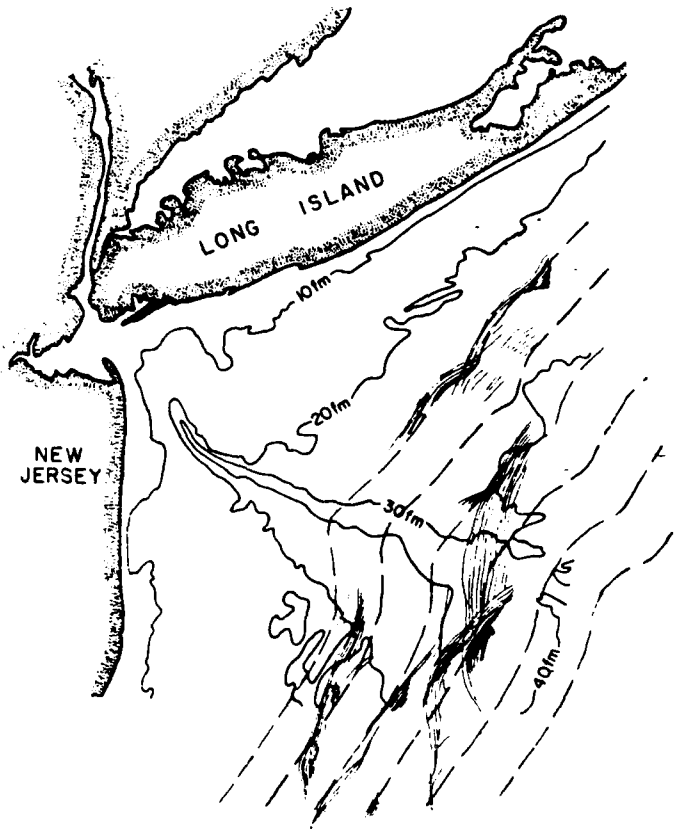

Figure A12. Geographically corrected line drawing of internal wave fields observed in LANDSAT image superimposed on bottom topography. The dashed lines show isophase contours as calculated from a two-layer model. (Apel et al., 1976)

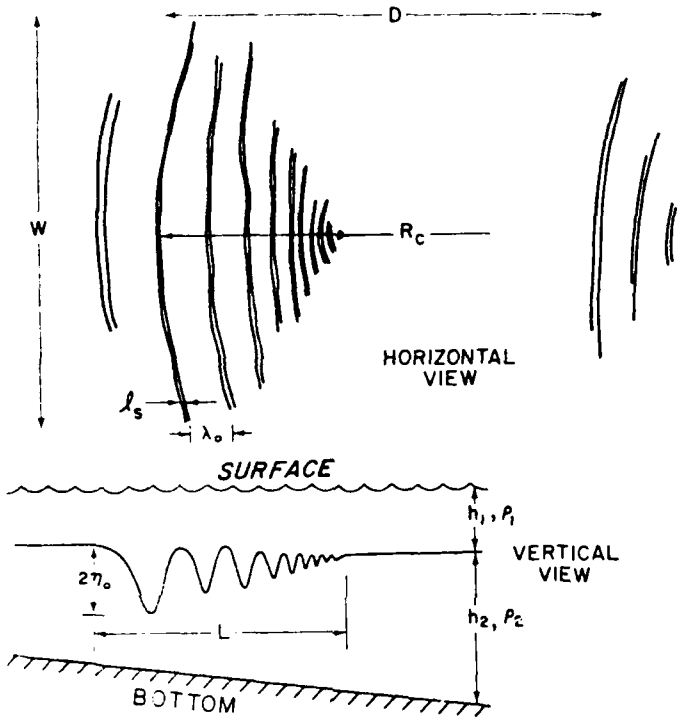

Figure A13. Schematic of internal wave packet showing characteristic lengths and features; (upper) view from surface; (lower) view in a vertical section (Apel, et al., 1976)

(2) the crests are nearly always oriented parallel to the local bottom topography or can be loosely associated with some topographic feature seaward of their observed position, or both;

(3) the wavelengths fall between 200 and 10,000 nautical miles depending on the geographical area; within a given packet, there is often a monotone decrease in wavelength, varying from λ_0 at the front to $\lambda < \lambda_0$ at the back of the group;

(4) the lengths of the crests (w) fall between a very few and perhaps 100 km, with a decrease in crest length occurring from front to back of the group;

(5) the widths of the slicks (ℓ_s) are often small compared to the lead wavelength (λ_0);

(6) the crests are curved in a horizontal plane with their convex sides pointed in the direction of propagation; the radii of curvature (R_c) range from essentially infinity to a few kilometers;

(7) as the packet progresses up on the shelf, there is some evidence of a continued increase in the wavelengths throughout; an accounting for this effect may result from a combination of linear dispersion and nonlinear effects akin to solitary wave behavior;

(8) few packets are ideally typical, but such a typical packet would show curved crests, with the length of the crests decreasing toward the center of curvature, so that the packet is wedge-shaped. The distance between successive slicks and the contrast of slicks also decrease toward the center of the curvature. This typical packet is simply interpreted, at least qualitatively, as advancing shoreward from the place of generation. The longer waves (and those of greater amplitude) have the greater velocity (Apel et al., 1976; Sawyer et al., 1976);

(9) in most packets, the leadi as interpreted above, is light the background and is followed darker strip. In packets that curved outward, apparently tra away from the shore, the light still appears at the leading e (Sawyer et al., 1976). Schema internal wave packets showing characteristic lengths and fea (taken from Apel et al., 1976) illustrated in Figure A13.

F. Bibliography

Apel, J. R. and R. L. Charnel Ocean Internal Waves Off the N American and African Coast fro ERTS-1. NASA Report SP-351, N Washington, D.C., p.1209-1316.

Apel, J. R., H. M. Byrne, J. R and R. Sellers (1976). A Stud Oceanic Internal Waves Using S Imagery and Ship Data. Remote of the Environment, 5(2): 125-

Bretschneider, C. L. (1959). Variability and Wave Spectra f Generated Gravity Waves. U. S Corps of Engrs., Beach Erosion Tech. Memo. no. 118, 192 pp.

Fett, R. and K. Rabe (1977). lite Observation of Internal W Refraction in the South China Geophysical Research Letters, 189-191.

Fett, R., P. La Violette, M. N Nickerson, K. Rabe (1979). Ve Environmental Phenomena and E (DMSP), NEPRF TR 77-04.

Johnson, J. W., M. P. O'Brien Isaacs (1948). Graphical Con of Wave Refraction Diagrams, Oceanographic Office, H. O. P 605.

Katz, E. J. (1967). Effect o Propagation of Internal Waves Underwater Sound Transmission Acoust. Soc. Am., 42, 83-87.

King, C. A. (1972). Beaches and Corals. Butler and Tanner Ltd., Frome and London.

Komar, P. D. (1976). Beach Processes and Sedimentation. Prentice-Hall, Inc., Englewood Cliffs, N.J.

LaFond, E. C. and C. S. Cox (1962). Internal Waves, The Sea. Vol. 1, M. N. Hill (Ed.), Interscience Publishers, New York, p. 731-763.

Lissau, S. (1975). Ocean Waves. Oceans, Sept.

Longuet-Higgins, M. S. (1963). The Generation of Capillary Waves by Steep Gravity Waves. J. Fluid Mech, Vol. 16, No. 1, p. 138-159.

Naval Oceanographic Office (1958). Breakers and Surf. N.O. Pub. No. 234.

Naval Oceanographic Office (1966). Glossary of Oceanographic Terms. Special Publication SP-35.

Naval Oceanographic Office (1966). Handbook of Oceangraphic Tables. Special Publication SP-68.

Naval Oceanographic Office (1963). Techniques for Forecasting Wind Waves and Swell. H.O. Pub. 604.

Neuman, G. and W. J. Pierson, Jr. (1966). Principles of Physical Oceanography. Prentice and Hall, Inc., Englewood Cliffs, N.J.

Pond, S. and G. Pickard (1978). Introductory Dynamic Oceanography. Pergamon Press.

Sawyer, C. and J. Apel (1976). Atlas of Satellite Images of Ocean Internal-Wave Signatures. NOAA S/T 2401.

Sverdrup, H. U., M. W. Johnson, and R. H. Fleming (1946). The Oceans. Prentice-Hall Inc.

Sverdup, H. U. and W. H. Munk (1947). Wind, Sea, and Swell. Theory of Relative for Forecasting. U. S. Hydrographic Office, H.O. Pub. No. 601.

APPENDIX B.

Appendix B. Sunglint

A. Sunglint Patterns

Sunglint or "sun-glitter" is observed whenever the sun's rays are reflected off a water surface (ocean, lake, river, delta, swamp, etc.). Sunglint patterns are regularly observed in aerial photographs and in the visible imagery obtained from geostationary and polar-orbiting satellites. The patterns vary in size, shape, and intensity of reflection, depending on

(1) the geometry of the scene (relative positions of the satellite subpoint, the area viewed, and the solar subpoint),

(2) the characteristics of the image forming system,

(3) sea state (smoothness or roughness of the water surface), and

(4) the low-level distribution of atmospheric aerosols and moisture, (Fett, et al., 1977).

B. Sunglint Patterns in Polar-orbiting Satellite Data

Examples of Apollo Spacecraft photography showing sunglint are displayed in Figures B-1 and B-2. Figure B1, which was taken during Apollo 6 (I.D. AS6-2-1495) is a vertical photograph centered in the West Atlantic Ocean at approximately 30°55'N, 76°18'W and covers approximately 77 square miles. A large, typical sunglint area is illustrated on the lower right, and an ocean front can be observed within the sunglint as a distinct variation in sea surface reflection. Possible explanations for the observance of the ocean front are variations in the sea surface roughness (resulting from local wind fields) and ocean color (resulting from the chemical/optical properties). Close examination of the sunglint area reveals a mottled texture characteristic of a highly wind stressed sea surface. (A similar texture can be observed in the Little Bahama Bank case history).

Note in Figure B-1 that the sunglint area appears to be concentrated in a central area, as illustrated by the bright orange intensity. With distance away from the area the brightness gradually decreases. At further distances the orange-colored sunglint grades to a light-blue color. The light-blue coloration grades to a darker blue as the effects of sunglint are reduced (as explained later, Landsat images can only contain sunglint from the light-blue area and not from the orange-colored area.)

Figure B-2, which was taken from Apollo 7 (I.D. A57-5-1632), depicts a classic example of sunglint occurring over the Gulf of California. The photograph was acquired on October 13, 1968, at 12:36 LST at an altitude of 226 km. Through the oval-shaped sunglint area on the west, a dark-blue, irregular-shaped area is shown. This dark area, when occurring within the sunglint area is an indicator of calm seas (see section C, Ocean Interaction with Sunglint). Because calm seas are directly related to low wind conditions, lower dark reflectant patterns which occur within the sunglint area provide a useful technique for estimating wind speeds and predicting local sea-breeze conditions. The small dark patch between San Pedro Nolasco Island (A), and Mexico (B) and the dark area in Concepcion Bay (C) are also indicative of calm seas. Remember that calm seas are not only the result of the wind field, but can be caused by other oceanographic phenomena, such as internal waves (as is described in Appendix A) and boundaries of surface currents. These calm areas, often referred to as slicks, can be observed within the sunglint area (right). These spiral-shaped, sinuous, dark-blue features indicate mixing patterns of surface currents. The clarity with which these sea surface features are shown, decreases with distance away

from the bright-orange-colored sunglint portion. It should be noted that at some distance from the central sunglint area, the techniques of interpreting sea surface roughness cannot be used, since sunglint is not occurring at that distance. Therefore, in the bay area (D) the dark-blue coloration cannot be interpreted as a calm sea area or that slicks are not present within the area. The light-blue colored water which follows the Mexico coast and intermittantly forms fingers into deep water (E) are sediment plumes from the local coastal processes and not the result of sunglint or sea surface reflectance. In Figure B-2 the primary specular point (PSP) appears at the left edge of the photograph (F).

C. Ocean Interactions with Sunglint

Sea state and atmospheric aerosols and moisture can modify the normal pattern so that sunglint may not be detected or, if detected, it appears asymmetrical or offset from the normally anticipated pattern.

Some rather complicated studies requiring computer services indicated that wind speed and direction can be determined grossly from the sunglint pattern (Kornfield, 1974). These studies have been conducted by applying statistical relationships to data from geostationary satellites. Similar relationships, further complicated by the geometry of polar-orbiting satellites, should be developed. With wind direction assumed constant, sunglint patterns over regions of increased wave height are enlarged in comparison to sunglint patterns over calmer seas. Similarly, total reflected brightness per unit area is reduced over areas of increased wave height. Reduction is such that little sunglint can be detected in extremely rough sea areas. Calmer seas reflect intensely over a small area.

Wave facets on the sea surface are continually varying the angles required for sunglint to occur. Capillary waves (see Appendix A) are mostly responsible for determining the amount of sunglint which will occur with an image. As the number of capillary waves increases (normally directly proportional to wind speed) the number of sea surface reflection facets increases, and the amount of sunglint appears diffused over a larger spacial area. In extremely rough seas the complex arrangement of capillary waves superimposed on large wind and gravity waves tends to diffuse reflection even more. Continued research is presently ongoing to quantify this relationship of wind, waves, and reflected radiation.

Other important principles are suggested, but require verification. For example, changes in sea state affecting height, period and direction, separately or in a combined manner, definitely influence total reflectivity measured from a given area. A symmetrical sunglint pattern implies relatively uniform moisture and sea state conditions. By the same reasoning, asymmetrical patterns suggest variable conditions.

D. Sunglint Effects on Landsat

The sunglint area will always fall in the region between the satellite subpoint and the solar subpoint. When a water surface is smooth (glassy or only small wavelets are present) the sunglint area will be small and intensely brilliant (i.e., a specular or mirror-like reflection of the sun); the most brilliant reflection will occur at the location of the primary specular point (PSP). The PSP is the point on the great circle arc passing through the satellite subpoint and the solar subpoint, where the angle of incidence of the sun's rays on a horizontal plane (measured from the local zenith) is equal to the angle of reflection of the sun's rays to the satellite in space. This occurrence appears on geostationary and certain polar-orbiting satellites.

In Landsat imagery because of the (1) position of the satellite, (2) position

of the sun at time of data collection, and (3) scan angle of the MSS, the PSP will never be imaged. However, there are conditions when Landsat is more likely to observe sunglint or the light-blue coloration surrounding the bright-orange area as illustrated in Figures B-1 and B-2. These favorable conditions are determined by the solar elevation at the satellite subpoint.

The unique orbit of Landsat causes the spacecraft to pass over the same point on the earth at essentially the same local time every 18 days. However, even though the local time remains essentially the same, changes in solar elevation angle, as defined in Figure B-3, cause variations in the lighting conditions under which imagery is obtained. These changes are due primarily to the north/south seasonal motion of the sun.

From the elevation of the sun the position of the PSP can be calculated, although the Landsat scanner does not image this area. However, the closer the PSP is to the satellite, the more favorable it is for sunglint to occur.

The distance from the Landsat satellite subpoint to the PSP is calculated for various solar elevations and illustrated in Figure B4. Notice that at 5° solar elevation the distance from the PSP to the satellite subpoint is 761 nautical miles, and since Landsat only images approximately 50 nautical miles each side of the subpoint, negligible sunglint will occur. However, at a solar elevation of 70° this distance has reduced to 179 nautical miles, and sunglint conditions are favorable to be observed in the image. From this figure it is evident that the solar elevation would have to be approximately 85° for the PSP to lie within the 50 nautical miles swath width of the Landsat system.

Figure B-5 shows the solar elevation angle as a function of time of year and latitude. This family of curves is for a 9:30 a.m. descending node time, which is the nominal time of equatorial crossing for Landsat satellites. By drawing a horizontal line for a given latitude, the solar elevation angle can be determined for any time of year. Portions of this data have been transferred to the global maps in Figure B-6. These maps show the range of possible sensor operation (i.e., daylight) for the various seasons. Depending on the scene, it may or may not be possible to obtain useful imagery at the lower solar elevation angles. At solar elevation angles greater than 30° it is expected that all scenes can be satisfactorily imaged. Normally, no attempt is made to obtain imagery for solar elevation angles less than 10°.

Notice that the greatest solar elevation present during Landsat coverage is approximately 60° (figure B-5). This elevation occurs during May and June at a latitude of 30°-40°N. From Figure B-4 the PSP is at a distance of approximately 268 nautical miles from the subpoint. Therefore, the PSP will not be imaged in the Landsat imagery. However, at this solar elevation more favorable conditions exist for sunglint to be present in the image than at lower solar elevations.

For an interpreter to determine whether sunglint is favorable in Landsat imagery, solar elevation should be calculated and used with figure B-4 to rule out possible misinterpretation.

Formulas for the calculation of solar elevation angle for any latitude, time of day and time of year are as follows (taken from U.S. Geological Survey, 1979):

$$a = \arcsin(\sin\delta \sin\phi + \cos\delta \cos h \cos\phi)$$

a = Solar elevation angle
δ = Solar declination
h = Hour angle (deg) to sun
ϕ = Latitude

Figure 6-1. Apollo 6, Vertical photograph, Western Atlantic Ocean

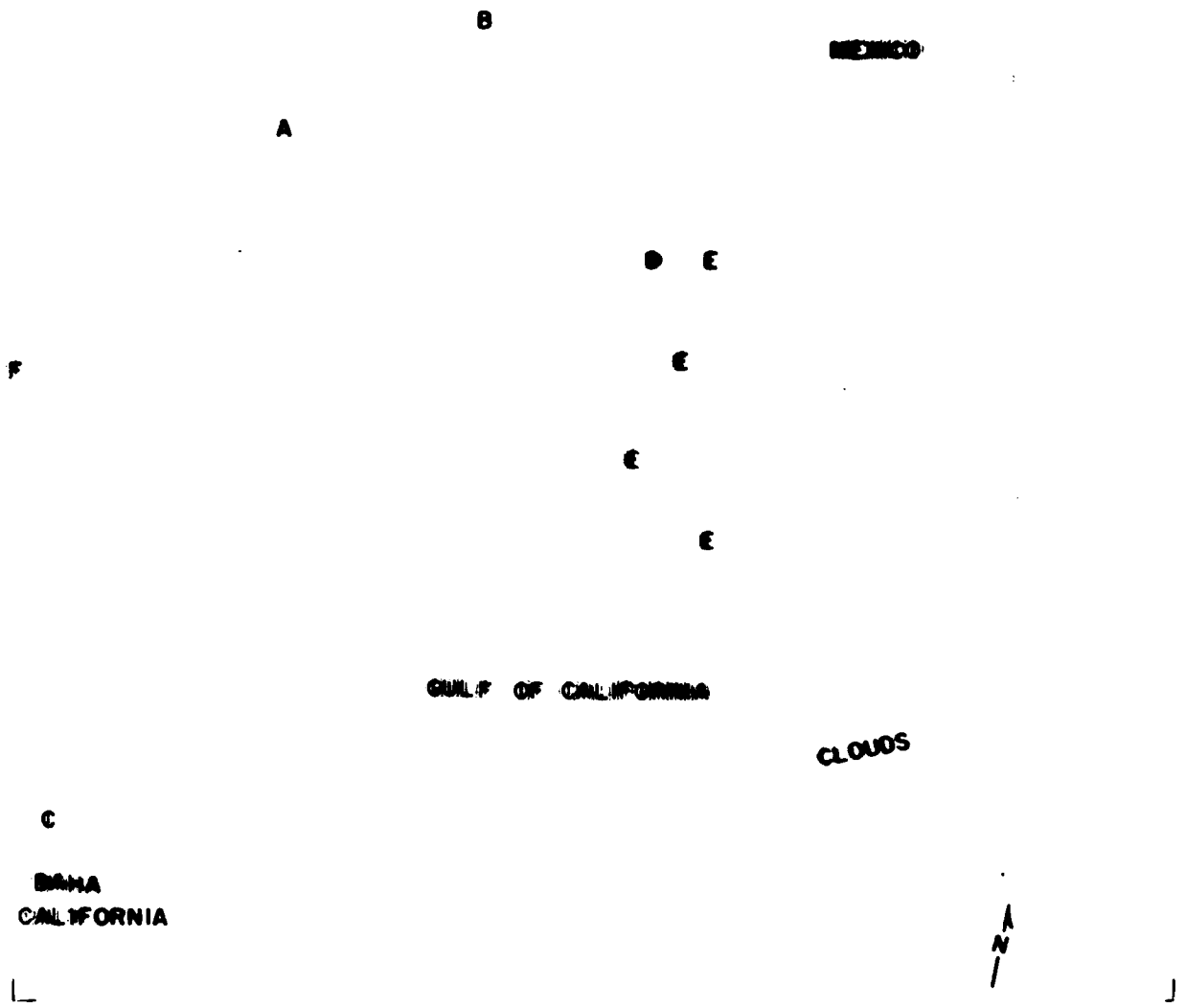
B
A
D
E
F
E
E
E
CLOUDS
C
CALIFORNIA
N

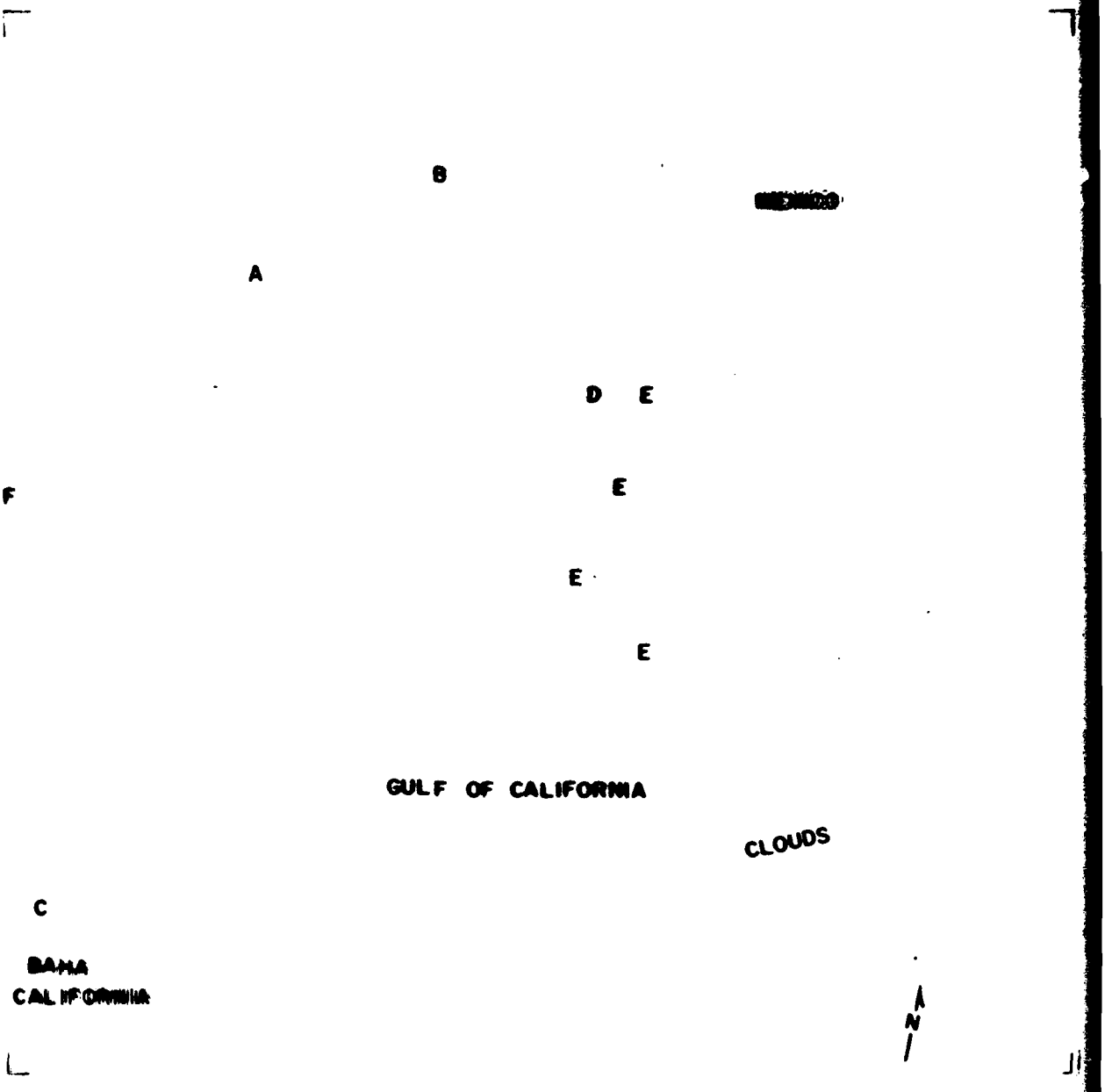
B
A
D
E
F
E
E
E
GULF OF CALIFORNIA
CLOUDS
C
BAJA
CALIFORNIA
N

Figure B-2. Apollo 7, Oblique photograph, Gulf of California (October 13, 1968).

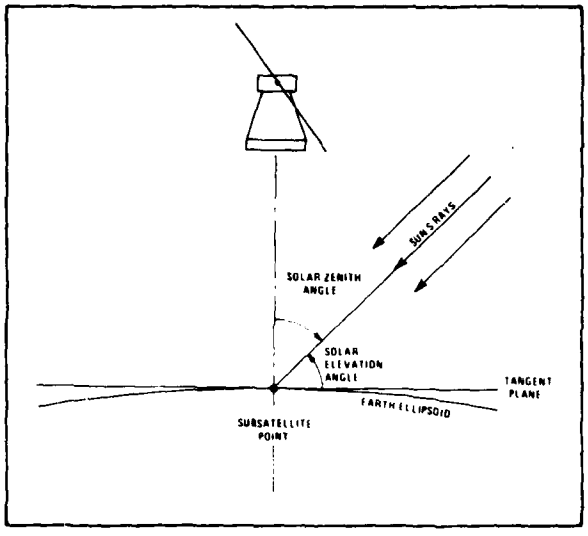

Figure B3. Solar elevation angle, (USGS, 1979)

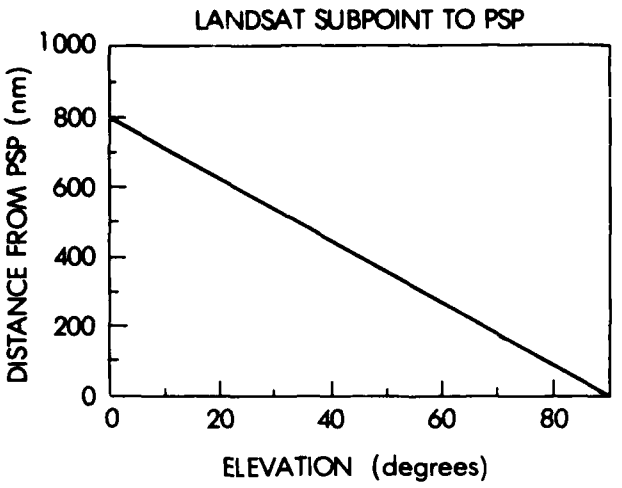

SOLAR ELEVATION DEGREES	DISTANCE NAUTICAL MILES
0.0	806.798
5.0	761.976
10.0	717.154
15.0	672.332
20.0	627.509
25.0	582.687
30.0	537.865
35.0	493.043
40.0	448.221
45.0	403.399
50.0	358.577
55.0	313.755
60.0	268.933
65.0	224.111
70.0	179.288
75.0	134.466
80.0	89.644
85.0	44.822
90.0	0.000

Figure B4. Distance of PSP to Landsat subpoint for various solar elevations (9:30 a.m.)

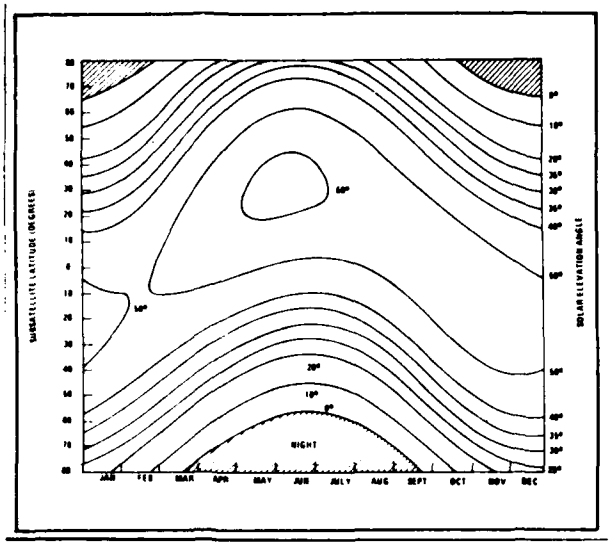

Figure B5. Solar elevation angle history as a function of subsatellite latitude - descending node at 9:30 a.m. (USGS, 1979)

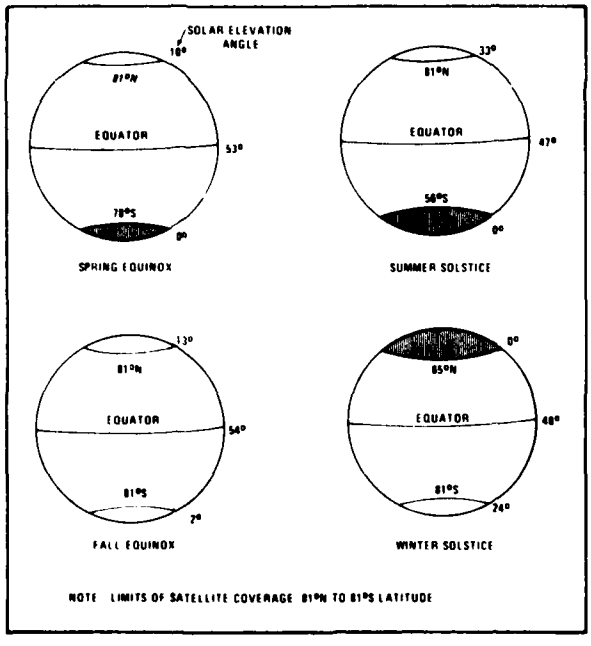

Figure B6. Seasonal variations in solar elevation angle - 9:30 a.m. - decending node (USGS, 1979)

Calculation of δ

Exact values of the Sun's declination can be obtained from the American Ephemeris and Nautical Almanac. A close approximation is given by the following formula.

$\sin = \sin i \sin \lambda$

i = Inclination to ecliptic=23.44°

λ = Sun's apparent position (0° at vernal equinox)

d = Days past vernal equinox ($\approx$21 March

δ = Arcsin [0.3978 sin (0.986°d)]

Calculation of h

1. Find the difference in hours and decimal hours, from 1200 (local standard time) to time of interest.

2. Change (1) to degrees by multiplying by 15°.

3. Using longitude of interest find difference in degrees to center longitude for respective time zone. (75°, 90°, 105°, or 120° for continental U.S.)

4. Add (3) to (2) if longitude of interest is to the east (of center longitude) and afternoon, or west and morning. Subtract (3) from (2) for opposite conditions. The final value is h.

Note: h has an error due to not accounting for the equation of time. This correction can be obtained from the American Ephemeris and Nautical Almanac. From the Table of the Sun, find ephemeris transit time for date of intrest and use instead of 1200 in step (1) above.

E. Spectral Sunglint Observations as Applied to Landsat

Sunglint occurs somewhat differently for each of the spectral channels of LANDSAT. Because sunglint is a reflection off the sea surface, it is observed in the spectral channels, including the two IR channels. Because the sun's IR radiant energy is absorbed by the water, the IR channels sense solely the reflected radiant energy off the sea surface. In the two visible channels of LANDSAT, the upwelling radiation of water color and the surface-reflected radiant energy are observed. A common technique to eliminate sunglint and enhance the water color is to subtract an IR channel (which represents surface reflectance) from a visible channel, thereby imaging the water color. This technique has problems, since reflectance is dependent on the incident intensity of the sun's energy.

Reflectance is defined as:

$$R = \frac{I_u}{I_I}$$

where:

I_u is the intensity of radiation reflected off the sea surface.

I_I is the intensity of the incident radiation at the sea surface.

For a fixed surface reflectance, R, the intensity of radiation of the surface reflectance, is directly proportional to the incident radiation; that is, the greater the intensity of the incident radiant, the greater the intensity of the reflected radiation.

By examining the sun's surface intensity of incident radiation on the ocean surface (Fig. 4) in each of the spectral channels of LANDSAT, note that the I_I is greater in Channels 4 and 5 than in the IR channels, 6 and 7. Therefore, the reflected intensity of radiation is greater in the visible channels than in the IR channels.

A simple subtraction of the channels, therefore, does not eliminate the radiation resulting from surface reflectance. It has been observed that in LANDSAT images the sea surface reflectance (sunglint) occurs most brilliantly in Channel 5 (see case

history for Cape Cod). This brilliance results from the high intensity of the sun's incident radiation (I_I), which occurs in this spectral channel as compared to the IR channels. In addition, between 0.6-0.7 μm (Channel 5) only a small amount of upwelling radiation from the water color occurs; therefore, the reflectance predominates. This combination is the optimum for imaging sea surface reflectance patterns.

F. References

Anderson, R. K., et al. (1974). Applications of Meteorological Satellite Data in Analysis and Forecasting. ESSA Tech. Report NESC 51 (including Supplement, Nov., 1971, and Supplement No. 2, March 1973), National Environmental Satellite Service, NOAA, Washington, D. C., 350 pp.

Fett, R. W. and W. F. Mitchell (1977). Vol. 1 Techniques and Applications of Image Analyses (DMSP), NEPRF Applications Report 77-03.

Kornfield, J. I. (1974). On the Determination of Sea Surface Wind or Stress From Sunglint Observed by an Earth Synchronous Satellite. Measurements from Satellite Systems, 1-60, Space Science and Engineering Center. Univ. of Wisconsin.

McClain, P. E. and A. E. Strong (1969). On Anomalous Dark Patches in Satellite-viewed Sunglint Areas. Mon. Wea. Rev., 97 875-884.

U. S. Geological Survey (1979). Landsat Data Users Handbook (Revised). Arlington, VA.

APPENDIX C

Appendix C. Oceanic Fronts and Major Surface Currents

Mean Positions of Major Oceanic Fronts (After Cheney and Winfrey, 1976)

Atlantic Ocean Fronts

1 Loop Current (Gulf of Mexico)
2 Gulf Stream
3 North Atlantic Current (North Polar Front)
4 Slope Front
5 Sargasso Sea Front
6 Subtropical Convergence
7 Iceland-Faeroe Islands Front
8 Denmark Strait Front
9 East Greenland Polar Front
10 Greenland-Norwegian Sea Front
11 Bear Island Front
12 Northwest African Upwelling
13 Gulf of Guinea Front
14 Guiana Current
15 Benguela Upwelling
16 Subtropical Convergence
17 Antarctic Convergence (South Polar Front)
18 Antarctic Divergence

Mediterranean Sea Fronts

19 Huelva Front
20 Alboran Sea Front
21 Maltese Front
22 Ionian Sea Front
23 Levantine Basin Front

Indian Ocean Fronts

24 Somali Upwelling
25 Arabian Upwelling
26 Indian Ocean Salinity Front
27 Equatorial Countercurrent Fronts
28 West Australian Front

Pacific Ocean Fronts

29 Kuroshio Front
30 Yellow Sea Warm Current
31 Korean Coastal Front
32 Tsushima Current
33 Oyashio Front
34 Kuril Front
35 Subarctic Front
36 North Doldrum Salinity Front
37 South Doldrum Salinity Front
38 Tropical Convergence
39 Mid Tasman Convergence
40 Australian Subarctic Front
41 Subtropical Front
42 California Front
43 East Pacific Equatorial Front

Mean Positions of Major Surface Oceanic Currents

1 Florida Current
2 Gulf Stream
3 Labrador Current
4 West Greenland Current
5 East Greenland Current
6 North Atlantic Current
7 North Equatorial Current
8 Equatorial Counter Current
9 South Equatorial Current
10 Brazil Current
11 Falkland Current
12 Antarctic Circumpolar Current
13 Benguela Current
14 Agulhas Current
15 North Equatorial Current
16 Equatorial Counter Current
17 South Equatorial Current
18 Kuroshio
19 Oyashio
20 North Pacific Current
21 Alaska Current
22 California Current
23 North Equatorial Current
24 North Equatorial Counter Current
25 Equatorial Current
26 South Equatorial Counter Current
27 South Equatorial Current
28 Humbolt Current

Appendix C. (Fett, et al., 1979)

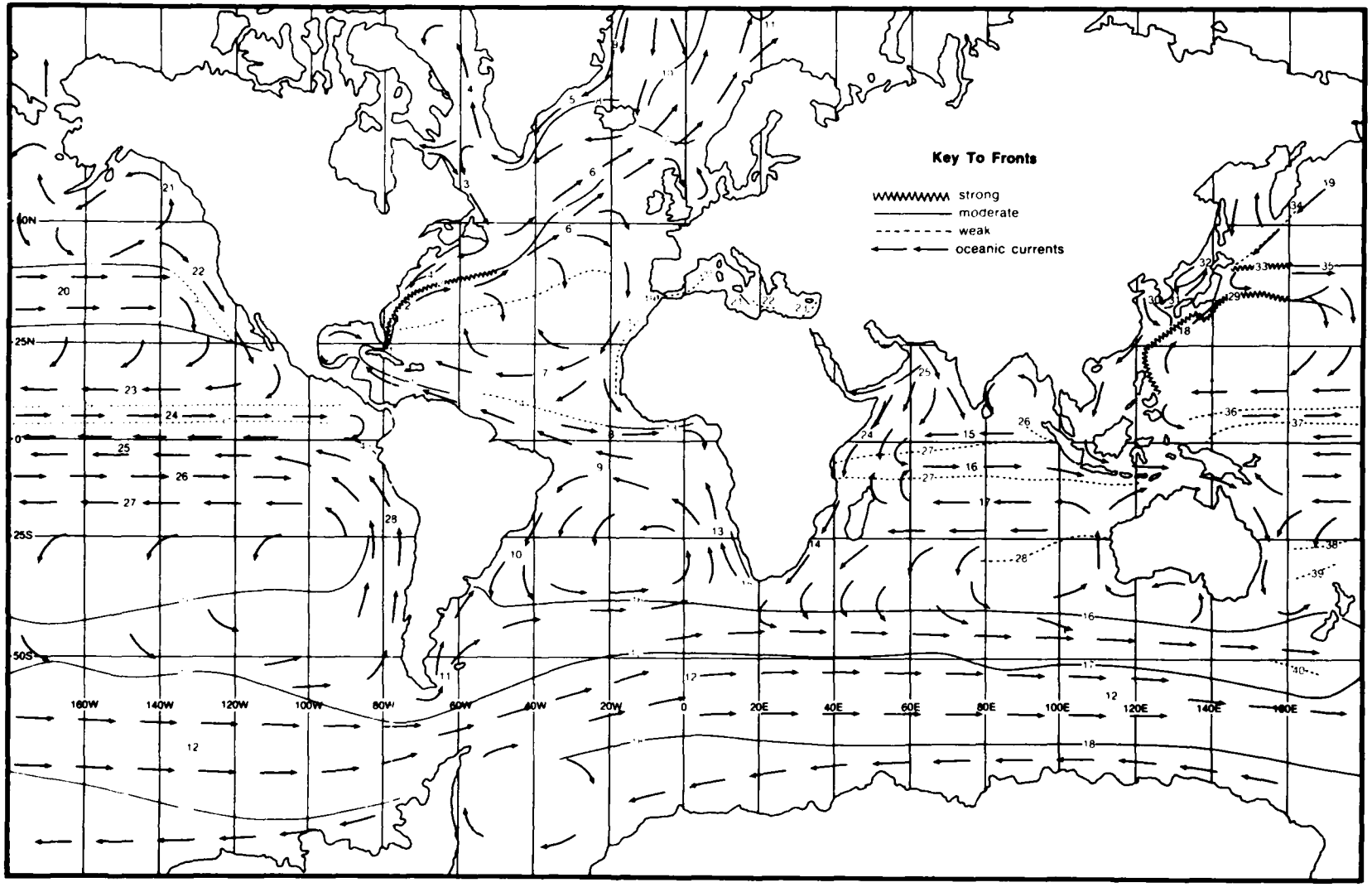

Figure C1. Major oceanic fronts and surface currents (Fett, et. al., 1979)

APPENDIX D.

Appendix D. Processes / Feature Index

Channels	
Dredged	1; 2-3,2-4; 4-6; 6-2,6-3,6-4,6-5,6-6; 9-3,9-6; 10-3,10-4
Subsurface (Dendritic)	1-2,1-3,1-6,1-7,1-9; 3-6; 4-6; 7-2,7-3,7-6,7-7,7-8,7-9; 10-3,10-4,10-7,10-8
Tidal	1; 2; 1-3,1-4,1-6,1-7,1-8,1-9; 2-3,2-4,2-5; 3-3,3-4,3-5,3-6,3-7; 4-6; 5-2,5-3,5-4,5-5,5-6; 6-2,6-3,6-4,6-5; 7-2,7-3,7-4,7-5,7-6,7-7,7-8,7-9; 9-2,9-3,9-4,9-6; 10-3,10-4,10-7,10-8
Clouds	2-3,2-4; 3-3,3-4,3-5; 4-7,4-8; 5-2,5-3,5-4,5-5,5-6; 6-2,6-3,6-4,6-5; 7-2,7-3,7-4,7-5,7-6,7-7,7-8; 8-2,8-3,8-4,8-5,8-6,8-7,8-8,8-9; 9-6; B2
Cloud Shadows	3-7; 6-2,6-3,6-4,6-5; 7-2,7-3,7-4,7-6; 10-3,10-4,10-7,10-8; B1;
Coral	B2 5-2,5-3,5-6
Currents	1-2,1-3,1-6,1-7; 3-3,3-4,3-6; 8-2,8-3,8-4,8-6,8-7,8-8; 9-2,9-3,9-4,9-6; 10-3,10-4,10-7,10-8; B1; B2
Deltas	1-2,1-3,1-4,1-5,1-8; 6-2,6-3,6-4,6-5; 8-2,8-3,8-4,8-5,8-6,8-8,8-9

Dredged Spoils	1-2,1-3; 4-2,4-3,4-7,4-8; 9-2,9-3,9-6
"Fish Whites"	7-2,7-3,7-6,7-7,7-8,7-9
Fog/Haze	1-2,1-3
Fronts (Ocean/Tidal)	2; 1-6,1-7; 3-3,3-4,3-6; 4-2,4-3,4-7,4-8; 6-6; 8-2,8-3,8-4,8-6,8-7,8-8; 9-2,9-3,9-4,9-6; 10-3,10-4,10-7,10-8; B1; B2
Islands	1; 2; 1-2,1-3,1-4,1-5,1-6,1-7,1-8,1-9; 2-3,2-4,2-5,2-6; 3-3,3-4,3-5,3-6; 4-2,4-3,4-4,4-5,4-6,4-7,4-8; 5-2,5-3,5-4,5-5,5-6; 6-2,6-3,6-4,6-5,6-6; 7-2,7-3,7-4,7-5,7-6,7-7,7-8,7-9
Oyster Reefs	4-2,4-3,4-6,4-7,4-8; 10-3,10-4,10-7,10-8
Reefs	1; 2; 1-2,1-3,1-6,1-7,1-8; 3-3,3-4,3-6,; 4-2,4-3,4-6,4-7,4-8; 5-2,5-3,5-6; 7-2,7-3,7-4,7-6,7-7,7-8,7-9
Rivers	6-2,6-3,6-4,6-5; 8-2,8-3,8-4,8-5,8-6,8-7,8-8,8-9; 10-3,10-4,10-5,10-6
Sea Surface Slicks	2-3,2-4; 6-6; B1; B2

Shoals	1; 2; 1-2,1-3,1-6,1-7,1-8,1-9; 2-3,2-4; 3-3,3-4,3-6; 4-2,4-3,4-6,4-7,4-8; 5-2,5-3,5-6; 6-2,6-3,6-6; 7-2,7-3,7-4,7-6,7-7,7-8,7-9; 9-2,9-3,9-6; 10-3,10-4,10-7,10-8
Spits (Submerged)	1; 2; 1-7; 2-3,2-4; 4-2,4-3,4-7,4-8; 6-2,6-3,6-6; 7-2,7-3,7-6,7-7,7-8; 9-6; 10-3,10-4,10-7,10-8
Sunglint/sea surface reflection	1; 1-6,1-7; 2-3,2-4,2-6; 6-6; 9-6; 10-7,10-8; B1; B2
Turbid Water Patterns	1-2,1-3,1-6,1-7,1-8,1-9; 2-3,2-4; 3-3,3-4,3-6; 4-2,4-3,4-6,4-7,4-8; 6-2,6-3,6-6; 8-2,8-3,8-4,8-5,8-6,8-7,8-8,8-9; 9-2,9-3,9-4; 10-3,10-4,10-7,10-8
Waves	
Breaking	1; 1-2,1-3; 4-2,4-3,4-7,4-8; 6-6; 7-2,7-3,7-4,7-6,7-7,7-9; 9-2,9-3,9-6; 10-7,10-8
Internal	2-1,2-3,2-4,2-5,2-6
Refraction	1; 2-3,2-4,2-5; 6-6; 9-6

Wetlands	1-2,1-3,1-4,1-5,1-6,1-7; 4-2,4-3,4-4,4-6,4-7,4-8; 6-2,6-3,6-6; 8-2,8-3,8-4,8-5,8-6,8-7,8-8,8-9; 9-2,9-3,9-4,9-5; 10-3,10-4,10-5,10-6,10-7,10-8

UNCLASSIFIED

SECURITY CLASSIFICATION OF THIS PAGE *(When Data Entered)*

REPORT DOCUMENTATION PAGE

READ INSTRUCTIONS BEFORE COMPLETING FORM

1. REPORT NUMBER: NORDA Report 39
2. GOVT ACCESSION NO.:
3. RECIPIENT'S CATALOG NUMBER:

4. TITLE *(and Subtitle)*: Interpretation of Hydrographic Features Using Landsat Images

5. TYPE OF REPORT & PERIOD COVERED:

6. PERFORMING ORG. REPORT NUMBER:

7. AUTHOR(s): Robert A. Arnone
B. Edward Arthur, Jr.

8. CONTRACT OR GRANT NUMBER(s):

9. PERFORMING ORGANIZATION NAME AND ADDRESS: Naval Ocean Research & Development Activity
Ocean Science & Technology Laboratory, Code 330
NSTL Station, Mississippi 39529

10. PROGRAM ELEMENT, PROJECT, TASK AREA & WORK UNIT NUMBERS:

11. CONTROLLING OFFICE NAME AND ADDRESS: Same as above

12. REPORT DATE: June 1981

13. NUMBER OF PAGES: 222

14. MONITORING AGENCY NAME & ADDRESS *(if different from Controlling Office)*:

15. SECURITY CLASS. *(of this report)*: UNCLASSIFIED

15a. DECLASSIFICATION/DOWNGRADING SCHEDULE:

16. DISTRIBUTION STATEMENT *(of this Report)*: Distribution Unlimited

17. DISTRIBUTION STATEMENT *(of the abstract entered in Block 20, if different from Report)*:

18. SUPPLEMENTARY NOTES:

19. KEY WORDS *(Continue on reverse side if necessary and identify by block number)*

Landsat
Hydrographic features
Coastal Processes
Imagery
Hazard Detection
Chart Revision
Zones of Safe Passage
Survey Planning
Aerial Photography

20. ABSTRACT *(Continue on reverse side if necessary and identify by block number)*

Landsat imagery provides a means for updating hydrographic charts. This manual is designed to instruct analysts in interpreting hydrographic features and coastal processes using Landsat imagery. Explanations are given of both the physical processes and remote sensing technology as related to interpretation of hydrographic features. Through comparisons of hydrographic charts, aerial photography and the various spectral channels of Landsat imagery, the manual clearly illustrates examples of interpreting hydrographic features and

(CONTINUED)

DD FORM 1 JAN 73 1473 EDITION OF 1 NOV 65 IS OBSOLETE
S/N 0102-LF-014-6601

UNCLASSIFIED

SECURITY CLASSIFICATION OF THIS PAGE *(When Data Entered)*

processes. Various case histories, illustrating different coastal regimes and hydrographic features, are presented with descriptions of the techniques used for interpretation. Methodologies for exploitation of Landsat imagery for updating nautical charts (inclusive of hazard detection, chart revision, zones of safe passages, and survey planning) are described.

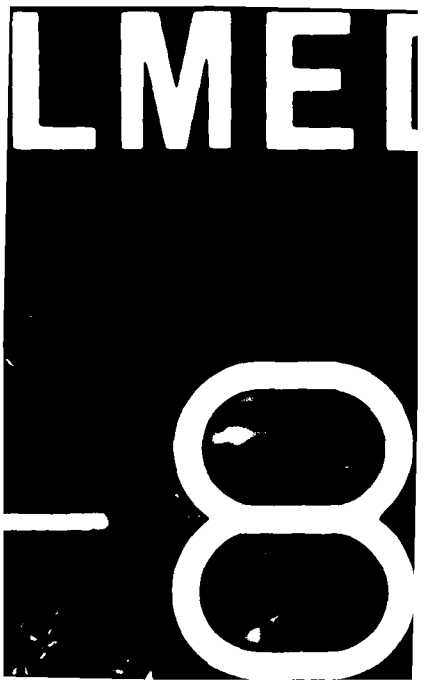
LME
8